SHRP-S-670

Control Criteria and Materials Performance Studies for Cathodic Protection of Reinforced Concrete

John Bartholomew, Jack Bennett, and Thomas Turk
ELTECH Research Corporation
Fairport Harbor, Ohio

William H. Hartt
Florida Atlantic University
Boca Raton, Florida

David R. Lankard
Lankard Materials Laboratory, Inc.
Columbus, Ohio

Alberto A. Sagüés
University of South Florida
Tampa Florida

Robert Savinell
Case Western Reserve University
Cleveland, Ohio

Strategic Highway Research Program
National Research Council
Washington, DC 1993

SHRP–S-670
Contract C-102D
Product Code: 2033

Program Manager: *Don M. Harriott*
Project Manager: *Joseph F. Lamond*
Consultant: *John P. Broomfield*
Production Editor: *Marsha Barrett*
Program Area Secretary: *Carina Hreib*

October 1993

key words:
bridges
cement and concrete
corrosion
cost information
mathematical modeling
structures design and maintenance

Strategic Highway Research Program
National Academy of Sciences
2101 Constitution Avenue N.W.
Washington, DC 20418

(202) 334-3774

350/NAP/1093

Acknowledgments

The research described herein was supported by the Strategic Highway Research Program (SHRP). SHRP is a unit of the National Research Council that was authorized by section 128 of the Surface Transportation and Uniform Relocation Assistance Act of 1987.

The work reported herein was conducted by several organizations and individuals, and each is acknowledged for his contributions of both research and writing. Test slabs were constructed and maintained by Dr. William H. Hartt at Florida Atlantic University for long-term effects. Concrete specimen preparation and petrographic work was done by Dr. David R. Lankard, Lankard Materials Laboratory, Inc. Mathematical modeling of concentration profiles in concrete was done by Dr. Robert Savinell of Case Western Reserve University. Mathematical modeling of current distribution was conducted by Dr. Alberto A. Sagüés and Dr. S. C. Kranc at the University of South Florida. The remainder of the work, including corrosion studies, long-term cathode effects, criteria studies and project direction, were done at ELTECH Research Corporation. Individuals at ELTECH contributing to this effort include Jack Bennett, John J. Bartholomew, Thomas A. Mitchell and Thomas R. Turk.

Contents

List of Figures

List of Tables

Abstract

The objective of this work was to investigate the feasibility of improved and simplified control criteria for cathodic protection of concrete structures. Corrosion rates of steel were established in a simulated concrete environment as a function of chloride contamination, pH, temperature and cathodic protection current. Mathematical models were developed to establish concentration profiles which develop as a result of cathodic protection current, and to study current distributions which result from geometric factors. These studies are combined to develop improved and simplified current-based control criteria. Long-term effects of cathodic protection current on concrete and aggregate near the steel and the anode were also investigated.

Executive Summary

The objective of this work was to investigate the feasibility of improved and simplified control criteria for cathodic protection of concrete structures. This objective has been accomplished with the investigation of two new current-based criteria.

The work was separated into three subtasks:

- Corrosion Rate Experiments
- Mathematical Modeling
- Long Term Effects

Corrosion rate experiments were conducted in a packed bed of sand wetted with simulated pore-water solution. This design permitted access of oxygen to the steel specimens and facilitated weight loss measurements. Corrosion rates were determined in such cells as a function of chloride concentration, pH and temperature at various levels of cathodic protection current. Increasing chloride concentration from 3 to 10#/yd^3 increased corrosion rate by a factor of five, while an increase of one pH unit decreased corrosion rate more than an order of magnitude. Although temperature had a small direct effect on corrosion rate, it has a significant indirect effect by increasing the ionic diffusion coefficients and concrete conductivity. Cathodic protection current was found to be a highly effective means of controlling corrosion in this environment.

Corrosion rates measured in these cells were then used to evaluate different criteria used for cathodic protection. The amount of polarization required to achieve an acceptable rate of corrosion (determined to be <0.1 mil/yr) was found to be a complex function of many variables. Although the data seem to verify 150 mV as an acceptable level of polarization initially, this criterion is likely to result in overprotection as the system matures.

A new current-based criterion was investigated which appears to be technically accurate and simple to apply. The technique, which makes use of a "Corrosion Null Probe"(CNP), calls for isolating a small piece of reinforcing bar in the most anodic location of the structure, and monitoring current flowing to or from this probe. Significantly, this technique does not rely on the long-term stability of embedded reference electrodes. Additional field experience is needed.

Other possible current-based criteria, which might be keyed to steel potential, chloride concentration, or linear polarization are also discussed. In particular, a cathodic protection current based on chloride concentration at the level of the reinforcement appears promising.

The feasibility of intermittent, as opposed to continuous, cathodic protection was also confirmed in experiments utilizing corrosometer probes in concrete. Short-term intermittent cathodic protection would allow the use of part-time power sources, such as photovoltaic arrays, wind power or nighttime lighting, without the need for battery storage.

Mathematical modeling was used to study concentration changes which occur in concrete as a result of the passage of cathodic protection current. The effects of several variables, such as chloride concentration, chloride distribution, pH, current density and temperature, on the development of concentration profiles were examined. All of these variables were found to have a significant effect on Cl^-/OH^- ratio, and therefore the corrosive state of the steel.

The mathematical model was then used in conjunction with results of the corrosion rate experiments above to predict the cathodic protection current requirement as a function of time. These results indicate that most mature cathodic protection systems are overprotecting.

The model was modified to predict and adjust the level of current needed to maintain acceptable corrosion (<0.1 mil/yr) as the cathodic protection system matured. Both current and polarization required at that time were significantly lower than required at system start-up. This work led to a simple current-based criterion dependent upon chloride concentration at the surface of the steel.

Another mathematical model was constructed to predict variations in current distribution which occur as a result of geometric factors such as anode resistance, concrete resistance, concrete cover, and potential of the steel. This model shows that anode resistance can be an important factor in determining uniformity of current, with delivered current tending to decay away from the power feed point. This concern deserves careful consideration during system design. Total voltage drop across the anode, due to its resistance, should be limited to about 250-300 mV. This constraint will be especially difficult to meet for conductive paint anodes.

This model also underscores the importance of locating reference electrodes in the most anodic areas of the structure.

Long term effects of cathodic protection current were examined near the surface of both anode and steel. Cathodic protection current was found to initiate or slightly accelerate alkali-silica reactivity in specimens containing chert and opal aggregate.

Analysis of samples taken near various embedded anodes revealed the effects of anode reaction products on concrete after a charge equal to 10 years of lifetime. Of the anodes tested, the titanium mesh resulted in the least alteration while Ferex™ wire and conductive polymer resulted in the greatest alteration. In no case did these alterations result in failure of the system during the test period, but they do suggest that criteria should be designed to avoid overprotection as well as to control corrosion.

Further work, both in the laboratory and the field, is recommended to confirm mathematical modeling of concentration profiles and simplified current-based criteria.

1

Introduction

The massive highway system that has been constructed in the United States has been an important element in the economic development of the nation. A key component of this infrastructure is steel reinforced concrete. A primary reason for the good long-term performance of this composite is that concrete provides an alkaline environment which causes the steel to "passivate", or become covered with a protective oxide film.[1] Unfortunately, with the advent of a widespread bare pavement policy in the early 1960's and significant coastal construction, a widespread corrosion problem began to occur at an increasing rate. In spite of the alkalinity of the concrete, it was determined that chloride ions, contained in deicing salt, seawater, or fresh concrete, could destroy the concrete's ability to keep the steel in a passive state.[2] Hausmann reported that if chloride to hydroxyl ion ratios exceed 0.6, embedded steel corrosion could occur, and such has been confirmed in recent investigations.[3] For bridge structures, it has generally been found that a concrete chloride content in the range of 1.0 to 1.4 lb chloride per cubic yard (0.6 to 0.8 kg per cubic meter) is the critical value above which steel corrosion in concrete can occur.[4,5,6] The corrosion product occupies more volume than the parent steel and this exerts tensile stresses on the surrounding concrete. When these stresses exceed the tensile strength of the concrete, cracking develops. This cracking often interconnects between reinforcing bars and the common undersurface fracture, or delamination, develops. As corrosion continues, the concrete cover breaks up and a pothole or spall is formed. This spalling is frequently accelerated by additional stress from freezing and thawing and traffic pounding.

Several practices which have the potential to extend the useful life of highway structures have been studied and implemented. Higher quality concrete, improved construction practices, increased concrete cover over the reinforcing steel, surface sealers, waterproof membranes, coated reinforcing steel, specialty concretes, corrosion inhibiting admixtures and other protective measures are being used extensively. It is generally agreed that new reinforced concrete structures constructed using selected protective systems will exhibit a long life. Many structures built prior to the 1980's remain chloride contaminated, however, and continue to deteriorate at an alarming rate.

In the early 1970s, it was recognized that concrete is an ionic conductor and capable of supporting a small flow of electric current. It was further recognized that this current could be used to alter the energy state of the reinforcing steel surface, and thus mitigate the corrosion process by the use of cathodic protection. This theory was first put into place by R.F. Stratfull and co-workers in the California Department of Transportation on the Sly Park Road Bridge in June, 1973.[7]

Since its first application, cathodic protection of concrete structures has expanded to its present use. A 1988-89 survey conducted by Battelle[8] indicated that more than 275 bridge structures in the United States and Canada have been cathodically protected. These structures represent a total concrete surface under cathodic protection of about nine million square feet. Cathodic protection anodes in use today include conductive polymer, paint, rubber and asphalt, catalyzed titanium, conductive polymeric wire, and zinc.

Cathodic protection has been demonstrated to be effective by a number of studies over the past few years. Test slabs and structures alike have shown a dramatic reduction in corrosion rate and deterioration when cathodically protected. Despite this experience, however, acceptance of cathodic protection for concrete structures has been slow. A major reason for this lack of acceptance has been the inherent difficulty of experimenting with steel in concrete to determine the effects of various control measures . Surfaces cannot be directly observed or readily measured in many of the conventional ways. Weight loss experiments are especially difficult to conduct. Without these quantitative measurements, the effectiveness of cathodic protection is very difficult to demonstrate.

Concrete is very inhomogeneous. Chloride and moisture content vary greatly throughout a structure, and these in turn affect the resistance and the distribution of current. Physical variations, such as concrete cover and reinforcing bar spacing, also affect the flow of protective current. Because of these complexities, the flow of current to the reinforcing steel is often unpredictable and may not always be adequate.

These factors have led to the need for establishing firm criteria for control of cathodic protection in concrete. Many different criteria have been suggested, primarily based on their use in cathodic protection applied in soil or seawater. These include criteria based on operating potential, potential shift, potential decay, current-potential relationship (E-log I) and a statistical treatment of static potentials. Although many such criteria have been proven effective in soil or seawater, their use in concrete has not been rigorously verified.

The objective of this research was to investigate the feasibility of improved and simplified control criteria for cathodic protection of reinforced concrete structures. A key element of this research was to measure the actual corrosion rate of steel in concrete under various conditions. These data allow, for the first time, a quantitative evaluation of protection and protection criteria. Second, the long-term effects of current were evaluated, especially in the vicinity of the anode and cathode. Harmful long-term effects can be used to establish a maximum level for criteria. Finally, mathematical modeling was used to improve our understanding of current distribution throughout a concrete structure, and of the concentration profiles which develop as a result of current flow.

2

Background

Criteria which are appropriate for inground use are not necessarily appropriate for use in concrete since the conditions in concrete are very different. Concrete is very basic with a pH of 12.5 or higher. The high pH facilitates the passivation of steel, and will moderate current requirements. The uniform distribution of current is more difficult in concrete, since the concrete-steel composite is inhomogeneous. The availability of oxygen is usually different in a concrete structure above ground compared with one inground. Also, overprotection is a greater concern in concrete since the anode is normally not easily serviced or replaced. Overprotection results in excessive acid production at the anode which may shorten the useful life of the system. Overprotection may also cause the reaction at the cathode to have detrimental effects on concrete and aggregate near the steel.

All of these factors suggest that current requirements and criteria for use in concrete should be based on data acquired in concrete. Criteria based on inground experience or on theory alone should not be considered sufficient.

The Battelle[8] survey showed that 223 structures were controlled using the 100 mV polarization decay technique. Second in frequency of use was the E-log I criterion, with 146 structures and the potential criterion of -850 mV versus copper/copper sulfate that was used on 58 structures. A number of other criteria were also being used to a lesser degree.

100 mV Polarization Decay

The 100 mV polarization decay was developed as a criterion in the inground cathodic protection industry and was first applied to reinforced concrete structures in the early 1980s. It is one of three criteria listed as acceptable in NACE Recommended Practice RP-0290-90, "Cathodic Protection of Reinforcing Steel in Atmospherically Exposed Concrete Structures."[9] The 100 mV polarization decay is described in that document as follows:

> "The reinforcing steel, and any other metallic embedments to be protected, shall be polarized a minimum of 100 mV at anodic locations. When using the polarization decay method, the decay is determined by interrupting the protective current and monitoring the reinforcement's potential measured relative to a stable reference electrode. When the current is interrupted, an immediate voltage shift will occur. This voltage shift is the result of eliminating the IR drop and is not to be included in the polarization measurements. The potential of the steel immediately after that shift shall be used as the initial reading from where to measure polarization decay. The polarization equals the initial reinforcement potential after interrupting the current subtracted from the reinforcement's final potential. .....Typically, the polarization decay criterion should be met within four hours."

Although the test described above seems straightforward, there are many questions unanswered. For example, how long after current interruption should the initial reading be taken? Are there cases when a test period longer than four hours should or should not be used? What is the effect of structure temperature on the outcome of the test? Exactly where should the test be conducted relative to physical parameters, such as concrete cover, reinforcing steel patterns, power feed points and salt concentrations? Is 100 mV too little or too much polarization? Any of these factors may profoundly influence the results of the test and the way a protection system is operated.

Some authors have recently tried to address such questions. Bennett and Mitchell[10] conducted an empirical evaluation and recommended that the amount of polarization be raised from 100 mV to 150 mV. In a technical review of polarization shift criteria, Funahashi and Bushman suggested that polarizations of 155 mV to 240 mV are needed, depending on the chloride content of the concrete.[11] This finding was reinforced in a subsequent paper by Funahashi and Young in 1992.[12] Other authors have suggested that 100 mV polarization is too high, and results in excessive polarization of the steel[13].

E-log I

The E-log I test is the second most used criterion. The E-log I criterion was first proposed for use in concrete by Stratfull in 1983[14], and is one of the three criteria listed in NACE RP0290-90.[9] It is described in the document as follows:

> "The E-log I test is performed by incrementally increasing the cathodic protection current from the installed system. At each interval, the IR drop free potential of the reinforcement is measured relative to a stable reference electrode. A plot of the

steel reinforcement potential versus the logarithm of the current applied is called an E-log I plot. When performing the E-log I test, the reference electrodes are placed at anodic locations. .....The current required for cathodic protection is the value determined to occur at the beginning of linear behavior of the plot. It should be noted that this is a purely empirical approach that is not supported by the electrochemical theory of corrosion. Under certain conditions, including nature of the structure, exposure conditions, etc., the linear portion of the plot may be difficult to determine. In these cases, alternative criteria should be applied."

The E-log I test is often difficult to interpret and apply. For this reason it is most commonly performed by consultants or service firms specializing in cathodic protection to initially energize the system. As pointed out in the NACE document, the linear portion of the curve is often very short, or non-existent. The slope of the linear portion of the curve, when it can be found, is much too high to have any theoretical meaning. These complications probably exist because electrode processes in concrete are normally controlled by diffusion. An E-log I curve, in order to have meaning in a theoretical sense, must not be limited by diffusion control, and the straight line portion must extend over about three orders of magnitude of current.

-850 mV Versus Copper/Copper Sulfate

The earliest criterion used was to polarize the reinforcing steel to a fixed potential versus a stable reference electrode. The fixed potentials most commonly used were either -700 mV or -850 mV versus CSE.[15,16] The application of these potentials originated in the cathodic protection of inground structures, and refer to controlling corrosion at a near neutral pH. Researchers soon found that the use of such criteria on concrete structures often resulted in very high and unneeded current levels. System operation based on these criteria therefore raises concern about premature deterioration of the anode and surrounding concrete. The dependency on a reference electrode which is stable over long periods of time also makes the use of such criteria difficult. Potential based criteria are generally no longer considered viable. It is somewhat surprising that the Battelle survey[8] found this criterion still being used on 58 highway structures.

Rebar Probes

Rebar probes (also known as macrocell probes) have been commonly used to monitor cathodic protection systems.[17] Typically, a rebar probe is a 5 in (13 cm) piece of bare #5 reinforcing bar with attached wire, cast into a mortar prism containing 15 # Cl^-/yd^3 concrete (9 kg/m^3). The precast probe is placed in an excavation where the reinforcing steel has been exposed on all sides. The excavation is then patched with chloride-free concrete. When the rebar probe is connected to the reinforcing steel through a 10 ohm resistor for monitoring purposes, a strong galvanic cell is established. The corrosion current flowing to the probe is monitored, and when proper cathodic protection current is applied the corrosion current is reversed. The rebar probe is usually constructed, and assumed, to be the most anodic site.

Therefore, if the rebar probe is observed to be protected, the other reinforcement may be assumed to be protected as well.

Although the theory and operation of the rebar probe is straightforward, and their use has been fairly extensive, they are not considered as a criterion in NACE RP0290-90.[9] It is the view of these authors that rebar probes have been underutilized in past practice, and deserve further consideration.

Rebar probes may have been lightly regarded in the past because of some practical concerns about their use. The construction of the probe and its installation, to create a strong macrocell, is artificial, and is usually not site specific. There is a concern that a probe installed in this way may not accurately represent the actual needs of the structure. A rebar probe installed in a structure with totally passive steel, for example, will still indicate a requirement for current. Also, duplicate rebar probes installed in the same cathodic protection zone will often indicate widely differing current requirements.

Statistical Distribution Analysis

The third criterion listed as acceptable by NACE RPO290-90 is based on a statistical distribution analysis of reinforcement half-cell potentials.[9] This method calls for the most electronegative reinforcement potential to be polarized to a more negative value by an amount that is equal to or greater than the standard deviation of the reinforcement potentials measured during the potential survey. This criterion has no history of use, however, and is not considered further in this report.

3

Corrosion Rate Experiments

The original experiments were designed to provide corrosion rate data for steel in a concrete environment and to use these data as a basis for the development of a criterion for cathodic protection. Prior to this study no such data were known to be in the available literature. The proposed approach for collecting the data was the corrosometer technique, designed with high sensitivity to measure corrosion rates as low as 0.01 mil/year.

Experiments during the first four months revealed a fundamental problem with this approach. Corrosion of steel in concrete is characterized by a high degree of pitting. The corrosometer technique relies on a uniform corrosion rate. The pitting that was experienced caused inconsistent results.

The magnitude of the problem required that an alternative approach be adopted. This involved the measurement of weight loss of steel specimens maintained in sand soaked with simulated pore-water solution. With this technique the specimens could be readily tested at several chloride and hydroxide concentrations, at different temperatures and under various levels of cathodic protection current. To this end, a corrosion cell was constructed that approximated a concrete specimen with a double mat of steel.

Sand Cell Experiments

Experimental Procedure

Cell Design

The cell, manufactured from 4 in. (10 cm) schedule 40 PVC pipe, had two chambers separated by Nafion® #N417, a cation exchange membrane, (Figure 3-1). One chamber contained the corroding coupon, or anode, in Ottawa sand (ASTM C109) saturated with simulated pore-water containing chloride. The other chamber contained the non-corroding coupon, or cathode, in Ottawa sand and pore-water without chloride. The pH of the pore-water was 13.37. The cation exchange membrane confined the chloride ion to the anode compartment.

Figure 3-1. Sand/Pore-Water Cell

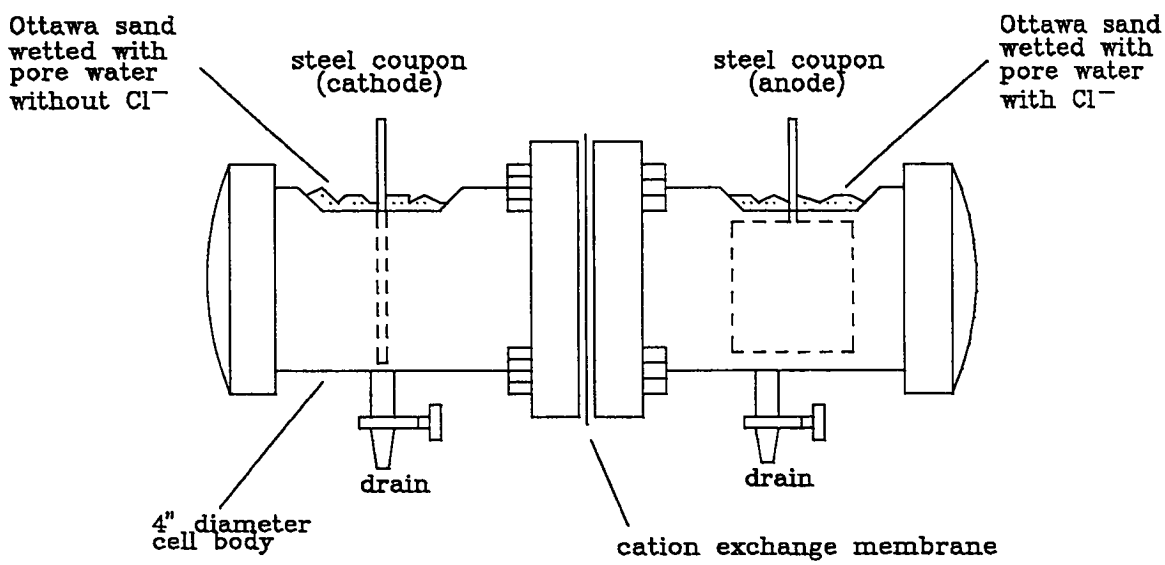

The cell design permitted testing the coupons under freely corroding conditions and also under cathodic protection. During the freely corroding tests, the coupons were placed perpendicular to each other with the anode situated parallel to the longitudinal axis of the cell. This anode orientation allowed for the placement of additional cathodic protection anodes during impressed current tests. During operation the two coupons were connected together through a 10 ohm resistor. The resistor provided a way to measure corrosion currents. Determination of i_3, either anodic or cathodic, was made by applying Kirchhoff's laws according to the schematic in Figure 3-2. Data monitored included corrosion potential, macrocell current, cathodic protection current and polarization decay.

Figure 3-2. Electrical Schematic of the Sand/Pore-Water Cell

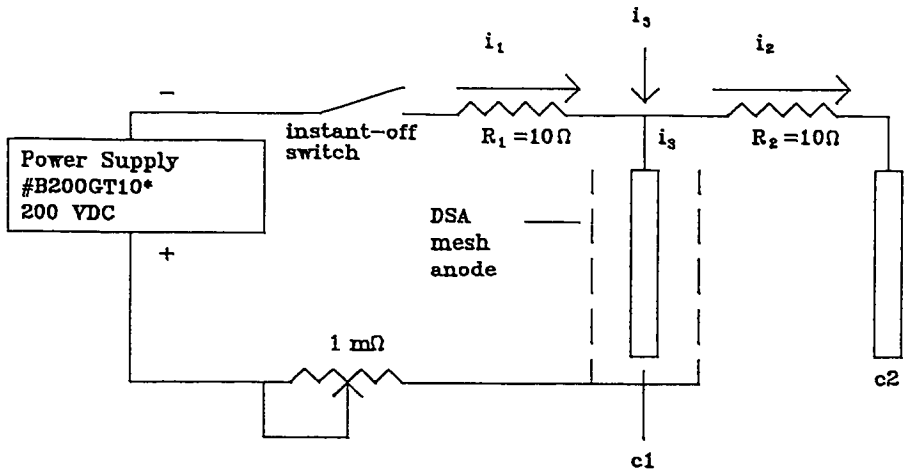

c1 = coupon #1 (corroding coupon)
c2 = coupon #2
E_1 = voltage drop across R_1
E_2 = voltage drop across R_2

i_1 = cathodic protection current = $E_1/10$
i_2 = macrocell current = $E_2/10$
i_3 = coupon #1 corrosion current
Since $i_1 + (-i_2) + (-i_3) = 0$
Then $i_3 = i_1 + (-i_2)$

Electrolyte Preparation

The corrosion rate experiments were conducted at Cl^- ion concentrations ranging from 1 to 30# Cl^-/yd^3 (0.6 to 18 g Cl^-/l) of sand. This was achieved by adding simulated pore-water with chloride to the sand in the anode compartment and standard pore-water to the sand in the cathode compartment. The composition of pore-water with chloride is found in Table 3-1.

Table 3-1. Simulated Cl^- Contaminated Pore-Water Composition

Chemical	Concentration wt. %
$Ca(OH)_2$	0.20
KCl*	3.20
KOH	1.00
NaOH	2.45

* - The KCl content varied, depending upon the desired Cl^- concentration

Chloride ion concentration was determined by adding an excess volume of pore-water to a known volume of sand. After draining the excess pore-water, the container was reweighed and the change in the weight attributed to the pore-water retained in the sand.

The concentration per unit volume was estimated by dividing the retained weight of chloride by the volume of sand. The use of a non-saturated electrolyte in this way ensured good access of oxygen to the steel coupons.

With a pore-water solution containing 3.2% KCl the resultant Cl^- concentration was 10.2#/yd^3 sand in the cell (6.1 g/l). The percentage of KCl in the pore-water was adjusted to yield the other concentrations.

Corrosion rate experiments were also conducted at various pH levels. The standard pore-water solution above has a pH in the range of 13.3 to 13.4. Tests were conducted in solutions ranging in pH from 12.89 to 13.92. The pH was adjusted by altering the concentrations of the NaOH and KOH as shown in Table 3-2. The pH was determined with a pH meter that was calibrated using a 3-point standardization method.

Table 3-2. Composition of Non-Standard Pore-Water Solutions Containing Salt

	pH			
Chemical	12.43	12.89	13.37*	13.92
$Ca(OH)_2$	0.2%	0.2%	0.2%	0.2%
KCl	3.2%	3.2%	3.2%	3.2%
KOH		0.25%	1.0%	2.45%
NaOH		0.61%	2.45%	9.8%

* - Standard pore water

Coupon Preparation

Coupons were first prepared by cutting SAE 1020 steel panels to the proper size. However, problems encountered with the preparation of the samples mandated that standardized pre-cut panels and a standardized cleaning procedure be implemented.

Pre-cut panels were purchased from the Q-Panel Co. The anode coupons measured 3 x 5 x .030 in. (7.6 x 12.7 x 0.08 cm). The cathode coupons measured 3.5 x 5 x .030 in. (8.9 x 12.7 x 0.08 cm). The panels were manufactured from standard cold-rolled steel complying with SAE 1010, ASTM A 366, and QQS-698. Both faces were abrasive ground at the factory to remove the mill scale.

Before testing, the coupons were weighed on an analytical balance. Due to the sensitivity required to determine weight losses, extreme care was taken during sample preparation to minimize contact with the surface of the coupons.

Following the completion of an experiment, weight loss determinations were conducted. The residual sand left on the coupon was rinsed off with tap water and the corrosion products were removed using ASTM G 1 - 90, "Standard Practice for Preparing, Cleaning and Evaluating Corrosion Test Specimens". Several procedures were tested until one was found that did not significantly attack the substrate.

The procedure chosen involved dipping the coupons for ten minutes in a room-temperature solution containing 20 g of antimony trioxide and 50 g of stannous chloride dissolved in 1 liter of concentrated hydrochloric acid (sp.gr. 1.19). After cleaning the test samples, a blank coupon was cleaned and the weight loss of the blank coupon was included in the final weight loss calculations.

The corrosion rate in mil/yr was calculated using the final weight loss according to the calculation below:

$$\frac{mils}{yr} = \left(\frac{gm}{day}\right)\left(\frac{365\ days}{yr} \times \frac{cm^3}{7.86\ g} \times \frac{inch^3}{16.387\ cm^3} \times \frac{1}{3\ inch} \times \frac{1}{3.5\ inch} \times \frac{1}{2\ sides} \times \frac{1000\ mils}{1\ inch}\right)$$

$$= \left(\frac{gm}{day}\right) \times 134.943$$

The detection limit for the experiments was based on the cumulative standard deviation of the weight losses from the blank coupons after etching. The detection limit for the experiments was 0.019 mil/yr. Weight losses below this number were reported as <0.02 mil/yr.

Effect of Cl^- Ion Concentration on Corrosion Rate

Non-Polarized Coupon Tests

Six different pore-water solutions ranging in concentration from 1 to 30# Cl^-/yd^3 (0.6 to 17.8 g Cl^-/l) sand were investigated for their effect on corrosion rate. Typically, the tests ran for twenty days during which time steel potentials and corrosion currents were monitored. Usually, four to six days elapsed before the onset of corrosion currents would occur. Figure 3-3 illustrates a representative response of corrosion current initiation to time on line.

Figure 3-3. Onset of Corrosion Current and Macrocell Potentials versus Time

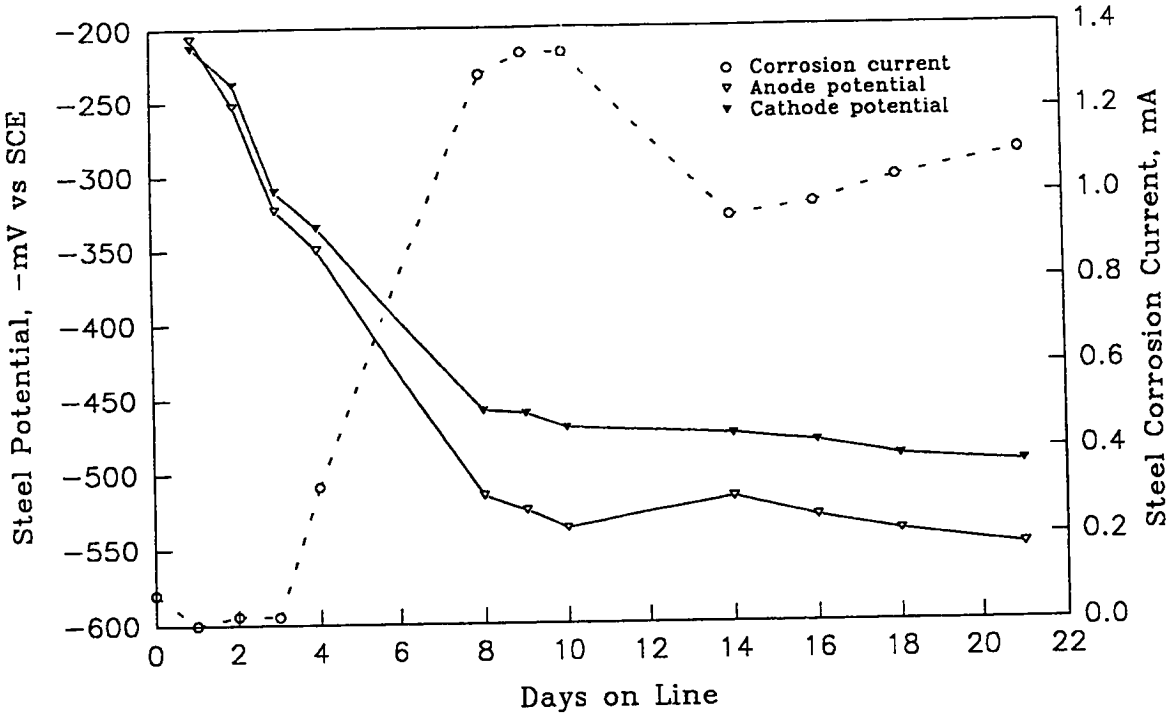

A marked negative shift in steel potential coincided with the onset of corrosion currents. Figure 3-3 shows the change in potential occuring at approximately the same time as the onset of macrocell currents.

Corrosion rates were determined on the unprotected coupons for each salt concentration. Although the weight loss results were variable, they show definite increase in the corrosion rate above 3# Cl^-/yd^3 (1.8 g/l) sand. Table 3-3 lists the results of the tests. Figure 3-4 is an important figure which illustrates the effect of chloride concentration on corrosion rate.

Table 3-3. Macrocell Corrosion of Non-Polarized Steel Coupons

	Cl^- lb/yd³	Coupon # 1	2	3	4	5
Avg. Corrosion Current (mA)	1	0.00	0.00	0.00	0.00	0.00
	3	-0.02	0.00	0.00	0.00	0.00
	5	-0.07	-0.04	-0.21	0.00	-0.05
	8	-0.18	-0.02	-0.21	0.00	0.00
	10	-0.01	-0.03	-0.25	-0.03	-0.16
	30	-0.48	-0.52	-0.81	-0.56	-0.40
1 Avg. Corrosion Current Density (mA/ft²)	1	0.00	0.00	0.00	0.00	0.00
	3	-0.11	0.00	0.00	0.00	-0.15
	5	-0.50	-0.25	-1.44	0.00	-0.33
	8	-1.20	-0.15	-1.44	0.00	0.00
	10	-0.08	-0.20	-1.71	-0.20	-1.10
	30	-3.30	-3.60	-5.60	-3.80	-2.70
Avg. Anode Potential (-mV vs SCE)	1	217	205	213	198	235
	3	297	214	219	223	276
	5	345	307	406	218	333
	8	431	304	460	226	242
	10	321	329	496	330	443
	30	481	498	533	455	459
Weight Loss (gm)	1	.0020	.0020	.0032	.0020	.0034
	3	.0098	<.0020	<.0020	<.0020	.0140
	5	.0360	.0161	.1054	<.0020	.0244
	8	.0903	.0132	.1366	<.0020	<.0020
	10	.0134	.0152	.1823	.0155	.1085
	30	.2674	.2770	.4591	.3184	.2080
2 Corrosion Rate (mil/yr)	1	<0.02	<0.02	0.02	<0.02	<0.02
	3	0.07	<0.02	<0.02	<0.02	0.09
	5	0.23	0.10	0.68	<0.02	0.16
	8	0.55	0.08	0.84	<0.01	<0.01
	10	0.09	0.10	1.23	0.10	0.73
	30	1.72	1.78	2.95	2.04	1.34
Average Corrosion Rate (mil/yr)	1			0.02		
	3			0.04		
	5			0.24		
	8			0.30		
	10			0.45		
	30			1.96		

1 - A negative number indicates net anodic current flow
2 - A corrosion rate of <0.02 was below the detection limit
1 mA/ft² = 11 mA/m²

Figure 3-4. Effect of Chloride Concentration on Corrosion Rate

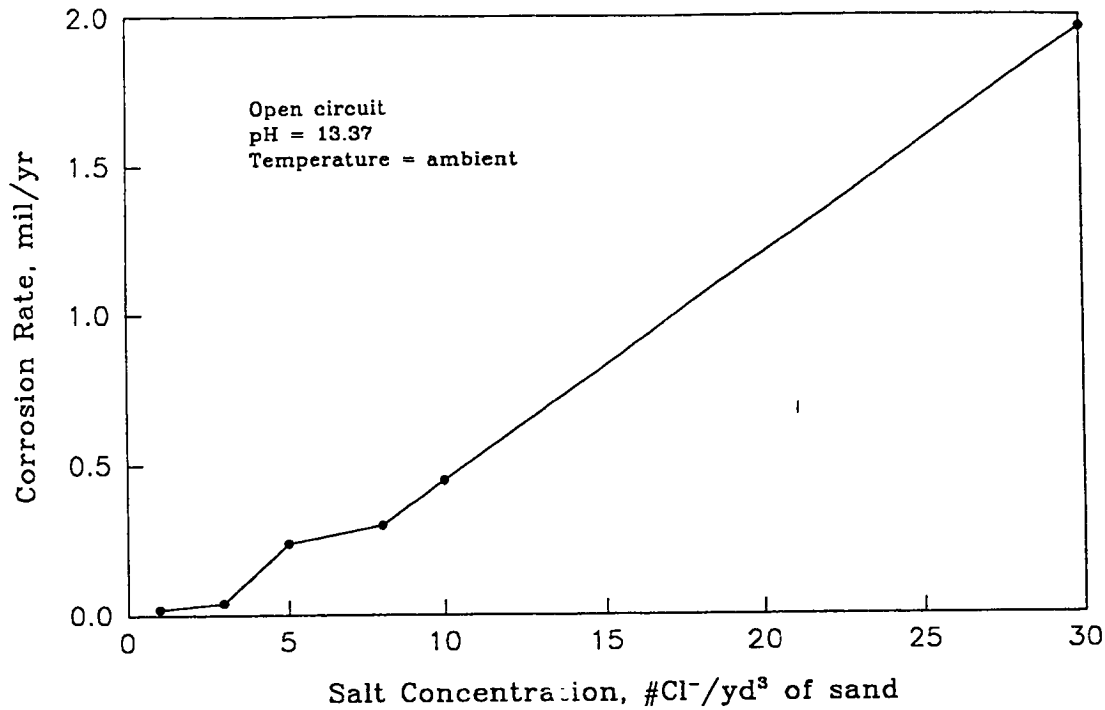

Polarized Coupon Tests

Tests under cathodically impressed currents were conducted based on an "allowable corrosion rate." A corrosion rate of 0.10 mil/yr was determined to be acceptable as established in time-to-cracking studies[18] (see discussion of potential shift criterion, Chapter 8). In that case, and based on data from these tests, a threshold chloride concentration for concrete deterioration appears to be about 2# Cl^-/yd^3 (1.2 g/l) concrete. Hausmann has suggested, however, a chloride/hydroxide ratio of 0.6 as a threshold for corrosion[3]. Calculations based on that ratio and a pH of 13.37, suggest that the threshold for corrosion in the sand cells should be 2.8# Cl^-/yd^3 (1.7 g/l) sand. The open circuit corrosion rate test results for coupons evaluated in 1# and 3# Cl^-/yd^3 (0.6 to 1.8 g/l) sand appear to be in good agreement with the calculated threshold number. Corrosion rates for those concentrations were below 0.05 mil/yr. Impressed current tests were not conducted under those conditions but were at the other concentrations beginning with 5# Cl^-/yd^3.

At an initial cathodic protection current density of 1.37 mA/ft^2 (13.7 mA/m^2) of steel, the coupons were evaluated and the average corrosion rate was determined. If the corrosion rate was grea · than 0.10 mil/yr, the test was repeated and the current density was increased to 2.74 mA/ft^2 (27.4 mA/m^2), or as in the case of 30# Cl^-/yd^3 (18 g/l) sand, increased to 4.11 mA/ft^2 (41.4 mA/m^2). Increasing the cathodic protection current resulted in consistently lower corrosion rates to below the threshold limit. During the tests, cathodic protection current, macrocell current, steel potential and polarization decay data were collected.

The data collected were highly variable, which is indicative of pitting corrosion. Some pits initiated, propagated and terminated in a short period of time. Other pits propagated over longer periods but eventually terminated, while others continued to propagate. The data clearly show a decrease in corrosion rate as the protection current was increased. Figure 3-5 illustrates this trend. Visual inspection of the coupons also showed a decrease in the amount of pitting corrosion corresponding to the increase in cathodic protection current.

Figure 3-5. Corrosion Rate versus Cathodic Protection Current Density

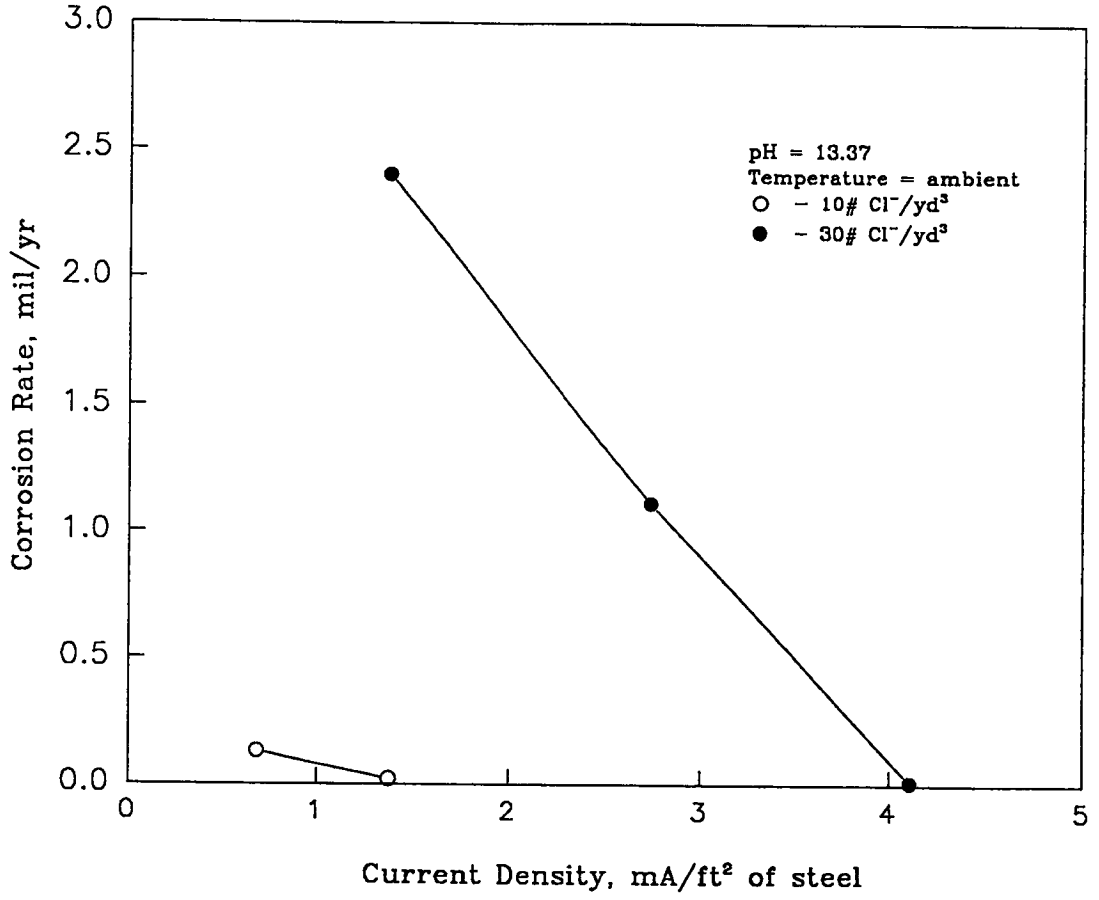

The polarization decay and steel potential data that were collected had consistent trends with increasing protection current. As cathodic protection current requirement increased due to increases in the chloride concentration at the steel surface, polarization increased and steel potentials became more negative. Figure 3-6 illustrates the change in polarization (plotted as polarization decay) as a function of cathodic protection current density.

Figure 3-6. Polarization Decay versus Cathodic Protection Current Density

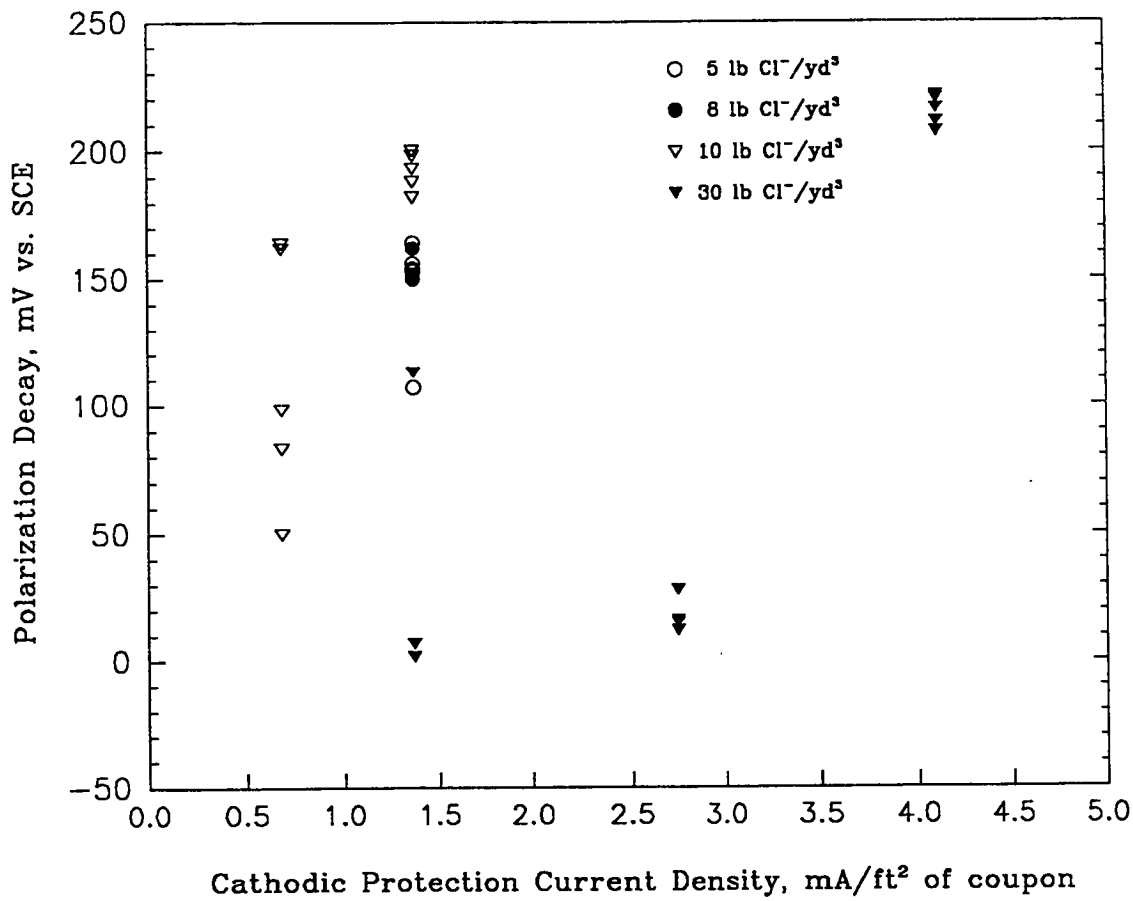

Among the criteria that have been applied to the cathodic protection of reinforced concrete is the 100 mV polarization decay over a 4-hour period. The trend that developed during these experiments was that the reduction of the corrosion rate to 0.10 mil/yr corresponded to a mean polarization decay of about 100 mV.

Twenty minute polarization decay tests were conducted three times per week. Initial tests indicated that much of the decay occurred during the first 20 minutes and 4-hour decays would have resulted in too much down time. Figure 3-7 illustrates these data.

Figure 3-7. Average Polarization Decay versus Corrosion Rate

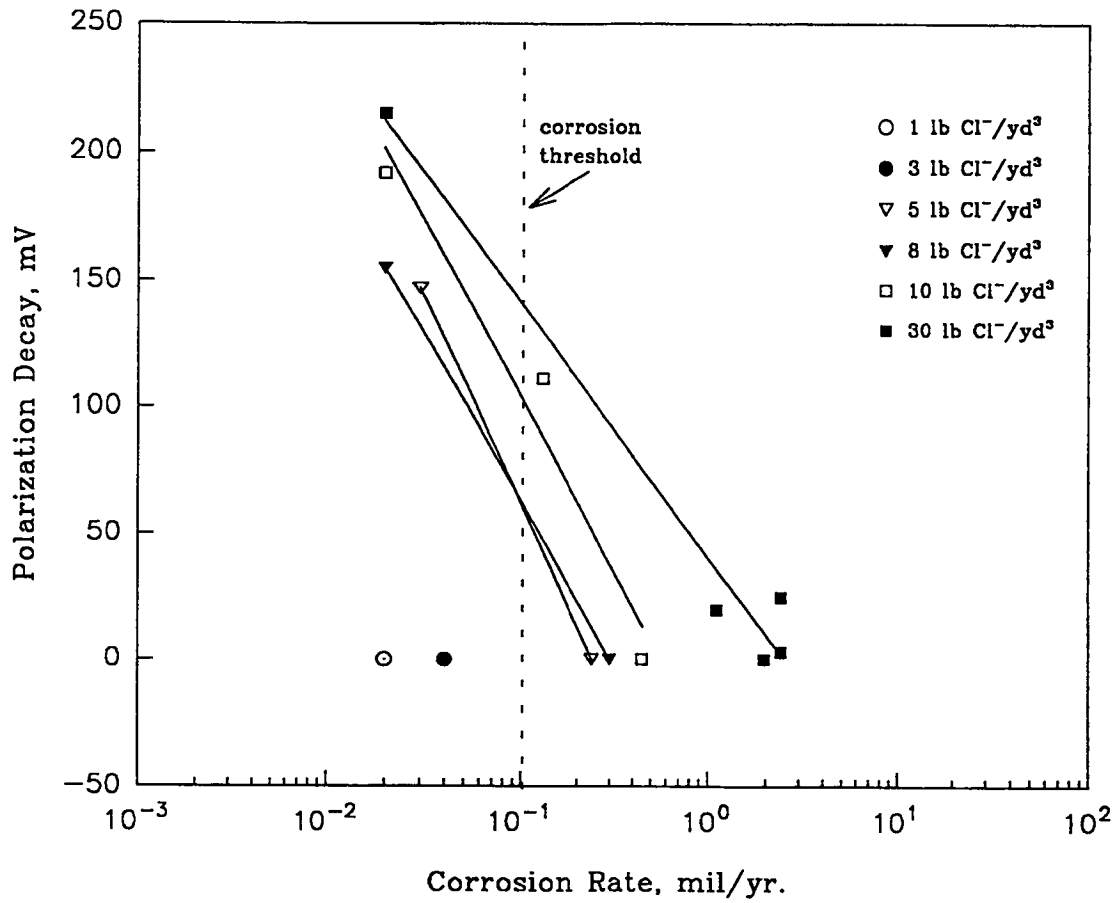

Coupons under Cathodic Protection in 5# Cl^-/yd^3 of Sand Based on the allowable corrosion rate criterion, only one test, conducted at 1.37 mA/ft^2 (13.7 mA/m^2) steel was needed to halt corrosion. The average polarization decay for the five coupons was 147 mV and the average corrosion rate was 0.03 mil/yr. Table 3-4 contains the data from the test.

Table 3-4. Corrosion Rate Data for Steel Coupons under Cathodic Protection in 5# Cl^-/yd^3 (3 kg/m^3) of Sand

		Current Density mA/ft^2	Coupon # 1	2	3	4	5
	Average	1.37	0.037	0.015	0.023	0.032	0.037
	Corrosion	2.74	-	-	-	-	-
	Current (mA)	4.11	-	-	-	-	-
1	Avg. Corrosion	1.37	0.25	0.10	0.16	0.22	0.25
	Current Density	2.74	-	-	-	-	-
	(mA/ft^2)	4.11	-	-	-	-	-
	Avg. Anode	1.37	423	399	390	401	400
	Potential	2.74	-	-	-	-	-
	(-mV vs SCE)	4.11	-	-	-	-	-
	Weight Loss	1.37	<.0020	.0112	<.0020	<.0020	<.0020
	(gm)	2.74	-	-	-	-	-
		4.11	-	-	-	-	-
2	Corrosion Rate	1.37	<0.02	0.08	<0.02	<0.02	<0.02
	(mil/yr)	2.74	-	-	-	-	-
		4.11	-	-	-	-	-
	Average	1.37	164	107	154	156	153
	Depolarization	2.74	-	-	-	-	-
	(mV)	4.11	-	-	-	-	-
	Average	1.37			0.03		
	Corrosion Rate	2.74			-		
	(mil/yr)	4.11			-		

1 - A positive number indicates net cathodic current flow, and hence, no macrocell corrosion.
2 - A corrosion rate of <0.02 was below the detection limit.
1 mA/ft^2 = 11 mA/m^2

Coupons under Cathodic Protection in 8# Cl^-/yd^3 of Sand The corrosion rate of the steel coupons fell below the threshold value after one experiment at 1.37 mA/ft^2 (13.7 mA/m^2) steel. Those data are presented in Table 3-5.

Table 3-5. Corrosion Rate Data for Steel Coupons under Cathodic Protection in 8# Cl^-/yd^3 (4.8 kg/m^3) of Sand

		Current Density mA/ft^2	Coupon # 1	2	3	4	5
	Average	1.37	0.044	0.042	0.048	0.040	0.056
	Corrosion	2.74	-	-	-	-	-
	Current (mA)	4.11	-	-	-	-	-
1	Avg. Corrosion	1.37	0.30	0.29	0.33	0.27	0.38
	Current Density	2.74	-	-	-	-	-
	(mA/ft^2)	4.11	-	-	-	-	-
	Avg. Anode	1.37	422	432	434	424	463
	Potential	2.74	-	-	-	-	-
	(-mV vs SCE)	4.11	-	-	-	-	-
	Weight Loss	1.37	.0042	.0020	<.0015	<.0015	<.0015
	(gm)	2.74	-	-	-	-	-
		4.11	-	-	-	-	-
2	Corrosion Rate	1.37	0.03	<0.02	<0.02	<0.02	<0.02
	(mil/yr)	2.74	-	-	-	-	-
		4.11	-	-	-	-	-
	Average	1.37	152	151	150	162	162
	Depolarization	2.74	-	-	-	-	-
	(mV)	4.11	-	-	-	-	-
	Average	1.37			<0.02		
	Corrosion Rate	2.74			-		
	(mil/yr)	4.11			-		

1 - A positive number indicates net cathodic current flow, and hence, no macrocell corrosion.
2 - A corrosion rate of <0.02 was below the detection limit.
1 mA/ft^2 = 11 mA/m^2

Coupons under Cathodic Protection in 10# Cl^-/yd^3 of Sand The initial experiment was conducted at 1.37 mA/ft^2 (13.7 mA/m^2) steel and the corrosion rate was below the threshold corrosion limit. The test was repeated at 0.68 mA/ft^2 (6.8 mA/m^2) to determine a relationship between cathodic protection current and corrosion rate. The corrosion rate was 0.13 mil/yr, and three out of the five coupons had average polarization decays below 100 mV. These data are found in Table 3-6.

Table 3-6. Corrosion Rate Data for Steel Coupons under Cathodic Protection in 10# Cl^-/yd^3 (6 kg/m^3) of Sand

		Current Density mA/ft^2	Coupon # 1	2	3	4	5
	Average Corrosion Current	0.68	0.03	0.03	-0.09	-0.02	0.01
		1.37	0.05	0.04	0.06	0.05	0.06
		2.74	-	-	-	-	-
1	Avg. Corrosion Current Density (mA/ft^2)	0.68	0.20	0.20	-0.62	-0.14	0.07
		1.37	0.34	0.27	0.41	0.34	0.41
		2.74	-	-	-	-	-
	Avg. Anode Potential (-mV vs SCE)	0.68	438	438	468	436	427
		1.37	470	463	488	463	457
		2.74	-	-	-	-	-
	Weight Loss (gm)	0.68	<.0020	<.0020	.0702	.0189	.0023
		1.37	.0032	<.0020	<.0020	<.0020	<.0020
		2.74	-	-	-	-	-
2	Corrosion Rate (mil/yr)	0.68	<0.02	<0.02	0.45	0.12	<0.02
		1.37	0.02	<0.02	<0.02	<0.02	<0.02
		2.74	-	-	-	-	-
	Average Depolarization (mV)	0.68	164	162	50	83	98
		1.37	198	193	200	188	182
		2.74	-	-	-	-	-
	Average Corrosion Rate (mil/yr)	0.68			0.13		
		1.37			<0.02		
		2.74			-		

1 - A positive number indicates net cathodic current flow, and hence, no macrocell corrosion.
2 - A corrosion rate of <0.02 was below the detection limit.
1 mA/ft^2 = 11 mA/m^2

Coupons under Cathodic Protection in 30# Cl^-/yd^3 of Sand Three experiments, at increasing cathodic protection currents, were conducted before corrosion could be lowered to less than 0.10 mil/yr. The data in Table 3-7 clearly show the relationship between cathodic protection current, polarization decay and corrosion rate.

Table 3-7. Corrosion Rate Data for Steel Coupons under Cathodic Protection in 30# Cl^-/yd^3 (18 kg/m^3) of Sand

		Current Density mA/ft^2	Coupon # 1	2	3	4	5
	Average	1.37	-0.55	-0.97	-1.10	-0.86	0.01
	Corrosion	2.74	-0.22	-0.25	-0.29	-0.14	-0.21
	Current (mA)	4.11	0.06	0.08	0.06	0.07	0.07
1	Avg. Corrosion	1.37	-3.77	-6.64	-7.53	-5.89	0.68
	Current Density	2.74	-1.51	-1.71	-1.99	-0.96	-1.44
	(mA/ft^2)	4.11	0.41	0.55	0.41	0.48	0.48
	Avg. Anode	1.37	467	496	512	483	359
	Potential	2.74	515	478	474	516	500
	(-mV vs SCE)	4.11	468	479	491	476	477
	Weight Loss	1.37	.2865	.5419	.6036	.4318	.0013
	(gm)	2.74	.1796	.1972	.2244	.1393	.1640
		4.11	<.0020	<.0020	<.0020	<.0020	<.0020
2	Corrosion Rate	1.37	1.84	3.48	3.88	2.77	0.01
	(mil/yr)	2.74	1.10	1.21	1.38	0.85	1.01
		4.11	<.02	<.02	<.02	<.02	<.02
	Average	1.37	7	2	2	2	113
	Depolarization	2.74	16	12	28	15	28
	(mV)	4.11	211	216	220	221	207
	Average	1.37			2.40		
	Corrosion Rate	2.74			1.11		
	(mil/yr)	4.11			<.02		

1 - A positive number indicates net cathodic current flow, and hence, no macrocell corrosion.
2 - A corrosion rate of <0.02 was below the detection limit.
1 mA/ft^2 = 11 mA/m^2

Effect of Hydroxide Ion Concentration on Corrosion Rate

Experiments were conducted in the sand/pore-water cells at 10# Cl^-/yd^3 (6 g/l) sand and 0.68 mA/ft^2 (6.8 mA/m^2) steel to investigate the effect of pH on corrosion rate. Four different pore-water solutions ranging in pH from 12.43 to 13.92 were evaluated.

Corrosion rates were 3.45 mil/yr in a solution of pH 12.43, and corrosion was not detected in the solution with pH of 13.92. The results in Table 3-8 highlight the significance of the Cl^-/OH^- ratio (at the steel/concrete interface) on the corrosion process.

Table 3-8. Effect of OH^- Concentration on Corrosion Rate

			Coupon #				
		pH	1	2	3	4	5
	Average Corrosion Current (mA)	13.92	0.02	0.01	0.01	0.01	0.005
		13.37	0.03	0.03	-0.09	-0.02	0.01
		12.89	-0.13	0.01	-0.12	-0.27	-0.12
		12.43	-0.63	-0.58	-0.58	-0.74	0.38
1	Avg. Corrosion Current Density (mA/ft^2)	13.92	0.14	0.08	0.09	0.07	0.03
		13.37	0.20	0.20	-0.62	-0.14	0.07
		12.89	-0.88	0.09	-0.82	-1.85	-0.84
		12.43	-4.32	-3.97	-3.97	-5.07	-2.60
	Avg. Anode Potential (-mV vs SCE)	13.92	497	502	515	459	445
		13.37	438	438	468	436	427
		12.89	557	468	588	589	580
		12.43	681	689	690	690	693
	Weight Loss (gm)	13.92	0.0000	0.0000	0.0000	0.0000	0.0000
		13.37	<0.0020	<0.0020	0.0702	0.0189	0.0023
		12.89	0.1660	0.0089	0.1409	0.2257	0.1873
		12.43	0.4806	0.4456	0.4045	0.6621	0.5609
2	Corrosion Rate (mil/yr)	13.92	0.00	0.00	0.00	0.00	0.00
		13.37	<0.02	<0.02	0.45	0.12	<0.02
		12.89	1.19	0.64	1.01	1.62	1.35
		12.43	3.24	3.01	2.73	4.47	3.78
	Average Depolarization (mV)	13.92	138	110	130	117	118
		13.37	164	162	50	83	98
		12.89	12	161	17	11	15
		12.43	-5	-7	-6	-4	3
	Average Corrosion Rate (mil/yr)	13.92			0.00		
		13.37			0.13		
		12.89			1.05		
		12.43			3.45		

1 - A positive number indicates net cathodic current flow, and hence, no macrocell corrosion.
2 - A corrosion rate of <0.02 was below the detection limit.
1 mA/ft^2 = 11 mA/m^2

Cathodic protection current depletes the Cl^- concentration and increases the OH^- concentration at the steel. The higher pH around the steel could promote passivation and this could mean a reduction in the amount of current required to achieve protection. This could mean a reduction of the amount of current required to achieve protection. Figure 3-8 illustrates the impact of OH^- concentration on corrosion rate.

Figure 3-8. Corrosion Rate versus pH

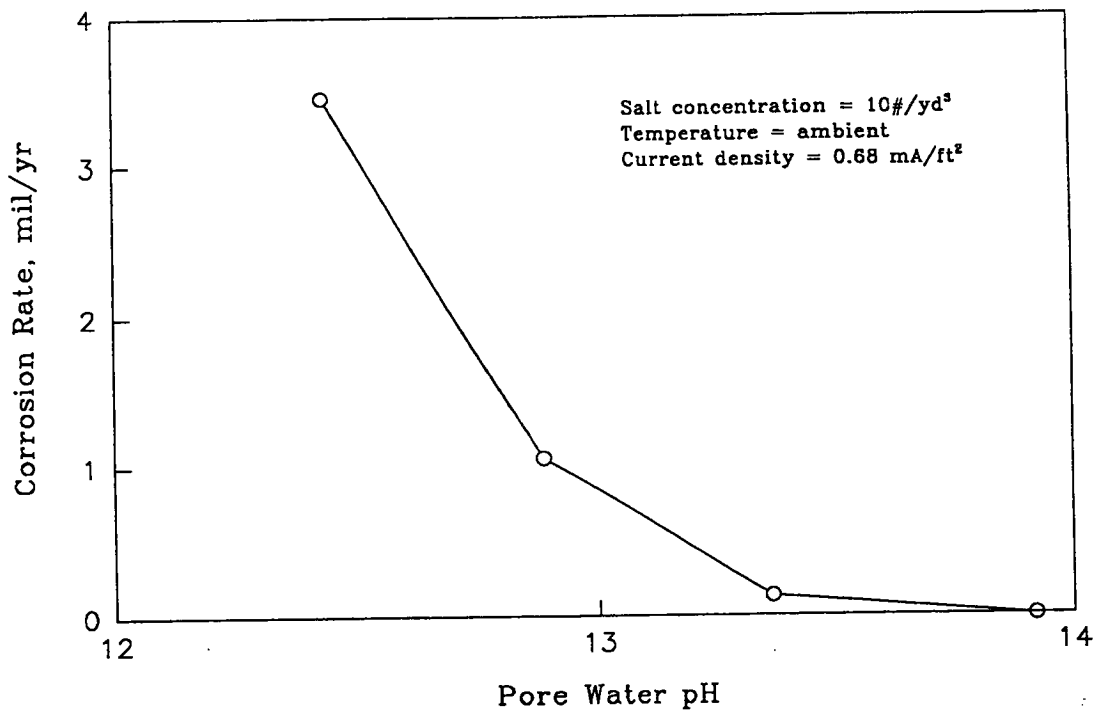

Effect of Temperature on Corrosion Rate

The effect of temperature on corrosion rate was evaluated using the data from the 10# Cl^-/yd^3 (6 g/l) sand tests for comparison. An insulated chamber was built to contain the cells during the tests. The temperature was controlled at 95°F (35°C). Operating data were collected without affecting the temperature.

Two cathodic protection current densities, 1.37 and 0.68 mA/ft^2 (13.7 and 6.8 mA/m^2) steel, were evaluated. The change in corrosion rate between 70 and 95°F (21-35°C) was not significant relative to experimental error and further testing was abandoned. Table 3-9 contains the results of these experiments.

Table 3-9. Effect of Temperature on Corrosion Rate

		Current Density mA/ft²	Temp. (°F)	Coupon # 1	2	3	4	5
	Average	0.68	75	0.03	0.03	-0.09	-0.02	0.01
	Corrosion	0.68	95	0.05	0.03	0.04	0.05	-0.004
	Current (mA)	1.37	75	0.05	0.04	0.06	0.05	0.06
		1.37	95	0.10	0.13	0.11	0.11	0.09
1	Avg. Corrosion	0.68	75	0.20	0.20	-0.62	-0.14	0.07
	Current Density	0.68	95	0.34	0.21	0.27	0.34	-0.03
	(mA/ft²)	1.37	75	0.34	0.27	0.41	0.34	0.41
		1.37	95	0.68	0.89	0.75	0.75	0.62
	Avg. Anode	0.68	75	438	438	468	436	427
	Potential	0.68	95	450	440	419	439	482
	(-mV vs SCE)	1.37	75	470	463	488	463	457
		1.37	95	482	470	493	484	467
		0.68	75	<.0020	<.0002	.0702	.0189	.0023
	Weight Loss	0.68	95	.0036	.0019	.0034	.0024	.0233
	(gm)	1.37	75	.0032	<.0002	<.0020	<.0002	<.0002
		1.37	95	.0172	.0293	.0009	.0026	.0012
2	Corrosion Rate	0.68	75	<0.02	<0.02	0.45	0.12	<0.02
	(mil/yr)	0.68	95	0.024	<.02	0.023	<.02	0.16
		1.37	75	0.02	<.02	<.02	<.02	<.02
		1.37	95	0.12	0.21	<0.02	<0.02	<0.02
	Average	0.68	75	164	162	50	83	98
	Depolarization	0.68	95	156	164	155	153	94
	(mV)	1.37	75	198	193	200	188	182
		1.37	95	111	108	205	207	201
	Average	0.68	75			0.13		
	Corrosion Rate	0.68	95			0.05		
	(mil/yr)	1.37	75			<0.02		
		1.37	95			0.07		

1 - A positive number indicates net cathodic current flow, and hence, no macrocell corrosion.
2 - A corrosion rate of <0.02 was below the detection limit.
1 mA/ft² = 11 mA/m²

Corrosometer Probe Experiments

Three different corrosometer probe experiments, running in duplicate, examined the effects of salt concentration and cathodic protection current on corrosion rate. The probes were operated under a constant cathodic protection regime due to their susceptibility to pitting corrosion. Although corrosometer probes have been found to be unreliable in situations where significant pitting corrosion occurs, they were found to be useful under these conditions. The current densities chosen were based on the chloride concentrations in the blocks and on the curren iensities examined in the coupon corrosion experiments. The results from the tests along with coupon corrosion rate data were correlated and used in the development of a cathodic protection criterion.

Concrete Specimen Design

Six 1-ft^2 blocks were prepared with two mats of #4 rebar. The mats were made continuous by soldering a copper conductor between the individual rebar. The lower mat was placed in three inches of concrete containing no chloride. The upper mat was placed in concrete containing 5 or 10# Cl^-/yd^3 (3 or 6 g/l) concrete. The probe was placed in the upper lift of concrete, with the measurement element directly in the center of the block and was coupled to the rebar via a pin on the probes connector. Figure 3-9 is a schematic of the block design.

Figure 3-9. Corrosometer Probe: Block Schematic

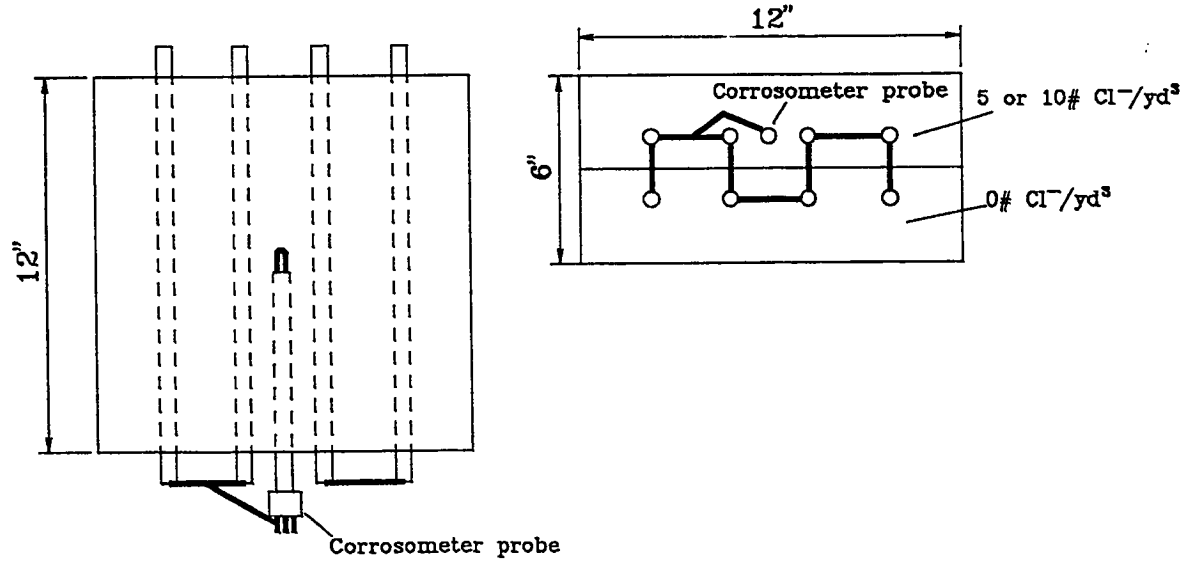

Operation

Two blocks containing 5# Cl^-/yd^3 (3 g/l) concrete were evaluated with a cathodic protection current of 1.37 mA/ft^2 (13.7 ma/m^2) of concrete. Four blocks containing 10# Cl^-/yd^3 (6 g/l) concrete were evaluated at 1.37 and 2.74 mA/ft^2 (13.7 and 27.4 mA/m^2) concrete. The tests were conducted in laboratory conditions. Water was ponded on the blocks weekly to prevent drying and to stimulate corrosion currents. Data were collected weekly and plotted as change in the resistance ratio of the measurement element to a second non-corroding check element versus the elapsed time.

The check element is located close to and made of the same material as the corroding element. The check element is connected, in series, to the corroding element through a bridge circuit. The check element is protected from corroding and therefore retains its original cross sectional area and hence its original resistance. A formula for calculating corrosion rates, as supplied by the manufacturer, Rohrback Cosasco Systems, is:

$$Corrosion\ Rate(\frac{mils}{yr}) = \frac{\Delta dial\ reading}{\Delta time(days)} \times 0.365 \times probe\ span$$

Figure 3-10 illustrates these data. Normally, a probe should exhibit a linear increase in resistance with respect to time. However, a probe element undergoing pitting corrosion will exhibit a characteristic upward curvature as shown by samples 13656-6 and 13656-9 in Figure 3-10.

Figure 3-10. Corrosometer Probe: Rate of Corrosion

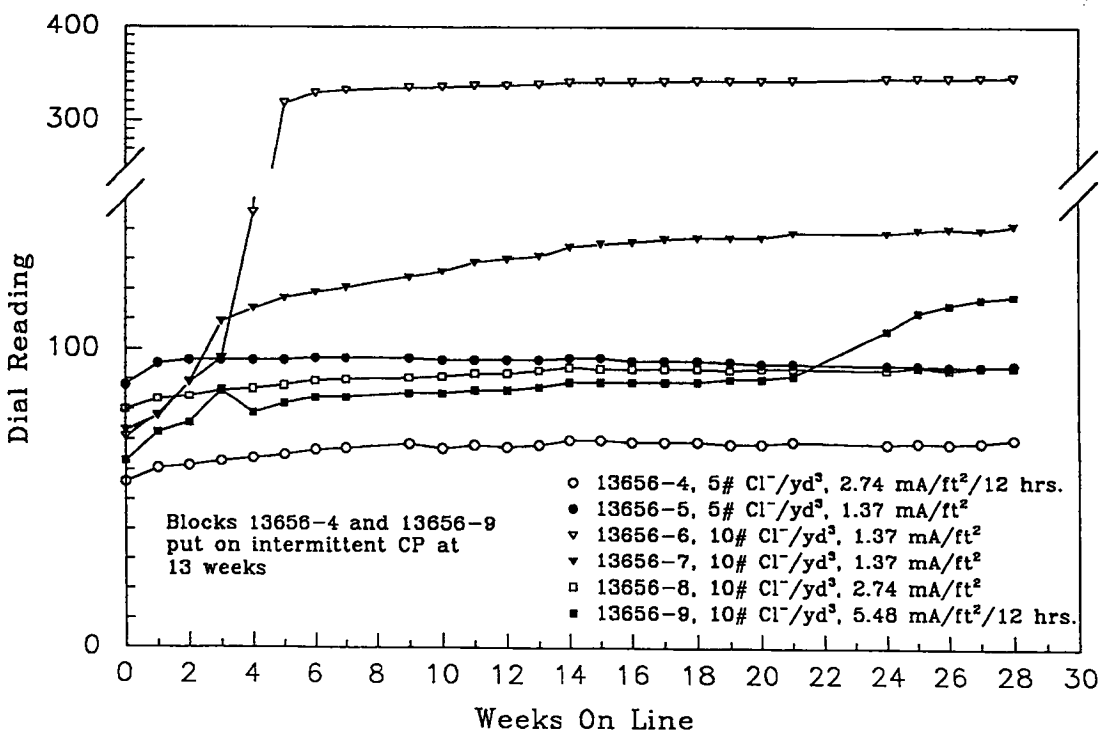

Bi-weekly polarization decays were collected on all the blocks. The polarization decay data and corrosion rate correlate well with the coupon corrosion tests. That is, as polarization decay increases corrosion rate decreases. Table 3-10 summarizes the corrosion rate and corresponding polarization decay for the six blocks. Figure 3-11 represents, graphically, the polarization decay data that were collected. All six blocks, regardless of operating parameters, show increasing polarization decay (polarization) and decreasing corrosion rate with time.

Table 3-10. Corrosometer Probe: Corrosion Rate and Polarization Decay

		Block ID.					
Date	Results	13656-4	13656-5	13656-6	13656-7	13656-8	13656-9
7-8-92	Corrosion Rate	.096	.091	2.652	.472	.086	.204
	Polarization Decay	103	101	33	45	131	60
7-21-92	Corrosion Rate	.091	.068	1.981	.361	.076	.160
	Polarization Decay	166	188	93	101	203	101
8-3-92	Corrosion Rate	.073	.053	1.551	.300	.062	.132
	Polarization Decay	184	137	106	109	212	122
8-17-92	Corrosion Rate	.058	.041	1.275	.269	.058	.119
	Polarization Decay	185	141	117	117	221	112
*9-1-92	Corrosion Rate	.049	.034	1.083	.235	.053	.099
	Polarization Decay	238	191	178	133	229	224
9-22-92	Corrosion Rate	.043	.026	.886	.206	.044	.085
	Polarization Decay	269	197	122	131	186	227
10-7-92	Corrosion Rate	.038	.023	.790	.187	.039	.076
	Polarization Decay	311	196	139	148	230	240
10-20-92	Corrosion Rate	.032	.018	.710	.168	.035	.071
	Polarization Decay	322	186	131	147	242	246
11-23-92	Corrosion Rate	.026	.014	.572	.139	.029	.102
	Polarization Decay	341	225	149	162	268	246
11-30-92	Corrosion Rate	.024	.012	.550	.135	.026	.104

Units for corrosion rate are mil/yr.
Units for polarization decay are mV.

* - blocks 13656-4 and 13656-9 switched to intermittent cathodic protection regime.

Based on corrosion rate calculations and polarization decay data, the coupon corrosion rate experiments and corrosometer probe tests have shown that sufficient cathodic protection can reduce or halt macrocell and pitting-type corrosion. Both experiments have illustrated an increased demand for cathodic protection current as the chloride concentration at the surface of the steel increases. The corrosometer probe tests have also shown, in the form of increased polarization decay over time, that the demand for cathodic protection current can decrease as a system matures.

Figure 3-11. Corrosometer Probe: Polarization Decay versus Time

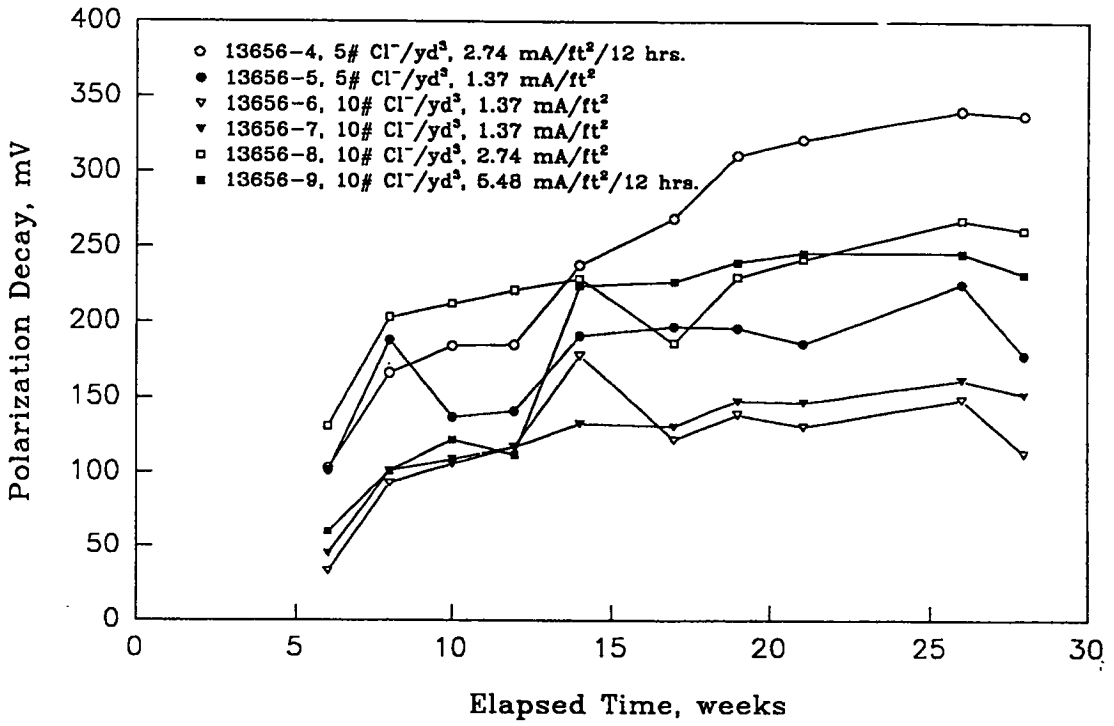

4

Corrosion Null Probe

An early objective was to determine a relationship between polarization and corrosion rate. This relationship was found to be complex. Although general trends were seen, for example, increasing chloride concentration increased corrosion rate, and increasing polarization sharply decreased corrosion rate, these relationships were complicated by changes in pH and to a lesser degree by changes in temperature. Much more data would have been required to establish the relationships quantitatively. Therefore, a procedure that attempts to define the exact amount of polarization necessary in all cases would be too complicated for practical use.

Another approach is to define and apply the amount of polarization necessary for the worst case, in which case all the steel should receive adequate protection. This is the theory behind the 100 mV polarization decay criterion.

Figure 4-1 is a graphic representation of the data collected from the non-polarized (open circuit) tests. It shows one interesting and relatively simple relationship between corrosion current (flow to or from the anode) and corrosion rate. The entire range of chloride concentrations, evaluated in the tests, from 1 to 30#/yd^3 (0.6 to 18 g/l) sand, are plotted on the same line. This graph implies that if corrosion could be measured and controlled, it could be used as an accurate and relatively simple criterion. In other words, making the steel net cathodic effectively stops corrosion. This is a well accepted principle of cathodic protection[19], but this is the first example of its effectiveness in concrete. It is clear from this graph that most of the corrosion is attributed to localized pitting corrosion, since measured weight losses far exceed that predicted by Faraday's Law. But it is also clear that cathodic protection current is capable of eliminating both the corrosion evidenced by macrocell current and corrosion due to pitting.

Figure 4-1. Corrosion Rate versus Macrocell Corrosion Current

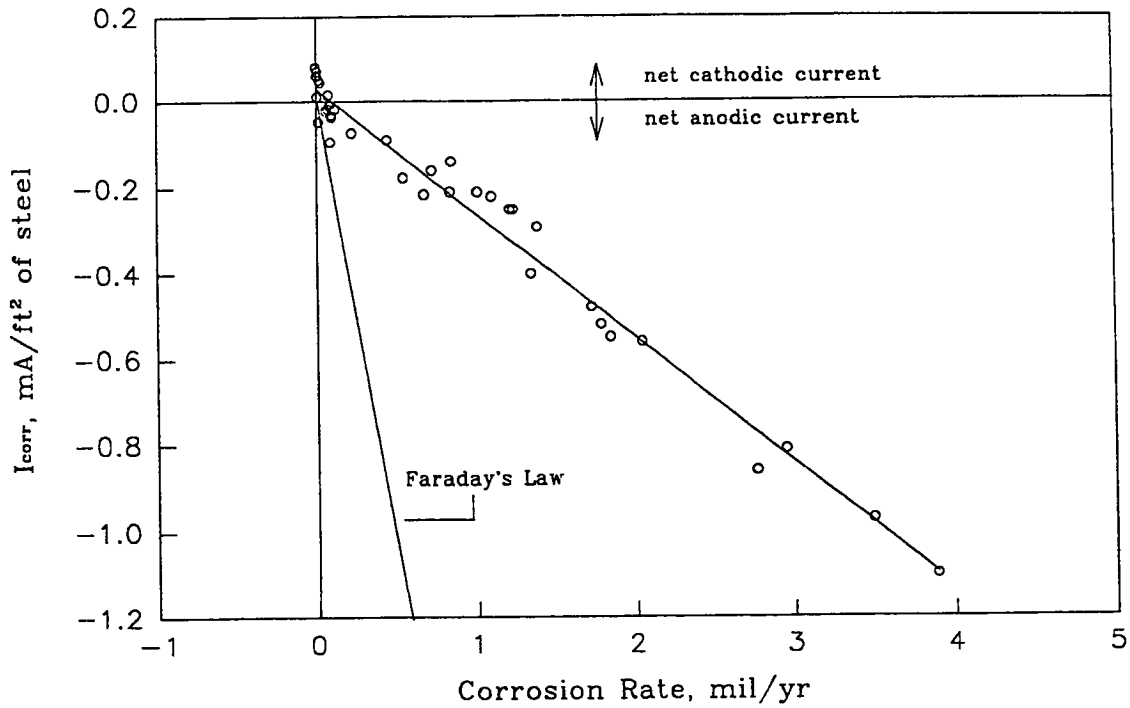

The concept of measuring corrosion current and applying cathodic protection to null or reverse that current, is applied when using a "rebar probe".[20] The rebar probe historically used with cathodic protection systems is illustrated in Figure 4-2. The probe is constructed by casting a 5 inch (13 cm) long piece of #5 rebar in mortar containing 15# Cl^-/yd^3 (9 g/l) concrete. The probe is then installed in an excavation in the structure where reinforcing bars have been exposed on all sides. The excavation is patched with chloride-free concrete. After the probe is attached to the system negative, through a 10 ohm resistor for monitoring purposes, a strong macro-corrosion cell is created. Cathodic protection is then applied to null or reverse the corrosion current, making the probe a net cathode. The probe is constructed to be the most anodic site in the structure. Hence, if the probe is sufficiently protected, the rest of the structure will be as well.

Figure 4-2. Rebar Probe Construction

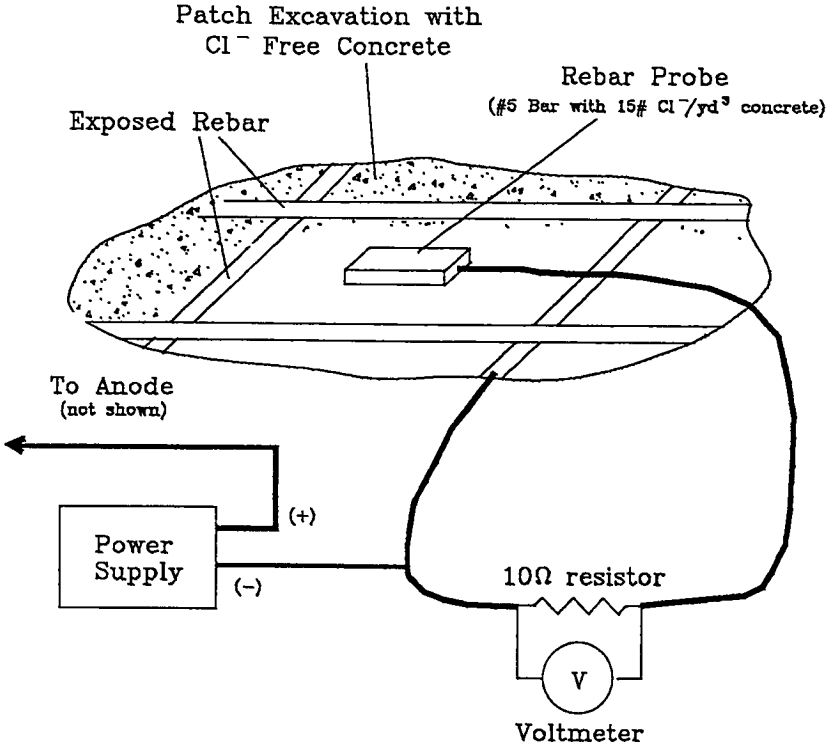

Figure 4-3 exhibits the cathodic protection requirement as determined from rebar probes installed in a cathodic protection system on 13th View Street Bridge in Norfolk, Virginia.[21] These data show a dramatic decrease in current requirement with time. This is an expected response in view of the depletion of chloride and the build-up of hydroxide concentration at the surface of the steel. This is a recognized consequence of the passage of cathodic protection current. Although rebar probes are considered useful, especially at start-up, they are not generally regarded as a cathodic protection criterion. In view of this, rebar probes probably have been underutilized in past practice, and deserve further consideration.

Figure 4-3. Cathodic Protection Current Density as Determined from Rebar Probes versus Time

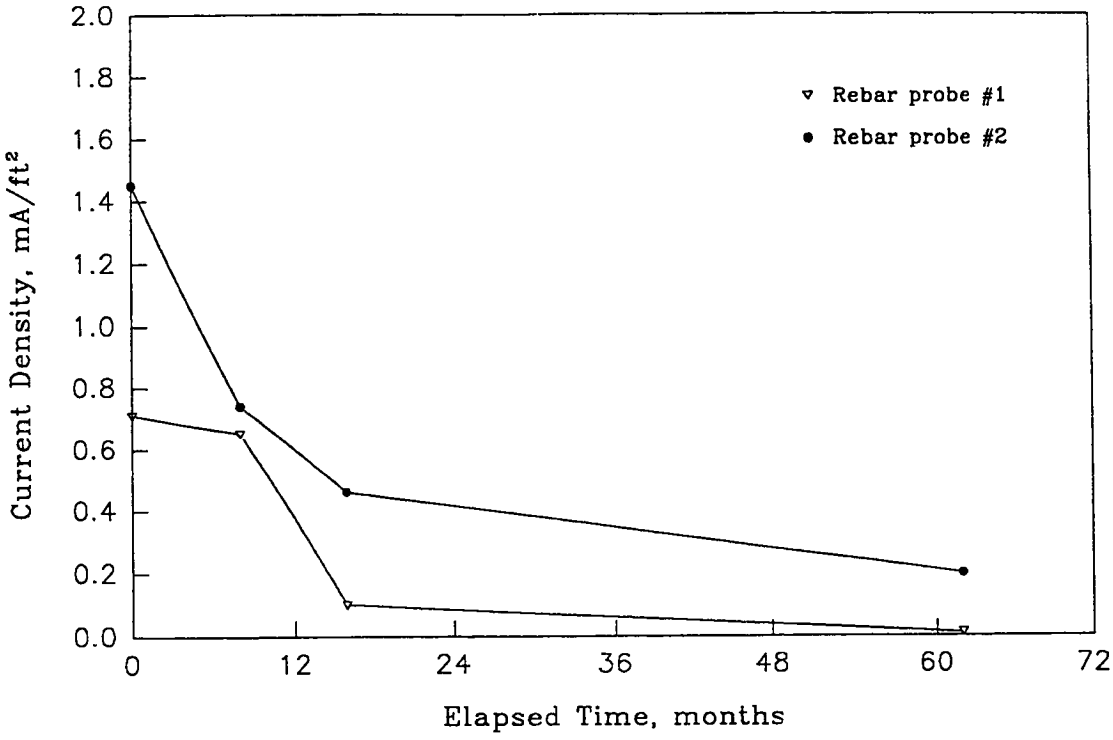

Rebar probes have been lightly regarded in the past because of some practical concerns about their use. First, the construction of the probe and its installation, to create a strong macrocell, is artificial, and is usually not site specific. There is a concern that a probe installed this way may not accurately represent the actual needs of the structure. A rebar probe installed in a structure with totally passive steel would still indicate a requirement for current. Also, duplicate rebar probes in the same cathodic protection zone often display widely differing current requirements.

Based on the above data and observations, a Corrosion Null Probe (CNP) concept was developed. The CNP, shown in Figure 4-4, is similar to the rebar probe described above, except that it is constructed from reinforcing steel and concrete native to the structure. Corrosion rate monitored in this way will be site specific, and cathodic protection current requirement will be completely relevant for the structure at the time of the test. To verify this concept, the sand/pore-water cells were set up, with auxiliary anodes, to null macrocell corrosion currents established at several different salt concentrations.

Figure 4-4. Corrosion Null Probe Schematic

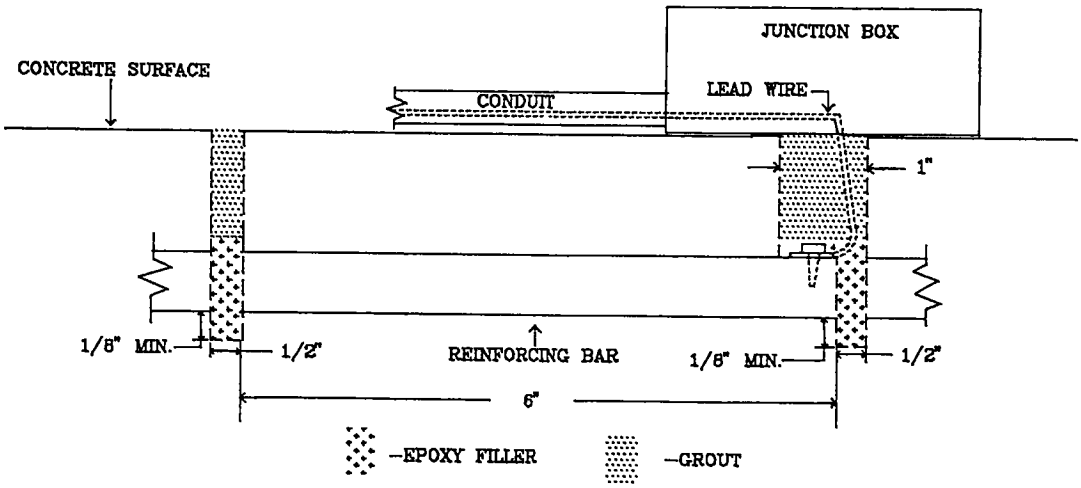

Corrosion Nulling Experiments

Sand/Pore-Water Cells

The tests were conducted in salt concentrations ranging from 1 to 20# Cl^-/yd^3 (0.6 to 12 g/l) sand. A set of five coupons were tested in 1, 3, 5, 8, 10 and 20# Cl^-/yd^3 sand (0.6, 1.8, 3.0, 4.8, 6.0, and 12 g/l). The tests operated for an average of six days at which point sufficient time had elapsed to initiate strong corrosion currents. After the onset of the corrosion currents, cathodic protection current was applied incrementally until the corrosion current was nulled to zero. Figures 4-5 through 4-10 show the results of these experiments.

In the figures I_c is defined as the macrocell corrosion current density on the steel. I_{cp} is defined as the cathodic protection current density that was impressed on the coupons to null the corrosion currents to zero. A horizontal line is included at $I_c = 0$, the point where the corrosion currents have been nulled.

Figure 4-5. Nulling of Corrosion Currents in 1# Cl^-/yd^3 of Sand

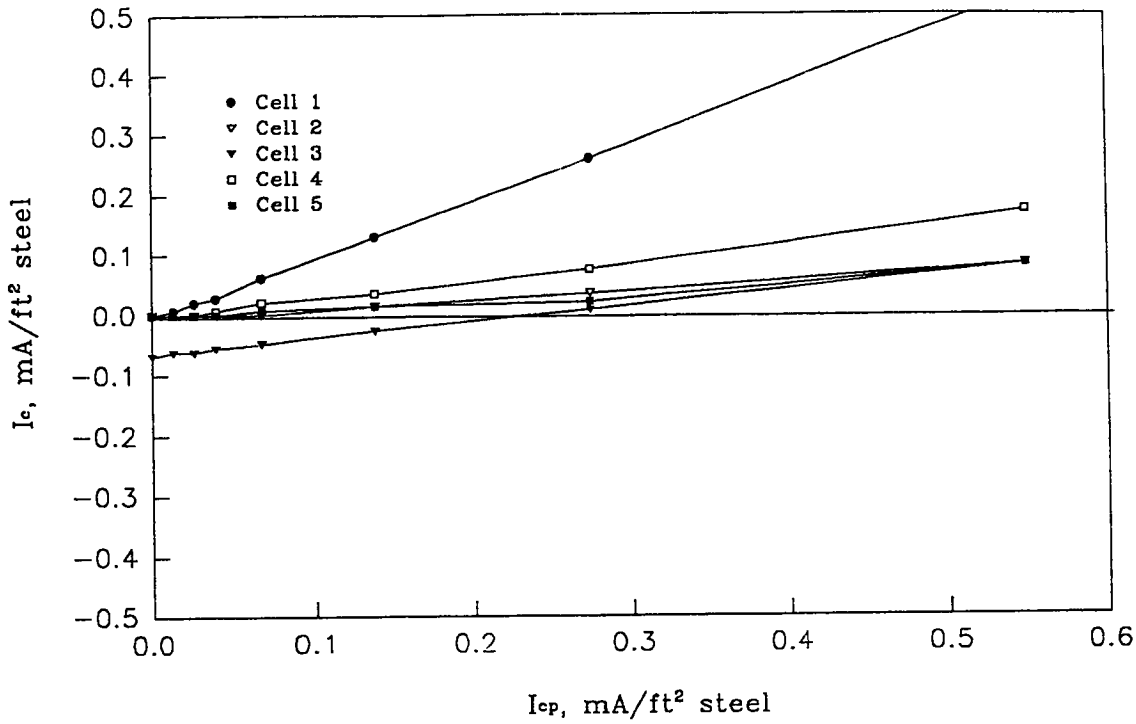

Figure 4-6. Nulling of Corrosion Currents in 3# Cl^-/yd^3 of Sand

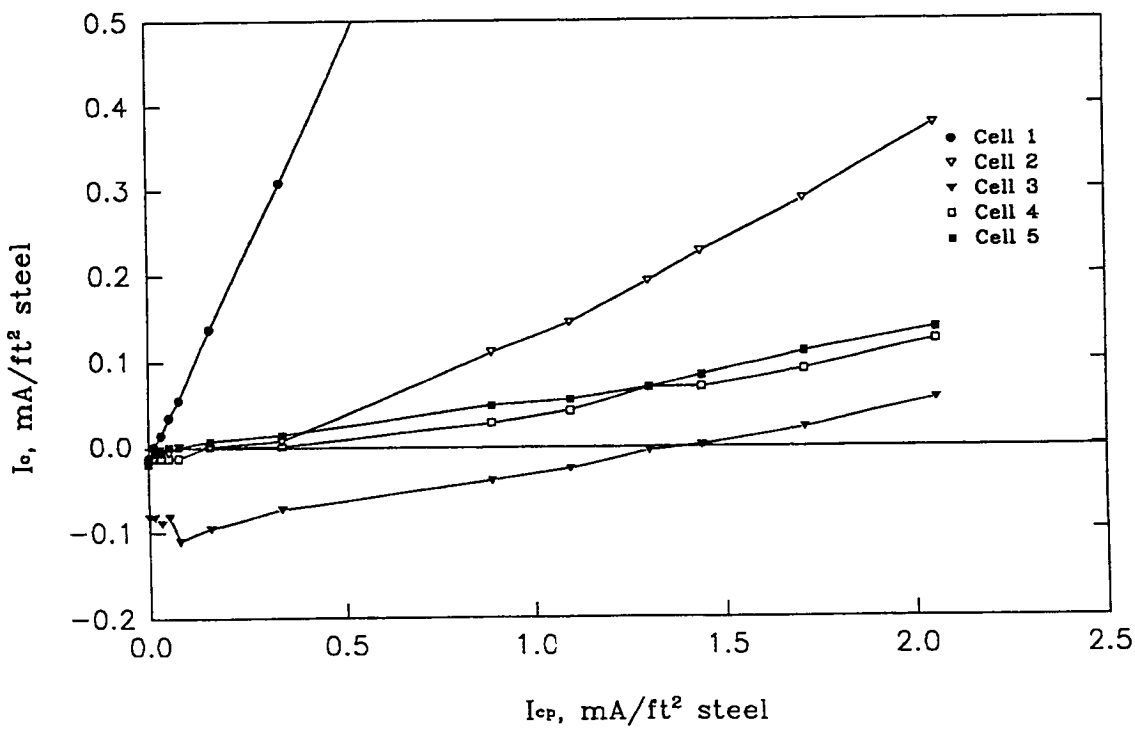

Figure 4-7. Nulling of Corrosion Currents in 5# Cl^-/yd^3 of Sand

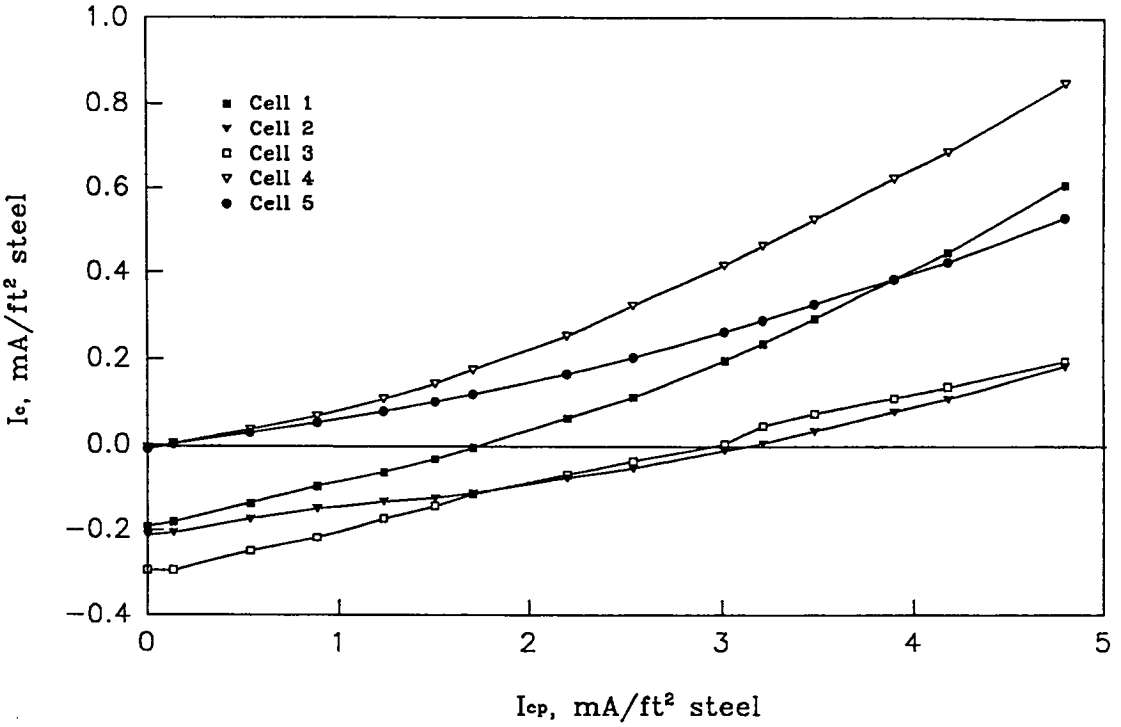

Figure 4-8. Nulling of Corrosion Currents in 8# Cl^-/yd^3 of Sand

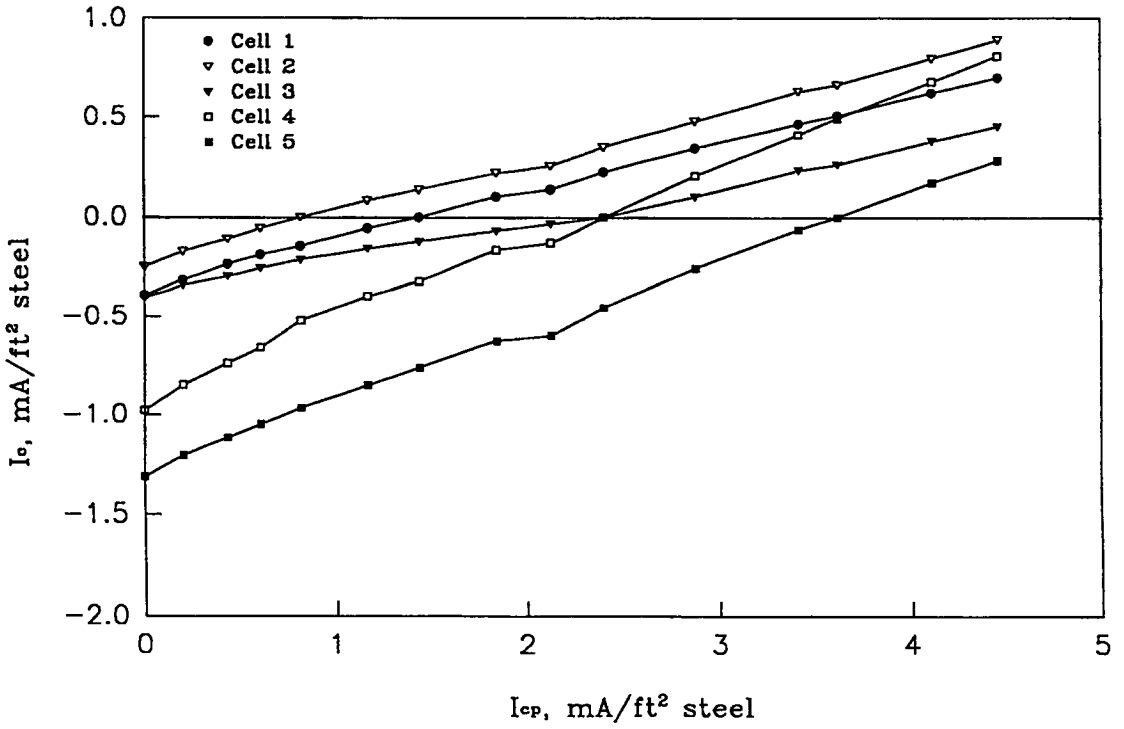

Figure 4-9. Nulling of Corrosion Currents in 10# Cl^-/yd^3 of Sand

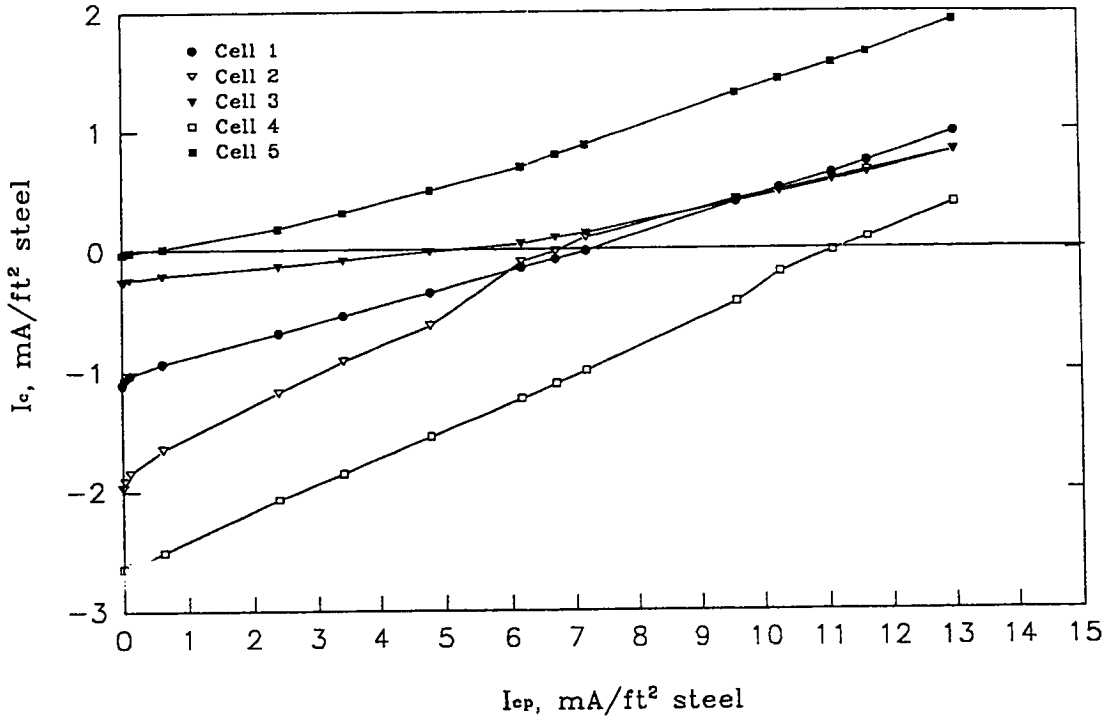

Figure 4-10. Nulling of Corrosion Currents in 20# Cl^-/yd^3 of Sand

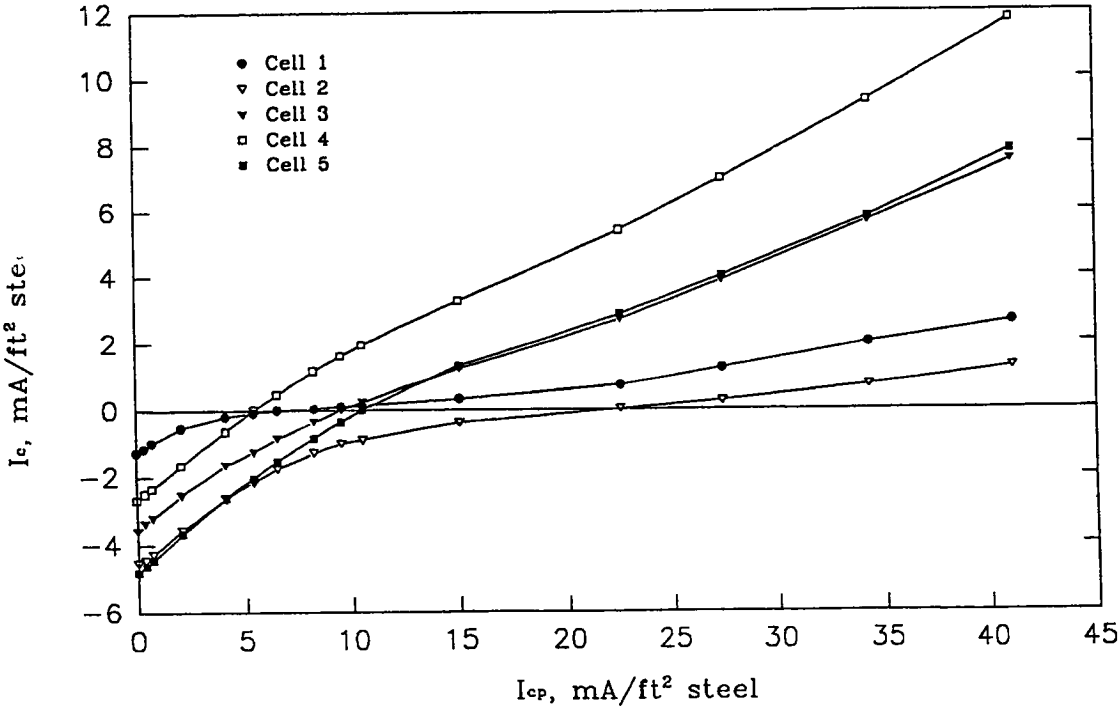

The relationship between cathodic nulling current and salt concentration is shown in Figure 4-11. The range of the data again shows the scatter caused by localized pitting corrosion. It also illustrates the increased current requirement with increasing salt concentrations.

Figure 4-11. Cathodic Nulling Current versus Chloride Concentration

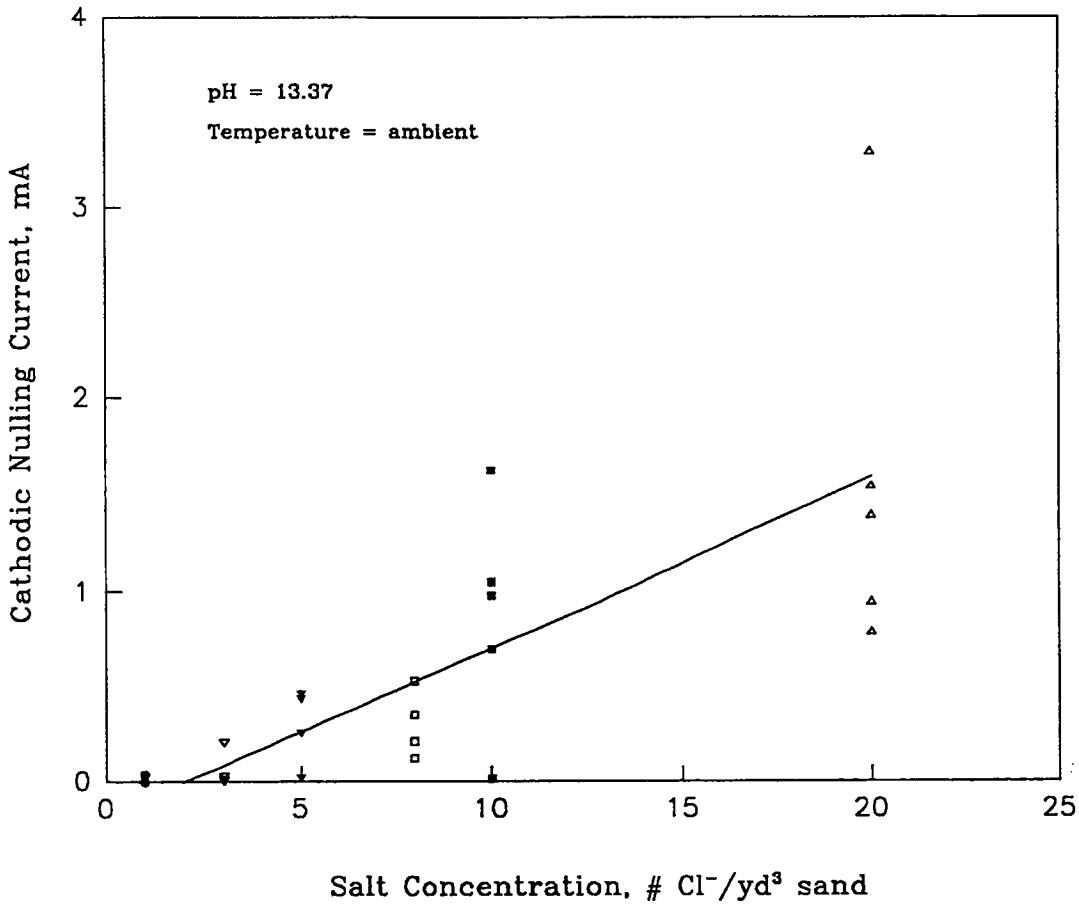

Table 4-1 lists the average cathodic protection current requirements along with the average polarization of the steel at the null point. Although the cathodic protection current requirement increases about two orders of magnitude for chlorides in the 1 to 20# Cl^-/yd^3 (0.6 to 12 kg/m^3) sand range, 150 mV of polarization is adequate protection over this range. These data tend to confirm the 150 mV polarization decay criterion as a technique, as has been suggested by others.[8,9,10]

Table 4-1. Average Cathodic Protection Current Density Requirement and Polarization versus Chloride Concentration

Salt Concentration (# Cl^-/yd^3)	Avg. CP Requirement (mA/ft^2 steel)	Avg. Polarization (mV)
1	0.05	9
3	0.34	53
5	1.64	114
8	2.14	102
10	5.98	140
20	10.90	155

Concrete Specimens

The Corrosion Null Probe technique was also utilized on two concrete test yard specimens. Results of these tests are shown on figures 4-12 and 4-13. The specimen in Figure 4-12 had top mat reinforcement in a state of mild corrosion. In this case, a cathodic protection current density of 0.05 mA/ft^2 (0.5 mA/m^2) of concrete was required to null out the corrosion current. A second test was then performed on a slab which was badly corroding and delaminated. For this slab a cathodic protection current density of 3.0 mA/ft^2 (30 mA/m^2) of concrete was required to null corrosion current, as shown in Figure 4-13.

Figure 4-12. Cathodic Protection Current Requirement for a Mildly Corroding Concrete Specimen with 6# Cl^-/yd^3 Concrete

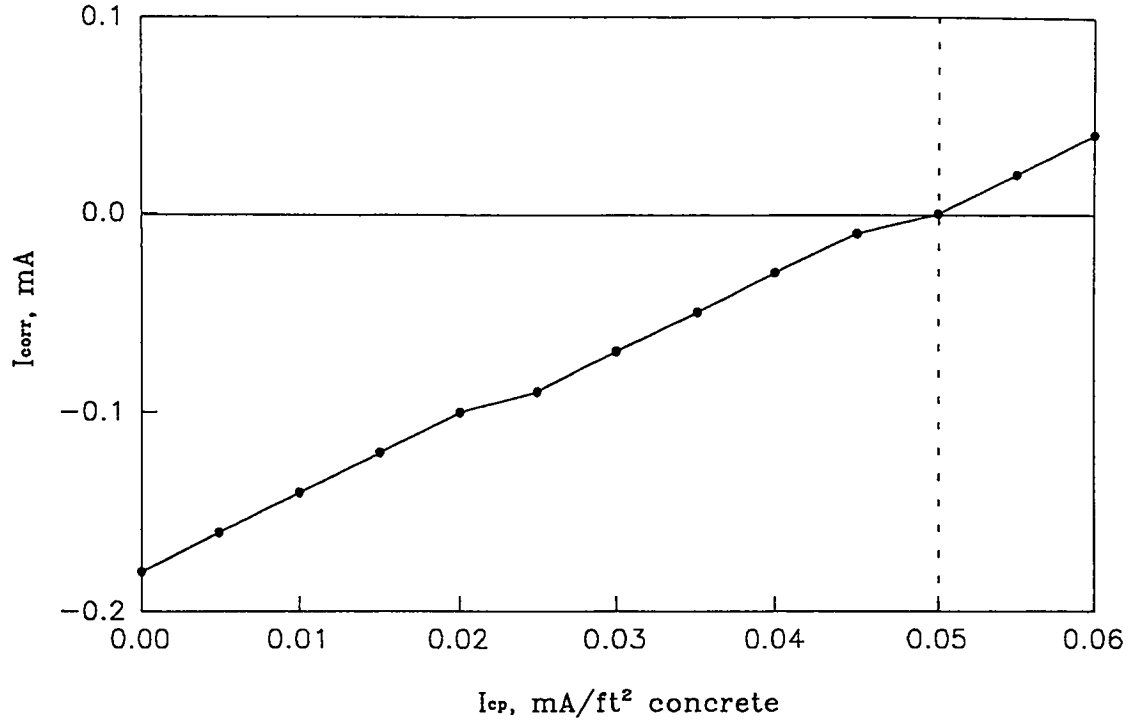

Figure 4-13. Cathodic Protection Current Requirement for a Badly Corroding Concrete Specimen with 15# Cl^-/yd^3 Concrete

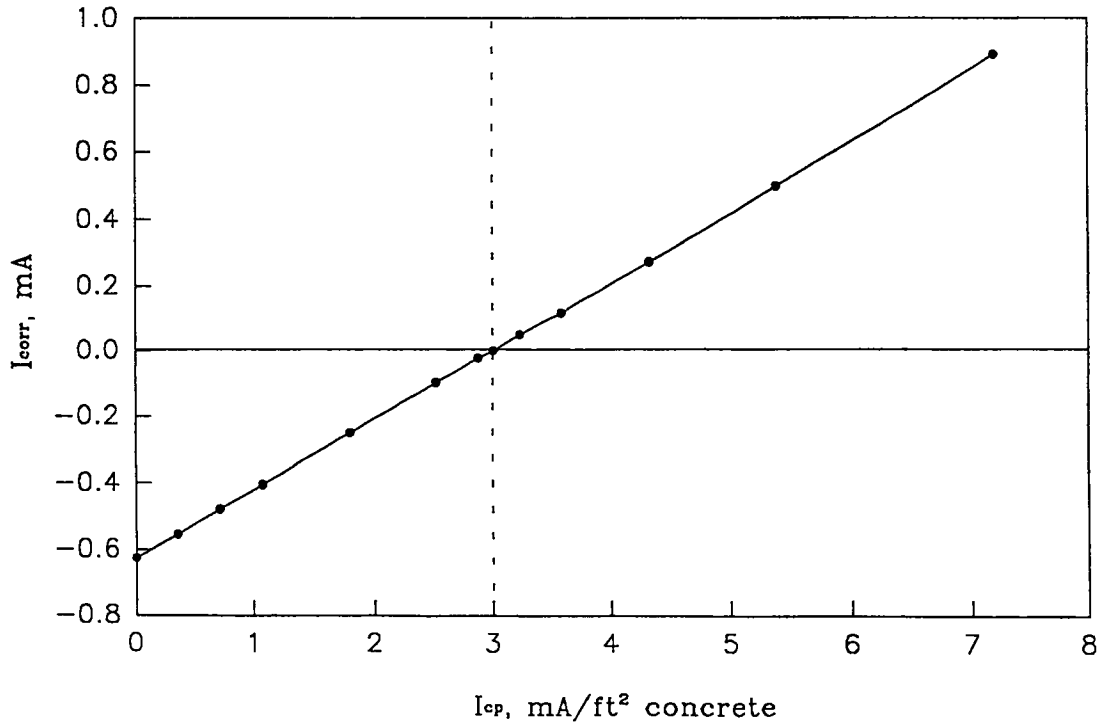

Both specimens were placed under long-term cathodic protection to determine the effect of total charge on the current requirement. The specimens are operating at 0.25 mA/ft^2 (2.5 mA/m^2) concrete area over the nulling current density. The extra current is a safety factor and was chosen arbitrarily. The preliminary results appear to correlate well with the data obtained from the rebar probe installation in Norfolk, VA., see Figure 4-3. That is, at a fixed cathodic protection current, an increase in net cathodic current indicates that less current is required to protect the steel. Figures 4-14 and 4-15 show the results of the mildly corroding and the badly corroding specimen respectively.

Figure 4-14. Effect of Time on Cathodic Protection Current Requirement, Mildly Corroding Specimen

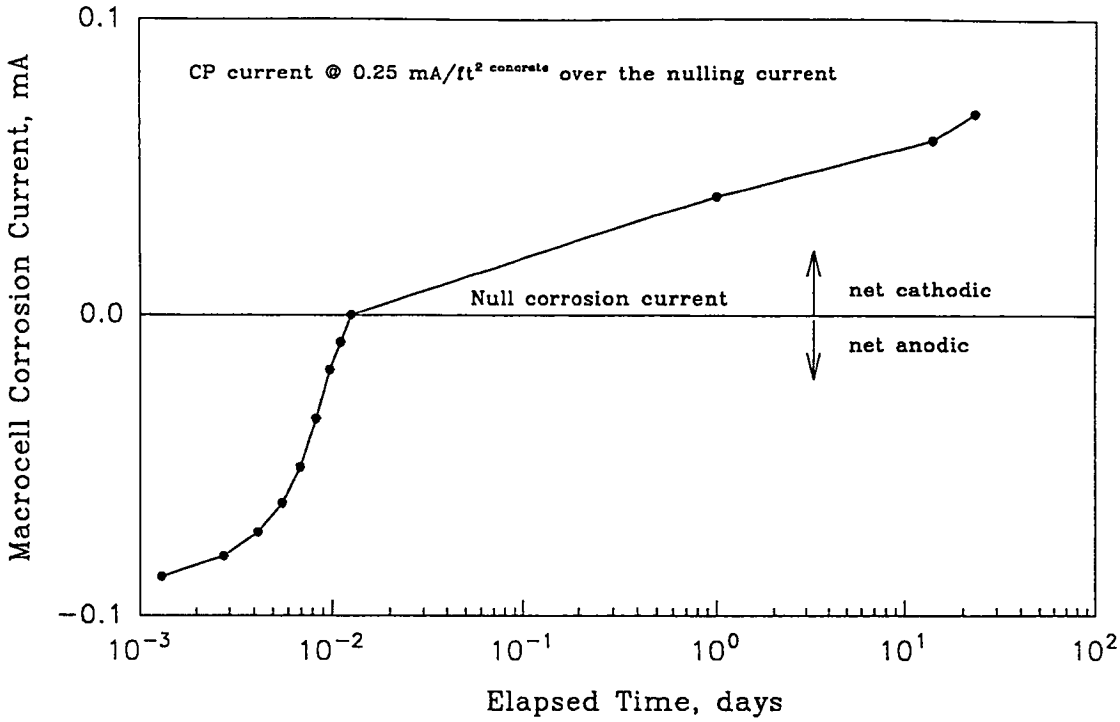

Figure 4-15. Effect of Time on Cathodic Protection Current Requirement, Badly Corroding Specimen

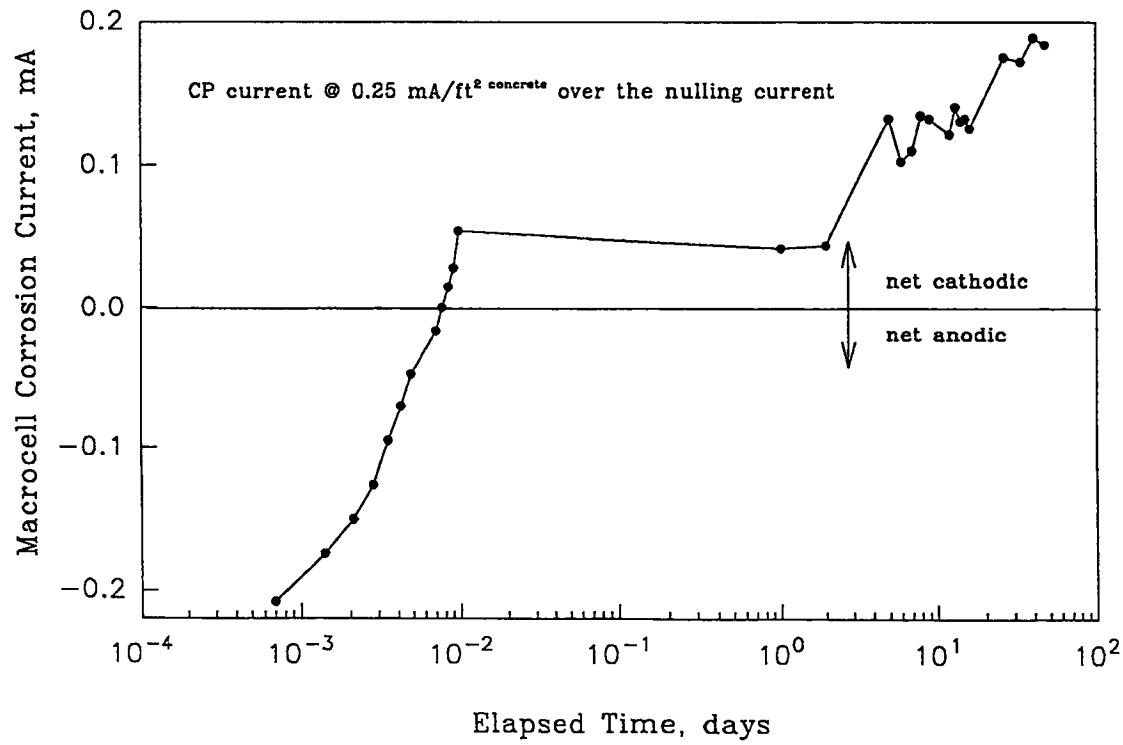

Based on the corrosion nulling experiments, the CNP appears to offer a technically accurate and simple to apply criterion for cathodic protection in reinforced concrete. It is site specific, and will reflect the diminishing cathodic protection current requirement with time. Significantly, it does not rely on the long-term stability of embedded reference electrodes.

The CNP technique does require that reinforcing steel be cut and isolated and in certain cases this may be objectionable. One such case would be where prestressed steel is involved, or when all the steel is structurally significant and cutting through would reduce safety margins.

Another concern is the need to identify the most anodic area for the construction of the probe. If the probe is installed in the wrong location, the cathodic protection current will be misjudged. Locating the CNPs in sites that are not the most anodic can cause less than adequate cathodic protection current to be applied to the reinforcing steel.

Field Trials

A field validation trial of the CNP technique is under way in Norwich, Connecticut. Eight probes were installed during the second phase of rehabilitation on the Wawecus Hill Rd. over I-395. Two null probes were installed in each of four cathodic protection zones. The system had not been energized at the time of this writing, so no data are available. A description and preliminary installation specification is included in Appendix A.

Probe Location

A potential survey was conducted on each of the four zones using ASTM C-876-91, "Standard Test Method for Half-Cell Potentials of Uncoated Reinforcing Steel in Concrete". A four-foot on-center survey was used to identify the two most anodic regions in each zone. A second, more precise survey, was conducted on the anodic regions using one-foot on-centers. The null probe location was determined from the second survey. An example of the static potential map of Zone 1 can be found in Figure 4-16.

Figure 4-16. Static Potential Survey on Zone 1, Wawecus Hill Rd.

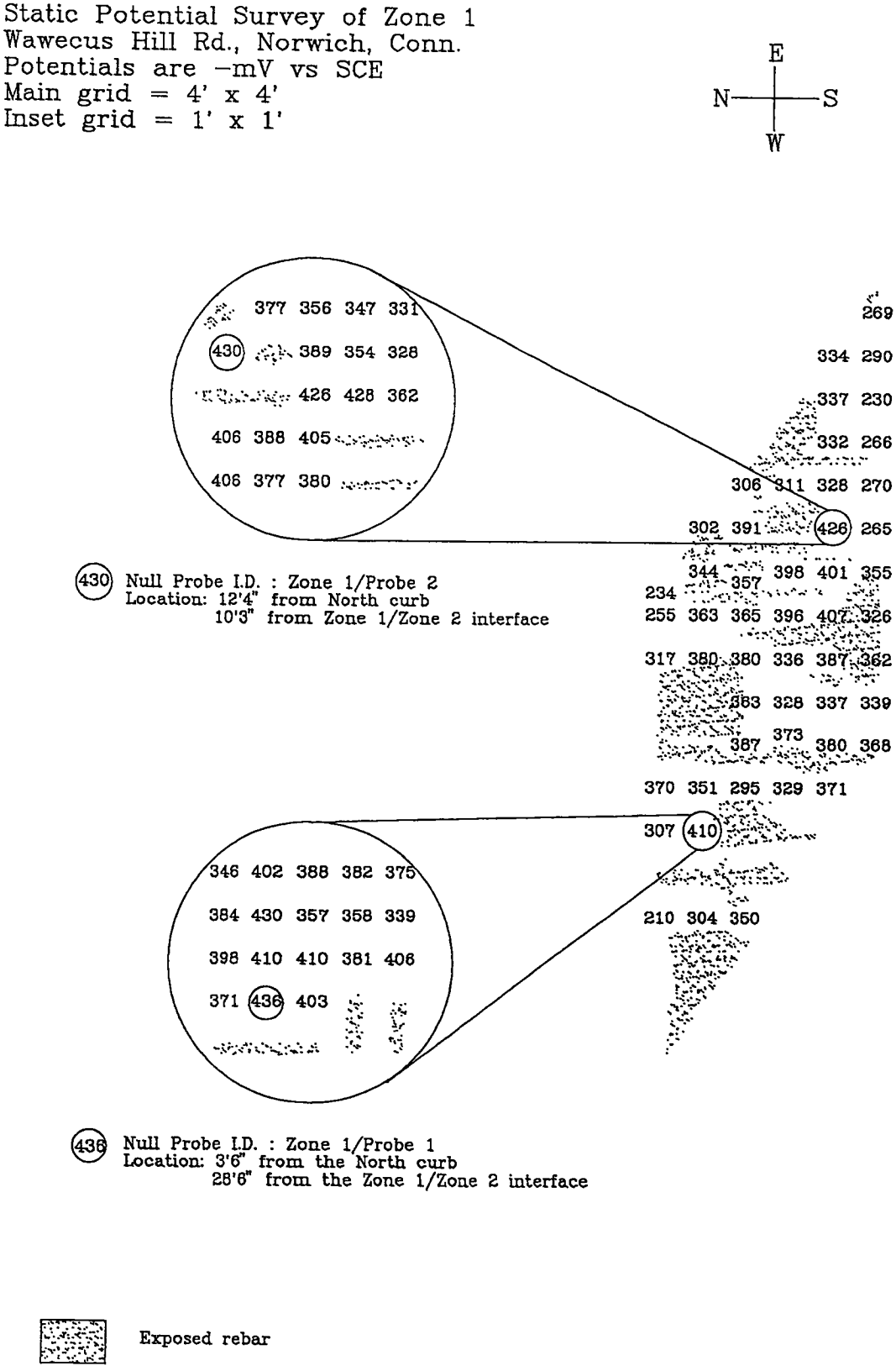

5

Long-Term Effects

Effects Near the Cathode

The effect of cathodic protection current in the vicinity of the cathode, or reinforcing steel component, of a cathodic protection system for reinforced concrete was investigated using concrete containing alkali-silica reactive aggregate. Alkali-silica reactivity (ASR) is an expansive reaction that causes concrete to crack.[22-30] The resultant cracks provide a means of entry for water borne deicing salts causing subsequent reinforcing steel corrosion. The evidence to date suggests that even relatively low current flows, such as those used in cathodic protection of reinforced concrete, can aggravate ASR under some conditions. That situation may be worsened by the presence of chlorides in the pore-water solution. Results have shown that concrete containing ASR aggregate had experienced severe deterioration, when subjected to chloride removal current densities of 0.1 to 0.5 amps/ft^2 (1.08 to 5.38 amps/m^2).[31] To assess the possible damage that may occur under normal cathodic protection current densities a laboratory evaluation program was conducted.

Sample Preparation and Testing

Two fine aggregates were selected for study in the experiment and included opal and chert. With respect to ASR activity, the opal is characterized as "highly reactive", while the chert is "moderately reactive". The opal and chert aggregates were obtained as 1 in. by 2 in. (2.5 cm by 5 cm) pieces that were crushed and sized to yield a gradation conforming to the requirements of ASTM C33 for fine aggregate in concrete.

The coarse aggregate was 1 in. (2.5 cm) maximum size quartz that is characterized as unreactive. Detailed information on all of the aggregates is presented in Appendix B.

The same Type I low-alkali portland cement (Midwest Portland Cement Company) was used in both concretes. This portland cement has an alkali content (Na_2O equivalent) of 0.4 percent. Historically, it has been assumed that if the alkali content of a portland cement is less than 0.6 percent, ASR activity will not be initiated even if ASR-prone aggregates are present. However, there are known instances of deviations from this "rule".

Since both chert and opal have been found to cause ASR, concrete cylinders were cast with each as the fine aggregate. Three 4-in. (10 cm) diameter cylinders were cast using chert, and three were cast with opal. ELGARD™ 210 Anode Mesh was placed on the sandblasted surface of each cylinder, and a 2-in. (5 cm) thick plain concrete overlay was cast on top encapsulating the anode mesh. Figure 5-1 shows the construction of the cylinders, and Table 5-1 lists the constituents of each concrete mix that was prepared.

Figure 5-1. Alkali-Silica Aggregate Test Specimens

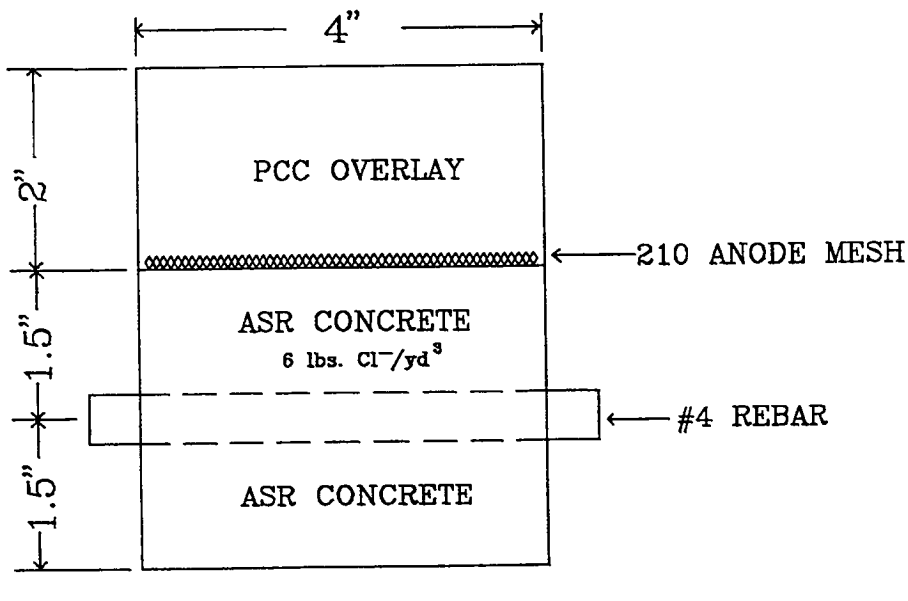

Table 5-1. ASR Concrete Mix Designs

Concrete Overlay Mix Design Constituent	lb/yd^3	kg/m^3
Type IA Portland Cement	612	363
Fine Aggregate- ASTM C33	1340	795
Coarse Aggregate- No. 8 ASTM C33	1800	1068
Water(0.4 w/c)	245	145
Alkali-Silica Aggregate Concrete Mix Design **Constituent**	**lb/yd^3**	**kg/m^3**
Type I Low-alkali Portland Cement	612	363
Fine Aggregate- Opal or Chert (Saturated Surface Dry)	1350	801
Quartz Coarse Aggregate- No. 67 ASTM C33 (Saturated Surface Dry)	1702	1010
Water(0.5 w/c)*	306	182
Sodium Chloride	To yield 6 lb Cl^-/yd^3 of concrete	

*4 oz/cwt of water-reducing admixture was used in the concrete containing the opal fine aggregate to provide a mix of similar consistency to that of the concrete containing the chert fine aggregate.

The cylinders were placed outdoors, and cathodic protection current was applied to each cylinder. Current was applied with a constant current power supply. The actual current densities supplied were 0.99, 1.70, and 3.74 mA/ft^2 (10.7, 18.3, and 40.3 mA/m^2). This converts to current densities based on concrete surface area of 0.5, 0.85, and 1.9 mA/ft^2 (5.4, 9.2, and 20.5 mA/m^2). Table 5-2 lists the current densities of the cylinders.

Table 5-2. ASR Cylinder Current Density

		Current Density*	
Cylinder No.	Type	mA/ft^2	mA/m^2
13641-4-31	Opal	0.99	10.7
13641-4-32	Chert	0.99	10.7
13641-4-33	Opal	1.70	18.3
13641-4-34	Chert	1.70	18.3
13641-4-35	Opal	3.74	40.3
13641-4-36	Chert	3.74	40.3

*Current density is based on the steel area of 0.0436 ft^2

The cylinders were powered for 283 days or 6792 hours. Table 5-3 contains the operational data on the cylinders.

Table 5-3. ASR Cylinder Operational Current Data

Cylinder No.	Type	Current Density, mA/ft² (mA/m²) Steel	Concrete	Applied Charge A·hr/ft²*	(A·hr/m²)
13641-4-31	Opal	0.99 (10.7)	0.5 (5.4)	3.4	(36.1)
13641-4-32	Chert	0.99 (10.7)	0.5 (5.4)	3.4	(36.1)
13641-4-33	Opal	1.70 (18.3)	0.85 (9.2)	5.8	(62.0)
13641-4-34	Chert	1.70 (18.3)	0.85 (9.2)	5.8	(62.0)
13641-4-35	Opal	3.74 (40.3)	1.90 (20.5)	12.7	(136.6)
13614-4-36	Chert	3.74 (40.3)	1.90 (20.5)	12.7	(136.6)

*Charge is based on the concrete area of 0.08722 ft² (0.0081 m²)

Evaluation of Results

After treatment the specimens were examined petrographically and tested by the gel fluorescence procedure. Control cylinders containing chert and opal aggregate that were not subjected to cathodic protection treatment were also examined at this time.

The chert aggregate control specimens showed no surface cracking and no evidence of ASR activity. The opal aggregate control specimens had slight polygonal cracking on molded surfaces. However, no alkali-silica gel was observed, and only a very few opal aggregate particles exhibited rimming and/or cracking.

The effect of the cathodic protection treatment on the chert aggregate concrete was to initiate alkali-silica reaction activity in the concrete for a distance of about 1 in. (2.5 cm) above the rebar. The ASR activity was evidenced by very fine polygonal cracking on molded surfaces which were less than 0.0005 in. (0.0013 cm) wide and by the presence of reaction rims and light cracking in a few of the chert aggregate particles. For the chert aggregate concrete, the amount of cracking observed on the molded surfaces was not greatly affected by current density. However, in the gel fluorescence test, a greater number of aggregate particles exhibited ASR activity, especially in the specimen treated at the highest current density (Chert-10 - 3.74 mA/ft² of steel - 37.4 mA/m²).

The cathodic protection treatment also increased the level of alkali-silica reaction activity in the opal aggregate concrete specimens. Efforts to quantify the accelerating effect were made difficult by the fact that the natural fluorescence of the opal aggregate is quite high, and the untreated autogenously cured specimens also exhibited fine polygonal cracking on molded surfaces.

Nevertheless, it was possible to confirm that the cathodic protection treatment at all three current densities had a slight accelerating effect on alkali-silica reaction activity. From the point of view of the amount of hairline, less than 0.001 in. (0.0025 cm) wide, polygonal cracking occuring in the specimens, the greatest amount of cracking occurred in the opal specimen treated at 3.74 mA/ft^2 (37.4 mA/m^2) of steel.

In the chert aggregate concrete, the majority of the ASR activity was confined to 1 inch from the surface of the rebar toward the anode. In the opal aggregate concrete, the ASR activity is widespread.

Effects of Long-Term Polarization decay

Sample Preparation and Testing

In order to verify the concentration profile model presented in Chapter 7, long-term polarization decay tests were conducted on reinforced concrete specimens that had been in operation for three years. The 1 ft by 1 ft by 6 in. (0.3 x 0.3 x 0.15 m) blocks shown in Figure 5-2 had been operated at anode current densities of 10, 20, and 80 mA/ft^2 (100, 200 and 800 mA/m^2). A set of control blocks were analyzed for chloride contents from the reinforcing bar to the surface and for pH at the reinforcing bar level.

The blocks were cast using the Class C concrete mix design for the Ohio Department of Transportation structural concrete. The mix design is listed in Table 5-4. The bottom half of each block was cast with chloride-free concrete, while the top half was cast with concrete containing 15 lb/yd^3 (8.9 kg/m^3) of chloride ion. The top of each block was thoroughly sandblasted, and ELGARD™ 210 Anode Mesh was placed on the prepared surface. Concrete overlays were then placed on the blocks. The commercially available overlay was 1/2 in. (1.27 cm) thick, the superplasticized concrete overlay was 2 in. (5.1 cm) thick, and the Latex Modified Concrete Overlay was 1-1/4 in. (3.2 cm) thick. Table 5-5 lists the background data, while Table 5-6 contains the chloride analysis and pH results.

Figure 5-2. Polarization Decay Test Block

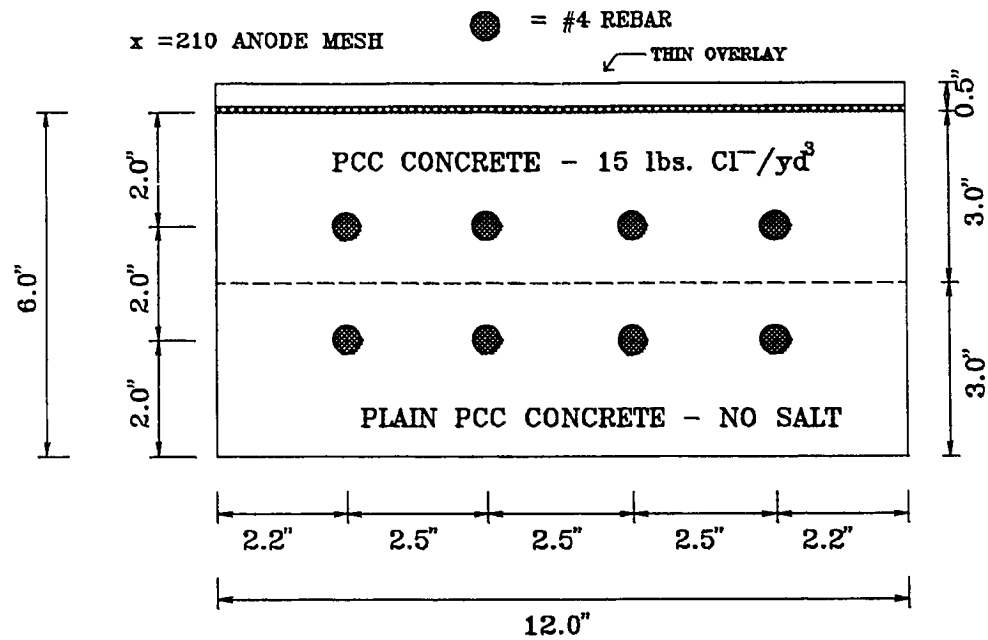

Table 5-4. Ohio Class C Concrete Mix Design Table

Component	Weight
Cement	607.1 lbs.
ASTM C 33 Coarse Aggregate, No. 57	1790.3 lbs.
ASTM C 33 Fine Aggregate	1209.4 lbs.
Air Content	6%
Slump	3 inches
Water/Cement	0.5

Table 5-5. Polarization Decay Test Block Data

Block No.	Anode Current	Charge-Amp-hr	Overlay
13509-13-1	10 mA/ft^2	250	Commercial
13509-13-2	20 mA/ft^2	501	Commercial
13509-13-3	80 mA/ft^2	2003	Commercial
13509-13-4	10 mA/ft^2	250	Superplasticized
13509-13-5	20 mA/ft^2	501	Superplasticized
13509-13-6	80 mA/ft^2	2003	Superplasticized
13509-13-7	10 mA/ft^2	250	Latex Modified
13509-13-8	20 mA/ft^2	501	Latex Modified
13509-13-9	80 mA/ft^2	2003	Latex Modified

Table 5-6. Polarization Decay Block - Chloride Profiles and pH Measurements

		Chloride Content, lbs/yd^3			
Block No.	pH	Surface	5/8 in.	1-1/4 in.	Steel
13509-13-1	12.00	8.61	8.61	7.44	5.48
13509-13-2	12.01	5.48	8.61	7.44	5.07
13509-13-3	12.07	3.52	2.74	2.35	1.96

The chloride contents were determined by taking a 4-inch (10.2 cm) diameter core from each block and removing powder samples parallel to the top reinforcing bar at the various depths shown in Figure 5-3.

Figure 5-3. Polarization Decay Block Chloride Sampling

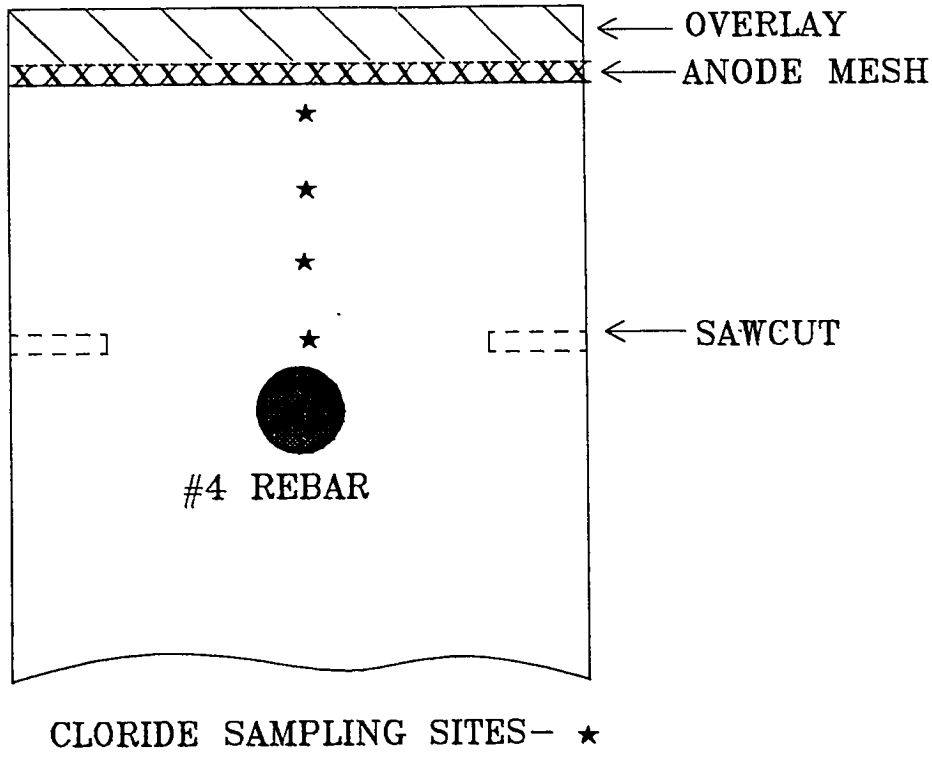

After the powder samples were extracted, the cores were split open along the top of the reinforcing bar. This was accomplished by circumferentially sawing 1/2 in. (1.3 cm) deep around the core just above the reinforcing bar. This allowed access to the bar for measurement of the pH. The pH measurements were made using a microtip Ag/AgCl pH electrode. Discrete sites along the top of the rebar were wetted with deionized water at the concrete/steel interface, and the electrode tip was placed on each site to obtain a reading. Six sites were measured along each bar, and the results shown in Table 5-6 are the average of those readings.

Polarization decay data was collected on the blocks for 3121 hours. Figures 5-4 to 5-15 show the plots for each block at 4, 56, and 3121 hours.

Figure 5-4. Block No. 4: 56-Hour Polarization Decay

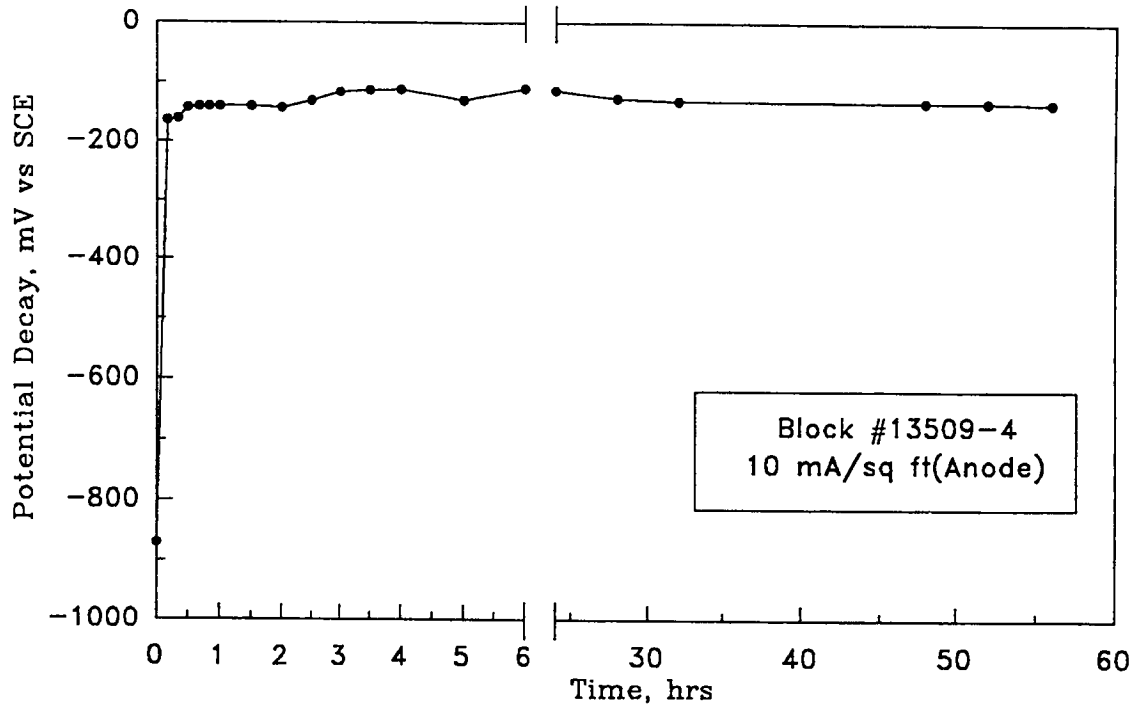

Figure 5-5. Block No. 4: 3121-Hour Polarization Decay

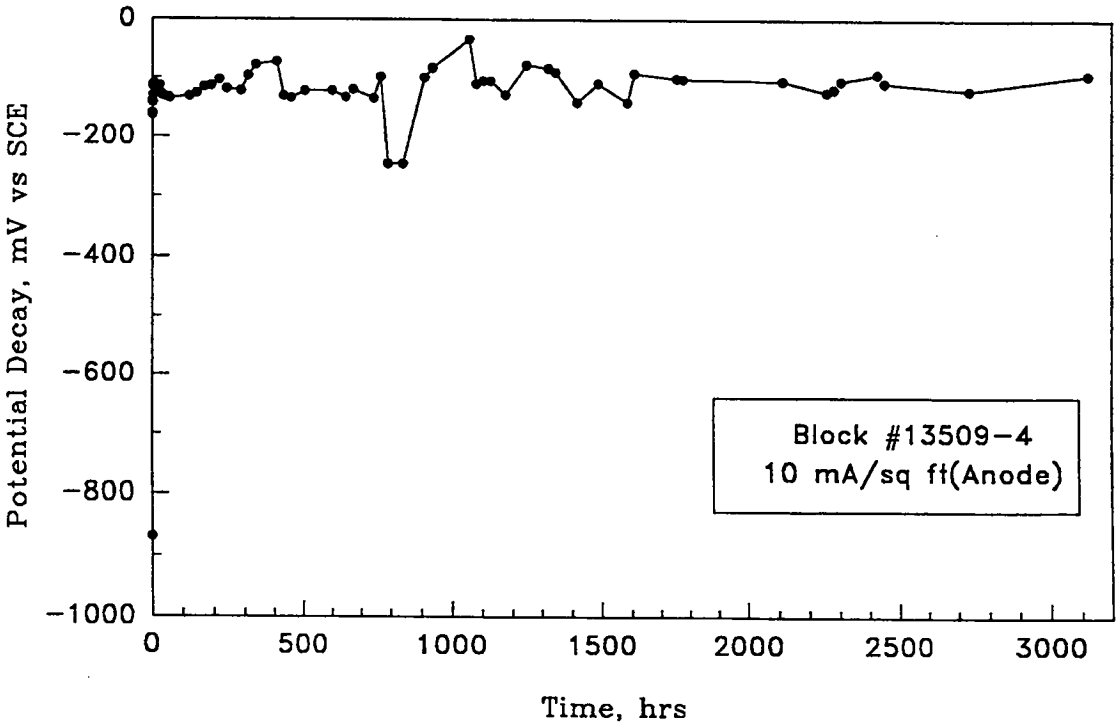

Figure 5-6. Block No. 5: 56-Hour Polarization Decay

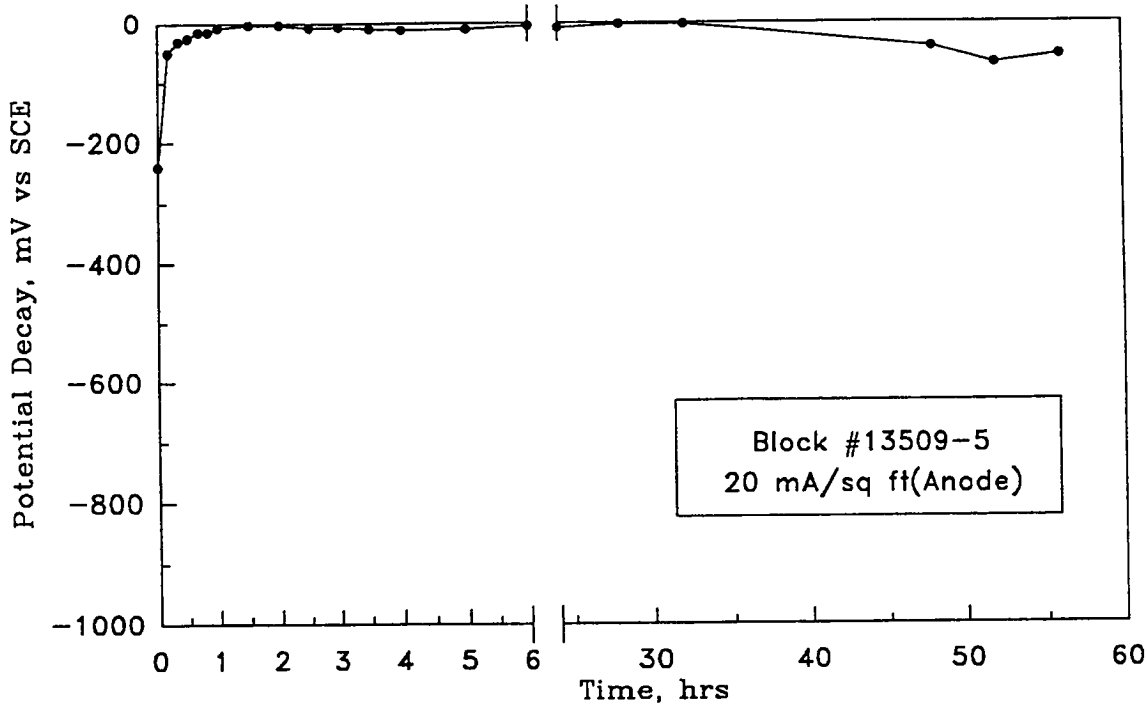

Figure 5-7. Block No. 5: 3121-Hour Polarization Decay

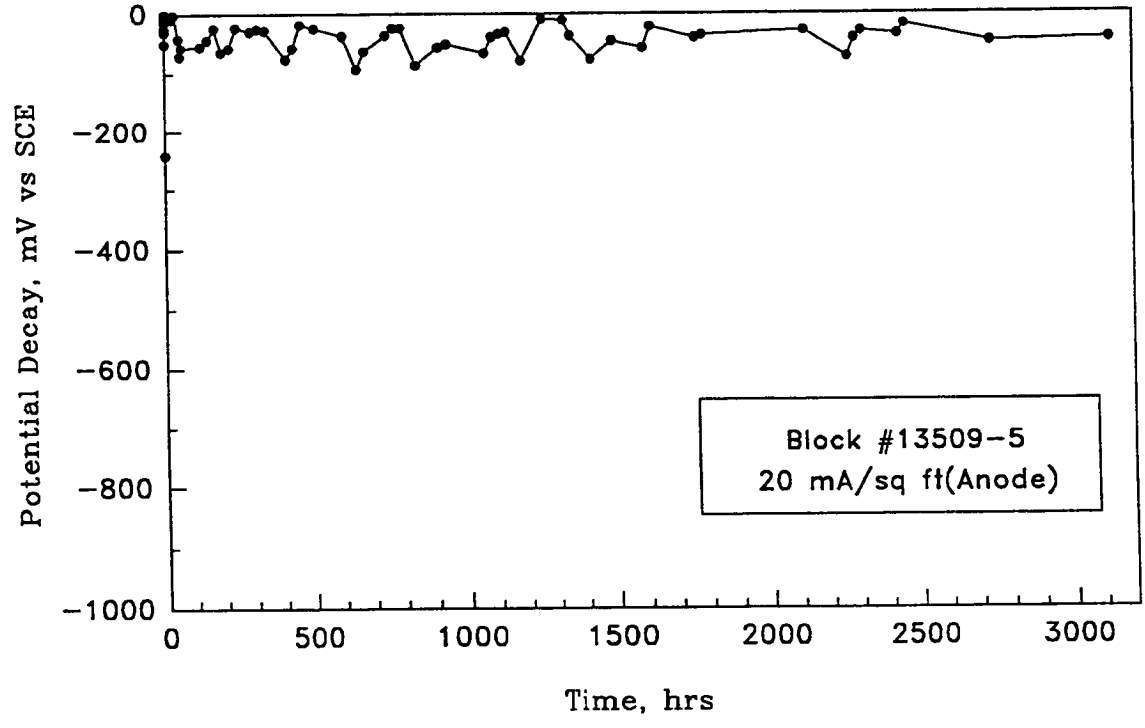

Figure 5-8. Block No. 6: 56-Hour Polarization Decay

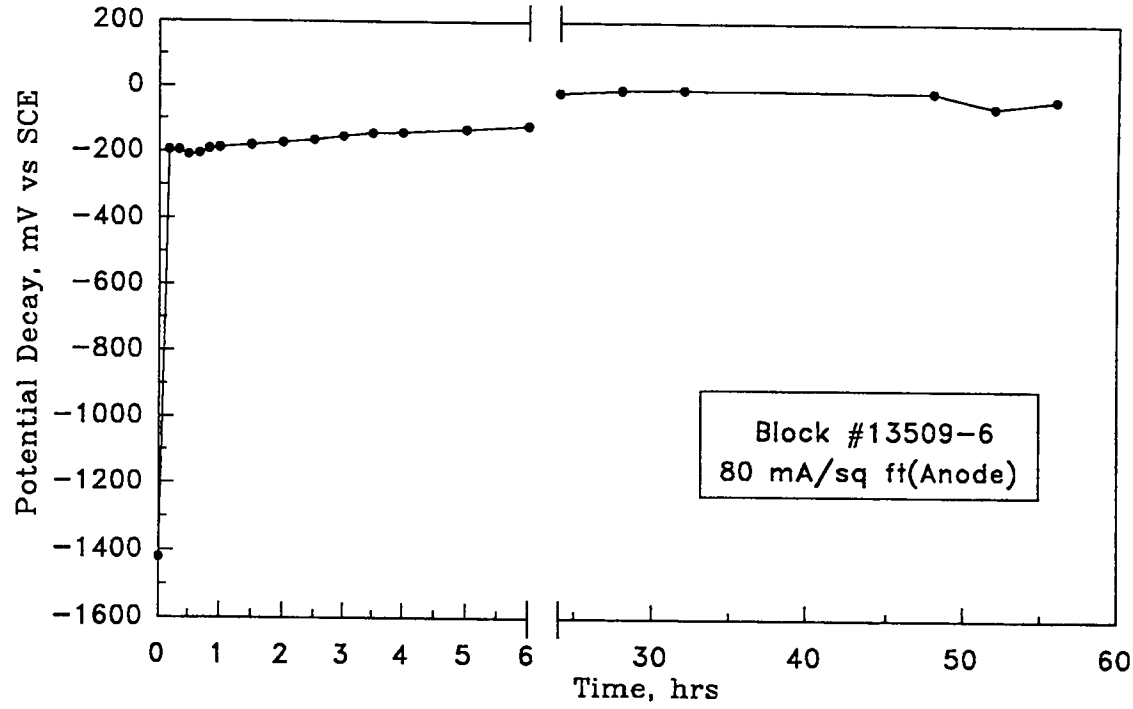

Figure 5-9. Block No. 6: 3121-Hour Polarization Decay

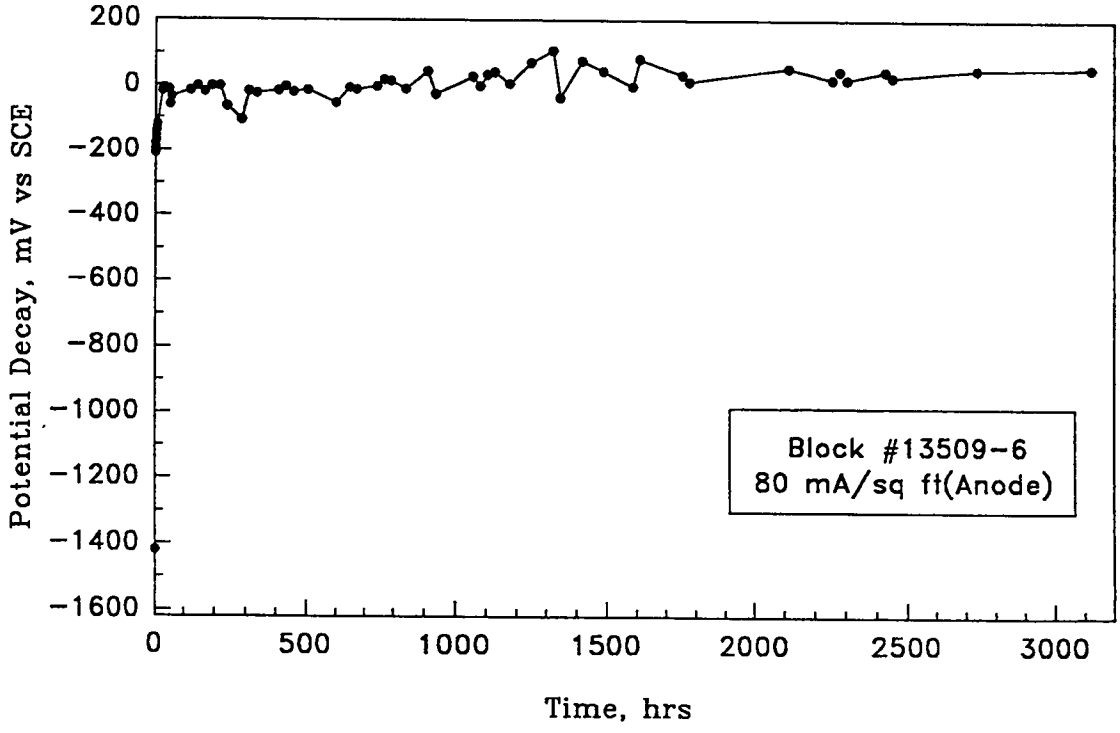

Figure 5-10. Block No. 7: 56-Hour Polarization Decay

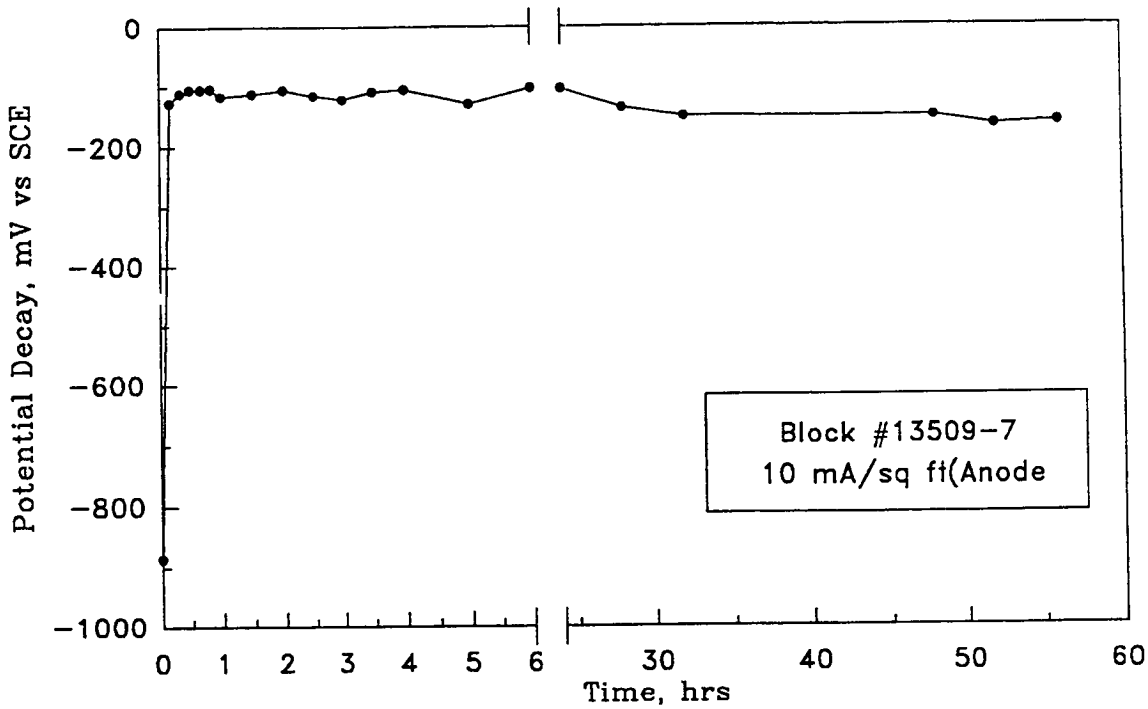

Figure 5-11. Block No. 7: 3121-Hour Polarization Decay

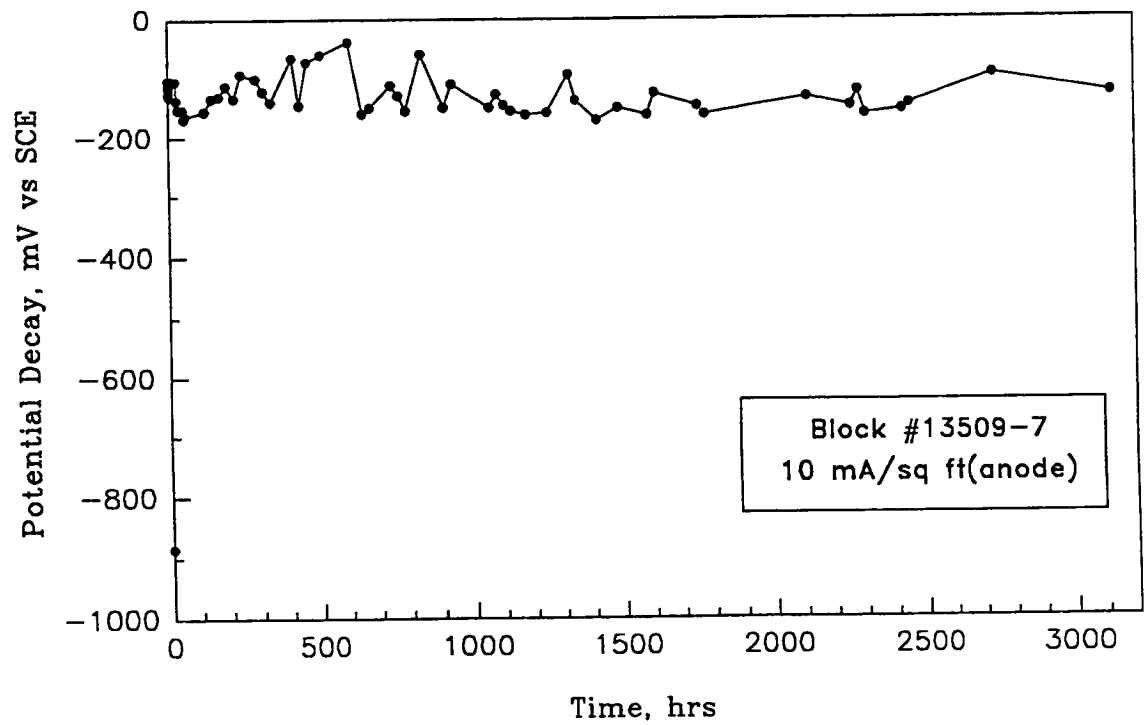

Figure 5-12. Block No. 8: 56-Hour Polarization Decay

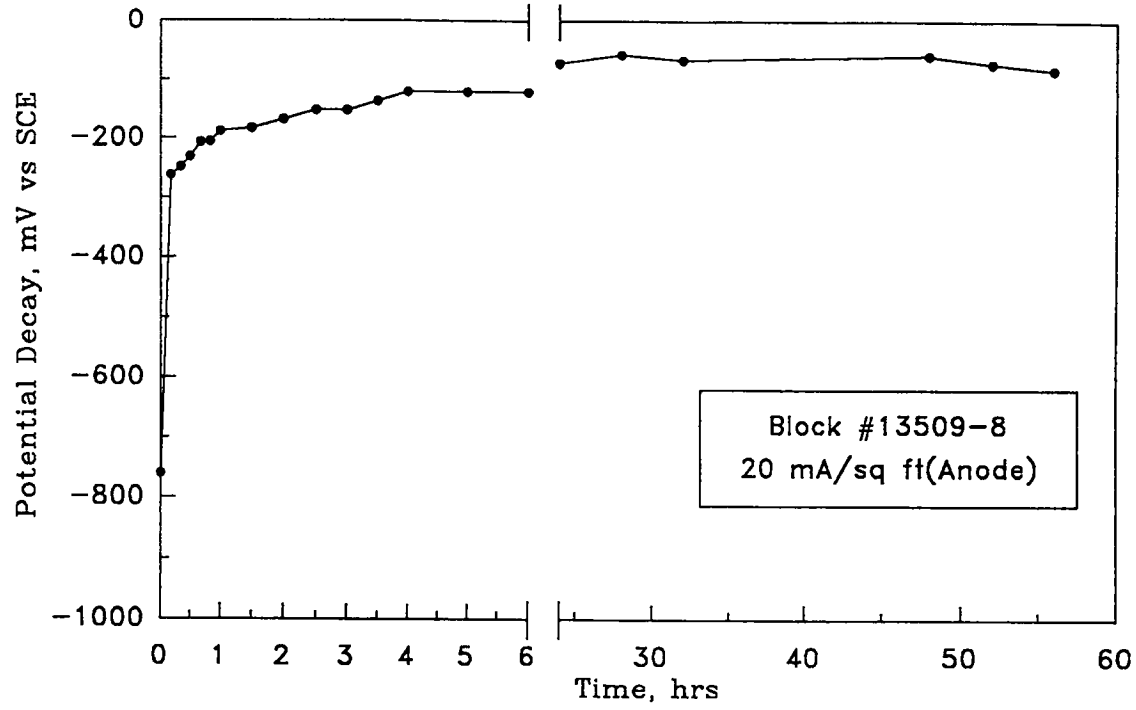

Figure 5-13. Block No. 8: 3121-Hour Polarization Decay

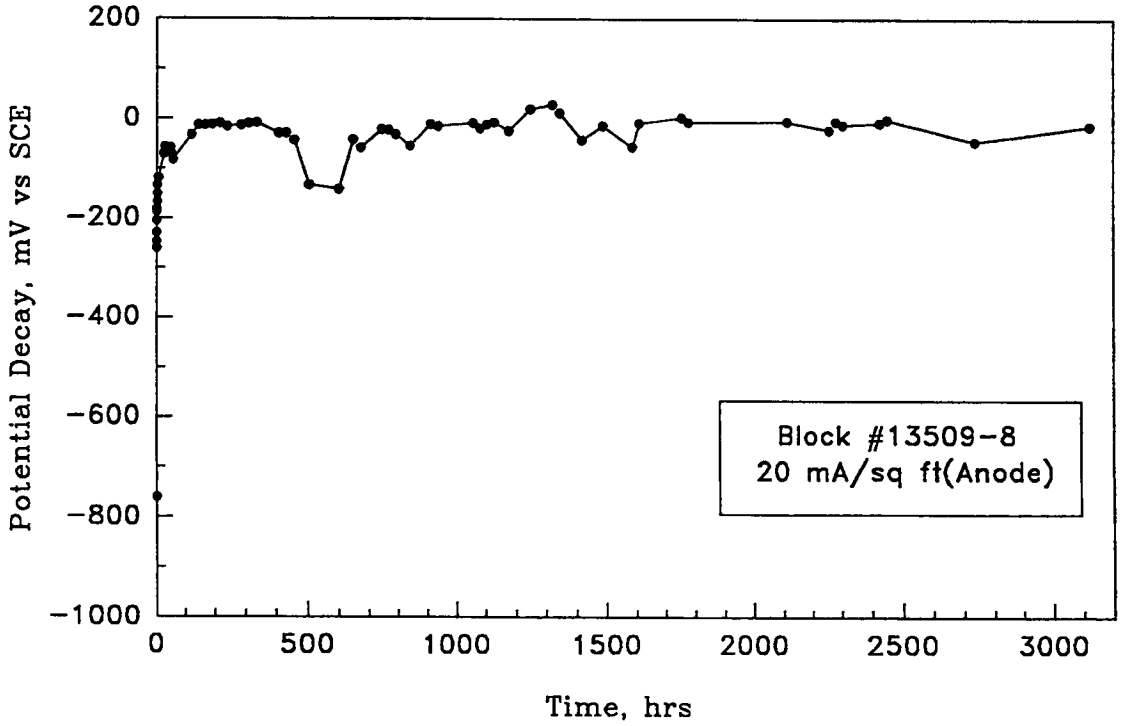

Figure 5-14. Block No. 9: 56-Hour Polarization Decay

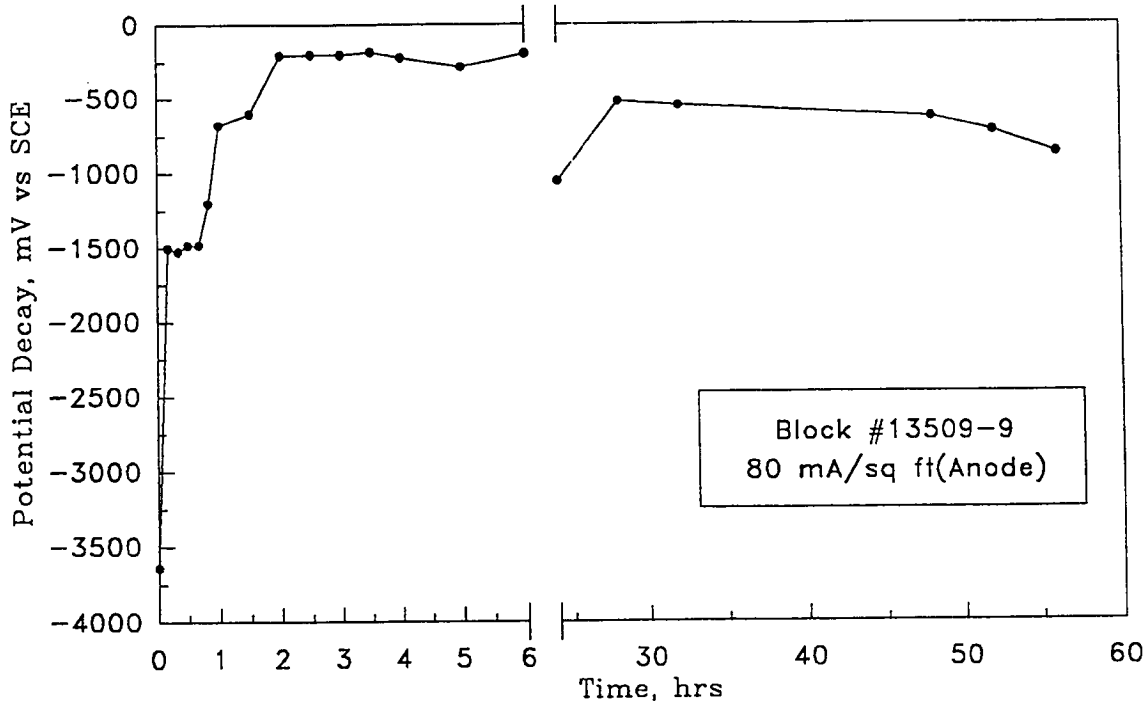

Figure 5-15. Block No. 9: 3121-Hour Polarization Decay

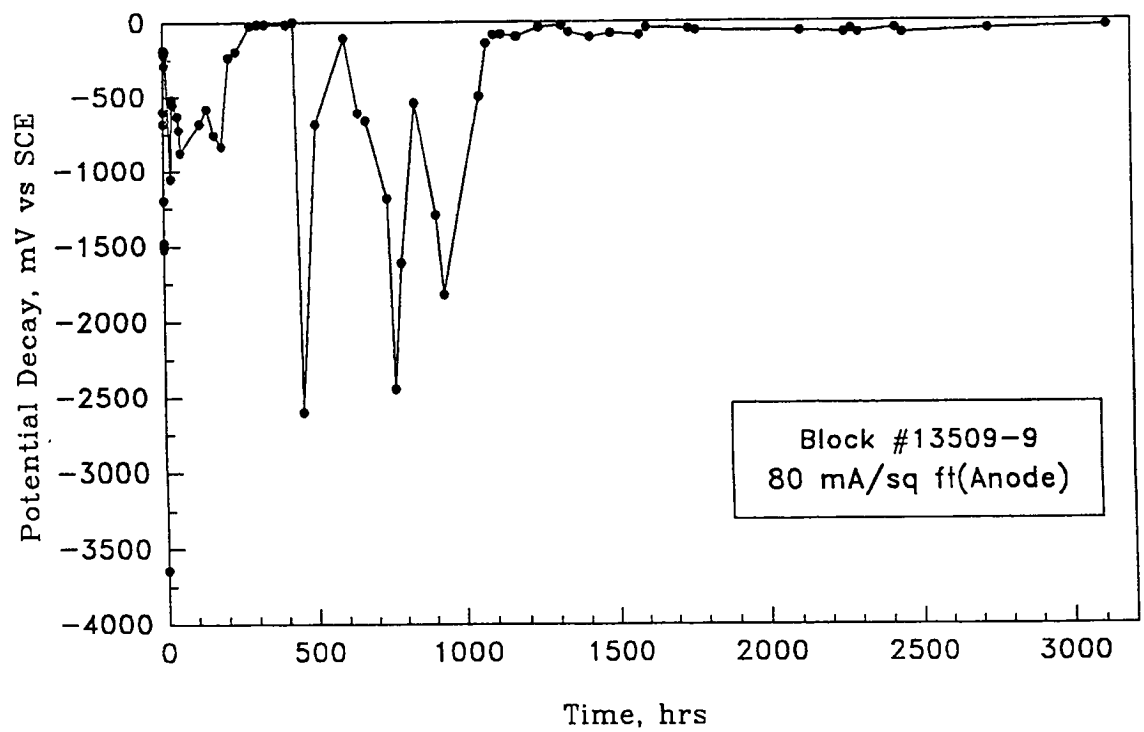

Results and Conclusions

The polarization decay of the blocks is relatively smooth and consistent for the first 4 hours. After that, the polarization decay data begin to show effects other than polarization decay. The data show that under the conditions of this test the polarization decay occurred in the first 24 hours. Then weather-related effects took over. The data then become distorted and somewhat random. The effect of temperature changes appears to cause this fluctuation.

The pH measurements and chloride contents indicated that the higher the current density, the higher the pH around the cathode (reinforcing steel). The chloride contents also show a similar effect in the higher current density blocks having less chlorides than the lower current density block(s). Also shown is a lower chloride content at the reinforcing steel level indicating that chlorides are migrating away from the cathode (reinforcing steel) during cathodic protection.

Impressed Current Effect on Static Potential

Sample Preparation and Testing

The long-term effect of passage of cathodic protection current on the static potential of the cathode (reinforcing steel) was investigated. Eight 1 ft^2 (0.09 m^2) reinforced concrete blocks shown in Figure 5-16 were energized at anode current densities of 2, 10, and 40 mA/ft^2 (21.5, 108, and 430 mA/m^2). Table 5-7 provides the mix designs for the base slab concrete and overlay concrete as well as the current density data. The mix design for the base slab concrete was that for Ohio Department of Transportation Class C structural concrete.

Figure 5-16. Static Potential Test Block

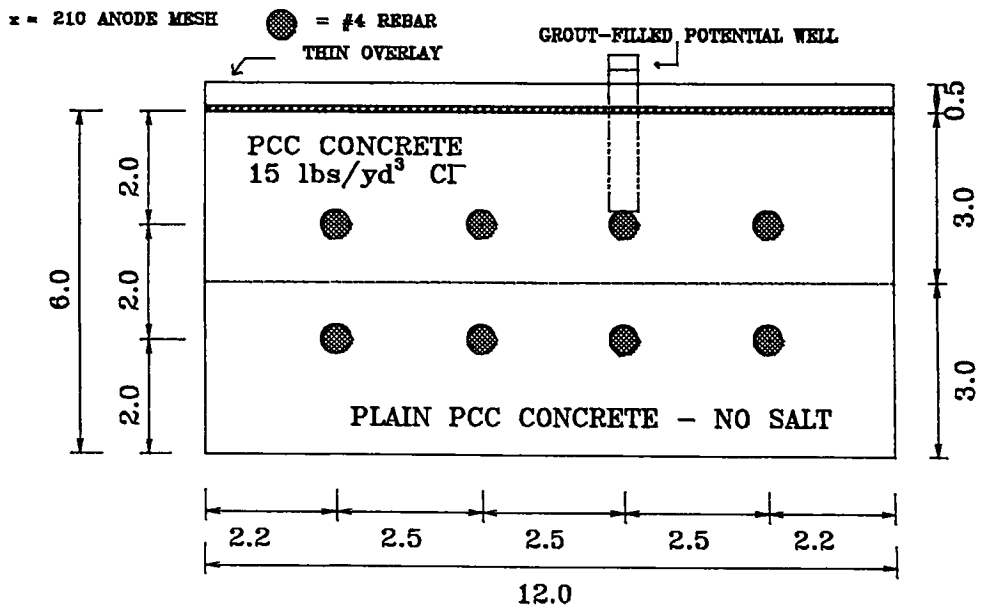

Table 5-7. Static Potential Test Block Concrete Mix Designs

Component	Weight
Cement	607.1 lb (275.4 kg)
ASTM C 33 Coarse Aggregate, No. 57	1790.3 lb (812.1 kg)
ASTM C 33 Fine Aggregate	1209.4 lb (548.6 kg)
Water/Cement	0.5
Air Content	6%
Slump	3 inches (7.6 cm)

Block No.	Anode Current Density	Overlay
13555-66-1	10 mA/ft^2 (107 mA/m^2)	Commercial
13555-66-2	40 mA/ft^2 (430 mA/m^2)	"
13555-66-3	10 mA/ft^2 (107 mA/m^2)	"
13555-66-4	40 mA/ft^2 (430 mA/m^2)	"
13555-66-5	2 mA/ft^2 (21.5 mA/m^2)	"
13555-66-6	2 mA/ft^2 (21.5 mA/m^2)	"
13555-66-7	10 mA/ft^2 (107 mA/m^2)	"
13555-66-8	40 mA/ft^2 (430 mA/m^2)	"

The blocks were energized for three weeks, and a 5-day polarization decay was conducted. This sequence was continued for six months. The polarization decay summary data are presented in Figures 5-17 to 5-24.

Figure 5-17. Block No. 1 Polarization Decay Summary - 10 mA/ft² (107 mA/m²)

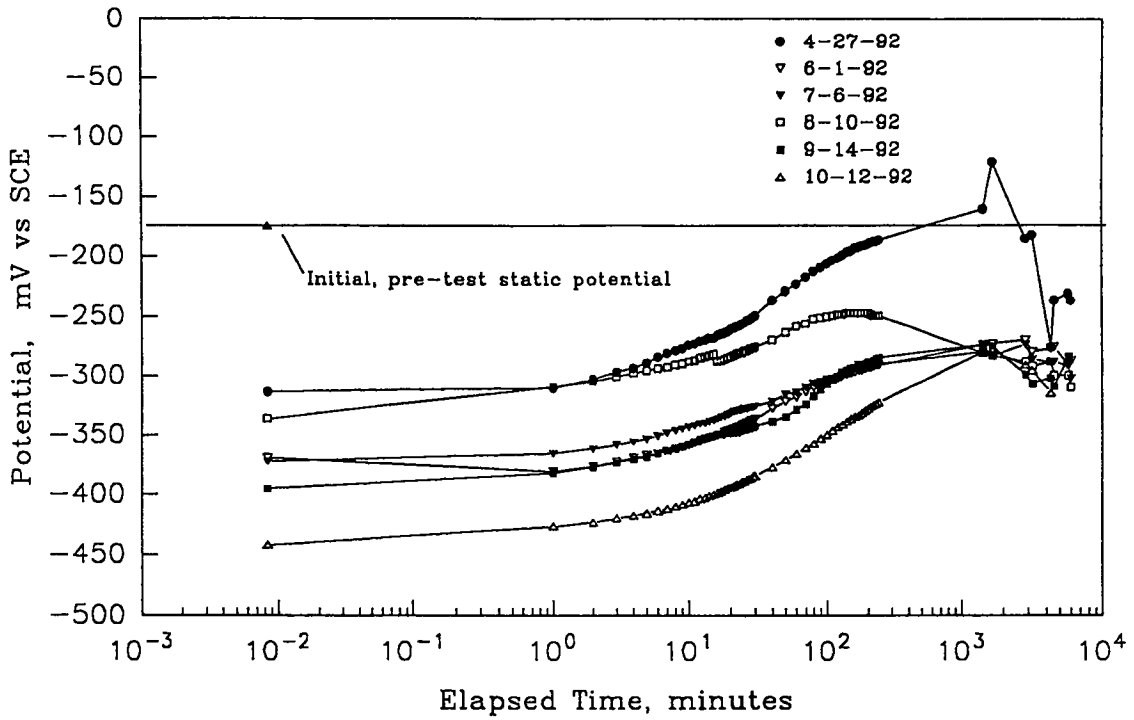

Figure 5-18. Block No. 2 Polarization Decay Summary - 40 mA/ft² (430 mA/m²)

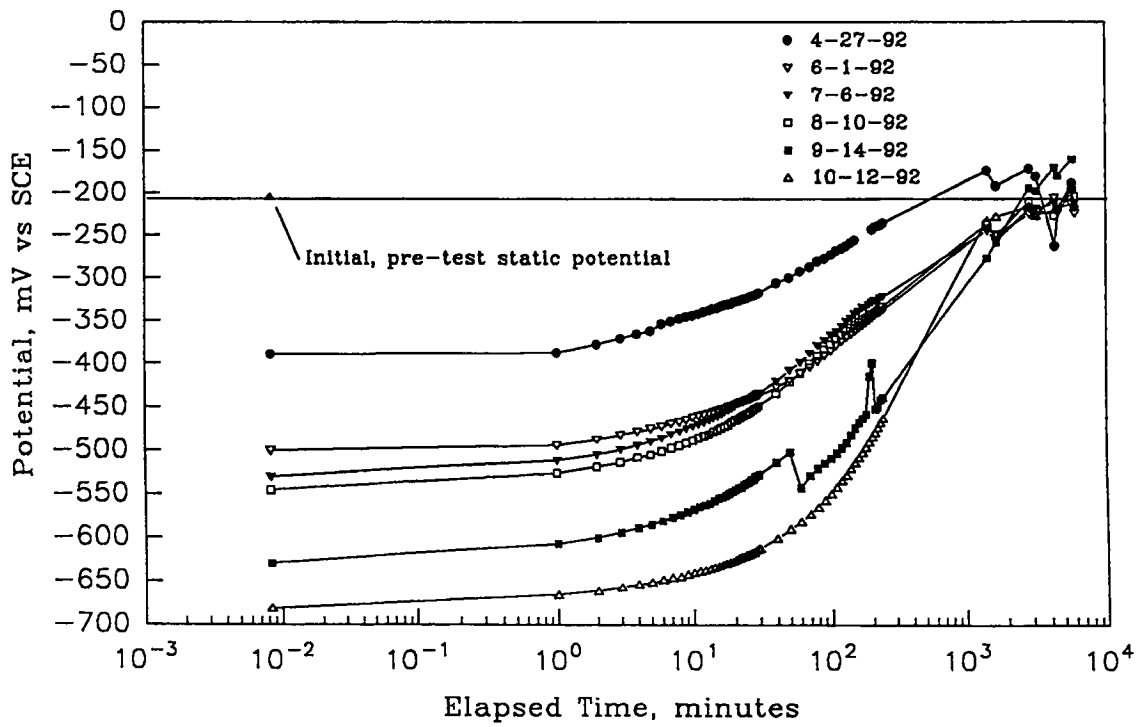

Figure 5-19. Block No. 3 Polarization Decay Summary - 10 mA/ft² (107 mA/m²)

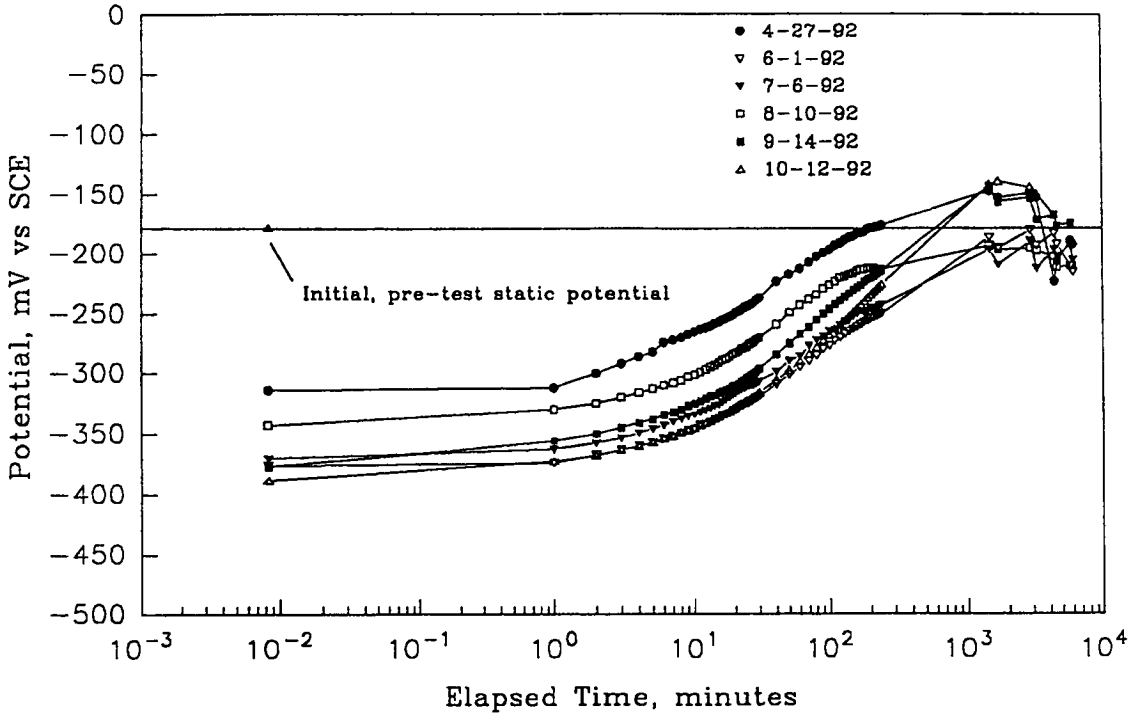

Figure 5-20. Block No. 4 Polarization Decay Summary - 40 mA/ft² (430 mA/m²)

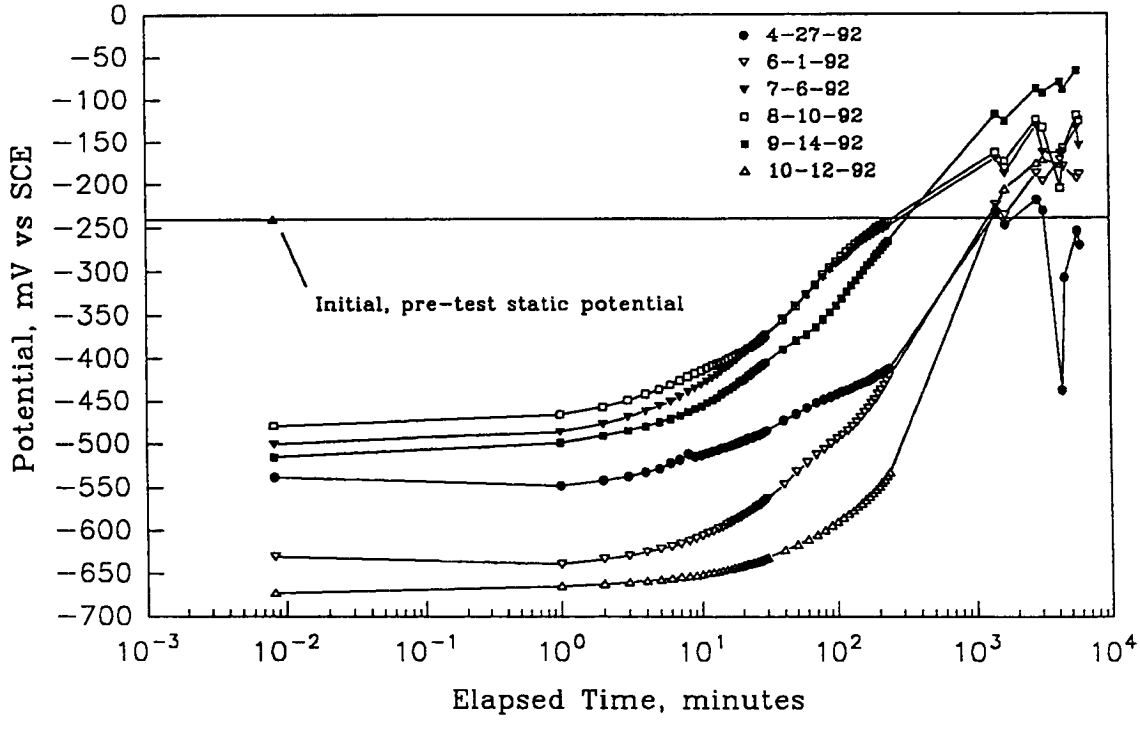

Figure 5-21. Block No. 5 Polarization Decay Summary - 2 mA/ft² (21.5 mA/m²)

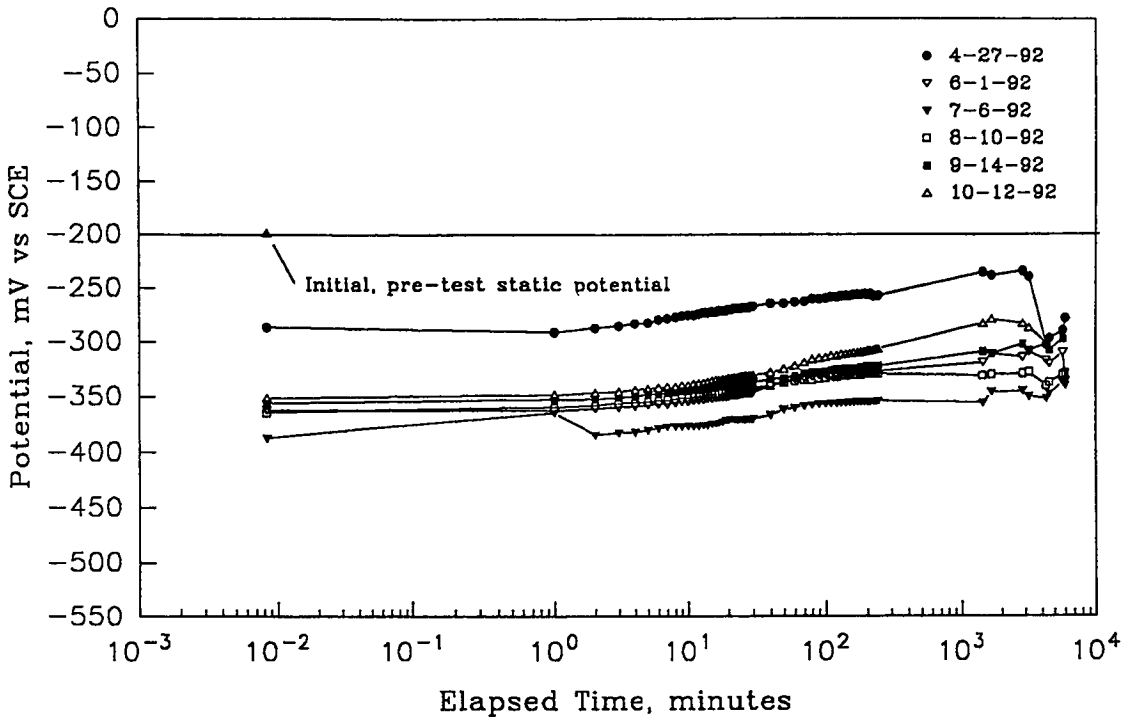

Figure 5-22. Block No. 6 Polarization Decay Summary - 2 mA/ft² (21.5 mA/m²)

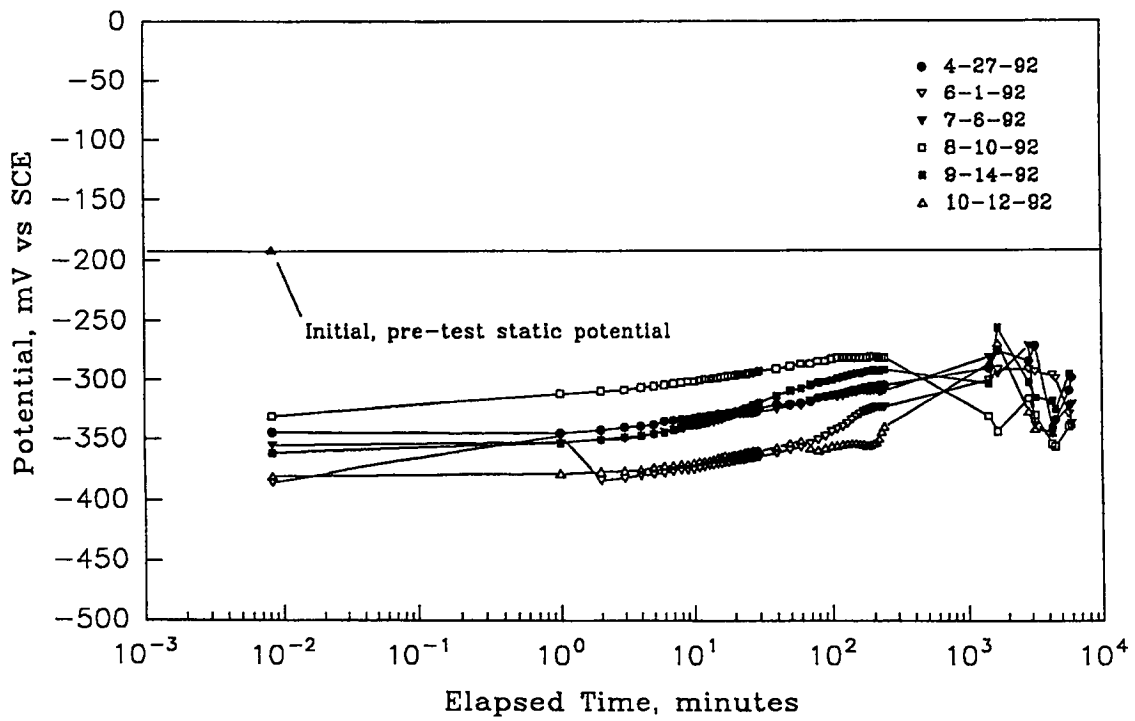

Figure 5-23. Block No. 7 Polarization Decay Summary - 10 mA/ft² (107 mA/m²)

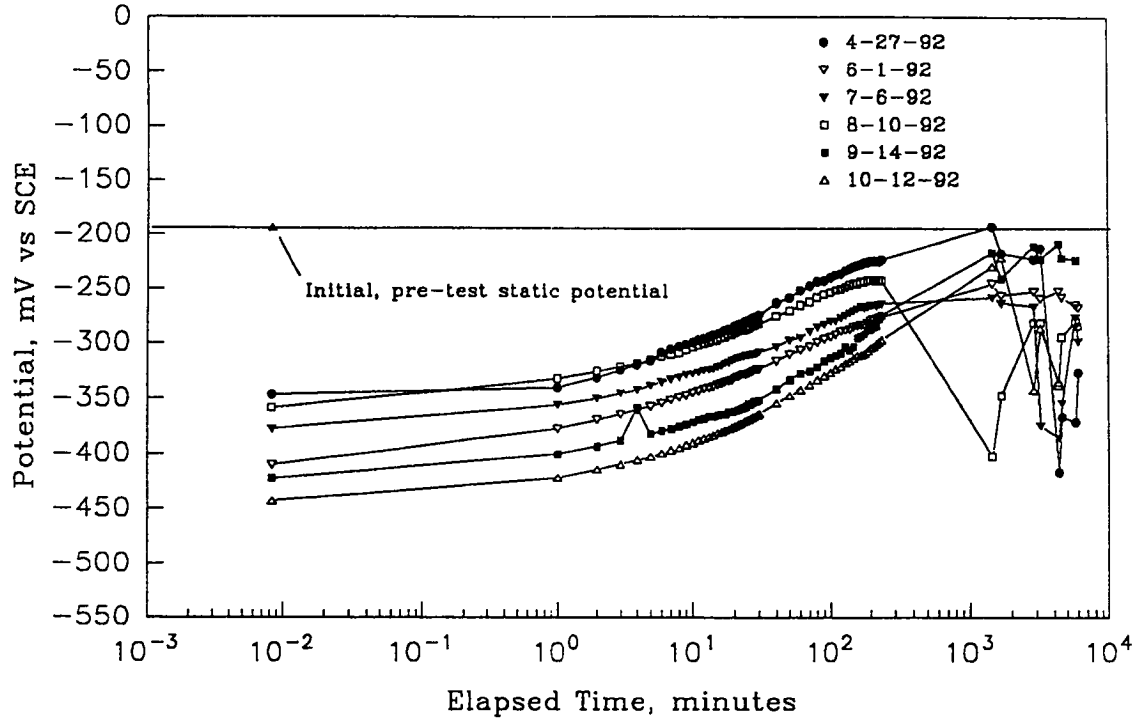

Figure 5-24. Block No. 8 Polarization Decay Summary - 40 mA/ft² (430 mA/m²)

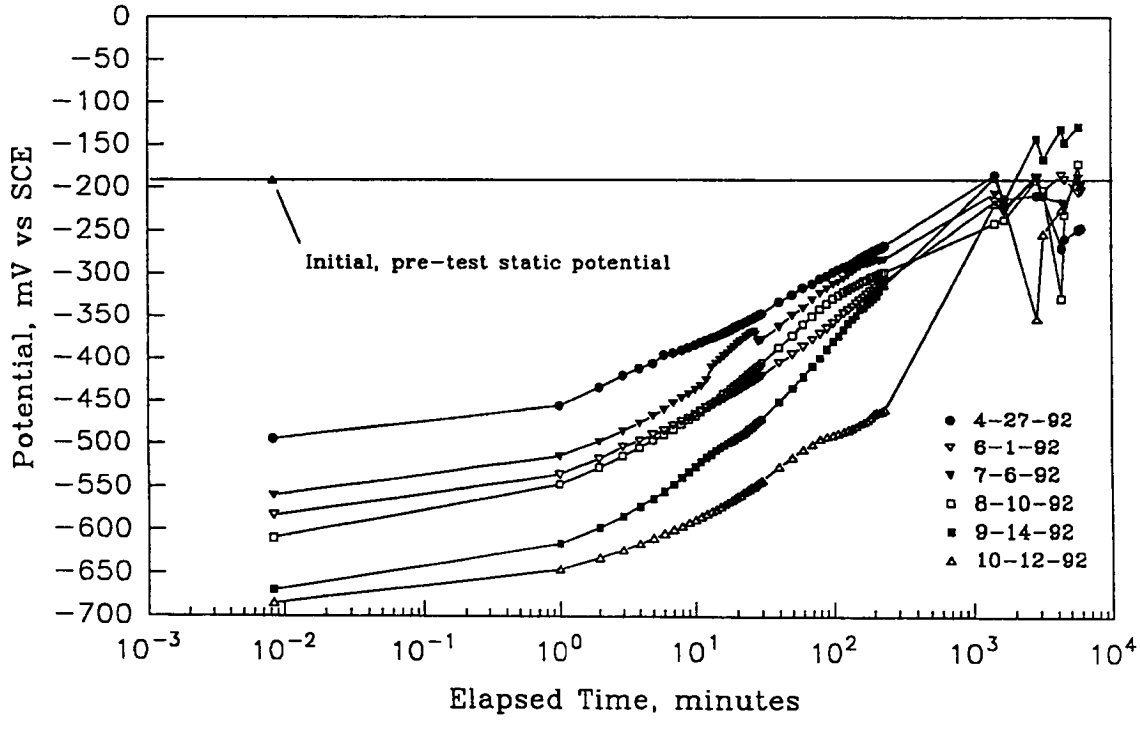

The 5-day polarization decay for each block was plotted for each measurement interval of one month, and the results are shown in Figure 5-25.

Figure 5-25. Polarization Decay Difference

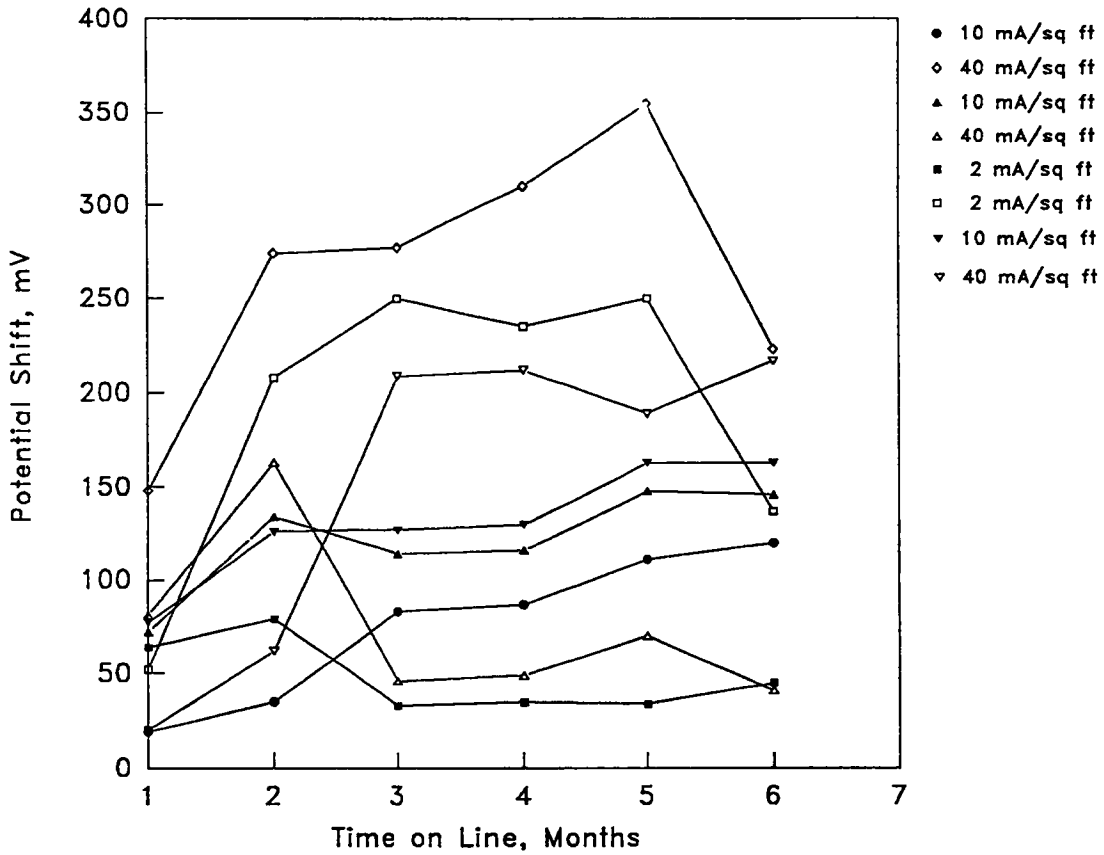

Results and Conclusions

From the data obtained the polarized potential moves steadily more negative as time-on-line increases during the first 7 months of application of cathodic protection current. This can be seen on each of the plots of polarization decay data at monthly intervals.

The 4-hour polarization decay (instant-off minus 4-hour potential) does not remain constant for each block tested. However, there is a slight increase in the total decay as current charge is accumulated.

The cathodic protection systems simulated by the test blocks indicate that cathodic protection systems do not fully depolarize in a 4-hour period. In fact it may take up to four days to occur as shown on the polarization decay plots.

A greater amount of cathodic protection charge results in potentials relaxing to less corrosive potentials after long-term polarization decay.

Potential measurements taken after 24 hours or more after current is off are likely to be greatly affected by environmental conditions making interpretation of the results difficult.

Effects Near the Anode

Sample Preparation and Testing

To test and evaluate the effect of cathodic protection current on the anode and area around it, 4 ft x 3 ft x 8.5 in. (1.22 x 0.9 x 0.19m) reinforced concrete slabs were fabricated in two stages. The first stage consisted of casting the base blocks, while the second consisted of installation of various anode systems.

The first stage consisted of two layers of concrete with the first or bottom layer being 0.09 m-thick and salt free. Nine No. 4 (13 mm) reinforcing bars were embedded in the layer with 5 in the 4 ft. (1.22 m) direction and 4 in the 3 ft (0.90m) direction. The reinforcing bar mat had a clear cover of 1 in. (2.5 cm) from the bottom of the slab. The second or upper layer of concrete was 2.5 in. (0.06m) thick with 25 lb Cl^-/yd^3 (14.8 kg Cl^-/m^3) concrete as admixed $CaCl_2$. $CaCl_2$ was used in lieu of NaCl, because it does not have an adverse effect on the concrete when admixed and is more compatible with concrete. Nine No. 4 (13 mm) reinforcing bars were placed in the 4 ft (1.22 m) direction. Figure 5-26 shows the details of this slab. An epoxy coating was applied to the bars from approximately 1 in. (2.5 cm) within the forms to the bar ends to minimize establishing any cell where the steel exited the concrete and to provide atmospheric protection at the bar ends. Electrical continuity of the steel within each layer was established by welding a single bar external to the ends of the embedded bars in the concrete.

One-in. (2.5 cm) ID PVC stubs were epoxied to the top slab surface to facilitate taking potential measurements irrespective of a subsequently placed overlay.

The actual chloride distribution varied from the planned quantity of 15# Cl^-/yd^3 (9 kg/m^3) in the top 2.5 in. (6.4 cm) of the six in. (15 cm) thick slabs. The measured chloride content was closer to 6 to 8# Cl^-/yd^3 (3.6 to 4.8 kg/m^3) for this region.

Figure 5-26. Reinforced Concrete Test Slab

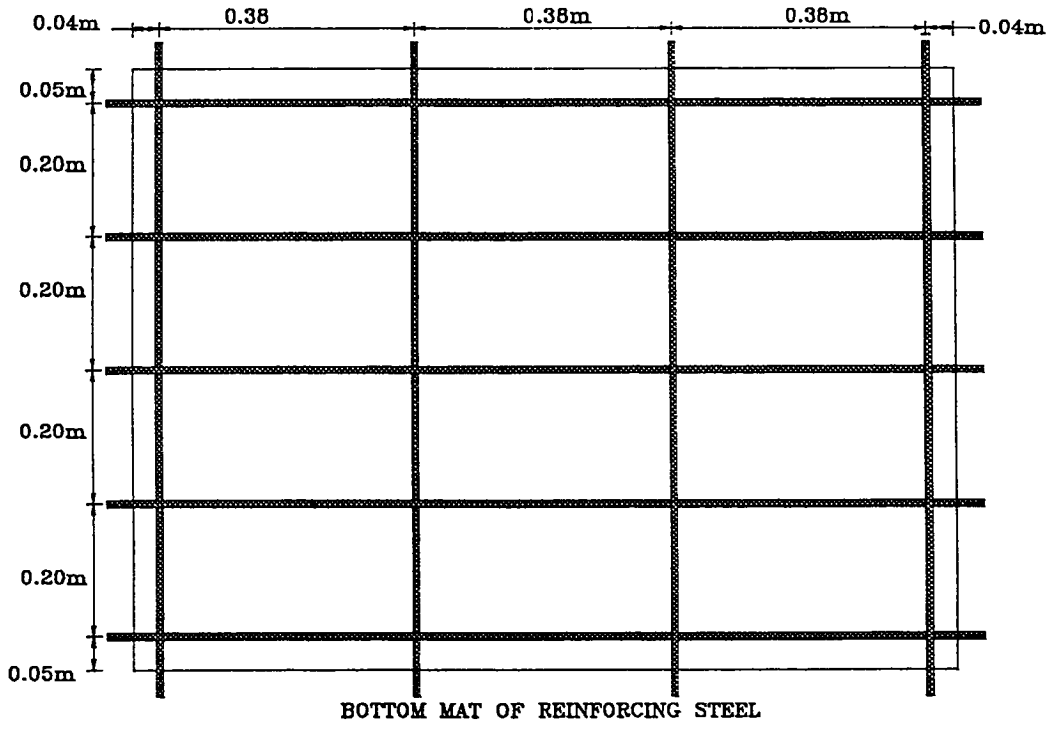

BOTTOM MAT OF REINFORCING STEEL

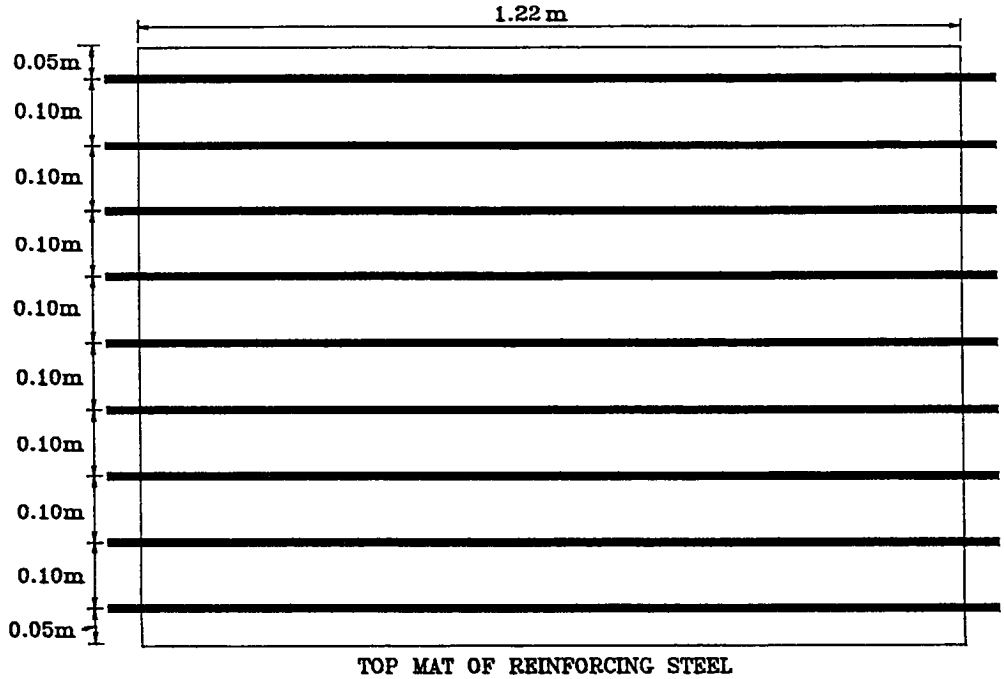

TOP MAT OF REINFORCING STEEL

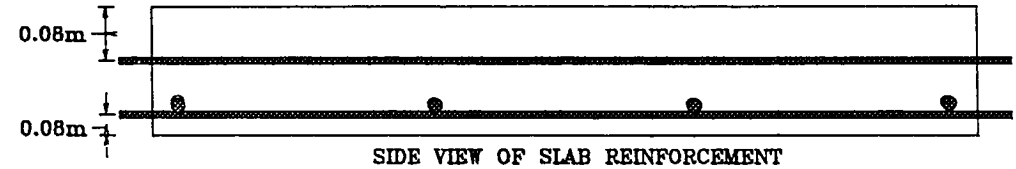

SIDE VIEW OF SLAB REINFORCEMENT

Four different anode materials were used, as listed in Table 5-8. The carbon conductive polymer consisted of a platinum wire primary anode and carbon fiber secondary anode. Both were covered with a conductive polymer first, to secure these in place, and, second, to provide reduced anode resistance and a more uniform current distribution than would otherwise be the case. The ELGARD™ ribbon, ELGARD™ 210 anode mesh, and Ferex™ 100 Wire were attached to the concrete using plastic screws and clips.

For the second stage of anode installation a 1.5 in. (0.04m) thick layer of superplasticized dense concrete was placed as the anode overlay. The concrete mix design for each layer is given in Table 5-9. Correspondingly, Table 5-10 lists the specimen, anode material, and test anode current density upon energizing.

Table 5-8. Selected Anode Materials

	Anode Material
1.	Conductive Polymer with platinum primary and carbon fiber secondary anode
2.	ELGARD™ Anode Ribbon
3.	ELGARD™ 210 Anode Mesh
4.	Ferex™ 100 Wire

Table 5-9. Concrete Mix Designs

Bottom Slab Layer	Quantity
Coarse Aggregate (Crushed Limestone)	765 kg (1684 lb)
Fine Aggregate (Florida Silica Sand)	528 kg (1162 lb)
Cement (Florida Portland Type I)	290 kg (638 lb)
Water	135 kg (296 lb)
Air Entraining Admixture (Sika AEA-15)	0.07 kg (0.16 lb)
Water Reducing Agent (WRDA 79)	1.2 kg (2.6 lb)
Slump	0.10-0.15 m (4-6 in.)
Water-to-Cement Ratio	0.46
Air Content	4%
28 Day Compressive Strength	42.1 MN/m^2 (6110 psi)
Top Concrete Layer	
Mix design was identical to that for the bottom layer but with the addition of 14.8 kg/m^3 of concrete (25 lb/yd^3) of crystalline CaCl2.	
Superplasticized Dense Concrete Overlay	
Coarse Aggregate	606 kg (1334 lb)
Fine Aggregate	620 kg (1364 lb)
Cement	389 kg (855 lb)
Water	177 kg (308 lb)
Superplasticizer (Sikament 300)	1.9 kg (4.1 lb)
Air Entraining Admixture	0.4 kg (0.9 lb)

Table 5-10. Slab Number With Anode Type and Current Density

Slab No.	Anode	Anode Current Density mA/ft^2	Anode Current Density mA/m^2
1	Conductive Polymer	20	215
2	ELGARD™ Ribbon	20	215
3	ELGARD™ 210 Mesh	40	430
4	ELGARD™ 210 Mesh	20	215
5	ELGARD™ 210 Mesh	10	107
6	Ferex™ Wire	20	215

Prior to cathodic polarization the half-cell potential of both the top and bottom steel mats was measured to assess the state of corrosion. Figure 5-27 provides a plan view of a slab showing the measurement points. Subsequently, both mats were connected through a 1-ohm resistor to form a macrocell and to facilitate current measurement between the two layers. Each slab was energized by an individual filtered power supply which provided a flat direct current signal. Polarization curves for the anodes and steel were obtained by increasing the current, in steps, to the final level. Instant-off potentials were taken at 500 msec after current was

interrupted. Figure 5-28 shows the locations where these measurements were made. The polarization scans were conducted for a given slab within two hours. Figures 5-47 through 5-54 show the polarization scans. Current-off potentials were monitored at irregular intervals thereafter. The slabs were exposed in the Ocean Engineering test yard at Florida Atlantic University approximately 3 km (1.9 mi) from the Atlantic Ocean. The slabs were polarized for 30 months. Cores were taken from each slab at 6-month intervals in order to document the condition of the anode and, in some cases, the cathode. This was done by qualitatively assessing the metal to concrete bond and by measuring the pH at, and adjacent to, the anode-concrete and steel-concrete interfaces.

The first pH measurements were made inside a glove box under a nitrogen atmosphere to minimize carbonation effects, using a combination pH electrode or pH paper.[32] Subsequently, this technique was relaxed and involved air exposure and pH paper only. Caution was exercised to ensure that anode continuity was maintained subsequent to a particular core being taken.

Figure 5-27. Slab Corrosion Potential Measurement Sites

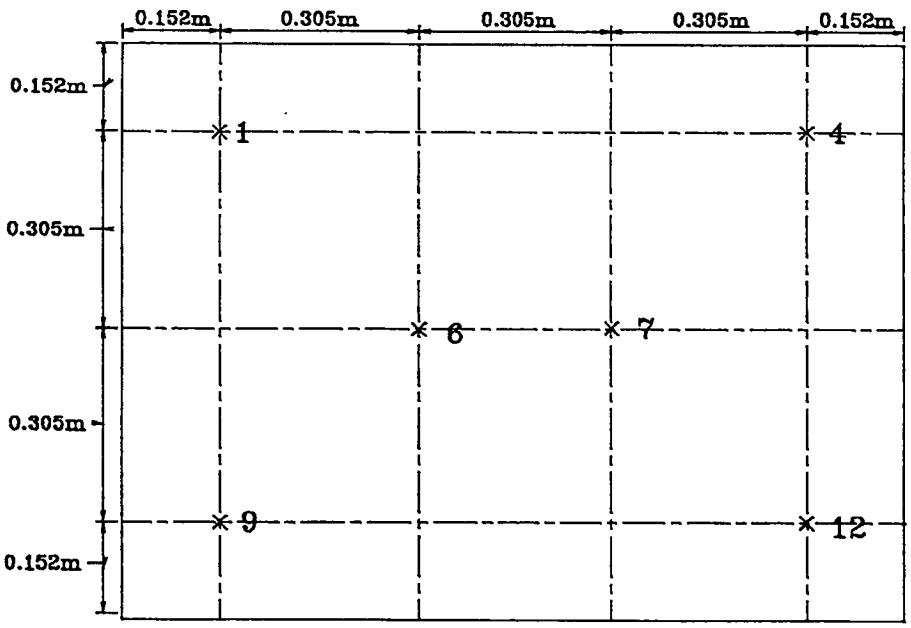

Figure 5-28. Slab Current-Off Potential Measurement Sites

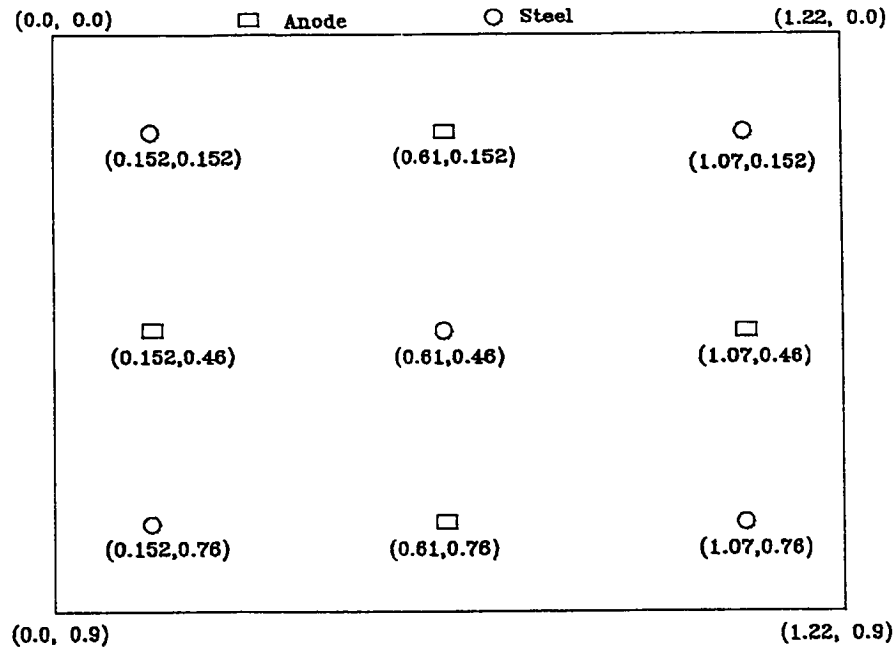

Evaluation of Results

Corrosion Potentials

Figures 5-29 to 5-34 present the corrosion potential data recorded 50 to 60 days after concrete placement and prior to anode and overlay placement. These indicate that the upper steel mat was relatively active and was expected to be corroding based upon established criterion that there is a greater than 90 percent probability that corrosion is occurring when the half-cell potential readings are less than -0.28 volts versus SCE. Conversion from an SCE potential to a CSE (Copper Sulfate Electrode) potential is done by adding a -0.074 volts to the SCE potential reading. A majority of the bottom mat potentials were in the "uncertain" range and, as such, were more negative than what might be anticipated. More positive values may have resulted with increased exposure duration.

Instant-off potentials (after energizing) of the interconnected mats at each of the five measurement locations for the entire test duration are shown in figures 5-35 to 5-40 and show that the potential of the reinforcing steel in slabs 1 and 3-6 became more cathodic during the first several weeks but increased thereafter and reached a maximum at 3 to 4 months and were subsequently more negative. Slab 2 showed less variation of potential with time in that the minimum at several weeks was not apparent.

Figures 5-35 to 5-40 also show the potential of the anodes as a function of time. The variations were generally a mirror image of those for the reinforcing steel. When the potential of the steel was relatively negative, the potential of the anode tended to be positive. It is unclear if the changes in the anode and cathode potential with time reflect actual trends or if they were a consequence of the outdoor exposure and weather changes coupled with the relatively infrequent data acquisition.

Figure 5-29. Corrosion Potential versus Time for Slab 1 Prior to Energizing

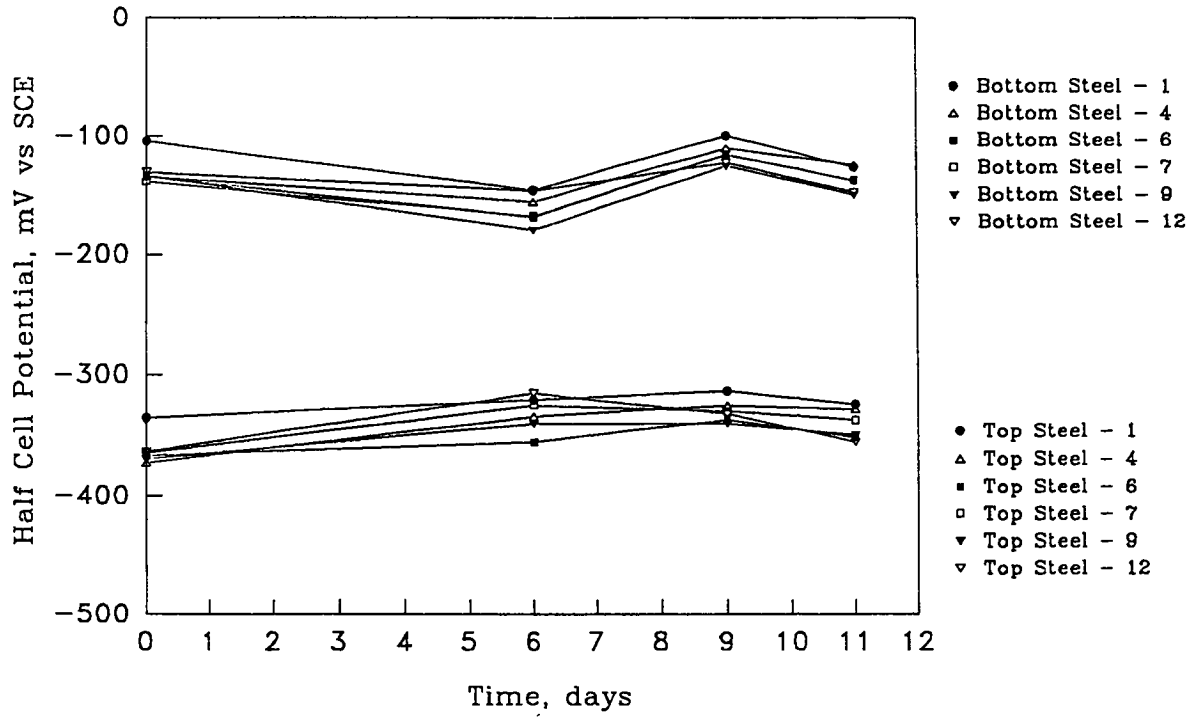

Figure 5-30. Corrosion Potential versus Time for Slab 2 Prior to Energizing

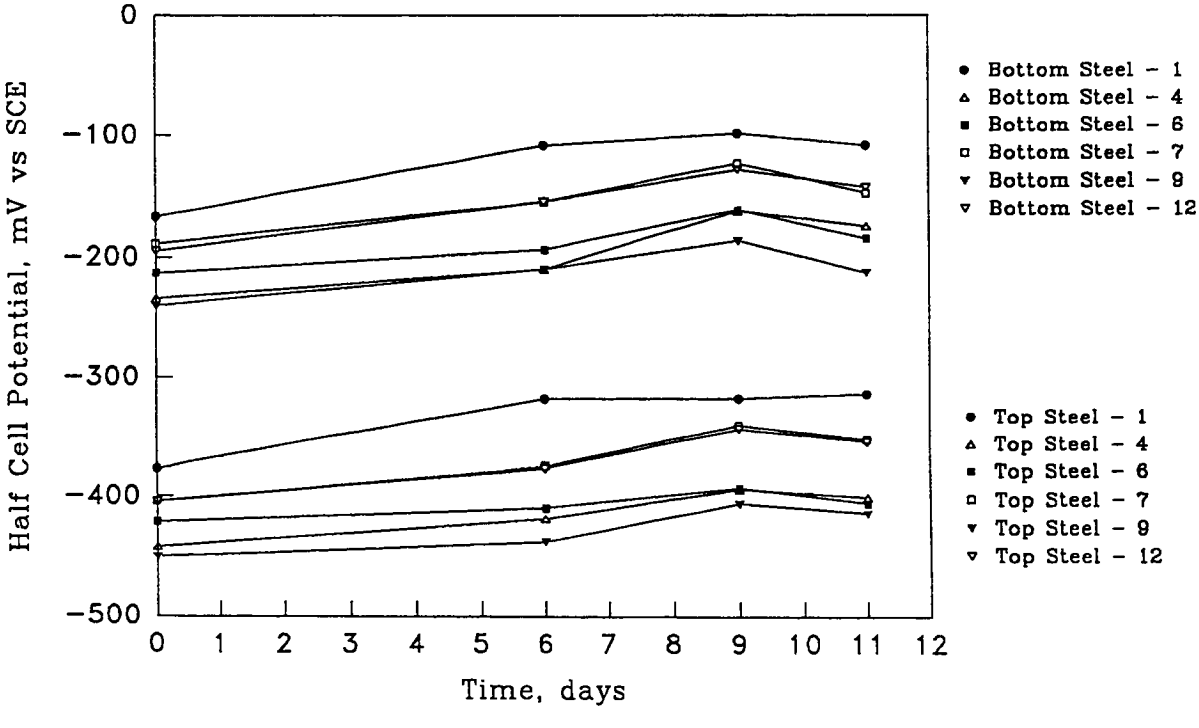

Figure 5-31. Corrosion Potential versus Time for Slab 3 Prior to Energizing

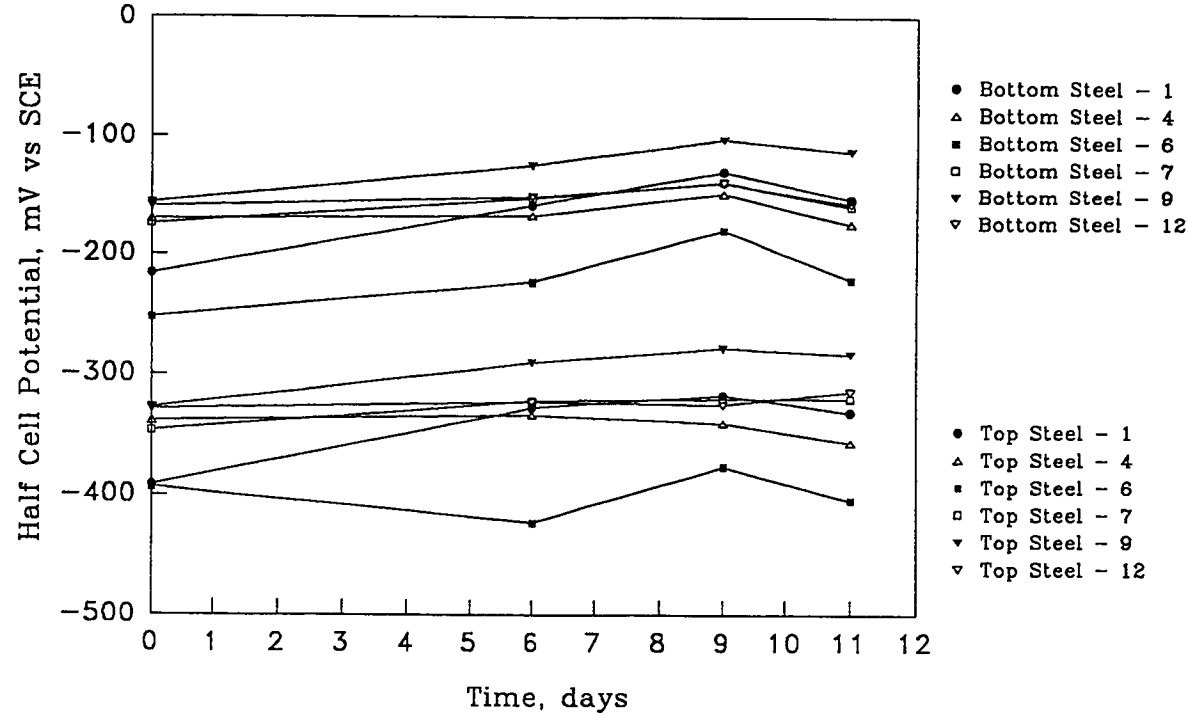

Figure 5-32. Corrosion Potential versus Time for Slab 4 Prior to Energizing

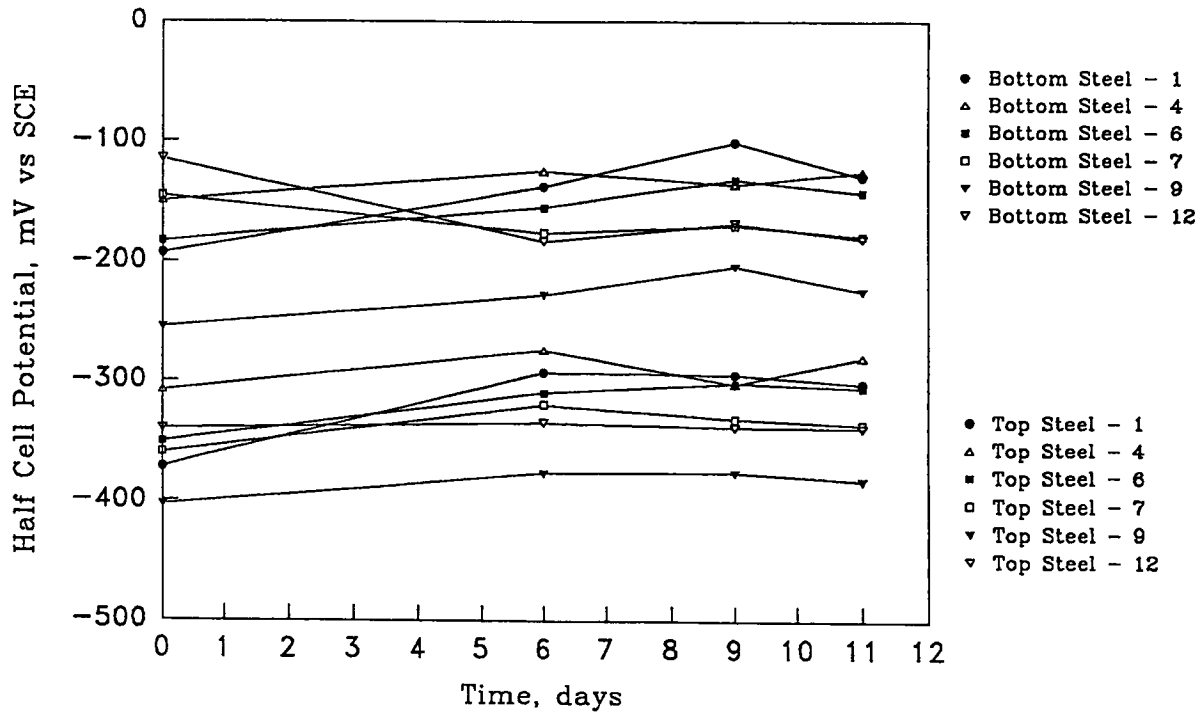

Figure 5-33. Corrosion Potential versus Time for Slab 5 Prior to Energizing

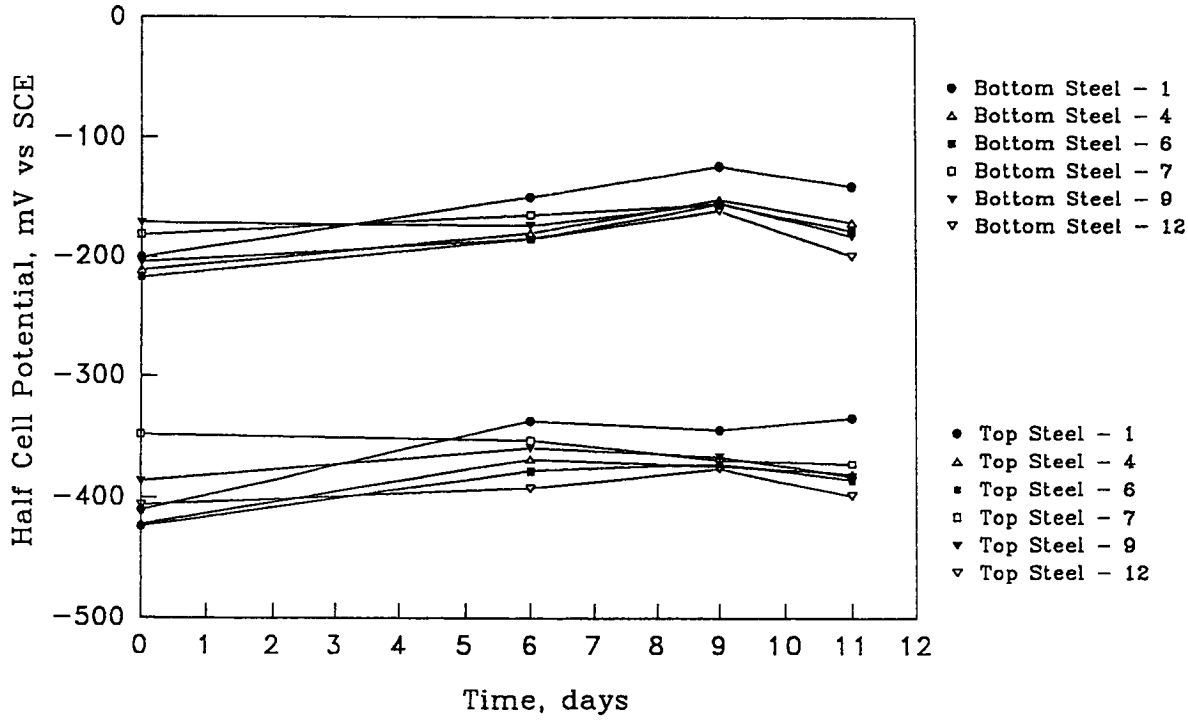

Figure 5-34. Corrosion Potential versus Time for Slab 6 Prior to Energizing

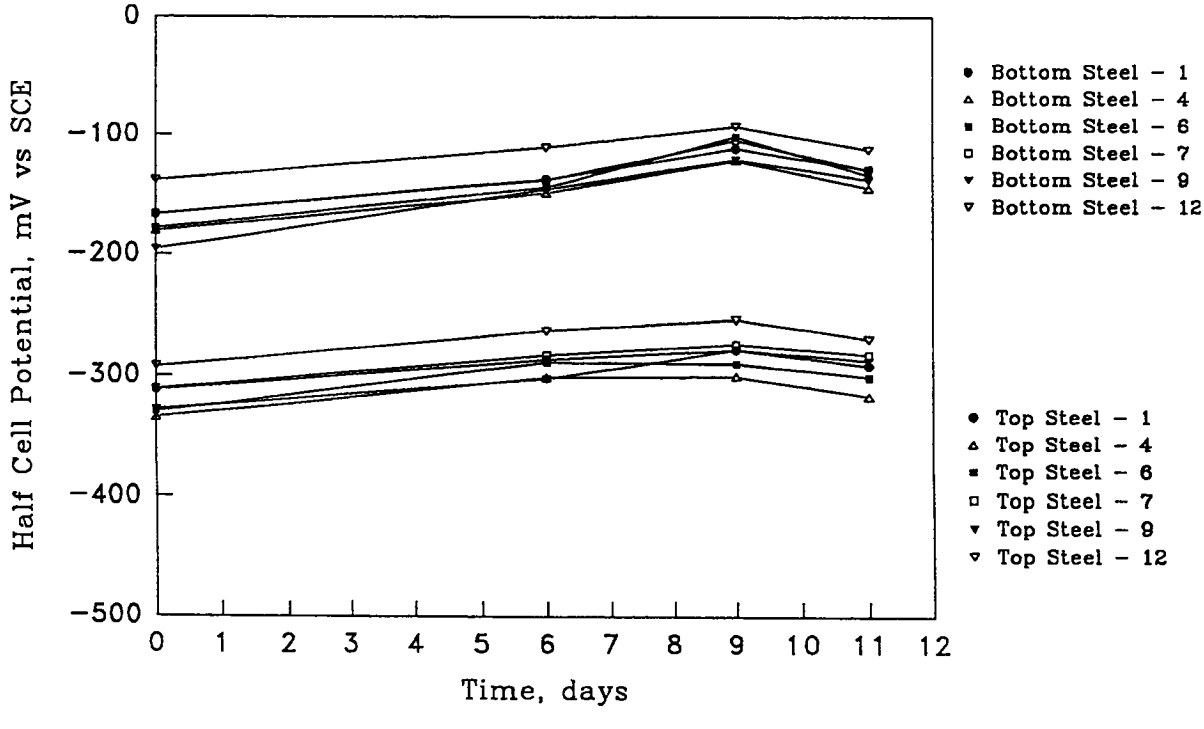

Figure 5-35. Instant-Off Potential versus Exposure Time for Slab 1

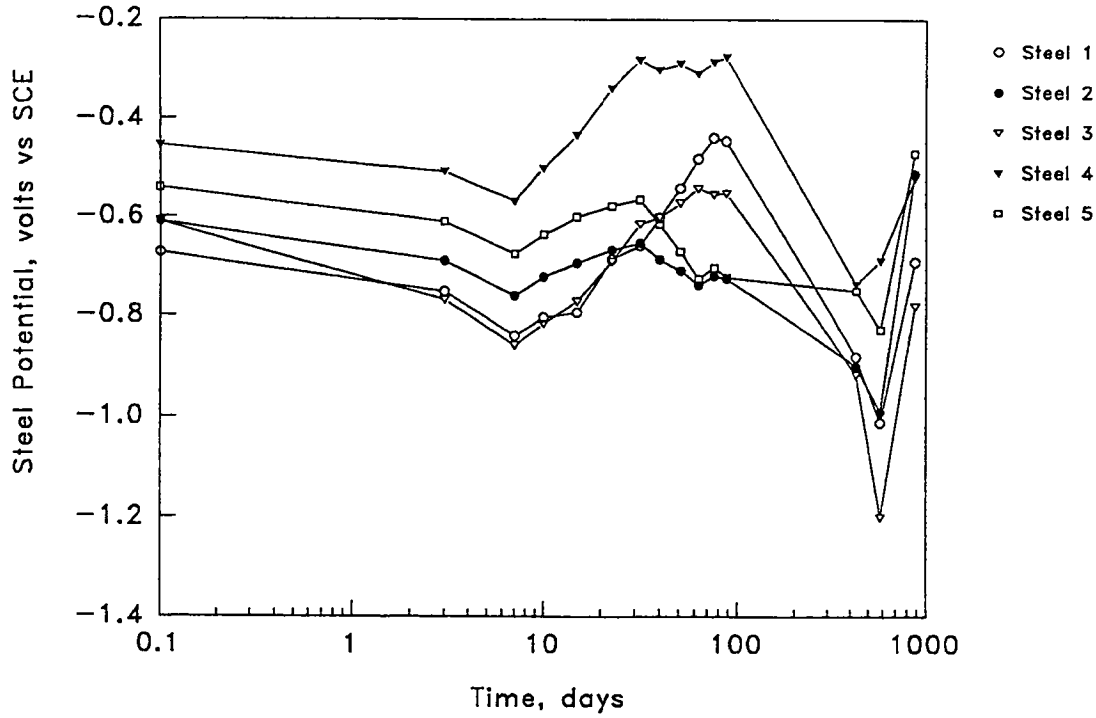

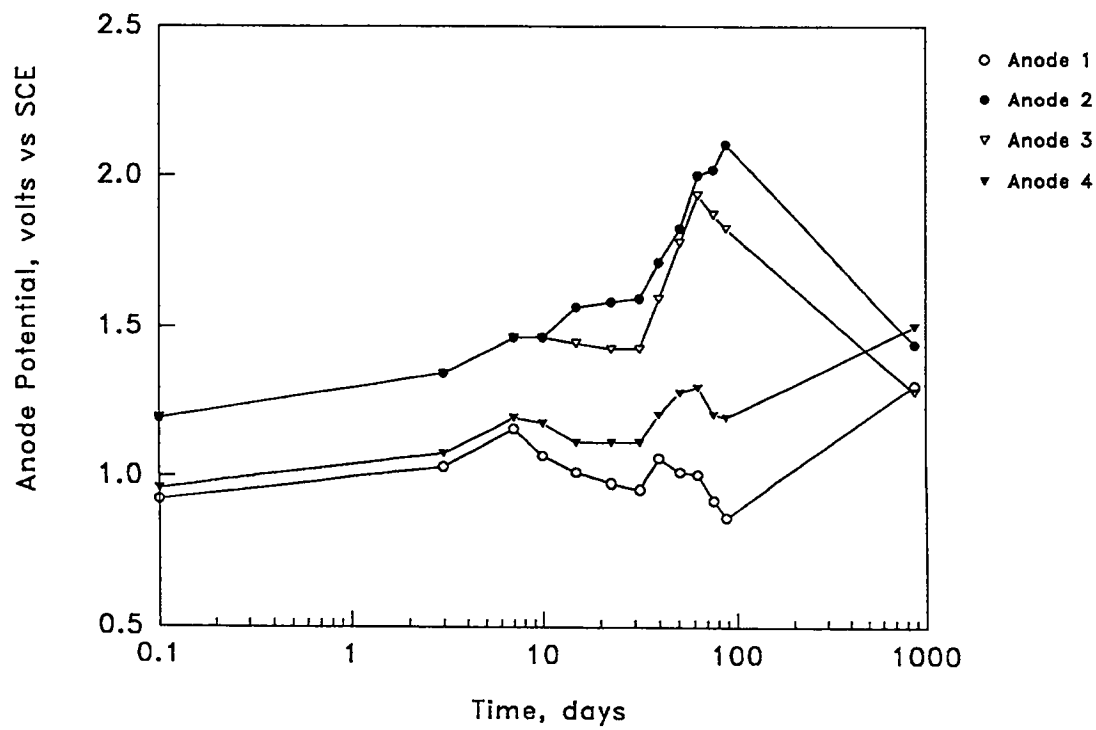

Figure 5-36. Instant-Off Potential versus Exposure Time for Slab 2

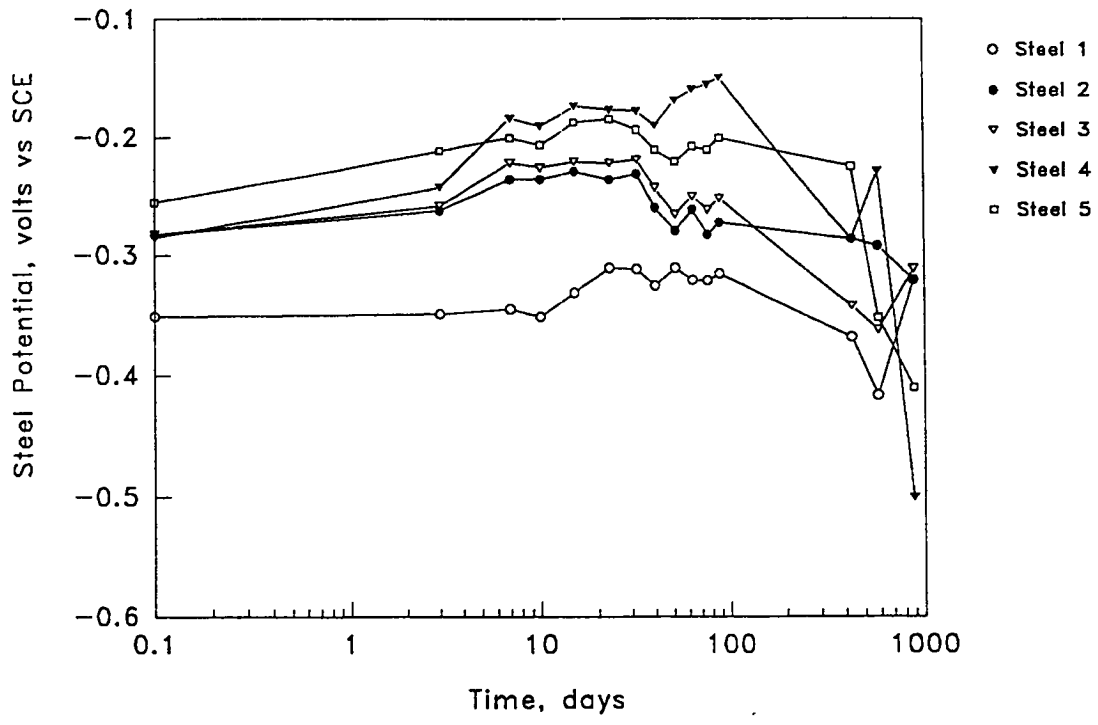

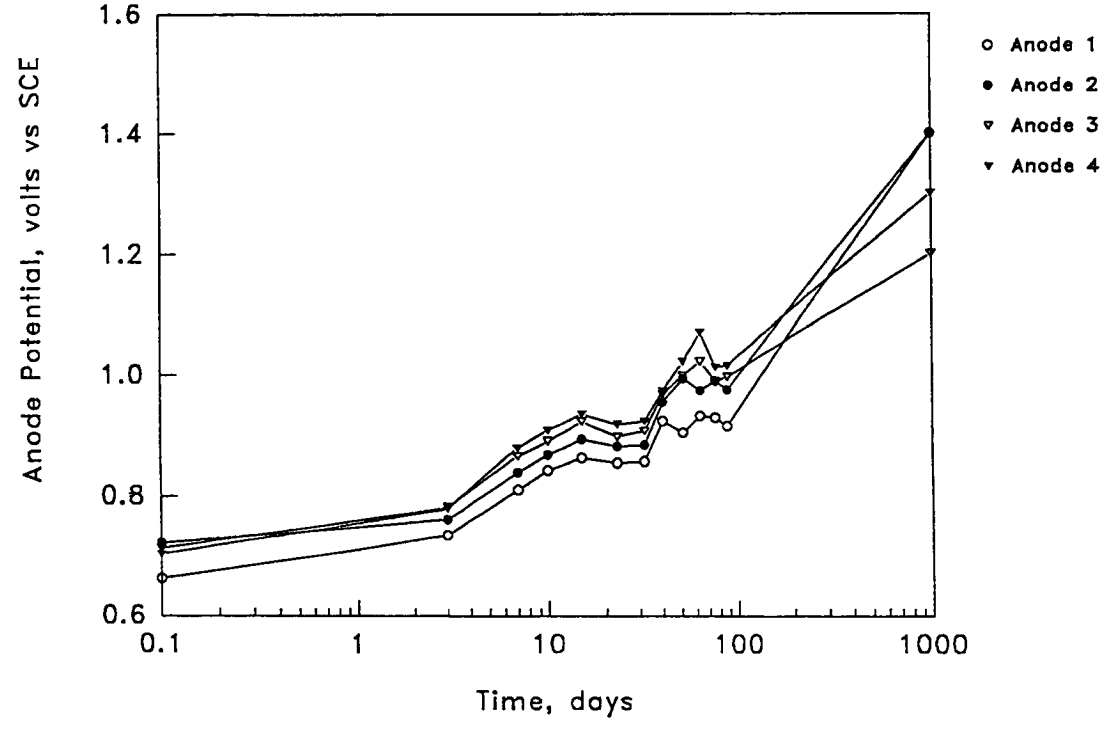

Figure 5-37. Instant-Off Potential versus Exposure Time for Slab 3

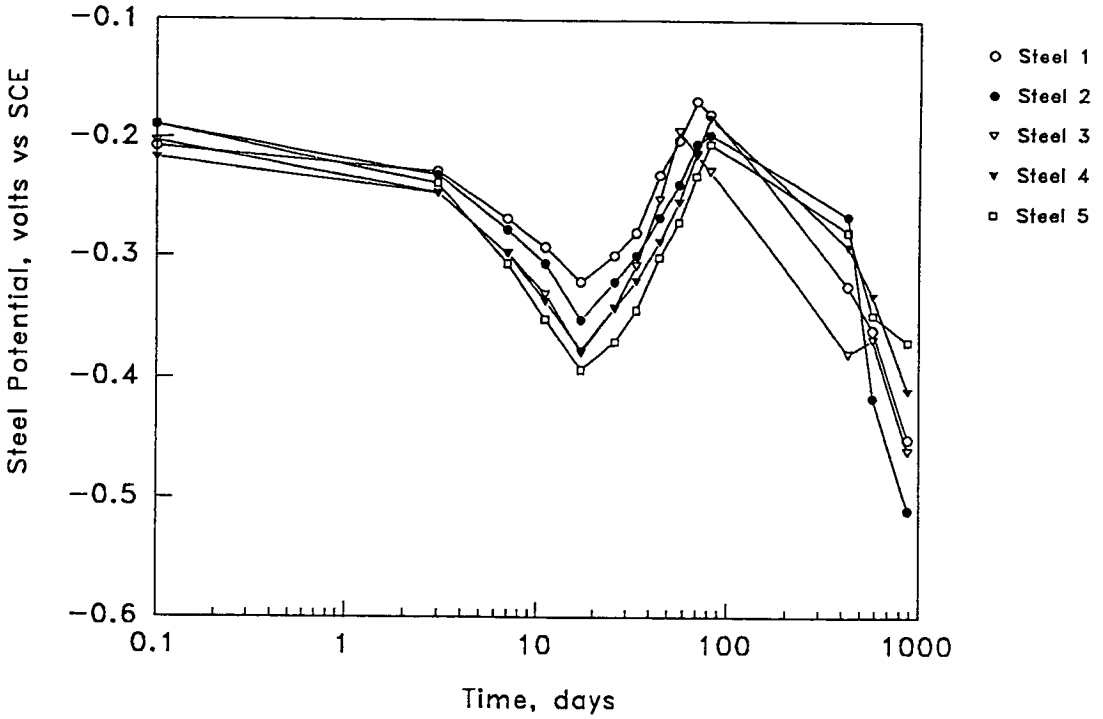

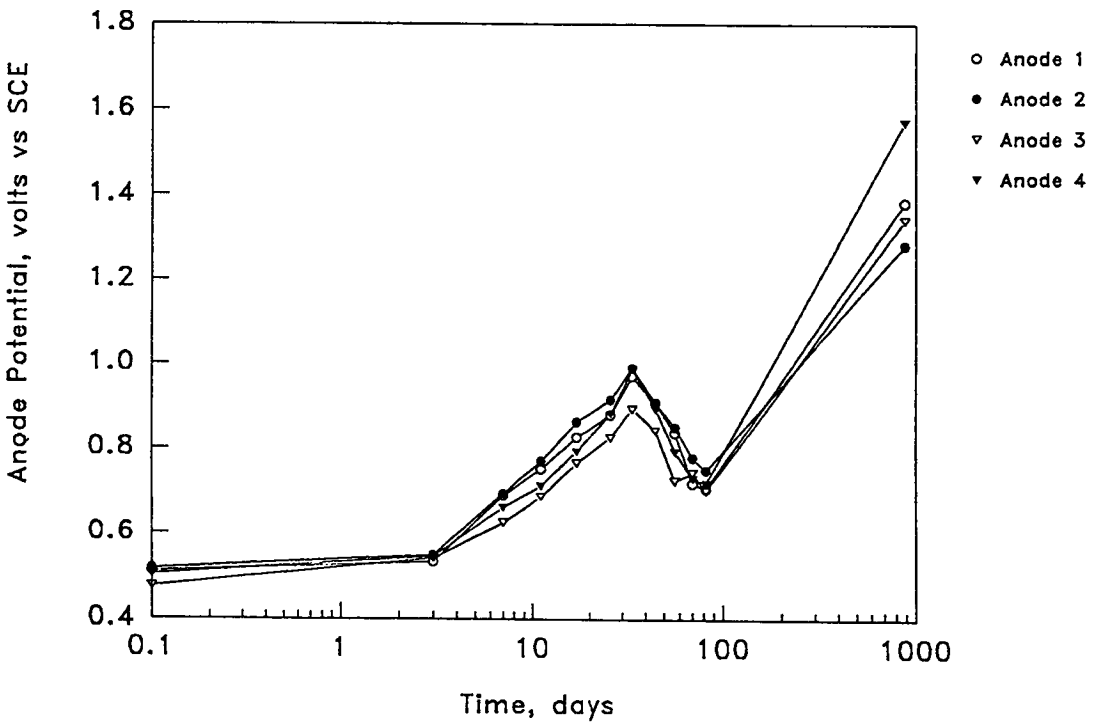

Figure 5-38. Instant-Off Potential versus Exposure Time for Slab 4

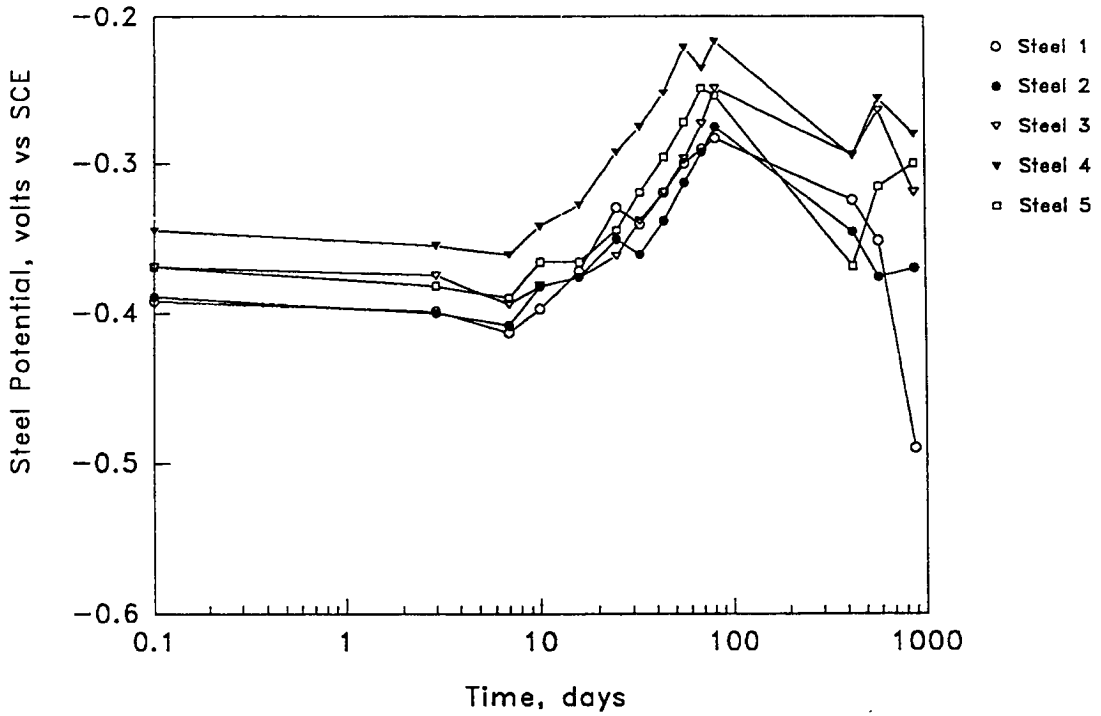

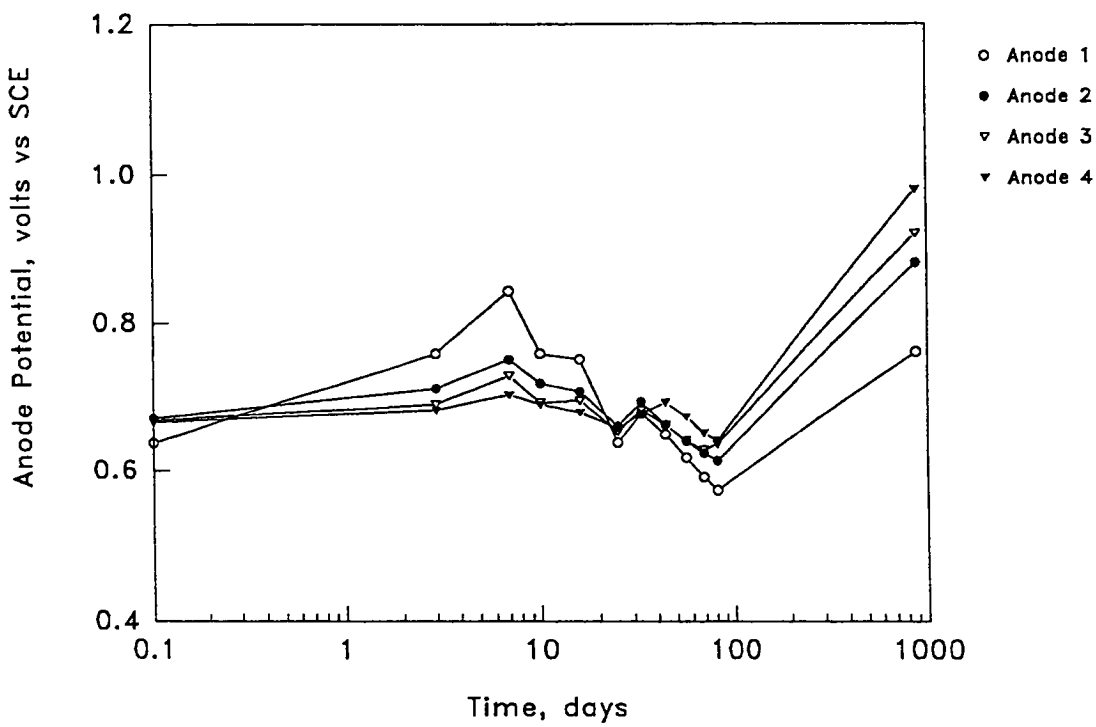

Figure 5-39. Instant-Off Potential versus Exposure Time for Slab 5

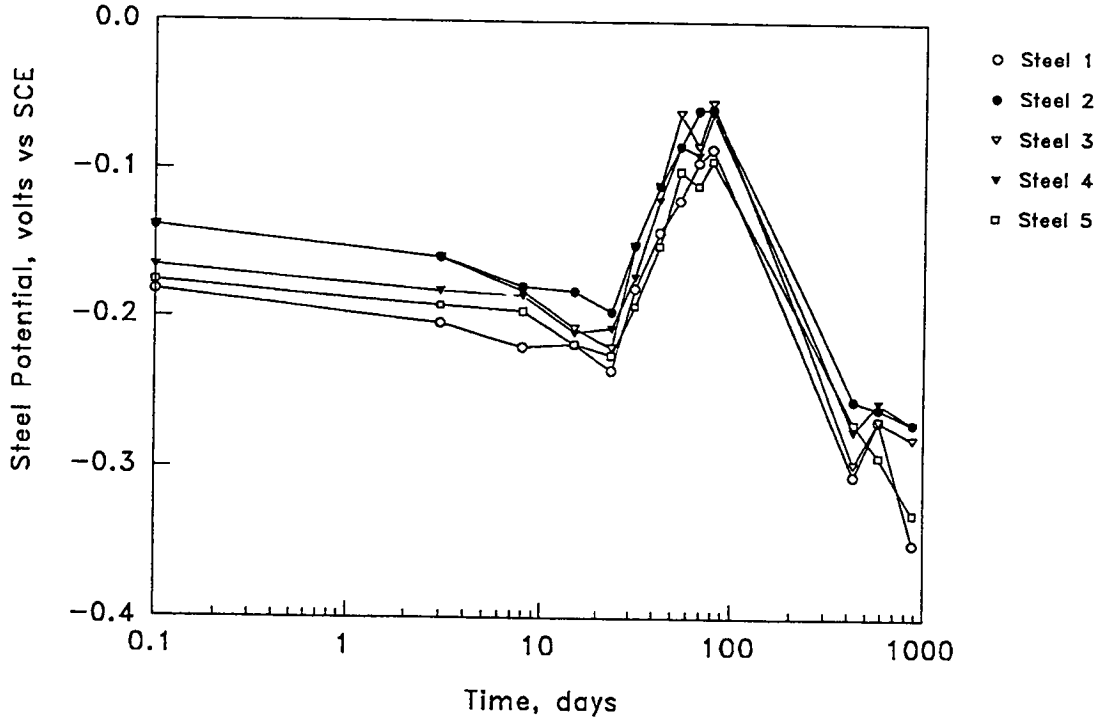

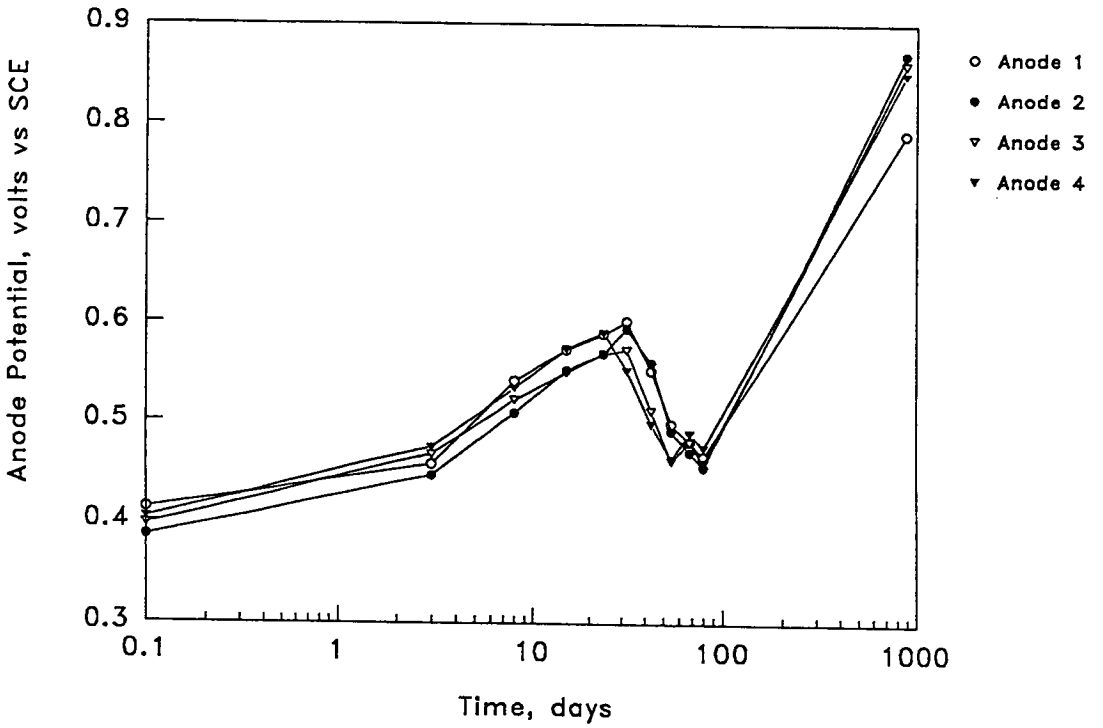

Figure 5-40. Instant-Off Potential versus Exposure Time for Slab 6

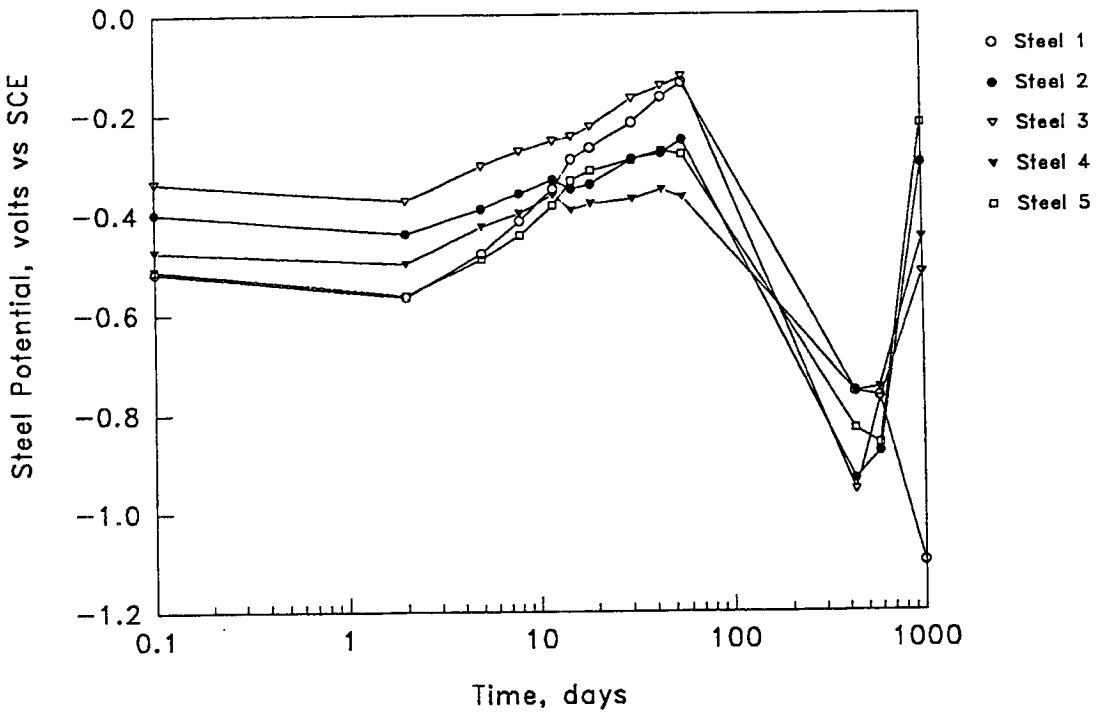

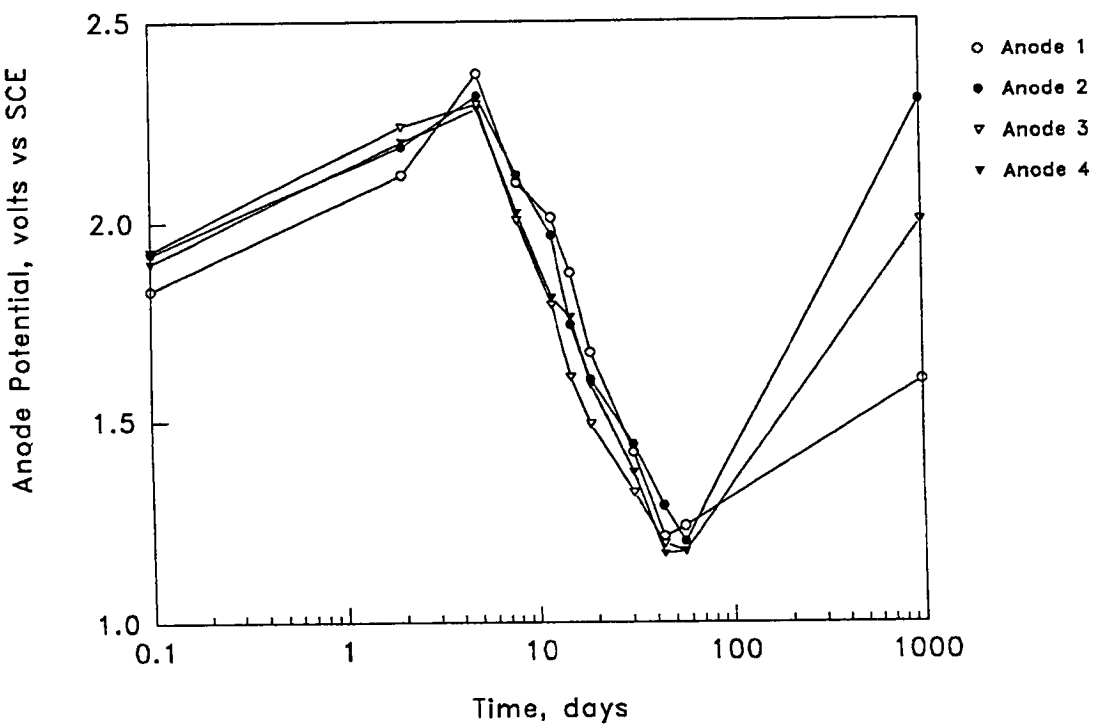

Anodic and Cathodic Polarization

The results of anodic polarization scans performed upon the different anodes prior to initial energizing and again at the termination of the experiments are presented in figures 5-41 to 5-46. The scans were performed to identify any anode deterioration or change in the electrochemical activity of the anode during operation. They were conducted by progressively increasing the current to the slab from the power supply and incrementally measuring the instant-off potential at the different measurement locations. The initial data were acquired as part of the energizing process, while the latter scans were performed subsequent to a polarization decay experiment during which current remained off for several days.

In some cases the variation in potential at the different electrode positions on the slabs was relatively modest, as shown in Figure 5-48, while on others the data were more spread as shown in Figure 5-47. The extent of these variations could not be correlated with the dimensions or size scale (mesh versus ribbon, for example) of the anode material. However, in all cases the scan for the ELGARD™ Ribbon anode material was displaced toward a more positive potential at the experiment conclusion compared to the beginning. The opposite was true for the carbon conductive polymer and Ferex™ Wire. Based on the scan data the operating potential at the end of the experiments was approximately the same for the carbon conductive polymer and ELGARD™ Mesh, which were energized at the same current density on Slabs 1 and 4 (215 mA/m^2 or 20 mA/ft^2). The potential was higher for the Ferex™ Wire (1.65 volts versus SCE) and the ELGARD™ Ribbon (1.4 volts versus SCE).

An apparent discrepancy exists, however, in that the potential of the ELGARD™ Mesh for Slab 3, which was energized at 430 mA/m^2 (40 mA/ft^2), was 1.23 V. The reason for this lower value compared to Slab 2 is unclear. Interestingly, the operating potential was only 0.66 V, and the slope of the anodic polarization curve was relatively shallow for the ELGARD™ Mesh in Slab 5 (current density 107 mA/m^2 or 10 mA/ft^2). Comparison of this with data for the same anode material operated at a higher current density (Slabs 2-4) suggests that the higher current densities altered the polarization character of this anode material in an unfavorable manner, although performance remained satisfactory for each. A factor that could have influenced the polarization scans at the conclusion of the experiments was that cores were taken during the exposure period, and this possibly affected current distribution in the slabs. No consideration was given to the core hole locations relative to the potential measurement sites or to the increase in actual anode current density that resulted.

Figure 5-41. Anodic Polarization Scan Data for the Anode in Slab 1 Prior and Subsequent to Energizing: Each Curve Represents the Average of Four Measurement Points

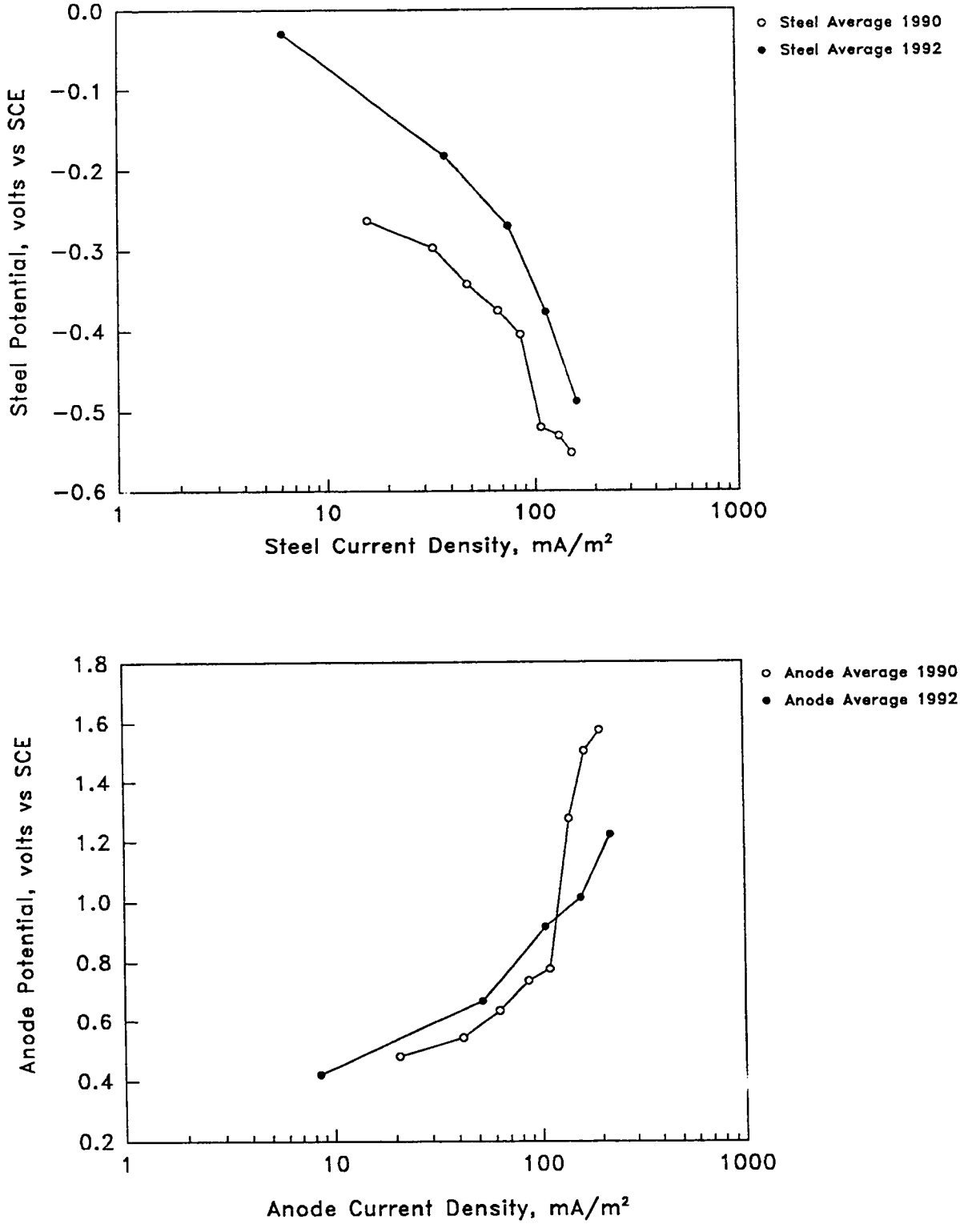

Figure 5-42. Anodic Polarization Scan Data for the Anode in Slab 2 Prior and Subsequent to Energizing: Each Curve Represents the Average of Four Measurement Points

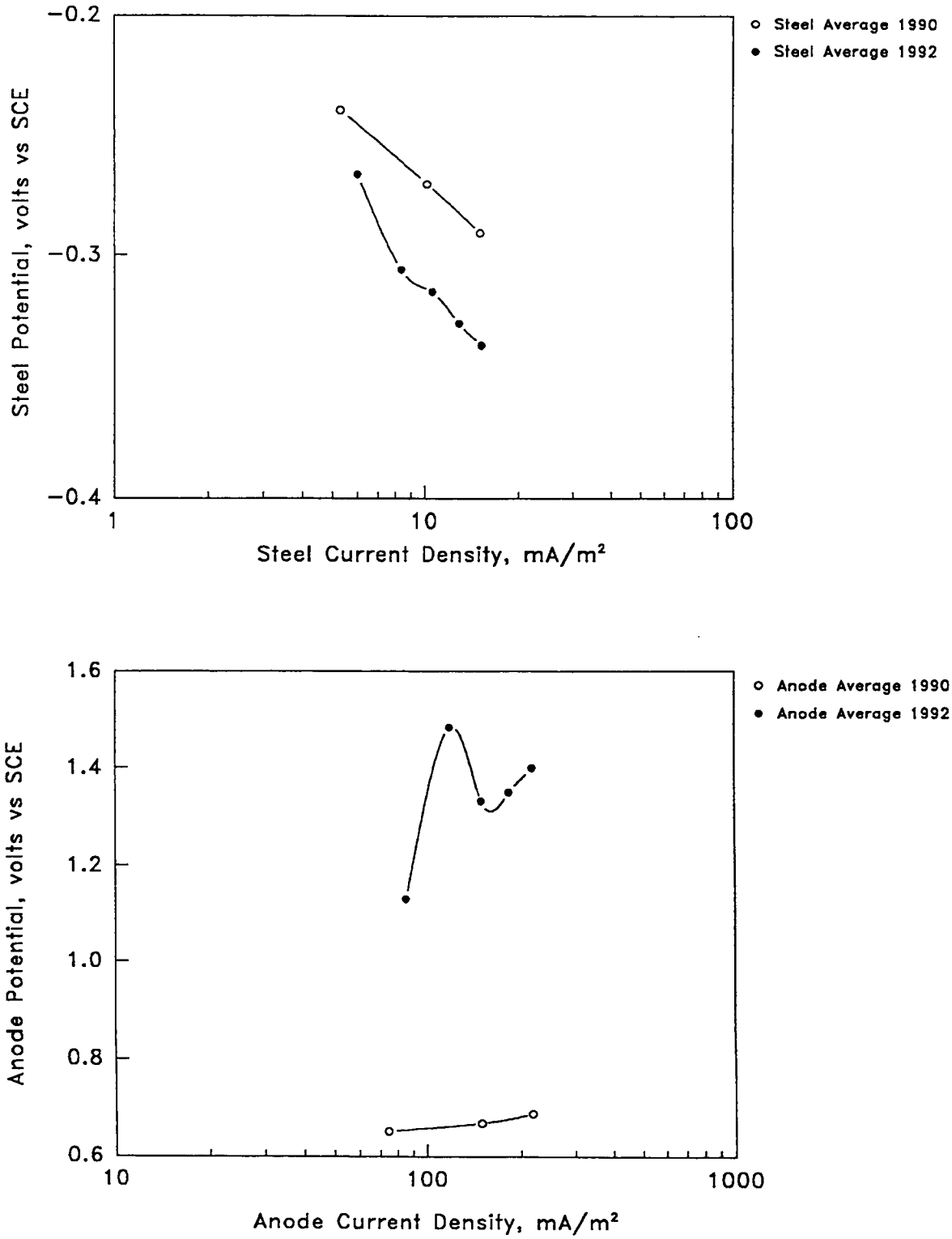

Figure 5-43. Anodic Polarization Scan Data for the Anode in Slab 3 Prior and Subsequent to Energizing: Each Curve Represents the Average of Four Measurement Points

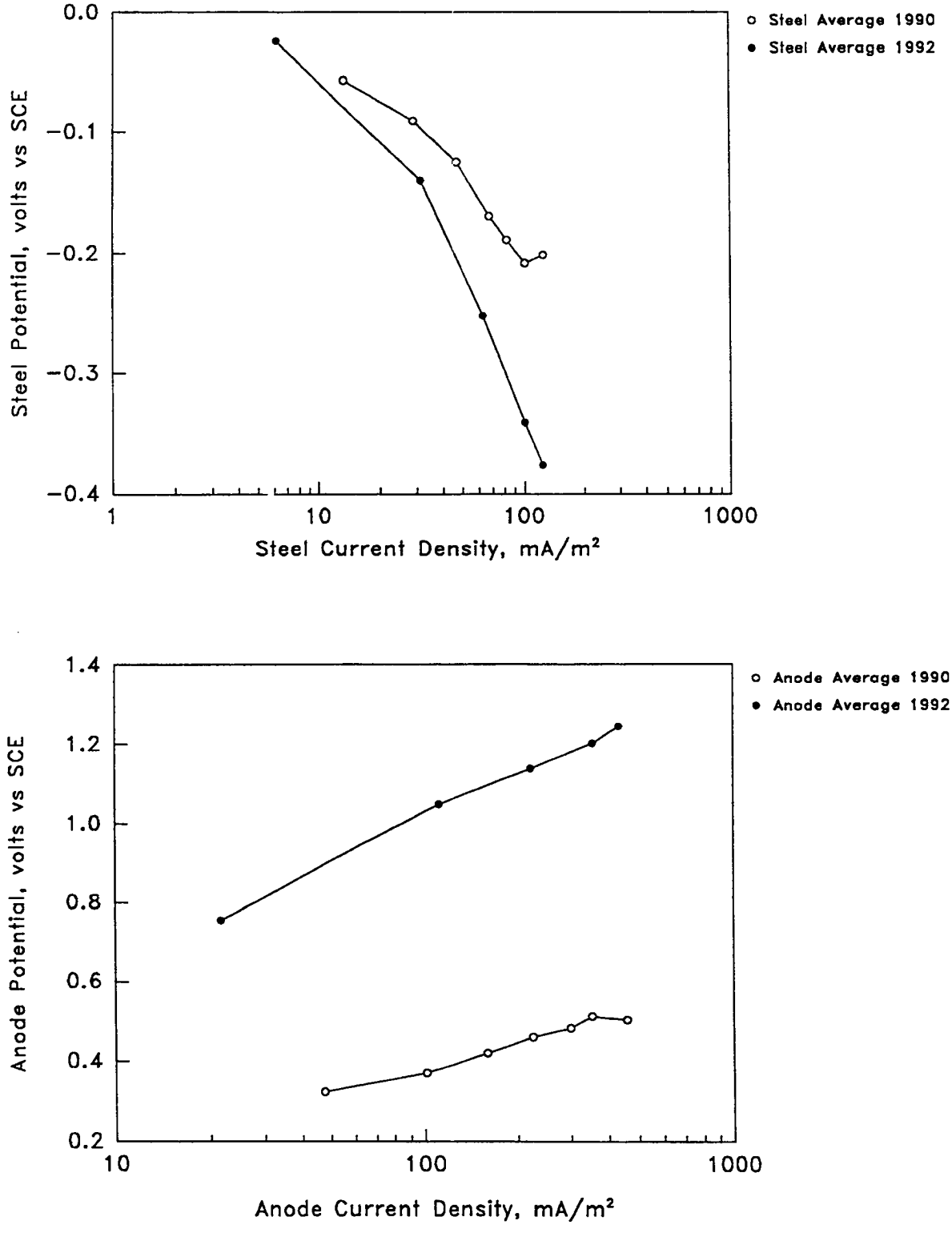

Figure 5-44. Anodic Polarization Scan Data for the Anode in Slab 4 Prior and Subsequent to Energizing: Each Curve Represents the Average of Four Measurement Points

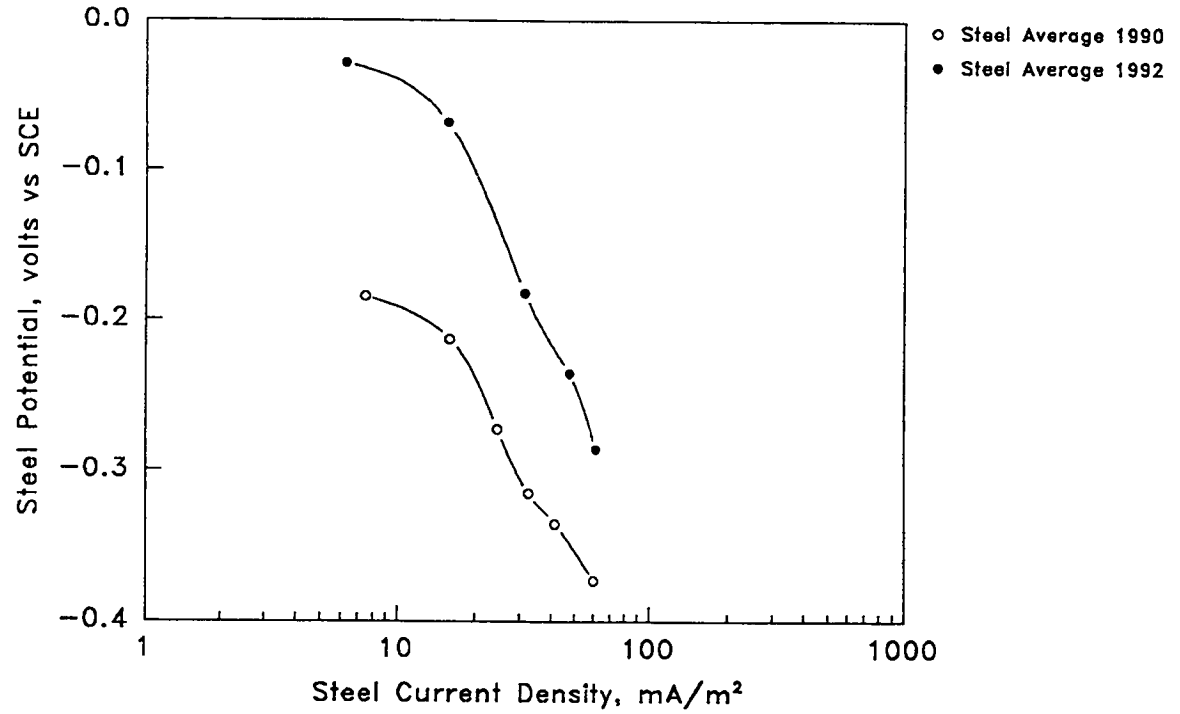

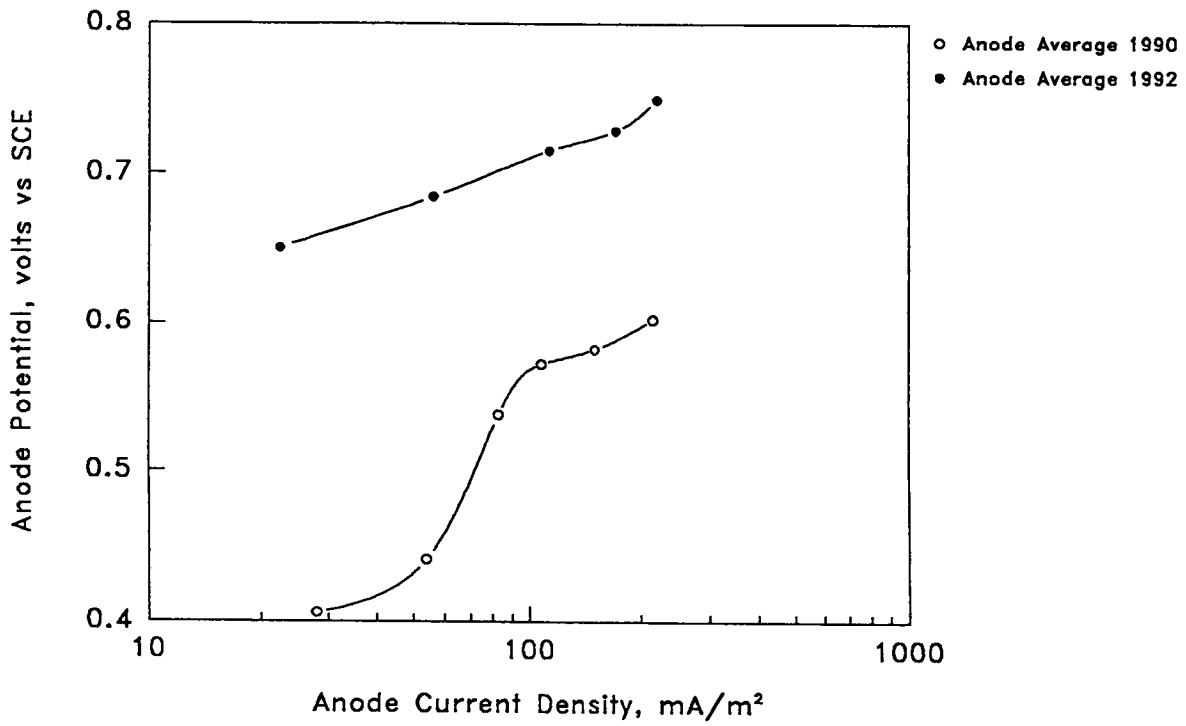

Figure 5-45. Anodic Polarization Scan Data for the Anode in Slab 5 Prior and Subsequent to Energizing: Each Curve Represents the Average of Four Measurement Points

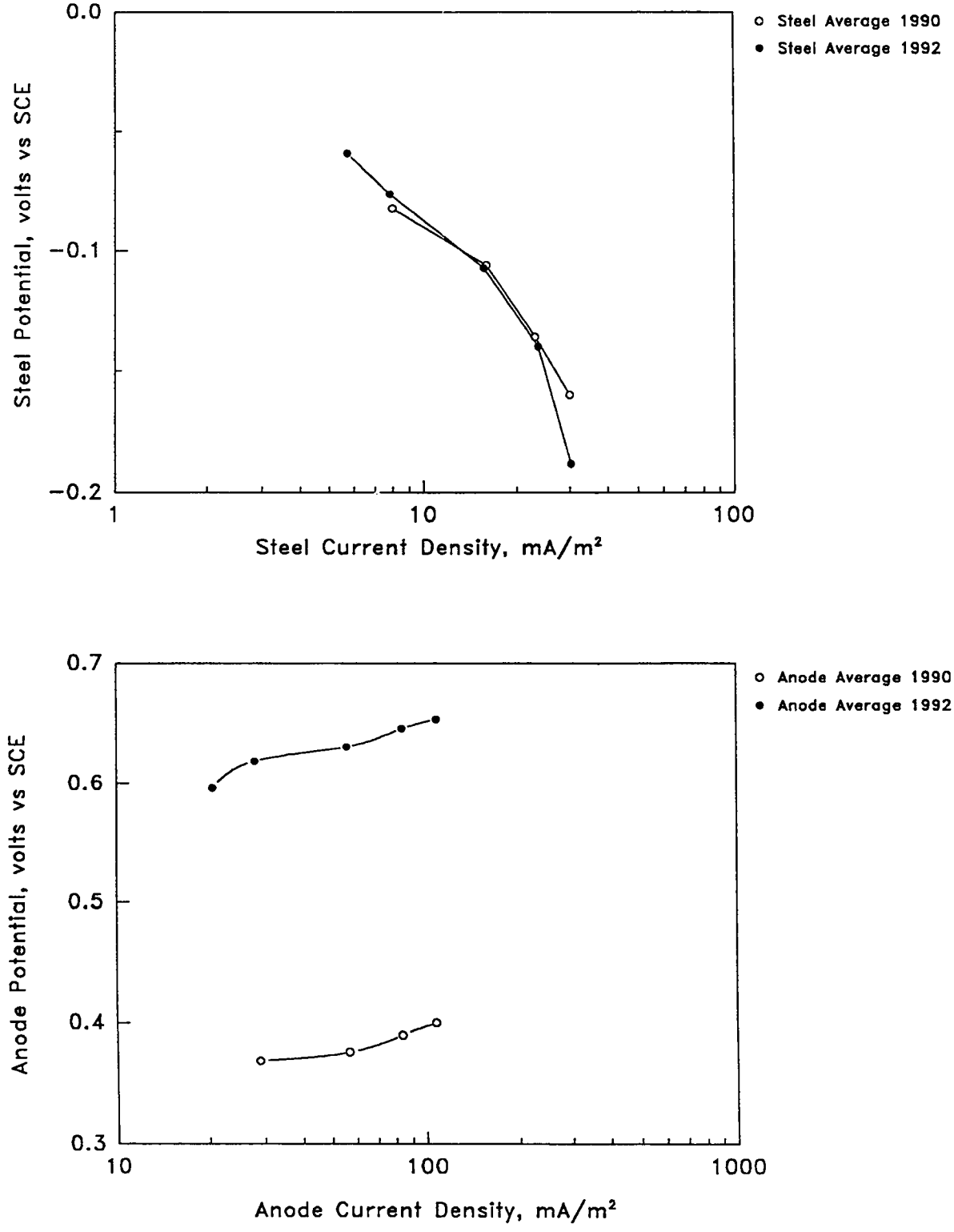

Figure 5-46. Anodic Polarization Scan Data for the Anode in Slab 6 Prior and Subsequent to Energizing: Each Curve Represents the Average of Four Measurement Points

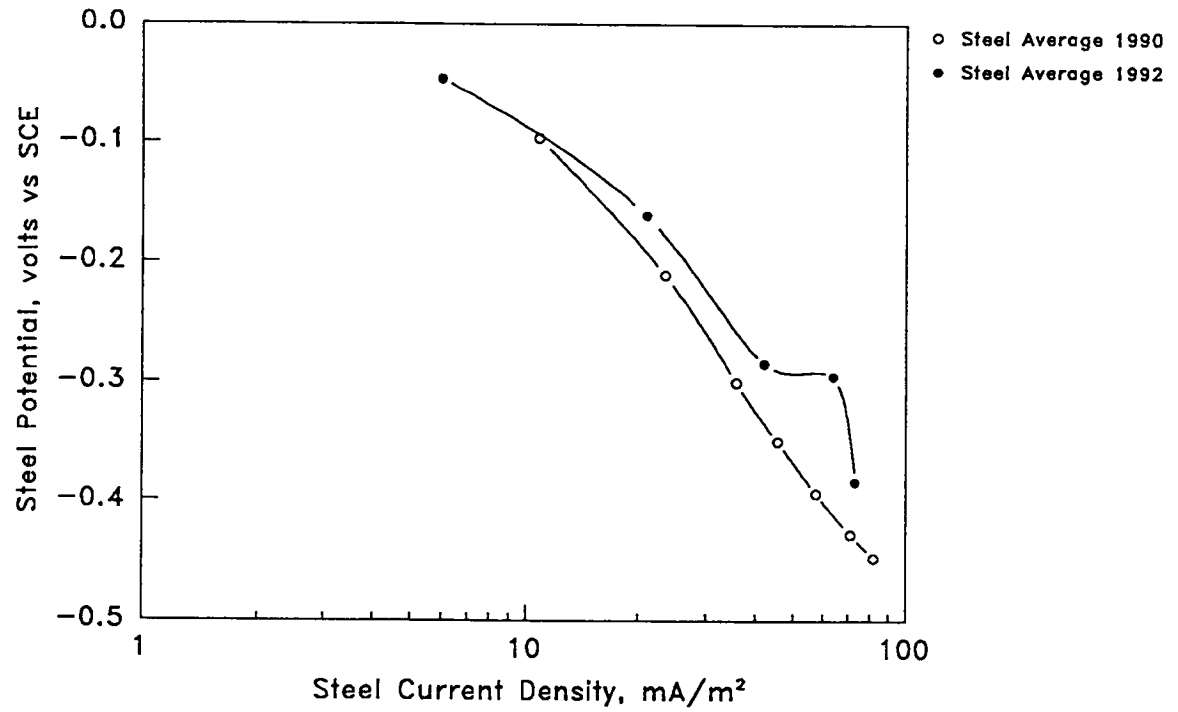

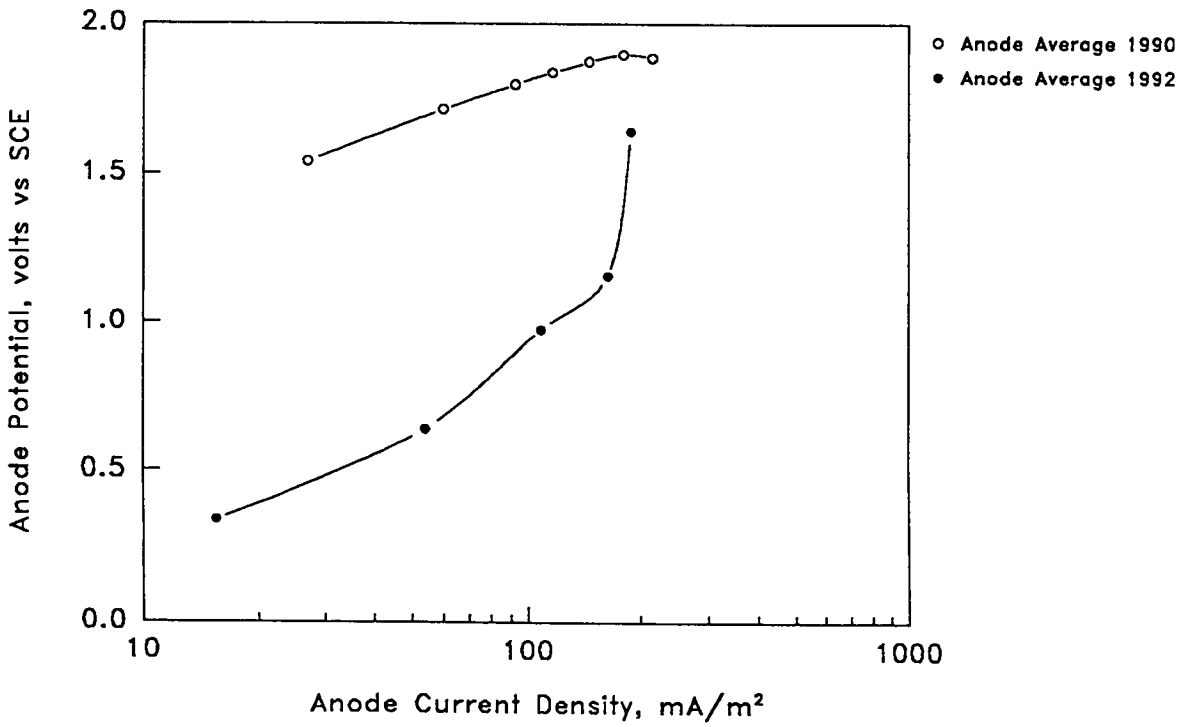

Figure 5-47. Example from Slab 2 of Anodic Polarization Scan Data from the Different Measurement Points Showing Relatively Large Variations

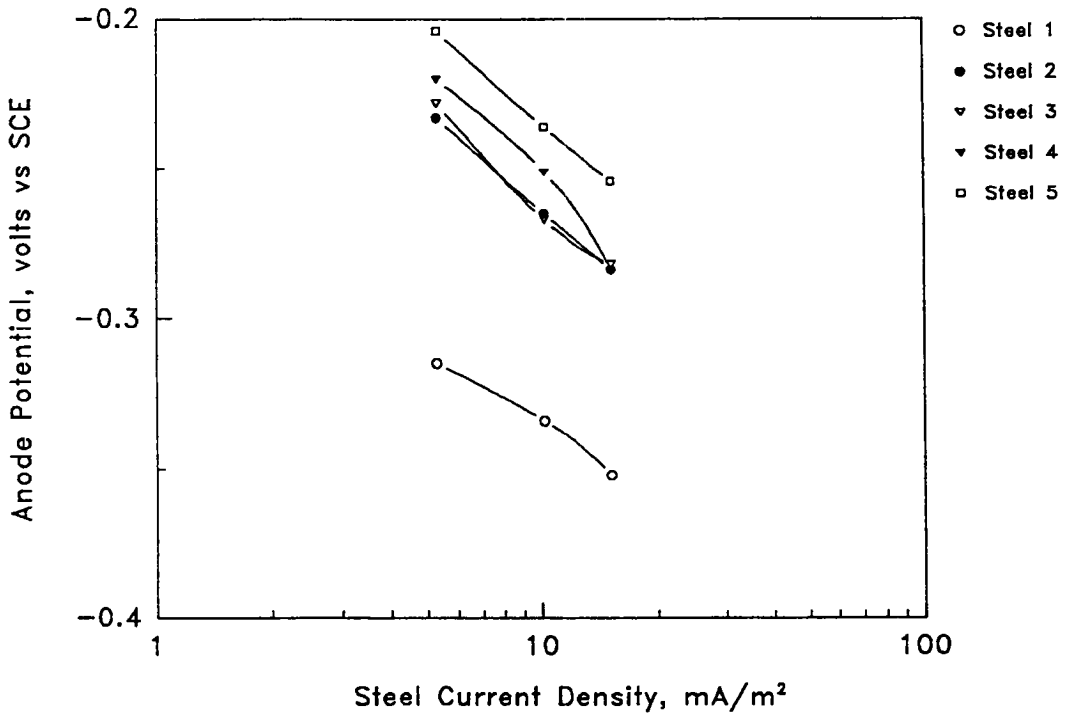

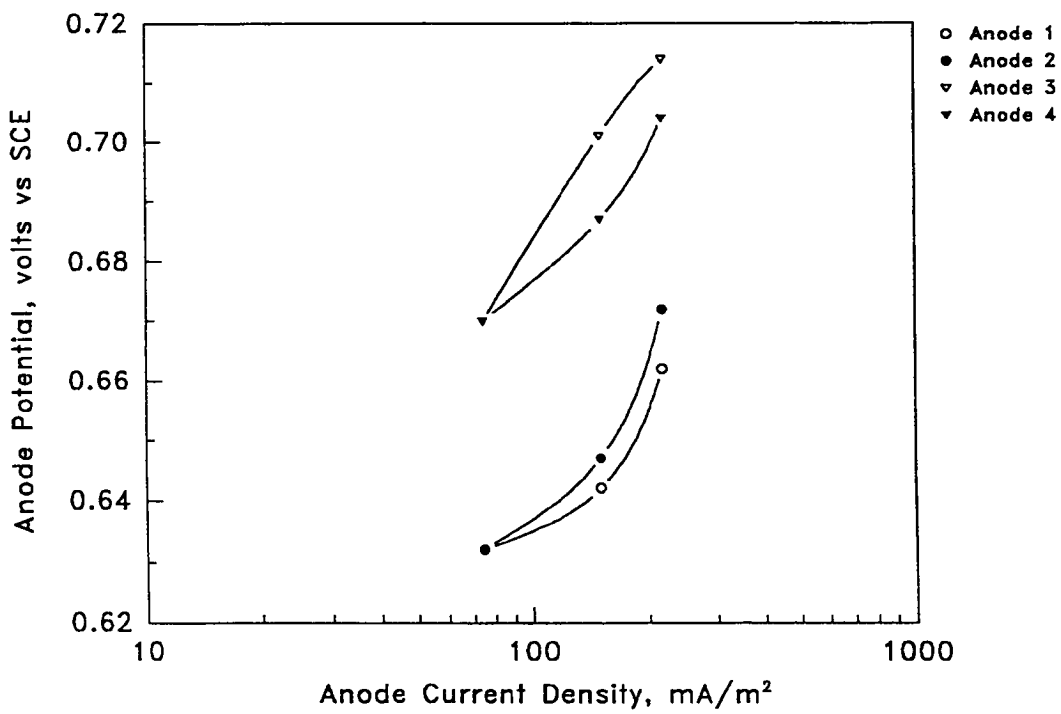

Figure 5-48. Example from Slab 3 of Anodic Polarization Scan Data from Different Measurement Points Showing Relatively Modest Variations.

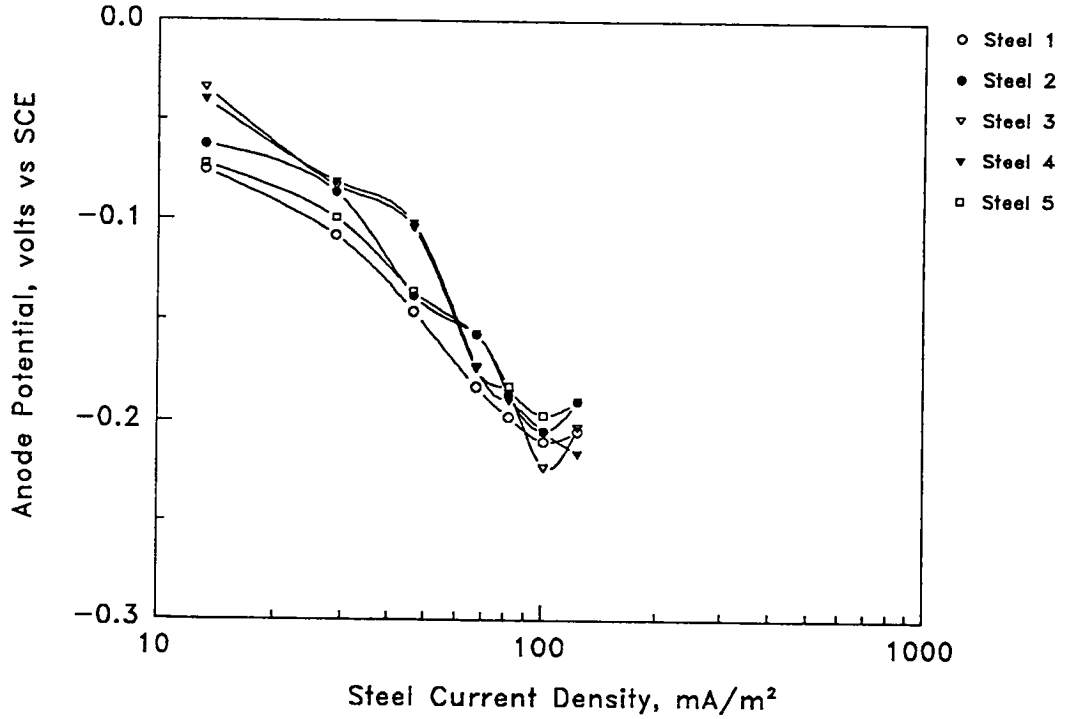

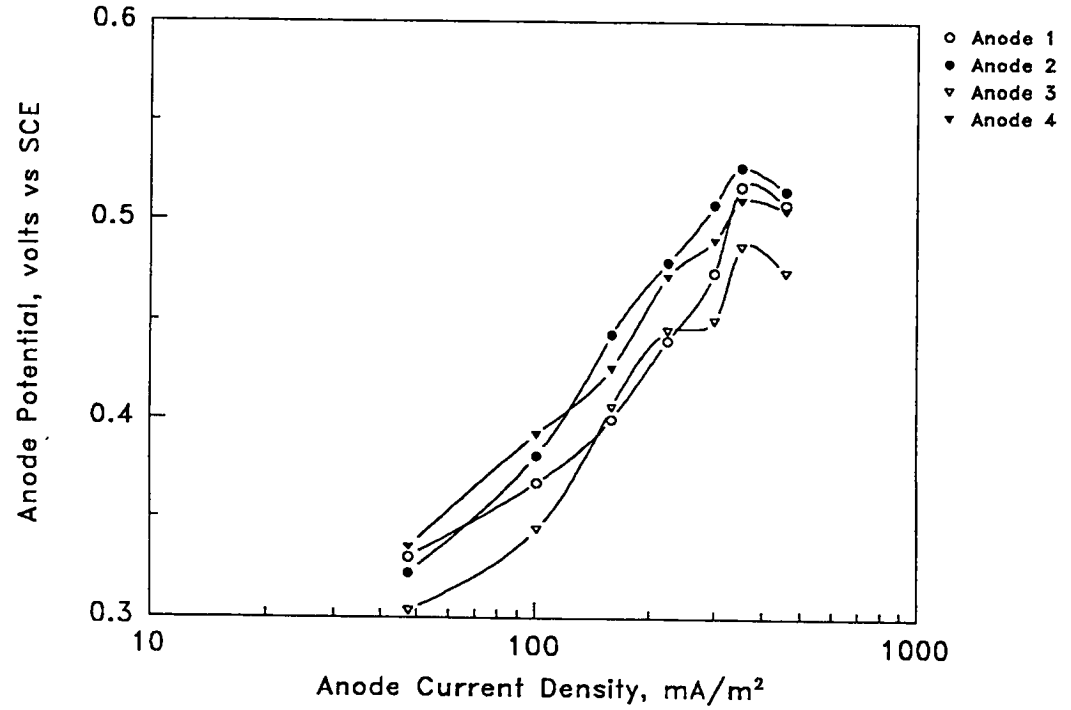

pH Measurements

Tables 5-11 to 5-16 present the pH measurements on cores that were obtained at the anode-concrete and steel-concrete interfaces at prescribed distances from these interfaces utilizing the cores acquired at six-month intervals during the test period.

Measured pH values at the anode-concrete interface of the ELGARD™ Anode Mesh (Slabs 3 through 5) were in the range of 10.5 to 12.4 with no indication of any variation with time or current density in the range investigated. Values for the ELGARD™ Ribbon (Slab 2) were lower than the mesh (pH = 9.0-12.4), but were still in the basic range. In contrast, most pH measurements for the carbon conductive polymer (Slab 1) and Ferex™ Wire (Slab 6) anodes were acidic and were in the range of 1-5.8 and 4.5-12 respectively. Probably the variation in the measured values was a consequence of the small sampling area.

Table 5-11. Slab 1 pH Measurement Results (Conductive Polymer Anode @ 215 mA/m²)

	Months on Line				
Location	6	12	18	24	30
Anode/Concrete interface	1-2	5.7	5.2	5.0	5.8
1 in. (2.5cm) away from anode			5.2	5.0	6.8
0.4 in. (1cm) away from anode					
Top Steel/Concrete interface	11.9	12.2	11.9	11.8	11.0
1 in. (2.5cm) away from top Steel	11.9		11.7	11.8	12.0
0.4 in. (1cm) away from top Steel		12.6			
Bottom Steel/Concrete interface			12.3	11.8	11.8
1 in. (2.5cm) away from bottom Steel			11.8	12.1	12.0
0.4 in. (1cm) away from bottom Steel					

Table 5-12. Slab 2 pH Measurement Results (ELGARD™ Ribbon Anode @ 215 mA/m²)

	Months on Line				
Location	6	12	18	24	30
Anode/Concrete interface	10.0	12.4	9.5	9.0	9.5
1 in. (2.5cm) away from anode	11.9		11.5	11.0	11.8
0.4 in. (1cm) away from anode		12.6			
Top Steel/Concrete interface	11.6	12.6	11.7	11.8	11.5
1 in. (2.5cm) away from top Steel	11.9		11.8	12.1	11.7
0.4 in. (1cm) away from top Steel		12.6			
Bottom Steel/Concrete interface			11.2	11.8	11.5
1 in. (2.5cm) away from bottom Steel			11.8	11.8	11.9
0.4 in. (1cm) away from bottom Steel					

Table 5-13. Slab 3 pH Measurement Results (ELGARD™ Anode Mesh @ 430 mA/m²)

Location	Months on Line 6	12	18	24	30
Anode/Concrete interface	11.9	12.2	11.8	11.5	11.2
1 in. (2.5cm) away from anode	11.9		10.5	10.0	11.6
0.4 in. (1cm) away from anode		12.4			
Top Steel/Concrete interface	11.9	11.9	11.0	11.8	11.5
1 in. (2.5cm) away from top Steel	12.2		11.9	12.1	11.8
0.4 in. (1cm) away from top Steel		12.4			
Bottom Steel/Concrete interface	12.4	12.4	11.5	11.5	11.5
1 in. (2.5cm) away from bottom Steel	12.4		11.8	11.5	11.8
1 in. (1cm) away from bottom Steel		12.4			

Table 5-14. Slab 4 pH Measurement Results (ELGARD™ Anode Mesh @ 215 mA/m²)

Location	Months on Line 6	12	18	24	30
Anode/Concrete interface	11.9	12.4	11.8	10.5	11.5
1 in. (2.5cm) away from anode	12.4		11.0	11.5	11.7
0.4 in. (1cm) away from anode		12.7			
Top Steel/Concrete interface	12.4	12.7	11.7	11.8	12.3
1 in. (2.5cm) away from top Steel	12.4		11.8	11.8	11.8
0.4 in. (1cm) away from top Steel		12.7			
Bottom Steel/Concrete interface		12.7	11.0	12.1	12.3
1 in. (2.5cm) away from bottom Steel			11.5	12.1	11.9
0.4 in. (1cm) away from bottom Steel		12.7			

Table 5-15. Slab 5 pH Measurement Results (ELGARD™ Anode Mesh @ 108 mA/m²)

Location	Months on Line 6	12	18	24	30
Anode/Concrete interface	12.0	12.4	11.8	11.5	10.7
1 in. (2.5cm) away from anode			10.5	11.5	11.9
0.4 in. (1cm) away from anode		12.7			
Top Steel/Concrete interface	12.0	12.7	11.5	11.0	11.9
1 in. (2.5cm) away from top Steel	12.0		11.8	12.1	11.5
0.4 in. (1cm) away from top Steel		12.7			
Bottom Steel/Concrete interface	12.2	12.7	11.5	11.5	11.8
1 in. (2.5cm) away from bottom Steel	12.2		11.8	12.1	12.8
0.4 in. (1cm) away from bottom Steel		12.7			

Table 5-16. Slab 6 pH Measurement Results (Ferex™ Wire Anode @ 215 mA/m²)

Location	Months on Line 6	12	18	24	30
Anode/Concrete interface	9.5	12.0	4.5	5.0	6.0
1 in. (2.5cm) away from anode			5.2	5.5	6.0
0.4 in. (1cm) away from anode		12.2			
Top Steel/Concrete interface	12.2	12.4	11.5	11.8	12.0
1 in. (2.5cm) away from top Steel	12.2		12.0	12.1	12.0
0.4 in. (1cm) away from top Steel		12.4			
Bottom Steel/Concrete interface	12.2	12.4	12.1		11.8
1 in. (2.5cm) away from bottom Steel	12.2		11.5		12.5
0.4 in. (1cm) away from bottom Steel		12.4			

Anode/Overlay Bond

The strength of the anode/overlay bond was qualitatively assessed from cores taken at six-month intervals. Because this determination involved a relatively small sample size, the slabs were mechanically broken apart upon termination of the test program, and bond strength characterized according to the ease with which the overlay was removed. The first technique using cores showed that the bond was essentially nil for the 12-month core from Slab 2 (ELGARD™ Anode Ribbon), while the core broke at the anode-concrete interface during coring for this same slab at 18 months. The cores obtained at 24 and 30 months were sound. This is in contrast to the cores from Slabs 3 to 5 which contained the ELGARD™ Mesh in that the anode-concrete bond for these was sound in each instance. For Slabs 1 and 6, carbon conductive polymer and Ferex™ Wire, respectively, the anode-concrete bond was either nil or the core was broken at this interface during coring in most instances, including the initial coring at six months.

Table 5-17 summarizes the observations made in association with the post-experiment mechanical destruction of the overlays. This indicates that loss of both overlay-concrete and anode-overlay bond occurred generally for Slabs 1 and 6. Also, the concrete-overlay bond was low for Slab 2 (ribbon), although the anode-overlay bond itself was good. On the other hand, both bond types maintained integrity in the case of the mesh slabs. The distinction that was apparent between the ribbon and mesh was probably related to the geometric factor with the mesh providing enhanced interlocking to the overlay compared to the more planar ribbon. It is not clear if this same factor played a role in the pH difference between these two anode materials.

Table 5-17. Condition of Anode and Overlay After 30 Months of Cathodic Protection

Slab No.	Anode Type	Ease of Removal* Overlay	Anode	Anode Condition**
1	Conductive Polymer	1	2	The interface between the concrete and overlay was an orange-brown color
2	ELGARD™ Ribbon	2	4	Yellow-orange powder at some locations of anode-concrete interface
3	ELGARD™ 210 Mesh	5	4	The anode mesh was well impregnated with concrete and was therefore difficult to separate. A yellow-orange powder was present at the anode-overlay interface
4	ELGARD™ 210 Mesh	5	4	The anode mesh was well impregnated with concrete and was therefore difficult to separate. A yellow-orange powder was present at the anode-overlay interface
5	ELGARD™ 210 Mesh	4	4	The anode mesh was well impregnated with concrete and was therefore difficult to separate. A yellow-orange powder was present at the anode-overlay interface
6	Ferex™ Wire	2	2	The anode surface detached in thin black pieces as large as 1 cm^2

* Rated from 1-5, where 5 corresponds to a strong bond between the anode and overlay or overlay and concrete, and 1 to a weak bond

** Anode condition after destruction of the upper concrete layer

An additional observation with regard to the carbon conductive polymer anode slab is that a black material was found to be extruding along a 6-in. (15 cm) length of the overlay-concrete interface after 24 months' exposure. This was probably a consequence of failure of this interface which facilitated migration of anodic reaction products.

Based upon the above observations it is concluded that, of the types of anode materials tested, the mesh was the anode material which performed most satisfactorily. This conclusion is

based primarily upon the relatively alkaline pH that was maintained within the overlay near and at the anode surface and upon the soundness of the anode-overlay and overlay-concrete bond after 30 months' exposure.

The ribbon anode material also performed well with the exception of the overlay-concrete bond, which became relatively weak. The reason for this is not clear, but it could be related to the fact that the ribbon contacted this interface such that ready access was available to anode reaction products.

Based upon these same criteria, the Ferex™ Wire was the next favorable material followed lastly by the carbon conductive polymer.

These conditions are intended to apply only to the conditions of the experiments, which involved relatively high current densities, and do not necessarily mean that satisfactory service performance could not be realized with even the least satisfactory anode material provided that the current density was more moderate.

Core Analysis

Examination Procedure

Six 2-3/4 in. (7 cm) diameter concrete core samples were taken from the reinforced concrete slabs. The slabs had been used in tests on cathodic protection anodes, operating under current for a 30-month period. At this point, the cores were taken from the slabs.

Characterization studies were conducted on the cores to assess the effects of the sustained cathodic protection current on the anode/concrete component and the cathode/concrete component of the cathodic protection system. Techniques used in the characterization studies included:

- Conventional petrographic techniques using reflected light microscopy at low magnification levels (10X-100X).
- Scanning electron microscopy (SEM).
- Energy dispersive x-ray spectroscopy techniques (EDS) in conjunction with SEM techniques.
- Chloride ion content measurements made in accordance with the procedures outlined in AASHTO Designation T260-82, The Standard Method of Test For Sampling and Testing For Total Chloride Ion in Concrete.
- Measurements of pH using color indicating chemicals (phenolphthalein and Rainbow Indicator*).

Description of Cores

One 2-3/4 in. (7 cm) diameter x 8-1/2 in. (21.6 cm) long core was taken from each of the reinforced concrete slabs. Table 5-18 correlates the core number with the type of anode and the anode current density.

Table 5-18. Identification of Six Slab Cores

Core No.	Slab No.	Cp Anode Type	Anode Current Density	
			mA/ft^2	mA/m^2
1	1	Conductive Polymer	20	215
2	2	ELGARD Ribbon	20	215
3	3	ELGARD 210 Mesh	40	429
4	4	ELGARD 210 Mesh	20	215
5	5	ELGARD 210 Mesh	10	107
6	6	Ferex 100 Wire	20	215

The cathodic protection system on Slab 1 was a conductive carbon-containing polymer operating at 20 mA/ft^2 (215 mA/m^2). Slab 2 used an ELGARD™ titanium ribbon anode also operating at 20 mA/ft^2 (215 mA/m^2). Slabs 3, 4, and 5 all used ELGARD™ 210 Anode Mesh operating at current densities of 40 mA/ft^2, 20 mA/ft^2, and 10 mA/ft^2 (430 mA/m^2, 215 mA/m^2, and 107 mA/m^2) respectively. The anode used on Slab 6 was the Ferex™ Wire anode operating at 20 mA/ft^2 (215 mA/m^2).

All six cores represent the entire thickness of the slab (original slab and overlay) at these coring sites. The location of the coring sites on the six slabs is shown in Figure 5-49.

* Germann Instruments, 4658 N. Monticello, Chicago, IL 60625

Figure 5-49. Location of Coring Sites for Cores from FAU Following Cathodic Protection Trials

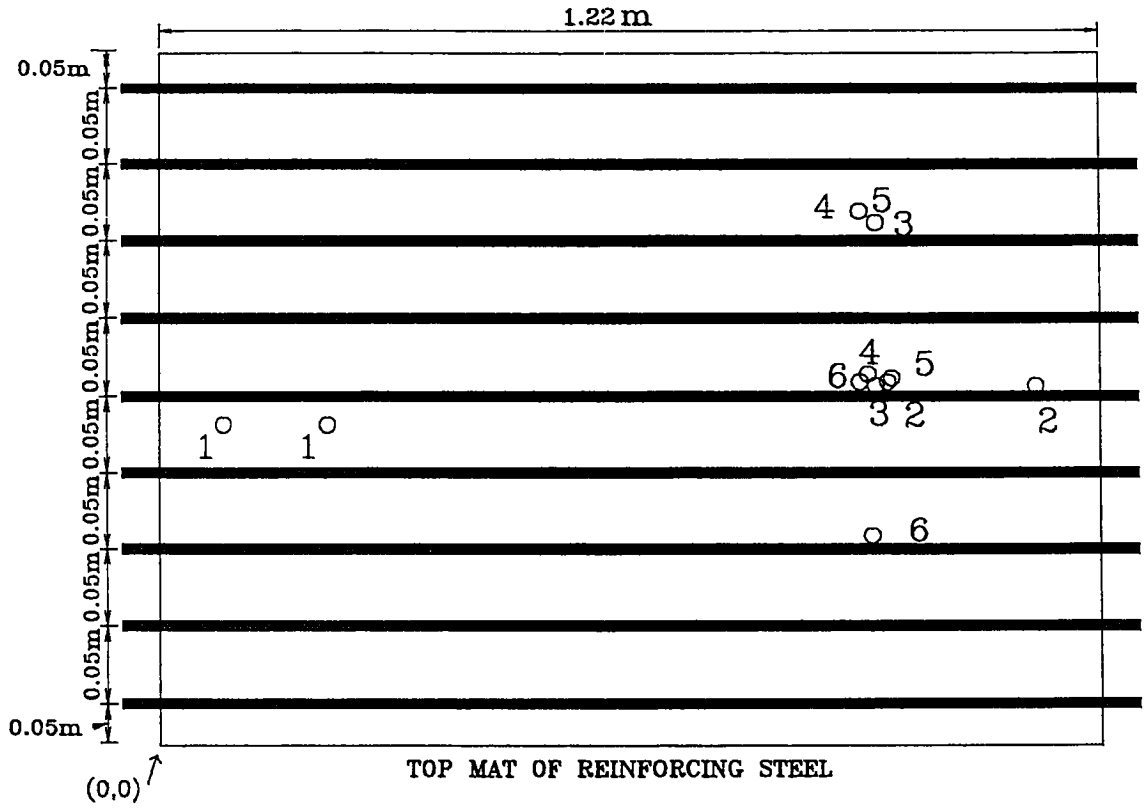

Numbers are Slab Numbers

After outdoor curing (under wet burlap) of the 6 in. (15.25 cm) thick concrete slabs for 28 days, the anodes were installed on the slab wearing surface. The slabs were then overlaid with a 2-1/2 in. (6.35 cm) thickness of superplasticized, dense concrete (see Table 5-9). Just prior to placement of the overlay, the slab wearing surface was brush-coated with a portland cement paste bonding agent (over the anodes).

The elapsed time between construction of the reinforced concrete slab and the initiation of the cathodic protection current was about 6 to 8 weeks. At this point, potential measurements indicated that corrosion was under way in all of the slabs.

The examination of the concrete cores was intended to determine the effect of the cathodic protection treatment on (1) the anode, (2) the concrete surrounding the anode, (3) the bond between the overlay concrete and the base slab concrete, (4) the cathode (top reinforcing steel), and (5) the concrete surrounding the cathode (top rebar). Each core was photographed in the as-cored condition and measurements were made on overlay and slab concrete thickness, depth of rebar cover, and location and placement depth of the anode.

The cores were then subjected to a detailed stereomicroscopic examination of as-cored surfaces which was followed by examinations of interface surfaces and fresh fracture surfaces. Sections perpendicular to the anode and cathode were provided by intentionally fracturing the samples at these locations to provide fresh fracture surfaces through the anode and cathode. Measurements of pH were made on the freshly exposed interface surfaces and on fresh fracture surfaces using spray-applied phenolphthalein and Rainbow Indicator. Small samples of cement paste/mortar were excavated from the interface surfaces and from fresh fracture surfaces for use in SEM examinations. Elemental chemical analyses were conducted on these samples using energy dispersive x-ray spectroscopy (EDS) techniques.

Changes in the elemental chemical make-up of cement mortar/paste samples were sought using a SEM in conjunction with EDS. This work was conducted on fresh fracture surfaces of cement paste/mortar samples excavated from known locations in the treated and untreated concrete specimens. The baseline for comparison made on untreated cement paste/mortar samples from the concrete used in the study. Relative to this untreated cement paste/mortar material, EDS measurements on treated concrete yields information on:

- The appearance of "foreign" elemental species.
- Relative increases or decreases in the amount of a given elemental species.

For the latter semi-quantitative work, sufficient areas of the cement paste/mortar were examined to assure that the reported EDS spectrum was typical.

Chloride ion content measurements were made on powdered samples obtained at various depths as drill debris in accordance with AASHTO Designation T260-82, The Standard Method of Test For Sampling and Testing For Total Chloride Ion in Concrete.

Description of the Concretes

Slab Concrete The base slab concrete in all six cores was characterized as an air-entrained portland cement concrete containing 1/2 in. (1.27 cm) maximum size coarse aggregate and a natural sand.

The coarse aggregate is composed principally of compact, sub-angular to angular sandy, fossiliferous limestone with a maximum particle size of around 1/2 in. (1.27 cm). The dominant lithology is a packed biomicrite containing a variety of skeletal allochems. Most allochems are replaced at least in part by sparry calcite and most clasts contain some medium to fine, sub-rounded, clear detrital quartz sand grains. Sparse biomicrite grains are also present. As much as 5 percent vuggy porosity is common in the limestone coarse aggregate particles.

The fine aggregate is composed of sub-rounded to rounded compact quartz grains 2 mm and smaller and rounded to sub-angular limestone grains similar to lithics and components of the coarse aggregate. Larger sand grains are predominantly sub-angular limestone fragments like the coarse aggregate. Clear, well-rounded quartz grains comprise the majority of the medium sand (0.5 to 0.25 mm) and finer. Carbonate grains finer than medium sand are dominantly sub-rounded to rounded micrite and sparite. Sub-angular to sub-rounded carbonate grains coarser than the medium sand strongly resemble the coarse aggregate. Occasional (less than 1 percent) rounded phosphate or oxide sand grains are present.

A tight bond persists between the aggregate particles and the cement paste matrix phase in the slab concrete.

The cement paste phase in the slab concrete is judged to be of good quality with a water-cement ratio estimated to fall within the range of 0.45 to 0.50. The total air void content of the concrete is estimated at 4 percent to 6 percent.

It is judged that the concrete comprising the six cores examined here is in reasonable compliance with the mix proportions shown in Table 5-9.

Overlay Concrete The overlay concrete in all six slabs is characterized as an air-entrained portland cement concrete containing the same coarse aggregate and fine aggregate as used in the base concrete slab.

The cement paste phase in the overlay concrete is of excellent quality with a water-cement ratio estimated to fall within the range of 0.34 to 0.38. The cement paste is well matured. The total air void content of the overlay concrete is estimated at 4 percent to 6 percent.

A tight bond persists between the aggregate particles and the cement paste matrix phase in the overlay concrete.

ELGARD™ Anode Mesh

The ELGARD™ 210 anode mesh is composed of a substrate of high purity titanium which is covered with a thin layer of an oxide catalyst. Individual strands of the mesh are approximately 0.035 in. x 0.035 in. (0.89 x 0.89 mm) in cross-section. The mesh forms a diamond pattern with the distance between apices of 3 in. and 1-1/3 in. The titanium is high purity, Grade 1. The catalyst controls the anodic reaction so that only oxygen is evolved. Active chlorine is normally not generated with this anode.

In the present investigation, the anode mesh was used in three of the cathodically protected slabs with anode current densities of 40 mA/ft2 (430 mA/m^2) on Slab 3, 20 mA/ft2 (215 mA/m^2) on Slab 4, and 10 mA/ft2 (107 mA/m^2) on Slab 5.

For all three slabs, the cement paste bonding layer was applied on the slab wearing surface over the anode mesh, and the superplasticized dense concrete was then placed as the overlay.

The three cores taken from these slabs (Cores 3, 4, and 5 from Slabs 3, 4, and 5) were intact with the overlay still bonded to the slab concrete. Overlay and slab concrete thickness for the three cores is shown below along with depth of rebar cover in Table 5-19.

Table 5-19. ELGARD™ Anode Mesh Core Thicknesses

Slab/Core No.	Overlay Thickness, in (cm)	Slab Thickness, in (cm)	Depth of Concrete Cover, in (cm) Top Rebar	Bottom Rebar
3/3	2-1/8 (0.84)	5-7/8 (2.3)	1-5/8 (0.64)	1-1/8 (0.44)
4/4	2-1/2 (1)	5-7/8 (2.3)	1-5/8 (0.64)	1-1/4 (0.5)
5/5	1-7/8 (0.74)	6-1/2 (2.6)	2 (0.8)	1-1/8 (0.44)

Core 3 is shown in the as-received condition in Figure 5-50. Core 4 and Core 5 have a similar appearance.

Figure 5-50. Core No. 3 After 30 Months of Cathodic Protection, Units are in Inches

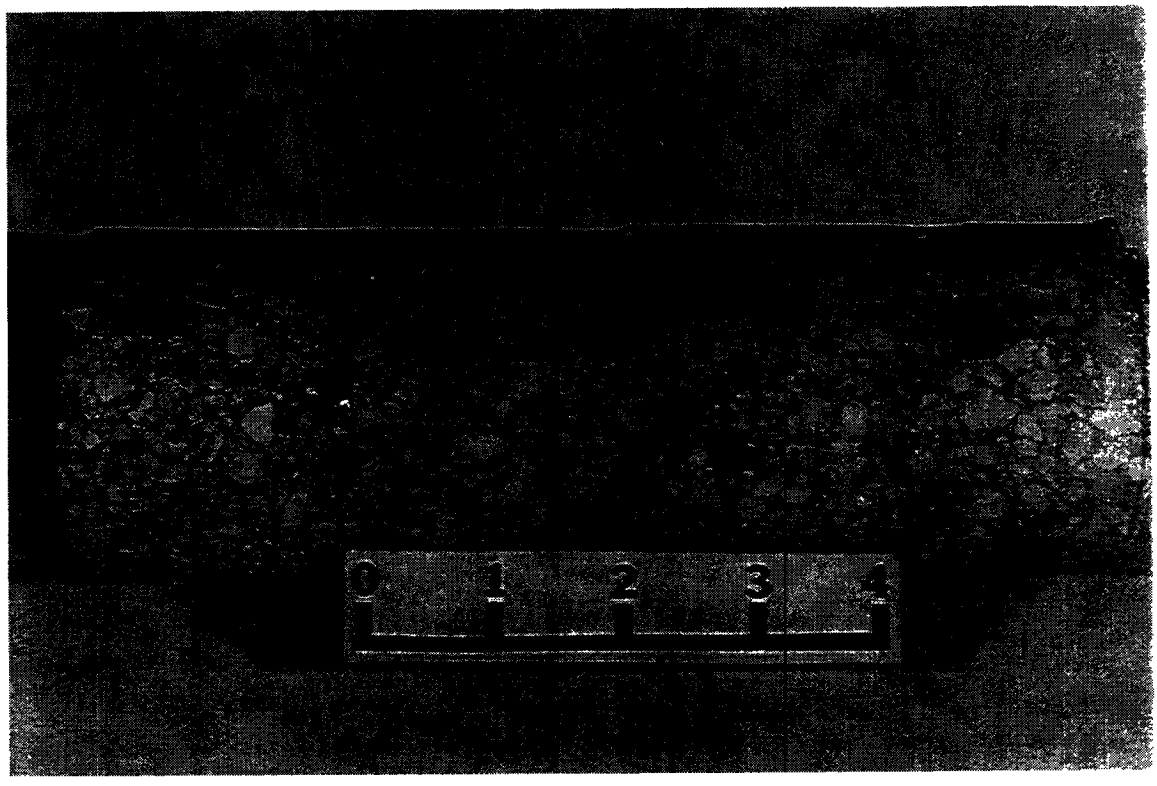

In all three cores, the mesh anode is completely encapsulated by the overlay concrete and the anode is 1 mm to 2 mm above the interface between the overlay concrete and the base slab concrete.

Initial Examination of As-Received Cores 3, 4, and 5 As soon as they were received in the laboratory, the cores were unwrapped and carefully examined under a stereomicroscope (10X - 100X). This examination revealed the following:

- Base slab concrete surrounding the top No. 4 rebar (cathode) was not cracked, discolored, or softened.
- In all three cores, the superplasticized, dense concrete overlay remained firmly bonded to the base slab concrete.
- In Core No. 3 (Slab 3: 40 mA/ft^2 or 430 mA/m^2), a thin annulus of the cement paste phase of the overlay concrete contacting the anode strands was discolored (from the normal grey to orange) and significantly softened. Under close scrutiny, this color change can be seen with the unaided eye. The orange discoloration of cement paste contacting the anode was not seen in Core 4 (Slab 4: 20 mA/ft^2 or 215 mA/ft^2) or Core 5 (Slab 5: 10 mA/ft^2 or 107 mA/m^2).
- No other evidence of distress (discoloration/softening/cracking) was observed in the overlay concrete or base slab concrete in the three cores.

Destructive examination of the cores followed the initial examination. As an aid in quantifying the extent of alteration of the cement paste phase surrounding the anode, the various stages of alteration are characterized here as:

- Severely altered - the extremely soft, porous, orange/white cement paste in immediate contact with the anode in Figure 5-52B.
- Heavily altered - the soft, porous, light-grey cement paste shown in Figures 5-52A and 5-52B.
- Moderately altered - The medium-grey cement paste shown in Figures 5-52A and 5-52B.
- Unaltered - The dark-grey cement paste shown in Figures 5-52A and 5-52B.

Alteration of the Overlay Concrete at Points of Contact With the Anode Mesh In all three slabs (3, 4, and 5) operating at 40 mA/ft^2, 20 mA/ft^2, and 10 mA/ft^2 (430, 215 and 107 mA/m^2) respectively, there was some alteration of the concrete in contact with the titanium mesh anode surfaces. This alteration took the form of discoloration and softening of a thin layer of the encapsulating concrete. There was no cracking in the concrete at points of contact with the anode.

The degree of softening/discoloration alteration of the concrete encapsulating the anode varied depending upon the level of current density. The extent and severity of alteration decreased with decreasing current density, from 40 to 10 mA/ft2 (430 to 107 mA/m^2). Examples of the alteration of the encapsulating overlay concrete at points of contact with the mesh anode are described below.

Typically, the concrete component that is in actual contact with the anode mesh surfaces is the cement paste phase of the concrete. Cement paste is the hardened cement hydrate phase resulting from reactions of the portland cement with water. The hardened material contacting the anode may also include a small amount of very fine material (typically less than 100 mesh) contributed by the aggregate phases. In all of the cores examined here, it is this fine-grained material (which is predominantly hydrated portland cement phases) that experienced the discoloration and softening phenomenon at points of contact with the anode. During the course of the alteration phenomenon, it was observed in some cases that limestone aggregate particles in close proximity to the anode were affected.

Figure 5-51 gives an example of the chemistry and microstructure of the cement paste phase of the superplasticized, dense overlay concrete that has not been altered in any way. This material was sampled from the "middle" of the 2-1/2 in. (6.4 cm) overlay well away from both the wearing surface and the anode. The EDS spectrum shown is typical for "normal" hydrated portland cement paste. The principal elemental phase is calcium (Ca) which reflects the fact that portland cement contains 60 percent to 65 percent calcium oxide (CaO). The next most abundant elemental phase is silicon (Si) which, in this case, has a moderately higher than normal peak due to the contribution of the fine quartz (SiO2) aggregates. Sulfur

(S) and aluminum (Al) are the next most abundant elements with even smaller amounts of iron (Fe) and magnesium (Mg).

The microstructure of the unaltered cement paste as shown in Figure 5-51 shows a relatively uniform color and texture. The fracture surface shows slight, blocky relief. The cement paste is quite dense and shows virtually no porosity larger than 10 microns and only a small amount of porosity in the 1 micron to 5 micron range with most in the 5 to 10 micron range. The water-cement ratio of the cement paste phase of the superplasticized, dense overlay concrete was judged to fall within the range 0.34 to 0.38.

Figure 5-51. EDS Spectrum (40X) and Microstructure (1000X) of the Hardened Cement Paste Phase of the Superplasticized Dense Overlay Concrete That Has Not Experienced Any Alteration or Modification.

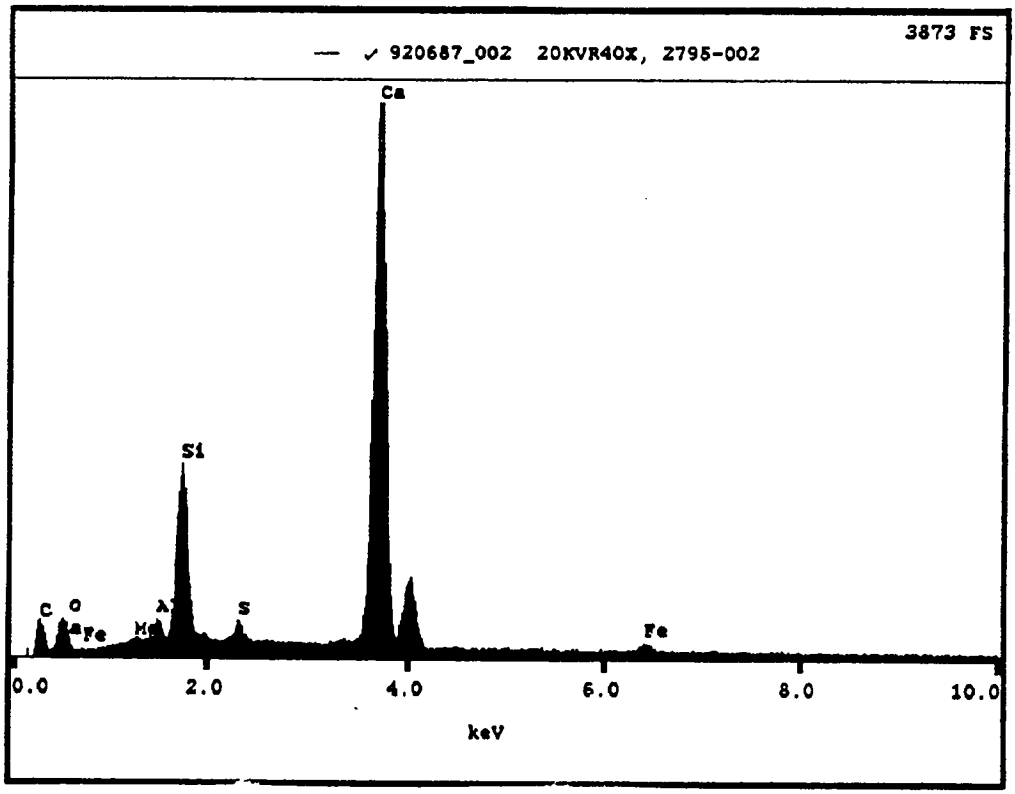

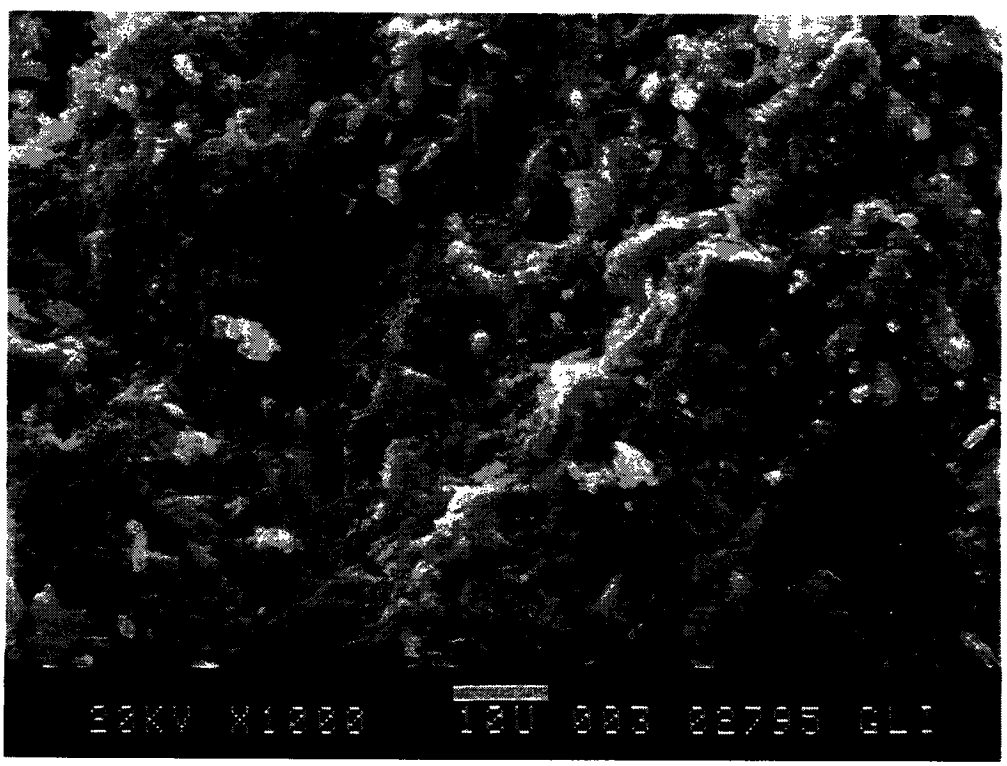

Core 3 (Slab 3) 40 mA/ft² Alteration of the overlay concrete contacting the mesh anode was most extensive and most severe in the slab operating at 40 mA/ft² (430 mA/m²) for 30 months (Slab 3). In Core 3, the anode was completely embedded in the superplasticized, dense overlay concrete at a distance of 1 mm to 2 mm from the interface between the overlay and the base slab. For the present examination, the overlay concrete was intentionally separated from the base slab concrete by hammer and chisel blows. The separation of overlay and base slab concrete occurred principally right at the interface and within the base concrete very near the interface surface. Less than 10 percent of the separation occurred in the overlay concrete. The effort required to separate the two concretes indicates that the bond between the concretes remained firm after the 30-month cathodic protection treatment.

The overlay-slab interface surface in the overlay concrete was destructively examined to reveal the anode mesh. The progression of this examination is illustrated in figures 5-52A to 5-52C.

Figure 5-52A. **Plan View (10X) of the Overlay Concrete-Slab Concrete Interface Surface (Intentionally Fractured) on the Overlay Concrete Portion of Core 3. Destructive excavation of the surface proceeded from A to C. The cement paste phase of the overlay concrete contacting the anode has been altered by the cathodic protection treatment as evidenced by both a color change and a softening. Depending upon the level of softening, the altered cement paste is characterized as severely altered (1), heavily altered (2), moderately altered (3), and unaltered (4). The anode is labeled (X).**

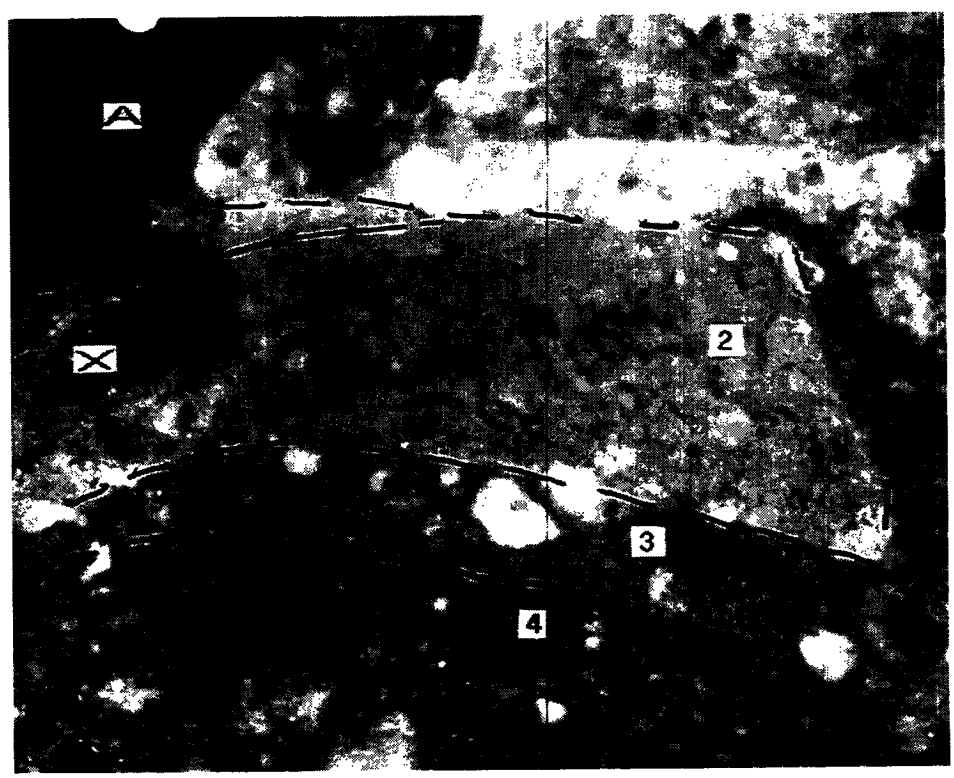

Figure 5-52B. **Plan View (10X) of the Overlay Concrete-Slab Concrete Interface Surface (Intentionally Fractured) on the Overlay Concrete Portion of Core 3.**

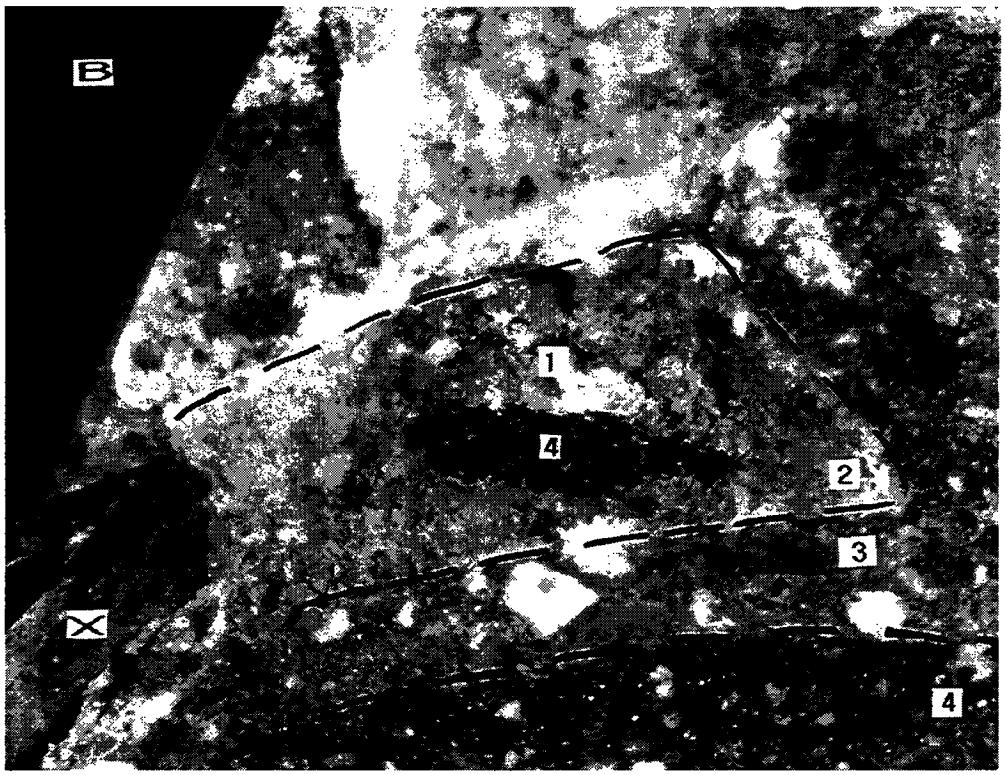

Figure 5-52C. **Plan View (10X) of the Overlay Concrete-Slab Concrete Interface Surface (Intentionally Fractured) on the Overlay Concrete Portion of Core 3.**

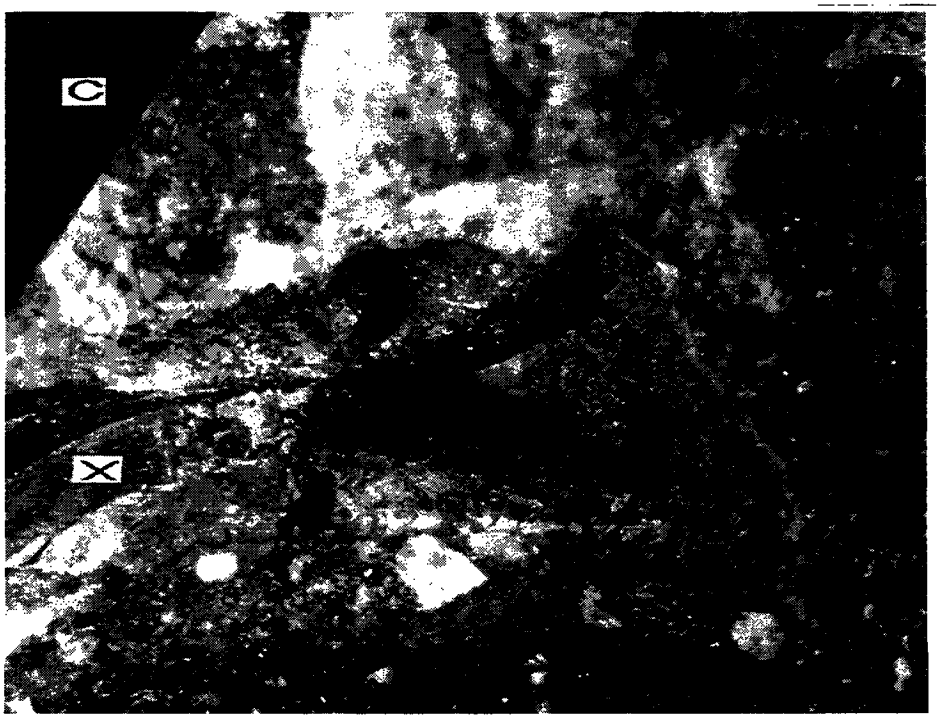

In Figure 5-52A, most of the anode has not yet been revealed but alteration of the concrete adjacent to the anode is evident. A trapezoidal-shaped area of light grey cement paste (2) covers the anode. At its widest point, this light-grey paste layer is 0.12 in. (3 mm) wide. The light grey cement paste is very soft and highly porous. The material shows virtually no binding ability and is easily dislodged with a pointed steel probe.

There is an abrupt transition from the soft, porous light-grey cement paste overlaying the anode (2) to a thin strip, about 0.06 in. (1.5 mm), of medium grey cement paste running approximately parallel to the long dimension of the anode strands (3) in Figure 5-52A. Also shown is that the medium-grey cement paste (3) grades abruptly into the dark-grey, unaltered cement paste (4). Relative to the unaltered portland cement paste, the medium-grey cement paste is moderately softer but is still quite competent.

In Figure 5-52B, the light-grey paste (2) has been removed to reveal the anode (X). In immediate contact with the anode is a thin, less than 0.02 in. (0.5 mm), layer of paste whose color has been completely altered from grey to white/orange (1). This white/orange paste is even softer, more porous, and less competent than the light-grey paste overlaying the anode (2). Typically, where this phenomenon has occurred, the cement paste in immediate contact with the anode is discolored white and grades irregularly into the orange color.

In Figure 5-52C, more of the altered paste over the anode has been removed revealing the fact that this examination site is a point of juncture of two mesh strands forming a "V" of the mesh diamond. Discoloration and alteration of the cement paste in contact with the second anode strand is similar to that described for the first strand.

As seen in Figure 5-52C, the region of greatest alteration of the cement paste is that lying between the two anode mesh strands where they part to form the "V" of the diamond mesh. This phenomenon was a typical occurrence in Core 3 although there were less frequent examples of "V" junctures where the paste alteration occurred but was not as severe.

In going from unaltered to severely altered paste, there is a reduction in hardness, an increase in porosity (loss of mass), and a color change from dark grey through lighter shades of grey to orange/white. This same nomenclature will be used in subsequent text to quantify the extent of alteration of concrete in contact with the various cathodic protection anodes.

In Core 3, where the anode mesh strands were more than about 0.15 in. (about 4 mm) apart, alteration of the cement paste is characterized as heavily altered (2) or moderately altered (3). Along the individual anode strands, none of the severely altered (1) cement paste was observed. The region of altered cement paste along single anode strands was typically around 0.05 in. to 0.10 in. (1 mm to 2.5 mm). This phenomenon is shown in Figure 5-53. The region of heavily altered paste (2) immediately contacting the single anode strand is typically less than 0.005 in. (0.1 mm) thick.

Figure 5-53. Plan Views of the Excavation of a Single Anode Mesh Strand (X) from Core 3. Where the distance between adjacent strands was greater than 0.1 in. (about 4 mm), alteration of the contacting cement paste is characterized as heavily altered (2) or moderately altered (3).

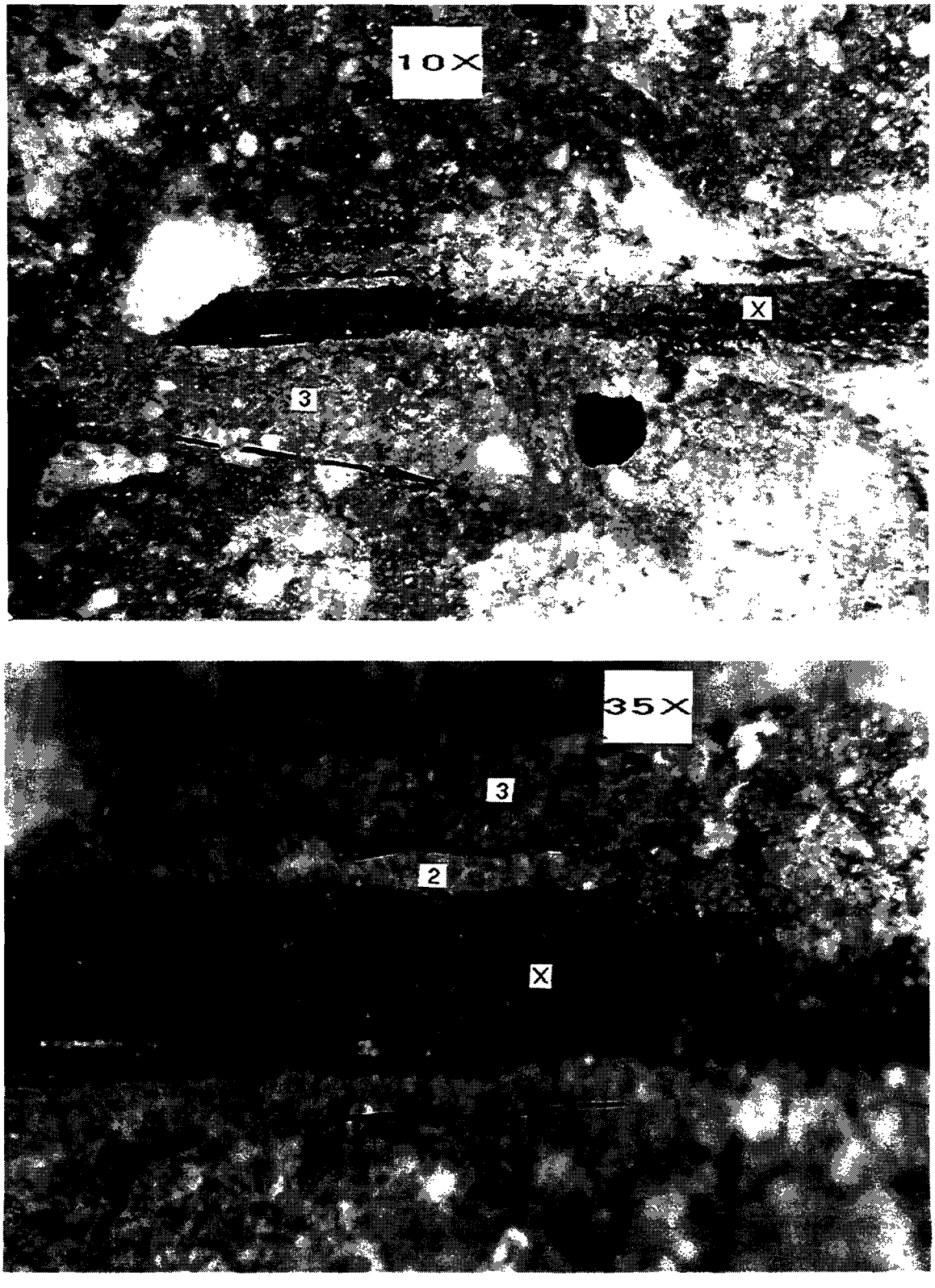

Figure 5-54 shows another example of severely altered cement paste (1) lying between the "V" juncture of the mesh anode strands in Core 3. Also shown in Figure 5-54 is a limestone aggregate particle (6) lying within this region that has been altered (softened) by the events taking place near the anode.

SEM/EDS examinations were conducted on the altered cement paste surrounding the anode in Core 3.

Figure 5-54. Plan View of Excavated Mesh Anode in Core 3 Showing Severely Altered Cement Paste (1) and a Softened Limestone Aggregate Particle (6) in the Overlay Concrete. The extent of alteration of the concrete (discoloration/softening) was greatest in the region lying between the "V" juncture of the anode mesh strands.

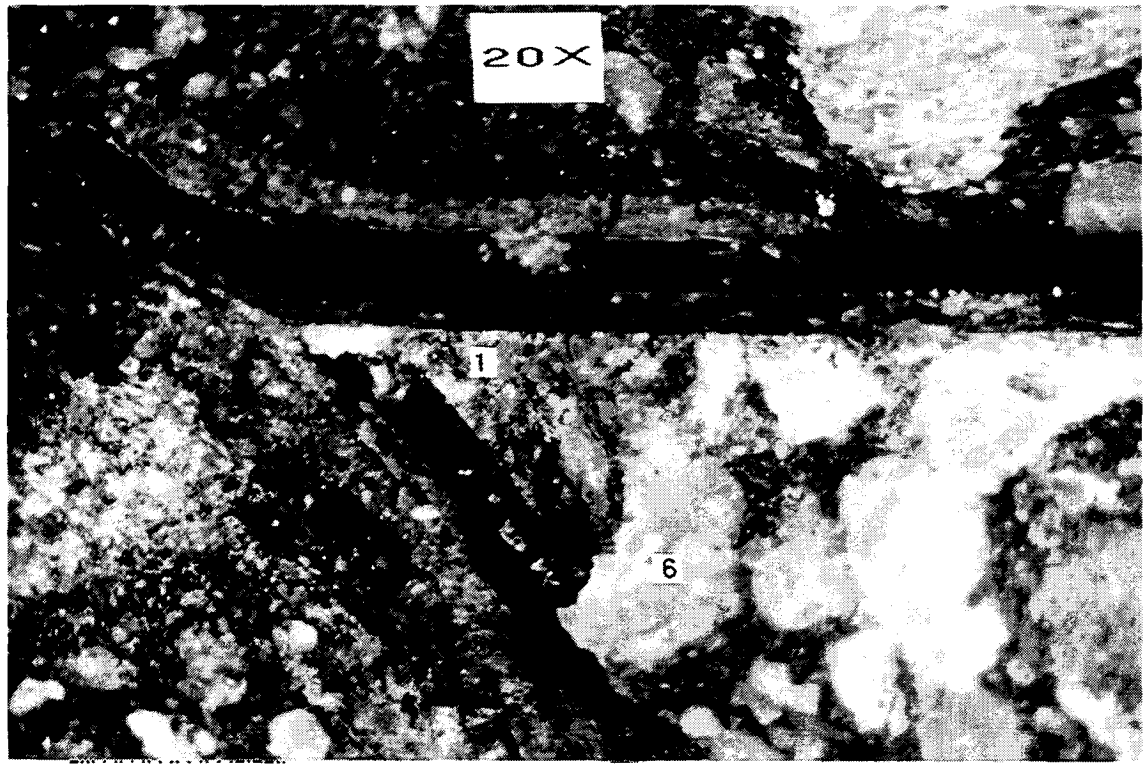

Severely Altered Paste (1) The most severely altered cement paste is shown in Figure 5-54 as the orange/white material lying between the anode "V" (1).

Measurements of pH made on this material at the time of excavation showed values in the range of 5 to 9.

Figure 5-55 shows the elemental chemical composition and microstructure of this severely altered paste. Relative to unaltered hydrated cement paste, this severely altered paste shows a significant depletion of calcium (Ca) and a total absence of sulfur (S) bearing phases. Silicon (Si) is the dominant elemental phase and both iron (Fe) and aluminum (Al) are at significantly higher values than would normally be expected in unaltered hydrated cement paste (see figures 5-52A, B and C).

The microstructure shows evidence of significant dissolution of the previously dense and isotropic paste. The dissolution has produced a significant amount of porosity in the 1 micron to 5 micron range and isolation of discrete granules of altered paste that have the same elemental phase composition as shown in the EDS for the bulk sample.

Several small regions on the SEM photograph show evidence of "mudflat" cracking, indicating that this material was gel-like at one time.

Figure 5-56 is an EDS spectrum and SEM photograph of the cement paste actually in contact with the anode near one of the "V" junctures of the anode strands. The EDS spectrum is very similar to that shown in Figure 5-55 with a significant depletion of calcium (Ca) and significant increases in the aluminum (Al), iron (Fe), and potassium (K) levels. Silicon (Si) is the most abundant elemental phase. A trace amount of titanium (Ti) is present in the cement paste at this location (derived from the anode). As shown in the SEM photograph in Figure 5-56, the cement paste has parted relatively cleanly from the anode at this location but the paste is quite soft and porous.

Figure 5-55. **EDS Spectrum (34X) and Microstructure (600X) of Severely Altered Cement Paste in Contact with the Anode Mesh in Core 3. This orange/white cement paste can be seen in Figure 5-59 and Figure 5-61.**

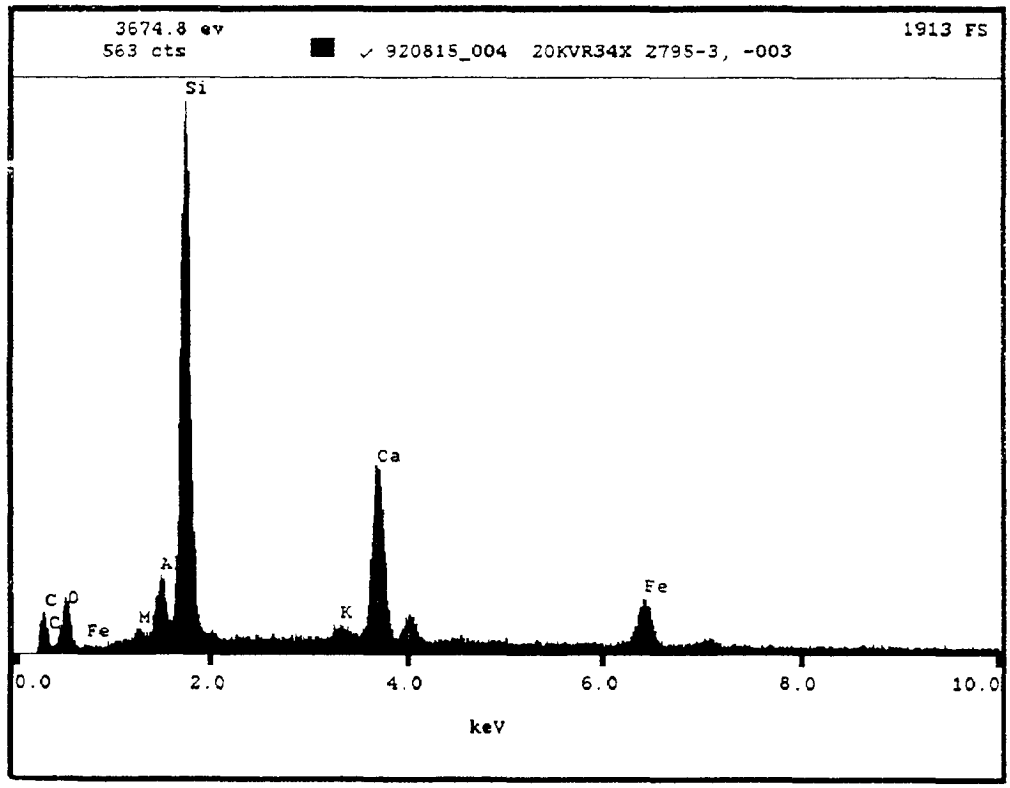

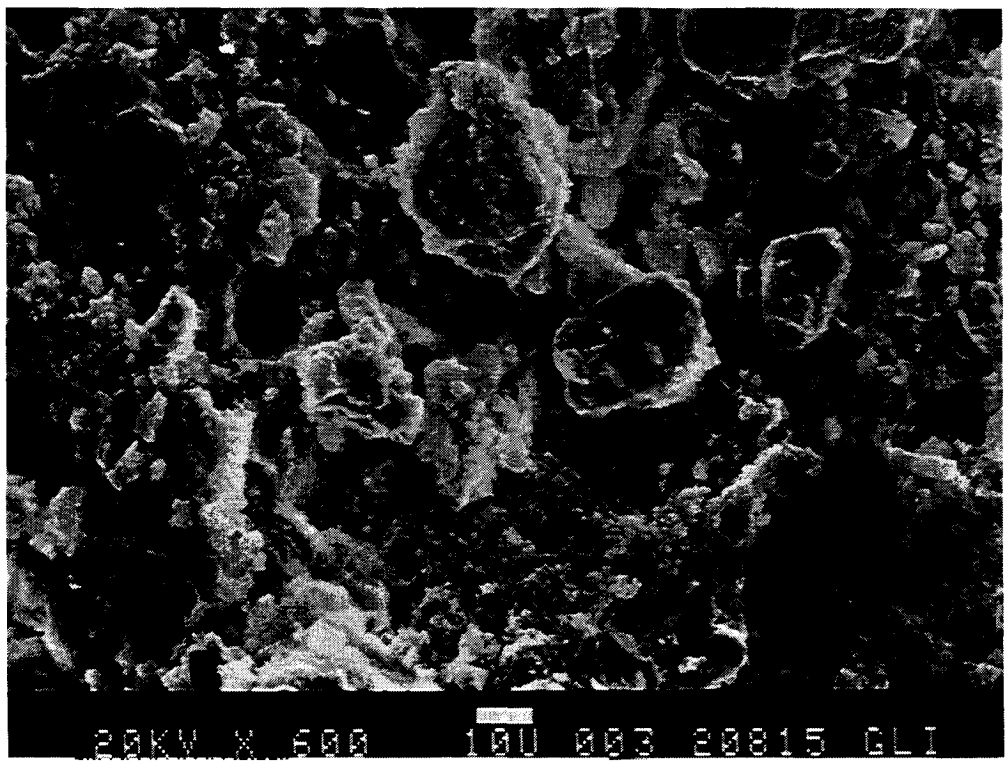

Figure 5-56. EDS Spectrum (100X) and Microstructure (200X) of Overlay Concrete in Core 3 Forming the Interface with the Anode Mesh in a Region Showing Severe Alteration of the Concrete.

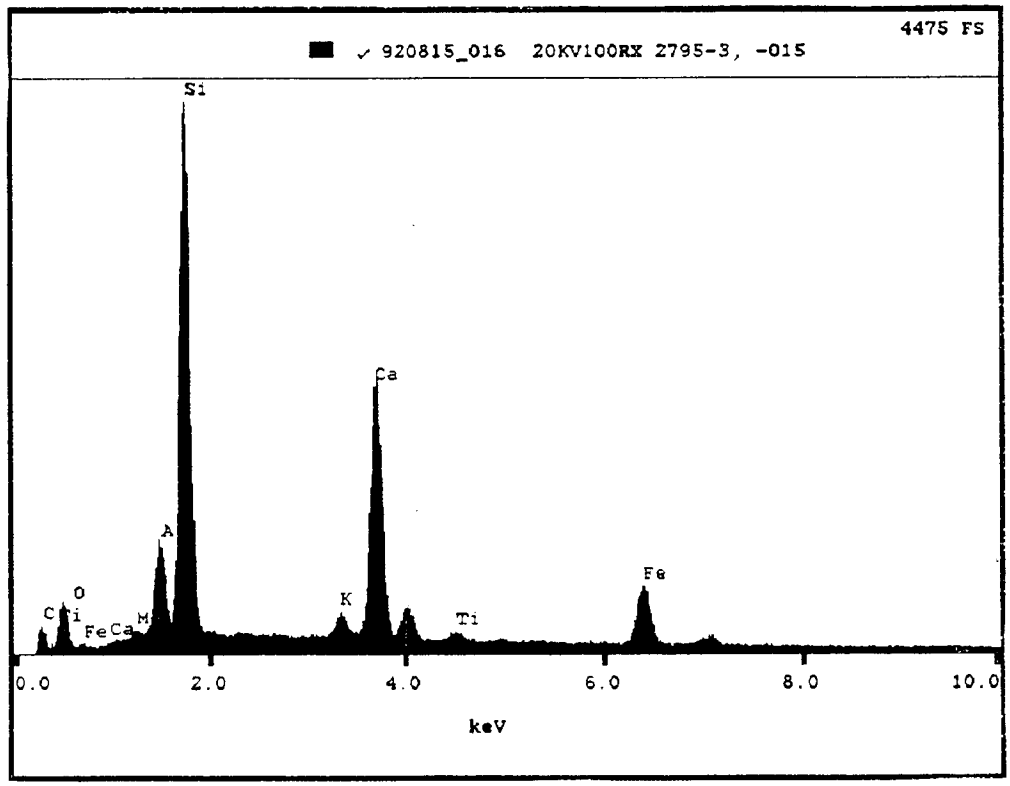

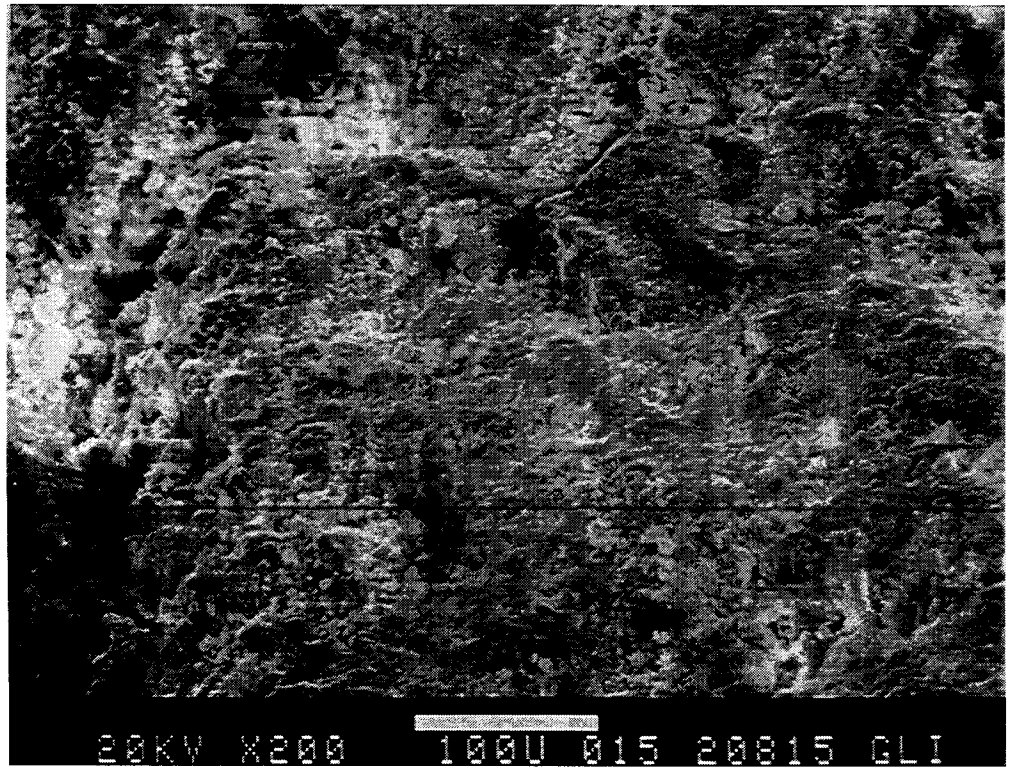

Moderately Altered Paste (3) Moderately altered paste was defined in figures 5-52A, B, and C and 5-53 as paste that is slightly lighter in color (medium-grey) and moderately softer than unaltered cement paste (4). EDS spectra taken from two different regions of moderately altered paste are shown in Figure 5-57. In the moderately altered paste material, the calcium (Ca) bearing phases have not yet been subject to significant attack. The sulfur (S) bearing phases are also still present. At both sites, however, there is an increase in the levels of iron (Fe) and aluminum (Al) and, at one of the sites (013), there is a small amount of chlorine (Cl).

Cores 4 and 5 (Slabs 4 and 5) 20 mA/ft^2 and 10 mA/ft^2 Destructive examinations were conducted on the overlay portion of Cores 4 and 5 to expose the anode mesh (using the same procedure as described previously for Core 3). In Core 4 (Slab 4: 20 mA/ft2 or 215 mA/m^2), none of the concrete surrounding the anode could be characterized as "severely altered." In the work on Core 3, severely altered concrete was characterized as showing a color change from the normal grey to orange/white, with a significant softening and increase in porosity.

A small amount of concrete surrounding the anode in Core 4 (20 mA/ft^2 or 215 mA/m^2) did experience an alteration which was characterized previously as "moderately altered." The moderately altered paste showed a slight color change from dark grey to a medium grey and a moderate amount of softening. Measurements of pH made on the concrete interface surfaces with the anode typically showed values in the 12 to 13 range. There were, however, a few small regions (less than 10 percent of total) where the pH was in the range of 9 to 11. Along the various anode strands in Core 4, the thickness of moderately altered paste varied from zero to as much as 0.04 in. (1 mm). The typical thickness of altered material is 0.03 in. (0.75 mm). As was observed in Core 3, the region of most active alteration of paste occurred within the space lying between two individual anode strands where they meet to form the "V" of the diamond mesh.

For the Slab 4/Core 4 treated at 20 mA/ft^2 (215 mA/m^2), the 30-month cathodic protection treatment had no adverse effect on the limestone aggregate particles in concrete near the anode.

In Slab 5/Core 5 powered at 10 mA/ft^2 (107 mA/m^2) for 30 months, the effect of the cathodic protection treatment on concrete surrounding the anode mesh was very similar to that observed in the slab treated at 20 mA/ft^2 (Slab 4/Core 4). Here, a thin layer of concrete surrounding the anodes is characterized as being moderately altered. The thickness of this layer varies from 0 in. to 0.3 in. (0 mm to 0.75 mm). No limestone aggregate particles were altered by the cathodic protection treatment at 10 mA/ft2 for 30 months.

In all of the cores containing the anode mesh (Cores 3, 4, and 5), the alteration of the paste was somewhat greater along the side and bottom surfaces of the anode (i.e., in concrete lying between the anode and cathode).

Figure 5-57. EDS Spectra (800X) of Moderately Altered Cement Paste in the Overlay-Concrete Adjacent to the Mesh Anode in Core 3.

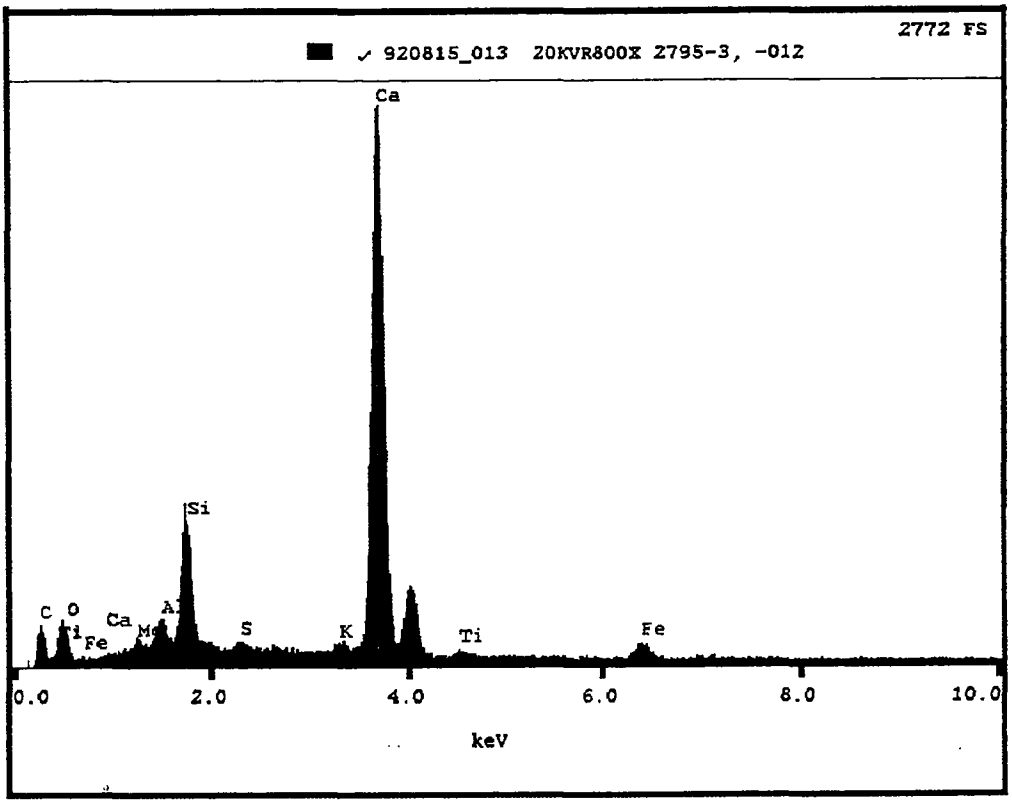

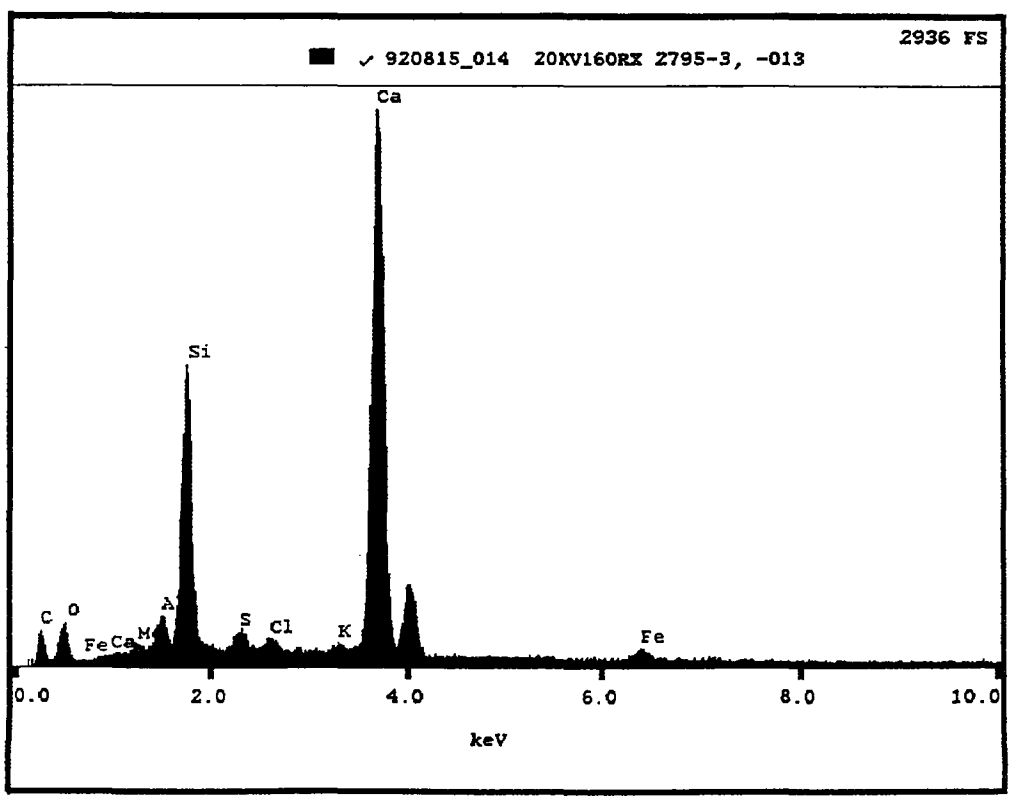

Summary The 30-month cathodic protection treatment at anode current densities of 40 mA/ft^2, 20 mA/ft^2, and 10 mA/ft^2 (430, 215, and 107 mA/m^2) using the anode mesh resulted, in all cases, in some alteration of the superplasticized, dense paste surrounding the mesh anode. Table 5-20 ranks the extent and severity of the alteration.

The alteration affects primarily the hydrated portland cement phase of the concrete and is defined as a discoloration, dissolution, and softening that is characteristic of attack by an acid aqueous solution. In the three cores containing the anode mesh, the alteration was characterized as "severely altered," and "moderately altered" (see Table 5-20).

Table 5-20. Extent and Severity of the Alteration of the Concrete Encapsulating the ELGARD™ Mesh Anode Following the 30-Month Cathodic Protection Treatment at 40, 20, and 10 mA/ft^2 (430, 215, and 107 mA/m^2)

	Current Density		Severely Altered Concrete[a]			Moderately Altered Concrete[b]		
				Max. Thickness			Max. Thickness	
Core/Slab No.	mA/ft^2	mA/m^2	Observed?	in	(mm)	Observed?	in.	(mm)
3	40	430	Yes	0.12	(3)	Yes	0.09	(2.3)
4	20	215	No	---		Yes	0.04	(1)
5	10	107	No	---		Yes	0.04	(1)

[a] Concrete characterized as "severely altered" shows a significant dissolution and softening of the hydrated portland cement paste phase to the point that virtually all binding qualities are absent along with a color change from the normal grey to orange and white. In "severely altered" concrete some limestone aggregate particles also show some softening (see Figures 3 and 5).

[b] In concrete that is "moderately altered," the hydrated cement paste phase has undergone a moderate softening relative to the unaffected concrete. The moderately altered paste still retains reasonably good binding qualities and does not show large increases in porosity. In "moderately altered" concrete, the hydrated cement paste phase shows a color change from the normal dark grey color to a noticeable lighter medium grey color. No limestone aggregate particles are affected in moderately altered concrete (see Figures 3, 4, and 5).

Condition of the Mesh Anode In all three of the slabs cathodically protected with the anode mesh, the anode itself was judged to be virtually unaffected by the 30-month cathodic protection treatment at 40 mA/ft^2, 20 mA/ft^2, and 10 mA/ft^2 (430, 215, and 107 mA/m2). In all three cores, the catalytic coating remained firmly bonded to the titanium strand. No pitting was observed on any of the anode strands.

The anode interface surfaces on the superplasticized, dense overlay concrete showed no visual evidence of the mesh anode material "sticking" to the concrete. However, in the slab operated at 40 mA/ft^2 (430 mA/m^2), EDS examinations of the anode interface surfaces on the concrete did show trace amounts of titanium (Ti [see Figure 5-57]). This is the only evidence that there has been any mass transfer of material from the titanium anode mesh.

Alteration of the Slab Concrete in Contact With the Cathode (Top Rebar) In all three cores containing the anode mesh, the base slab concrete was intentionally fractured to reveal the interface between the concrete and the cathode (top rebar).

In all three cores, the cathode interface on the base slab concrete appeared to be virtually unaffected by the 30-month cathodic protection treatment for current densities ranging from 10 mA/ft^2 to 40 mA/ft^2 (107 to 430 mA/m^2). The pH at the cathode interface on the concrete showed values in the range of 12 to 13.

The cement paste defining the interface surface was relatively hard and dense and was virtually indistinguishable from cement paste in the concrete away from the rebar interface.

The top reinforcing steel (cathode) showed a slight amount of corrosion in Cores 3 (40 mA/ft^2, 430 mA/m^2) and 4 (20 mA/ft^2, 215 mA/m^2) and a slightly greater amount of corrosion (characterized as light) in Core 5 (10 mA/ft^2, 107 mA/m^2). In Core 5, over 60 percent of the rebar surface was covered with a very thin layer of cement paste. This was not the case for the rebars in Cores 3 and 4 where the bars were relatively clean.

The base slab concrete lying between the anode and the cathode was intentionally fractured (hammer/chisel) parallel to the top rebar direction. The pH of the concrete was then measured. In all three cores, the failure mode of this concrete was virtually 100 percent aggregate fracture and the entire thickness of the concrete showed pH values in the 12 to 13 range.

For these cores, it is judged that the 30-month cathodic protection treatment had no significant effect on the composition or quality of the concrete lying between the cathode and anode or on the quality of the bond between the cathode (top rebar) and the concrete.

ELGARD™ Anode Ribbon

The anode ribbon was used in Slab 2 which operated at a current density of 20 mA/ft^2 (215 mA/m^2) for 30 months. Core 2 (from Slab 2) is shown in Figure 5-58 in the as-received condition. The core is composed of a 2-1/4 in. (5.72 cm) thickness of overlay concrete and a 6 in. (15.24 cm) thickness of the base slab concrete. Clear cover of the top No. 4 reinforcing steel (cathode) is 1-5/8 in. (4.13 cm). Clear cover of the bottom reinforcing bar is 1-1/8 in. (2.86 cm).

The anode ribbon is completely embedded in the overlay concrete about 1/4 in. (0.64 cm) from the overlay/slab interface. The anode ribbon is a 7 mm wide x 1 mm thick titanium strip containing a catalytic surface coating. At this coring site, the 7 mm dimension of the ribbon is roughly perpendicular to the slab wearing surface.

Initial Examination of Core 2 Core 2 was thoroughly examined using a stereomicroscope (10X - 100X) with the following observations:

- There was no discoloration, softening, or cracking of the base slab concrete surrounding the cathode (top rebar).
- Bond failure occurred between the overlay and base slab concrete.
- The overlay concrete contacting the anode ribbon was softened and discolored.

Bond Failure Between the Overlay and the Base Concrete Slab Figure 5-58 shows the 2-1/4 in (5.72 cm) thick superplasticized, dense concrete overlay containing the anode that was separated from the base slab concrete. Examination of the failed interface surfaces suggests that the separation probably occurred during the coring operation. Bond failure between the two concretes occurred principally within the cement paste used as a bonding grout (60 percent to 70 percent of total surface area). The remaining 30 percent to 40 percent of failure occurred principally within the superplasticized, dense concrete overlay within 0.04 in. (1 mm) of the actual interface surface.

Figure 5-58. Core 2 from Slab 2 Following 30 Month Cathodic Protection Treatment at 20 mA/ft^2 (215 mA/m^2). The anode is the ELGARD™ anode ribbon. The overlay is completely disbonded from the base slab (Scale in Inches).

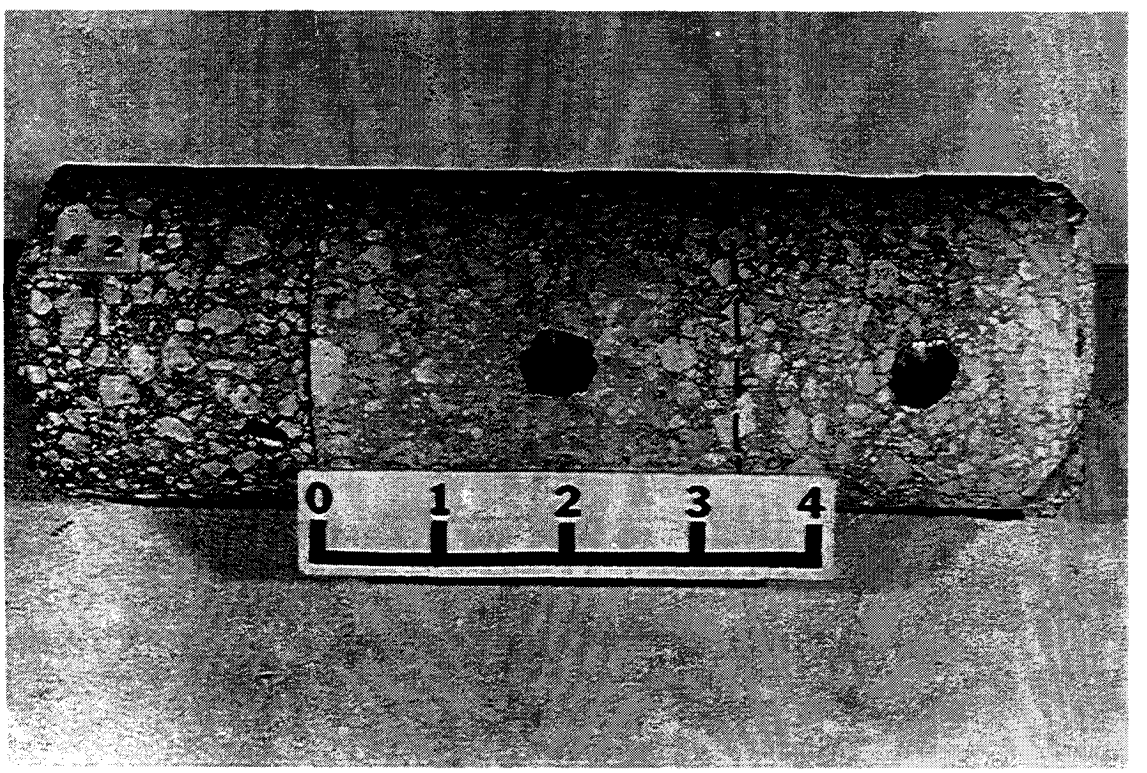

At this coring site, the cement paste bonding grout was of relatively low quality, characterized by a high water-cement ratio (greater than 0.70). Strings of an amber-colored resinous material were also present on the disbonded interface surfaces. In addition to the resinous material, another "foreign" material observed at the interface is small particles (less than 0.04 in. (1 mm)) of a hard black material with a vitreous texture.

All of the overlay/base slab interface surface features just described are illustrated in Figure 5-59.

An EDS examination was conducted to learn the identity of the two foreign materials found at the interface. The black vitreous particles showed only silicon (Si). The surface texture and color of the particles suggests that they were silicon carbide (SiC). However, the EDS examination showed insignificant levels of carbon. The particles may be a form of silica (SiO2), although their source is still unclear.

Figure 5-59. Overlay/Slab Interface Surface on the Bottom of the Superplasticized, Dense Concrete Overlay in Core 2. The white material is the cement paste bonding grout placed between the base concrete slab and the overlay. The bonding grout contained inclusions of an amber-colored organic polymer and hard black vitreous particles (→).

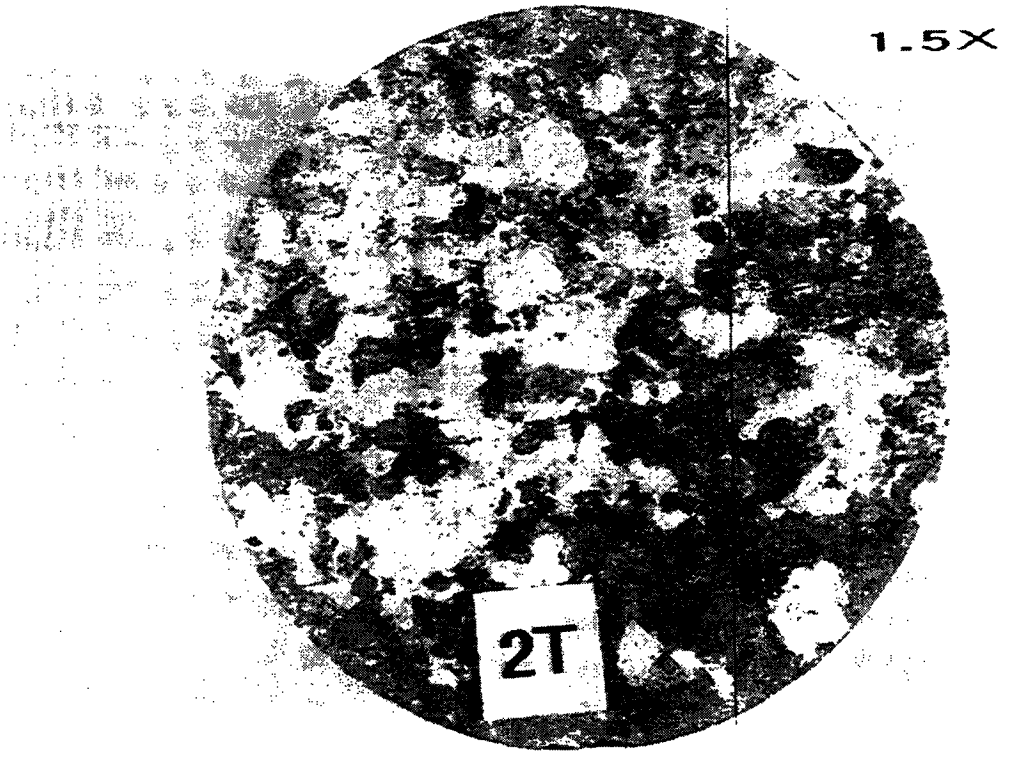

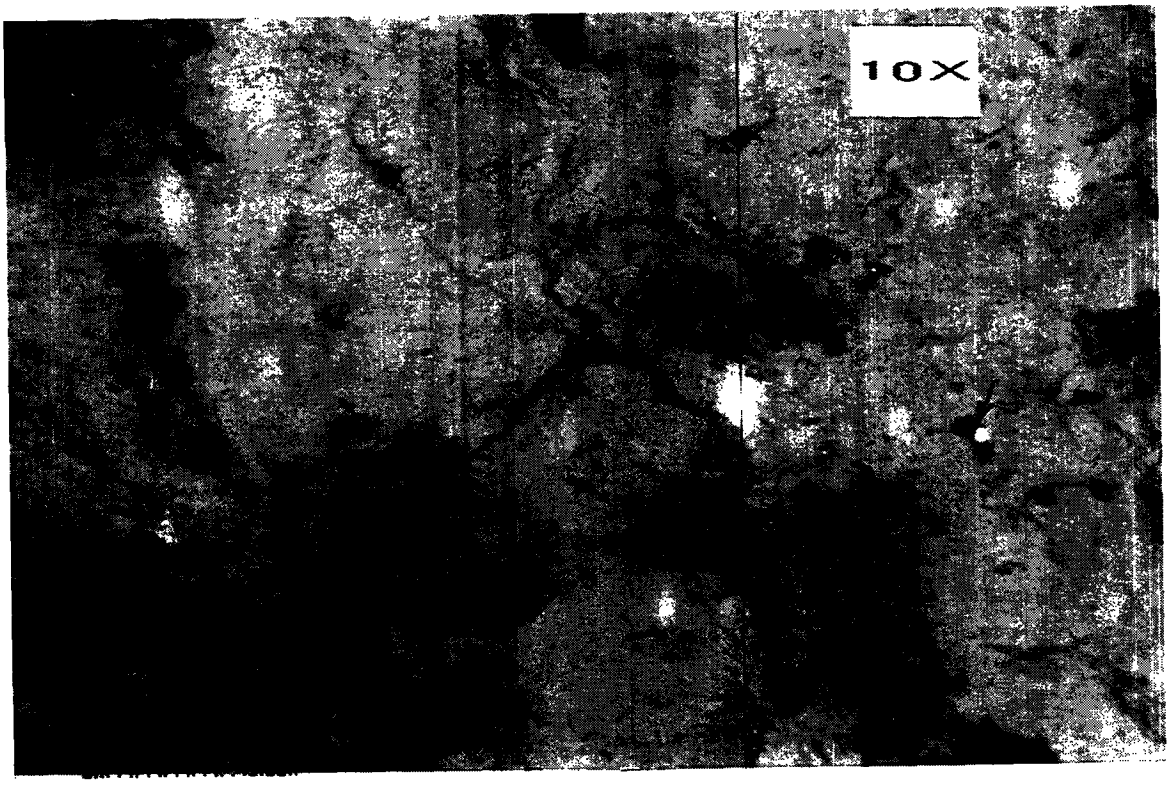

As shown in Figure 5-59, the amber-colored resinous material occurred principally as nodules and strings within the cement paste bonding grout. EDS analysis of the amber-colored material showed very high levels of carbon (C) indicating that the material is some type of organic polymer. Here, too, the origin of this material is unclear.

It is judged that the bond failure in this specimen did not occur as a result of the cathodic protection treatment but rather as a consequence of the relatively weak, contaminated interface surface dominated by the low-quality bonding grout.

Alteration of the Superplasticized Dense Overlay Concrete at Points of Contact With the Anode Ribbon At this coring site, the ELGARD™ anode ribbon was completely embedded in the overlay concrete about 1/4 in. (0.64 cm) from the overlay/base slab interface. Figure 5-60 shows section views of the anode ribbon on the as-cored surface of Core 2. Concrete surrounding the anode had been softened to the point that some material was washed out during the coring operation.

The overlay portion of the core was intentionally fractured (hammer and chisel) to reveal the anode/overlay concrete interface surfaces. Photographs of the interface surface, taken at 10X and 20X, are shown in Figure 5-61. The cement paste in immediate contact with the large anode surface has been severely/heavily altered as characterized by the color change from normal grey to very light grey, orange, and white and a softening to the point that binding qualities are virtually lost. As shown in Figure 5-61, the alteration is not uniform, with the interface surface showing mottled islands of severely altered orange/white paste lying within the heavily altered light grey paste.

Figure 5-60. Cored Surface of the Overlay Concrete Portion of Core 2 Showing the Loss of a 1 mm Thickness of Paste Surrounding the Anode Ribbon.

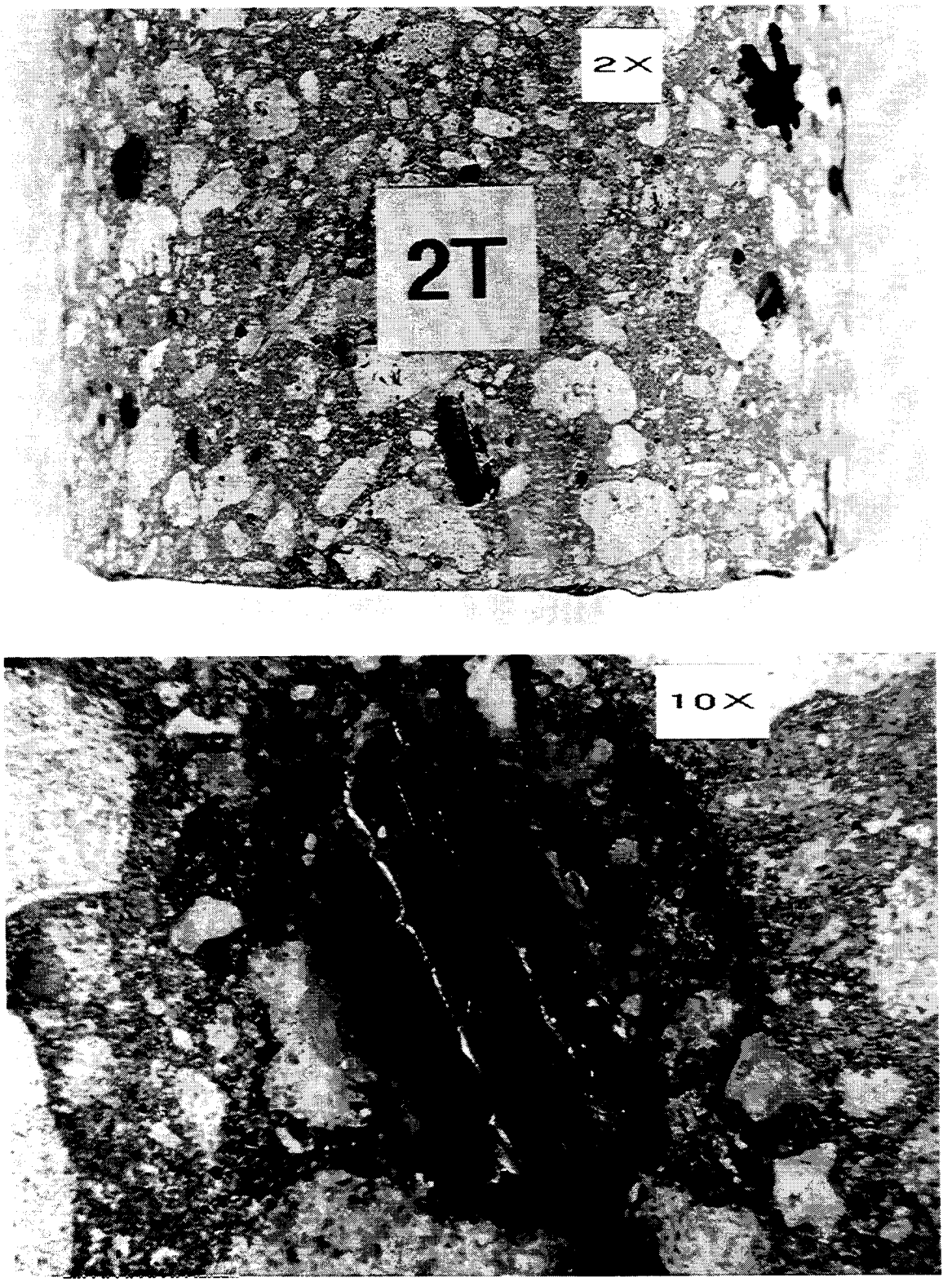

Figure 5-61. **Interface Surface of the Overlay Concrete with the Anode Ribbon in Core 2 (within the dashed lines). The white/orange paste is characterized as severely altered (1) and the light-grey paste is characterized as heavily altered (2). Adjacent to the anode is moderately altered paste (3) which grades abruptly into unaltered concrete (4).**

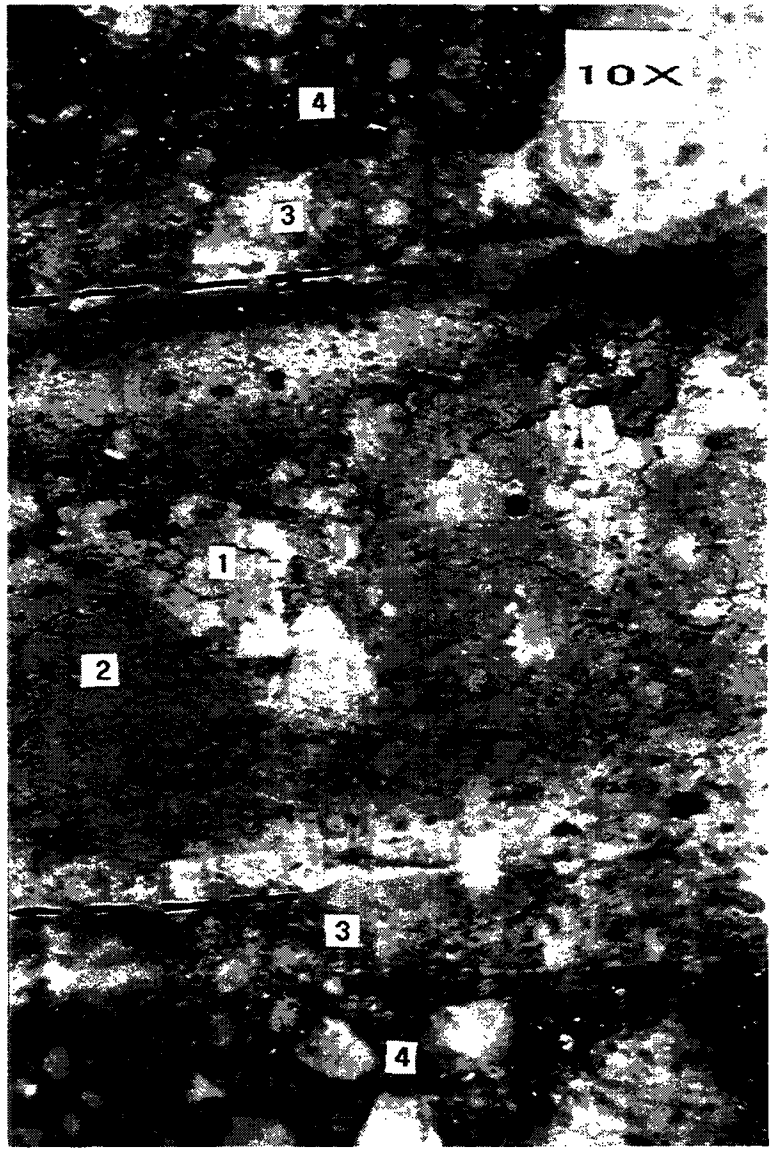

Along the thin edges of the anode, the alteration of the cement paste is somewhat less extensive (see Figure 5-60 and Figure 5-61). Here, the paste is characterized as moderately altered.

As shown in Figure 5-61, the moderately altered concrete near the anode surface grades abruptly into unaltered concrete.

EDS analyses were conducted on samples of the cement paste phase showing the various degrees of alteration. These results are shown in figures 5-62A to 5-62C. In unaltered concrete, located approximately 3 mm above the anode, the EDS spectrum is quite similar to that expected for "normal" hydrated portland cement paste. One exception is the presence of trace amounts of chlorine (Cl) in the overlay concrete.

In the heavily altered light-grey cement paste surrounding the islands of white/orange cement paste on the anode interface surface (see Figure 5-61), there has been a significant reduction in the level of calcium (Ca) bearing phases and a modest increase in the amount of iron (Fe), aluminum (Al), and potassium (K) bearing phases. Both sulfur (S) and chlorine (Cl) bearing phases are absent.

Figure 5-62A. **EDS Spectra (40X - 200X) of Superplasticized Dense Concrete in Contact with or Adjacent to the Anode Ribbon in Core 2 which show Various Degrees of Alteration.**

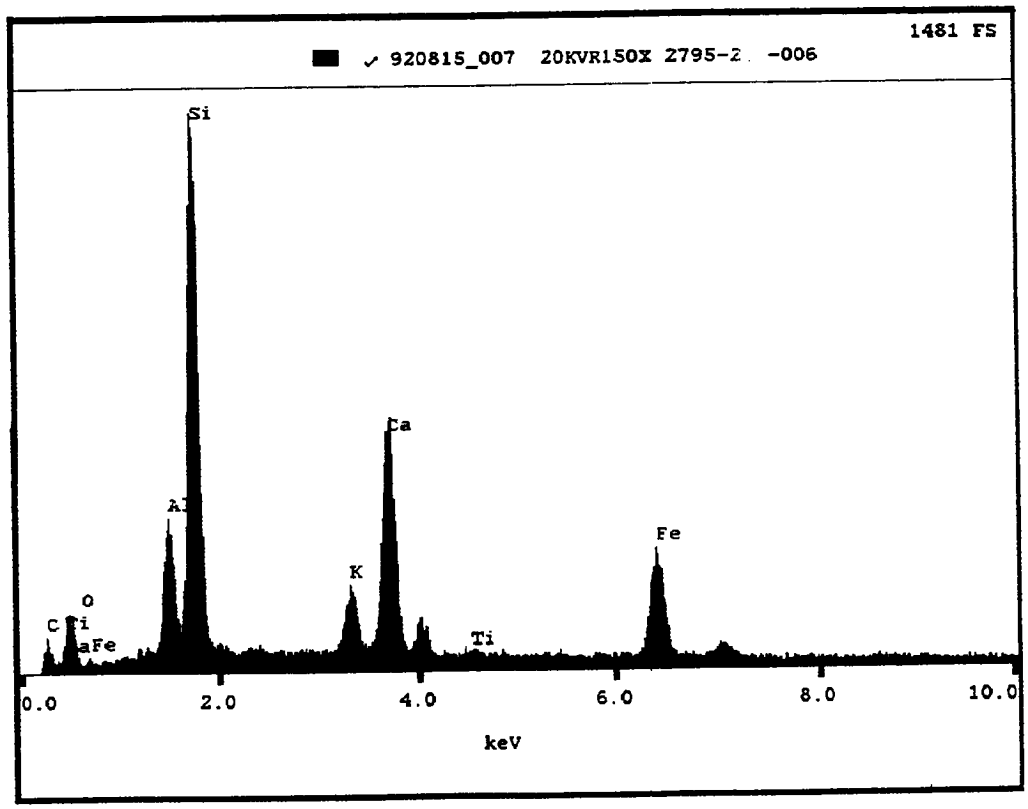

Figure 5-62B. **EDS Spectra (40X - 200X) of Superplasticized Dense Concrete in Contact with or Adjacent to the Anode Ribbon in Core 2 which show Various Degrees of Alteration.**

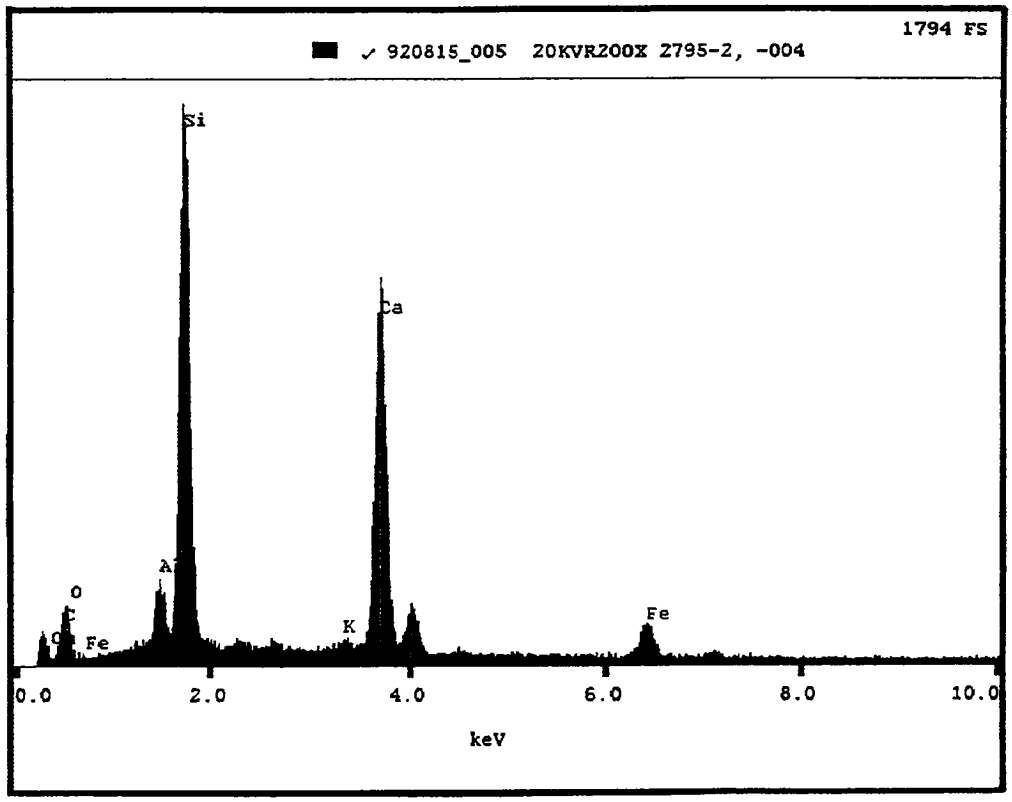

Figure 5-62C. **EDS Spectra (40X - 200X) of Superplasticized Dense Concrete in Contact with or Adjacent to the Anode Ribbon in Core 2 which show Various Degrees of Alteration.**

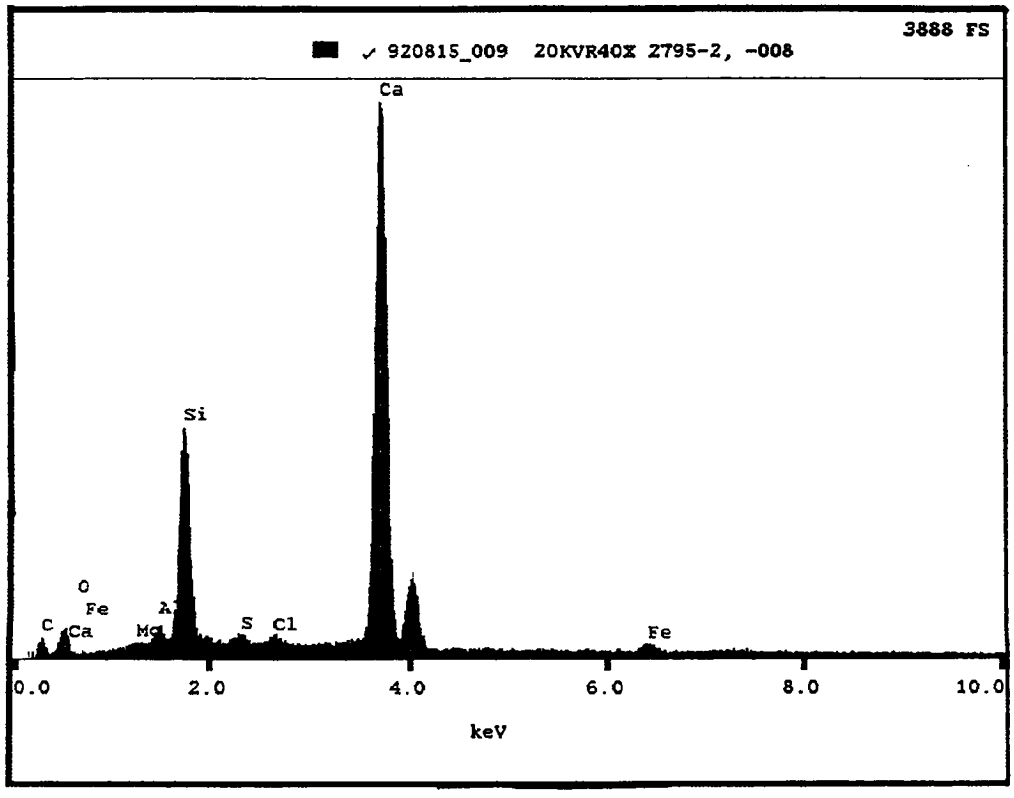

In the severely altered orange/white cement paste regions on the anode interface surface (see Figure 5-61), there is a further reduction in the level of calcium (Ca) bearing phases and a significant increase in the level of aluminum (Al), potassium (K), and iron (Fe) bearing phases. Within the altered orange/white paste regions, trace amounts of titanium (Ti) appear.

Limestone aggregate particles in close proximity to the large surface of the anode ribbon also have experienced softening.

Measurements of pH on the anode interface surfaces show values as low as 9. Along the top edge of the anode ribbon, the pH is typically 11 to 12.

Concrete adjacent to the thin edges of the anode show a minimal depth of alteration, less than 0.5 mm (20 mil). Along the sides of the anode ribbon, the depth of alteration varies from 1 to 2 mm (40 to 80 mil), see Figure 5-60.

Condition of the Anode Ribbon Following the 30 month cathodic protection treatment at 20 mA/ft^2 (215 mA/m^2), the anode ribbon has a mottled appearance although the surfaces remain smooth and there is virtually no pitting or loss of section (see Figure 5-63). The islands of iridescent color shown in Figure 5-63 may correspond to the islands of orange/white cement paste shown in Figure 5-61. The other surface of the ribbon anode shown in Figure 5-63 is considerably more uniform in color.

Figure 5-63. Condition of the Anode Ribbon Following the 30-Month Cathodic Protection Treatment at 20 mA/ft^2 (215 mA/m^2)

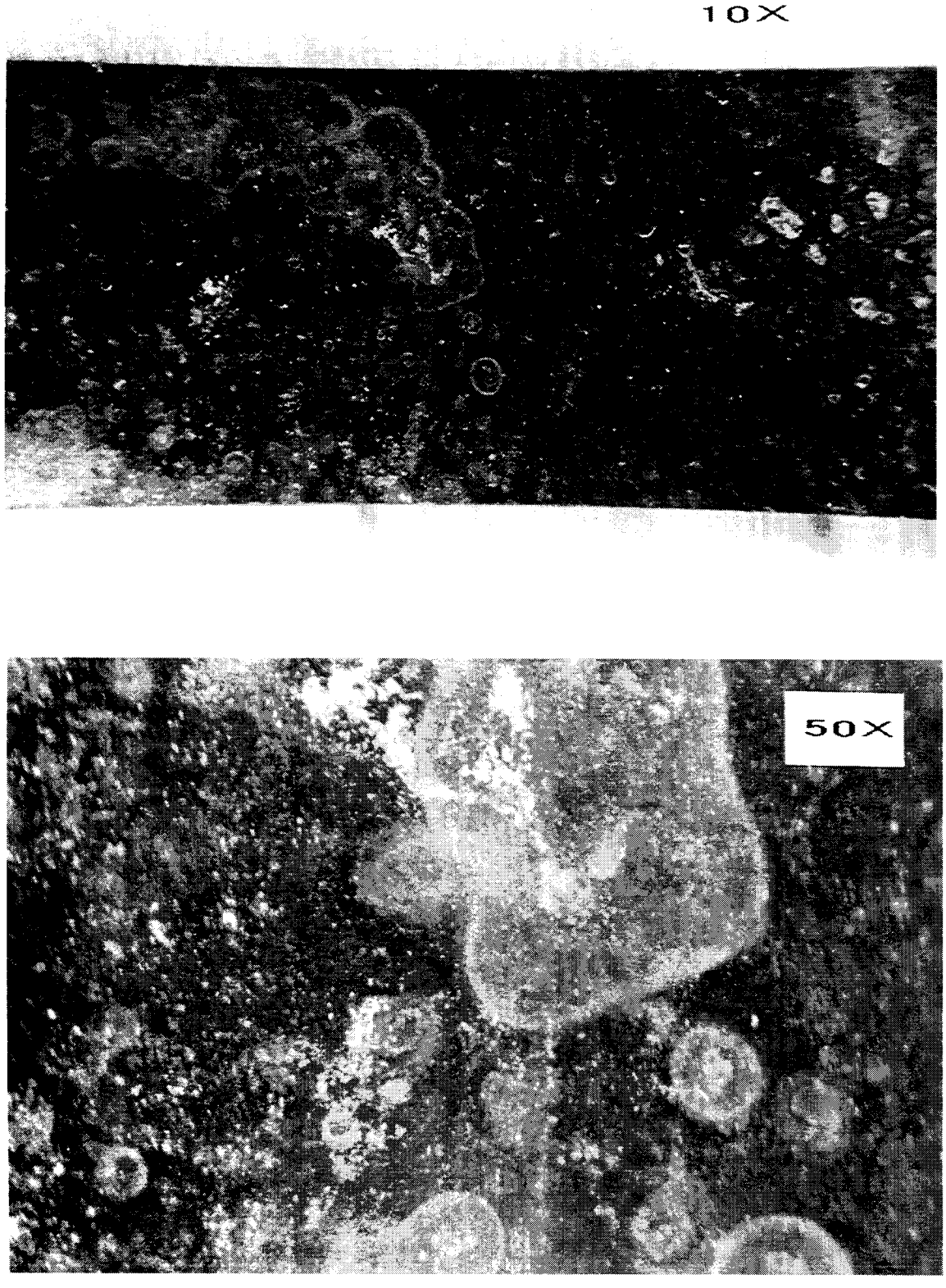

Alteration of the Base Slab Concrete in Contact With the Cathode (Top Rebar) There is virtually no effect of the cathodic protection treatment on the quality of the concrete surrounding the cathode (top rebar). Cement paste defining this interface has the same hardness as cement paste at lower levels in the core.

The pH of the concrete encapsulating the cathode is principally at the "normal" level of 12 to 13.

The base slab concrete lying between the anode ribbon and the cathode (top rebar) appears to be unaffected by the 30-month cathodic protection treatment. Intentional fracture of the concrete directly over the top rebar showed complete aggregate fracture and a pH of the entire section of concrete in the 12 to 13 range.

The cathode (top reinforcing steel) had virtually no corrosion and the cathode interface surface on the base slab concrete contained only slight traces of corrosion product (normal scale/rust-red oxides).

Ferex™ Wire Anode

The wire anode was used in Slab 6 which was operated at a current density of 20 mA/ft^2 (215 mA/m^2) for 30 months. Core 6 (taken from Slab 6) is shown in Figure 5-64 in the as-received condition. This core is composed of a 2 in. (5 cm) thickness of overlay concrete and a 5-3/4 in. (14.6 cm) thickness of the base slab concrete. Clear cover over the top reinforcing bar is 1-3/8 in. (3.5 cm) and 1-1/4 (3.2 cm) over the bottom reinforcing bar.

The wire anode is a 0.06 in. (1.5 mm) diameter copper wire surrounded by 0.33 in. (0.8 cm) diameter conductive polymer encapsulant. At this coring site, the wire anode was completely surrounded by the superplasticized, dense concrete. The anode was positioned about 1/8 in. (3.2 mm) above the overlay concrete/base slab concrete interface.

Initial Examination of Core 6 The following features were identified during the preliminary examination of the as-received core with the stereomicroscope (10X - 100X).

- There was no softening, discoloration or cracking of the base slab concrete surrounding the cathode (top reinforcing steel).
- There was softening in the wearing surface of the base slab concrete at locations which overlie the top reinforcing steel (cathode).
- The overlay concrete containing the wire anode was completely disbonded from the base slab.
- There was cracking in the overlay concrete emanating from points of contact with the anode.

Figure 5-64. Core 6 from Slab 6 Following the 30 Month Cathodic Protection Treatment at 20 mA/ft^2 (215 mA/m^2). The core was in two pieces with the separation occurring at and near the interface of the overlay concrete with the base slab concrete (Scale in Inches).

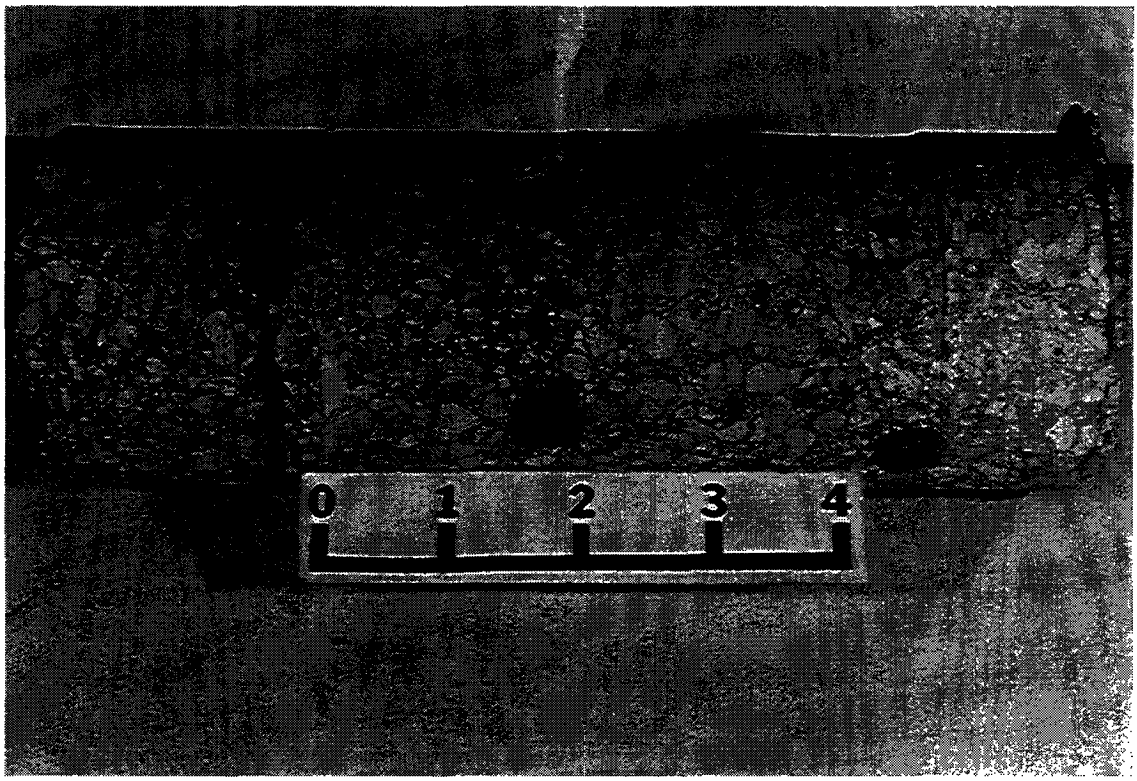

Characterization of Failure of the Bond Between the Overlay Concrete and the Base Slab Concrete In this core, the overlay concrete containing the wire anode completely delaminated from the base slab concrete during the cathodic protection treatment. The delamination fracture plane was 50 percent within the cement paste bonding grout and 50 percent in the superplasticized, dense concrete of the overlay (at the level of its contact with the anode). It is judged that this delamination was present at the time of coring.

Figure 5-65 shows the delaminated interface surface on the overlay concrete which occurred at the level of the wire anode. A significant amount of the overlay concrete on either side of the anode shows a red discoloration. EDS analysis of this discolored, existing fracture surface showed principally calcium (Ca). It is expected that moisture movement along this existing fracture surface would deposit calcium hydroxide from solution (subsequently converting to calcium carbonate.

Cracking in the overlay concrete emanating from the location of the wire anode (see Figure 5-64) strongly implicates the anode as playing a major role in the delamination of the overlay concrete.

Figure 5-65. Delaminated Overlay Concrete/Base Slab Concrete Interface Surface on the Overlay Concrete. About 50 percent of the delamination occurred within the overlay concrete (O) and 50 percent right at the interface (I) within the cement paste bonding grout. In the overlay concrete, the delamination fracture occurred right at the level of the Ferex™ wire anode (F).

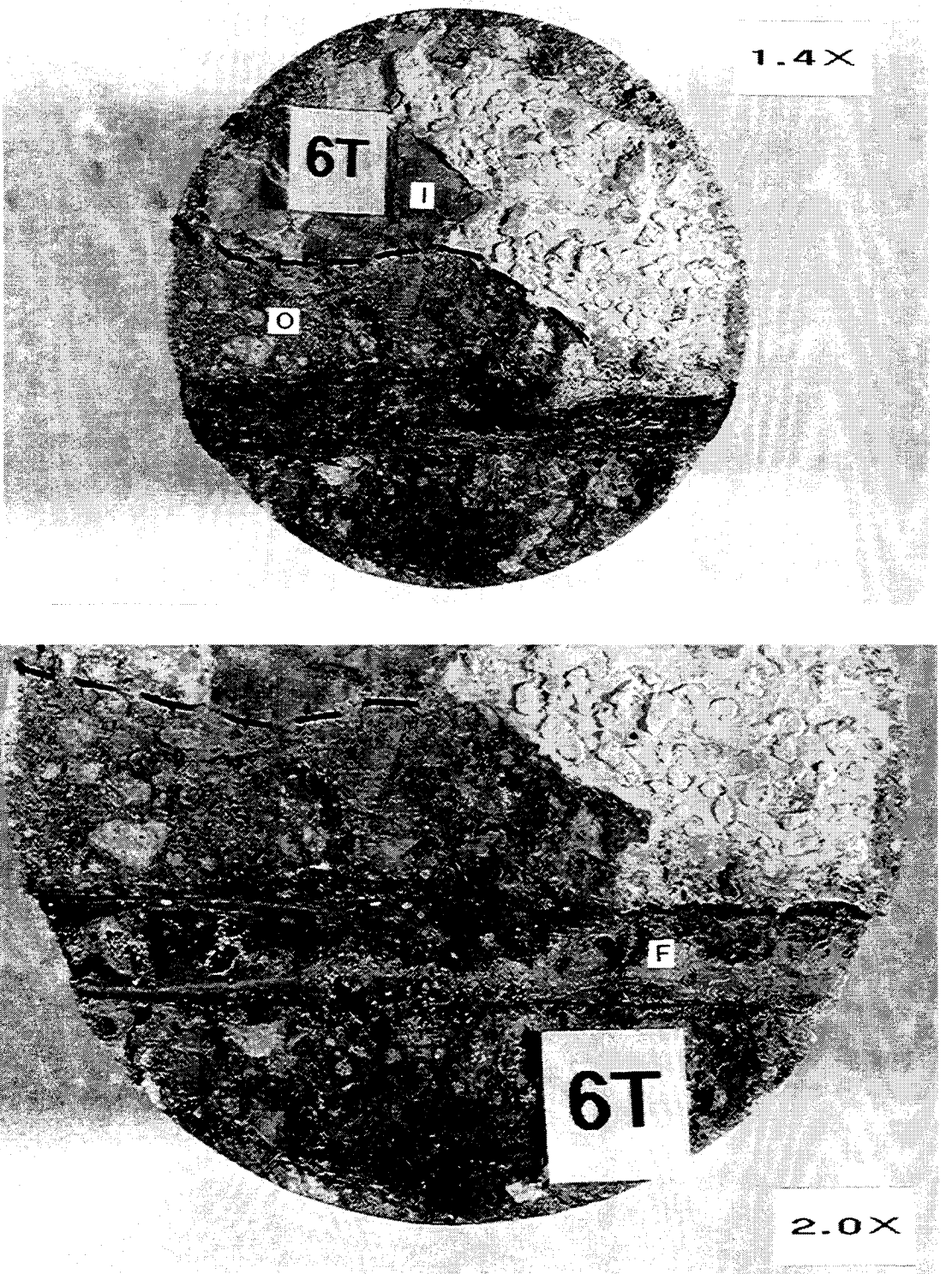

Alteration of the Superplasticized Dense Overlay Concrete at Points of Contact With the Wire Anode At this coring site, the wire anode was fully encapsulated by the overlay concrete at a distance of about 1/8 in. (3 mm) from the overlay concrete/slab concrete interface.

Overlay concrete surrounding the wire anode has been adversely affected by the cathodic protection treatment of 20 mA/ft^2 (215 mA/m^2) for 30 months. The effect is one of discoloration, softening, and cracking of the concrete contacting the anode.

Most of the overlay concrete interface surface with the anode is a thin, relatively hard black skin (see Figure 5-65). This thin skin can easily be punched through to reveal underlying regions of cement paste that were severely softened, orange to white in color, with pH values as low as 5. There were also isolated islands of very soft white paste that actually make up a portion of the anode interface surface with the concrete. These features can be seen in Figure 5-65. Figure 5-66 shows close-ups of the wire anode interface surface on the superplasticized, dense overlay concrete. EDS analyses were made of the softened, discolored concrete comprising and underlying the anode interface surface. This spectrum is shown in Figure 5-67.

The chemical species characterizing the severely altered cement paste in the concrete surrounding the wire anode differs significantly from the severely altered cement paste in the concrete surrounding the titanium mesh and ribbon anodes.

Figure 5-66. Enlarged (10X) Views of the Wire Anode Interface Surface on the Superplasticized, Dense Overlay Concrete. The black areas represent a hard, thin skin of cement paste that is easily broken through to reveal underlying regions (→) of cement paste that is severely softened, orange to white in color, with pH values as low as 5.

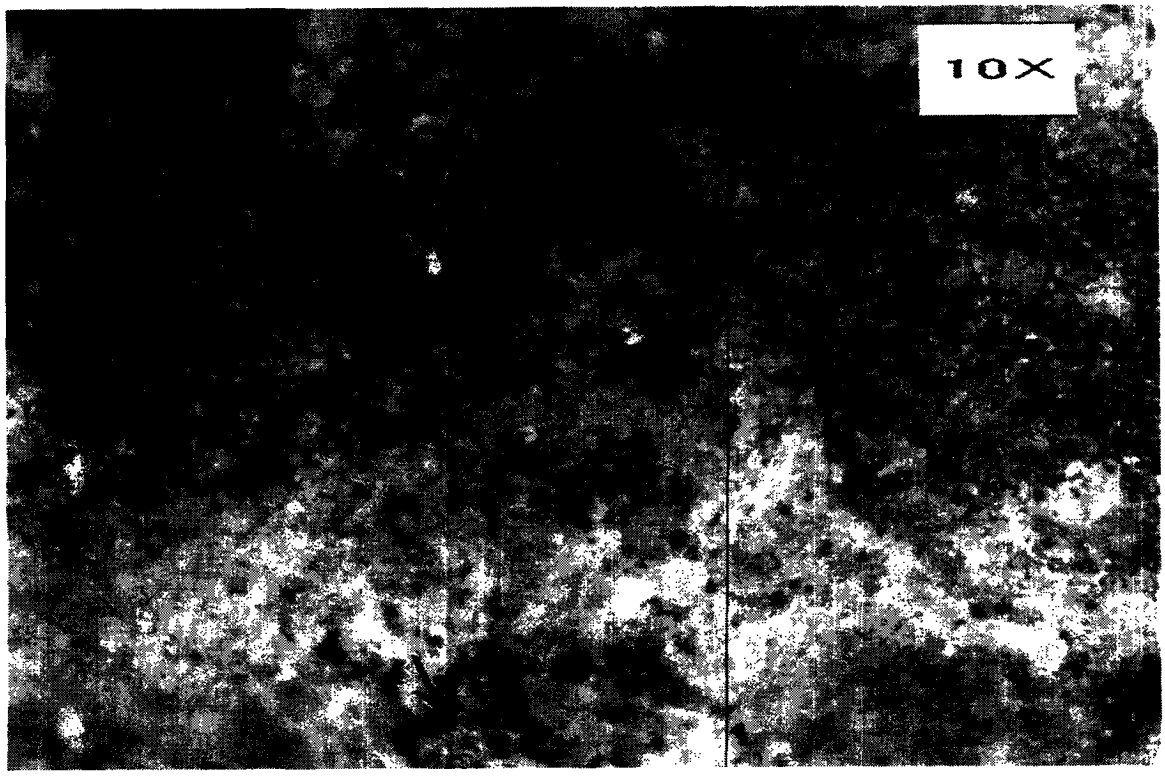

Figure 5-67. EDS Spectrum of Severely Altered Cement Paste Underlying the Ferex™ Wire Anode in the Overlay Concrete of Core 6.

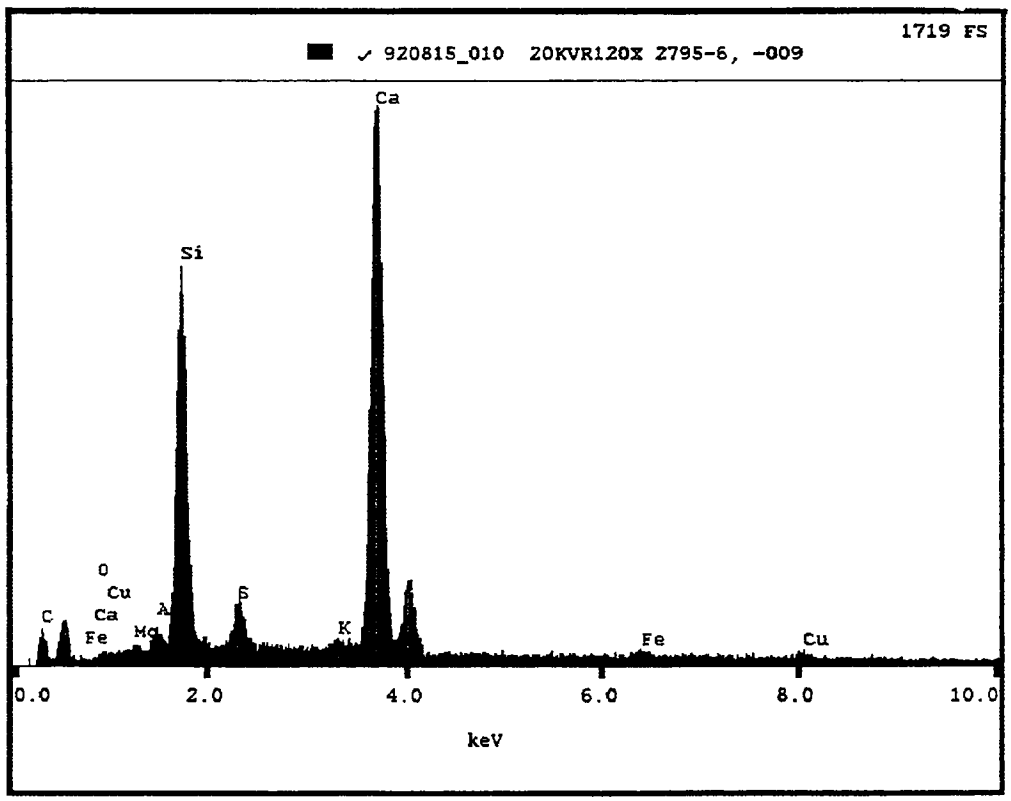

With the titanium anodes, concrete immediately adjacent to the anode showed a significant reduction in calcium (Ca) bearing phases and a significant increase in the levels of aluminum (Al), potassium (K), and iron (Fe) bearing phases.

Overlay concrete in contact with the wire anode shows calcium-bearing phases as the most abundant but the Ca/Si ratio is significantly lower than in "normal" concrete. Additionally, overlay concrete in contact with the showed relatively high levels of the sulfur-bearing phase although iron and aluminum-bearing phases are present at relatively normal levels. No chlorine (Cl) bearing phases were identified in any of the EDS work on samples taken from the overlay concrete in the region of the anode. Trace amounts of copper (Cu), undoubtedly derived from the anode, show up in concrete adjacent to the wire anode.

Limestone aggregate particles in the overlay concrete within 1 mm or 2 mm of the Wire anode also exhibit softening.

Condition of the Wire Anode Overall, the wire anode appears to have been relatively unaffected by the 30-month cathodic protection treatment at 20 mA/ft^2 (215 mA/m^2). However, it is evident that there has been some reaction between the anode surface and the surrounding concrete. The black skin formed on the concrete at the interface very likely was derived from the anode. Some copper (Cu) had migrated through the anode to the adjacent concrete. A considerable amount of altered cement paste remained adhered to the anode surface when it was intentionally removed from the overlay concrete.

Alteration of the Base Slab Concrete in Contact With the Cathode (Top Rebar) In Core 6, containing the wire anode, the top rebar showed a light to moderate amount of corrosion over 30 percent of its length. At one point, the corrosion products migrated into the concrete a distance of 1/2 in. (1.27 cm) from the rebar. Cement paste was well bonded to the rebar.

The base slab concrete in contact with the top rebar maintained a pH of 12 to 13 and showed no reduction in hardness or increase in porosity.

Figure 5-68 shows the overlay concrete/base slab concrete delaminated interface surface. The dashed lines in Figure 5-68 show the orientation of the top rebar which underlies the interface surface at a depth of 1-3/8 in. (3.49 cm). An interesting phenomenon was observed in Core 6 that was not seen in any of the other cores in this investigation. Over this entire area (between the dashed lines), the cement paste in the base slab concrete wearing surface was significantly softened to depths up to 1/8 in. (3 mm) below the base slab wearing surface elevation. With this exception, all of the base slab concrete lying between the anode and cathode has not been altered showing a pH value of 12 to 13 and normal hardness and porosity levels.

Figure 5-68. Plan View of Overlay/Slab Interface Surface on the Slab Concrete. The dashed lines show the orientation of the top rebar which lies 1-3/8 in. (3.49 cm) below the interface surface. There is deterioration of the cement paste in the base slab concrete wearing surface lying directly over the top rebar.

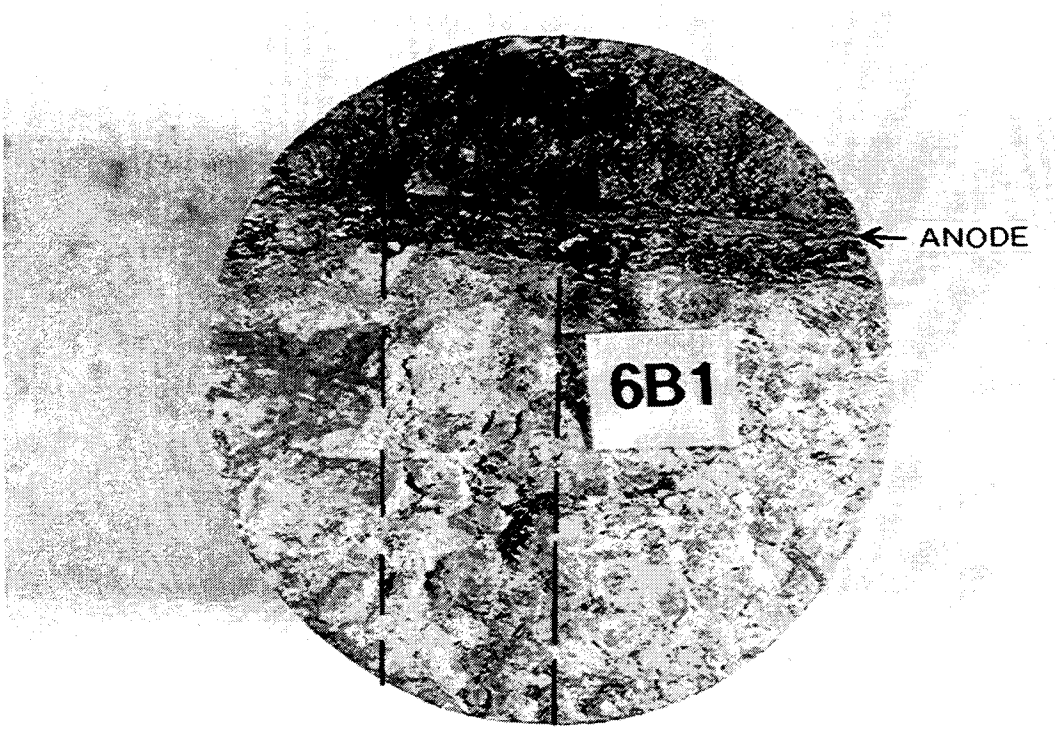

Carbon Conductive Polymer Anode

Slab 1, containing the conductive polymer anode, was operated for 30 months at 20 mA/ft^2 (215 mA/m^2). The conductive polymer anode was placed directly on the slab wearing surface as strips 2 in. to 3 in. (5.08-7.62 cm) wide (one longitudinal, 3 transverse). Platinum wire served as the primary anode and carbon fiber as the secondary anode.

Core 1 (taken from Slab 1) is shown in Figure 5-69 in the as-cored condition. The core consisted of the 5-3/4 in. (14.61 cm) thick base slab concrete and a 2-1/2 in. (6.35 cm) thickness of the overlay concrete. The mounded conductive polymer anode was about 1 in. thick (maximum) and 2-1/4 in. (5.72 cm) wide on this core. Core 1 was cored in two pieces with a delamination occurring at the overlay/base slab interface.

Initial Examination of Core 1 Preliminary examination of the as-received core yielded the following information:

- The base slab concrete surrounding the cathode (top reinforcing steel) showed no obvious softening, discoloration, or cracking.
- The overlay concrete was completely disbonded from the base slab concrete in this core.
- It appears that a good bond persisted between the anode material and the overlay concrete.

Figure 5-69. Core 1 from Slab 1 Following 30 Month Cathodic Protection Treatment at 20 mA/ft^2 (215 mA/m^2). The anode is conductive carbon polymer. The overlay is delaminated from the base slab (Scale in Inches).

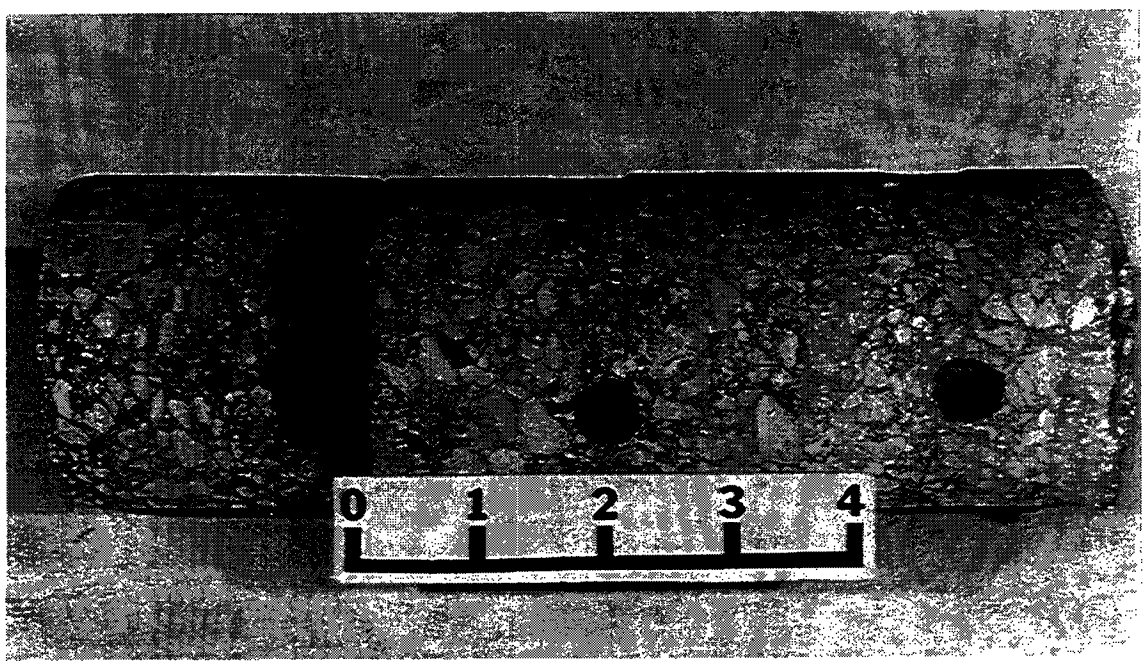

Bond Failure Between the Overlay Concrete and the Base Slab Concrete In Core 1, taken through the conductive polymer anode, delamination occurred at the interface between the overlay concrete and the base slab concrete. At this coring site, the anode covered about 80 percent of the wearing surface of the slab. For the other 20 percent, the overlay concrete was in contact with the slab concrete, with a thin interface layer of cement paste grout. It is judged that the overlay was disbonded from the concrete slab at the time of coring.

The overlay/base slab interface surfaces are shown in Figure 5-70. Sample 1B is the base concrete slab interface surface and Sample 1T is the overlay concrete interface surface. The area covered by the anode is delineated in Figure 5-70.

The actual disbonding at this interface occurred about 50 percent in the cement paste bonding layer of the slab concrete and 50 percent in the anode material (within 1 mm of its contact with the slab concrete).

Characterization of the Base Slab Concrete Interface With the Anode Both the cement paste and the limestone aggregate in the base slab concrete in contact with the conductive polymer anode have been altered by the 30-month cathodic protection treatment at 20 mA/ft^2 (215 mA/m^2). This effect is a moderate to severe softening of the cement paste phase and a moderate softening of the aggregate particles to a depth of 1 mm to 3 mm from the point of contact with the anode.

Figure 5-70. Delaminated Interface Surfaces Between the Overlay Concrete (1T) and the Base Slab Concrete (1B). Zone (X) is the original base slab concrete wearing surface not covered by the anode. In Zone (Y), the covering layer of cement paste has been removed revealing coarse limestone aggregate particles on (1B). In Zone (Z), the cement paste on the base slab (1B) is still intact.

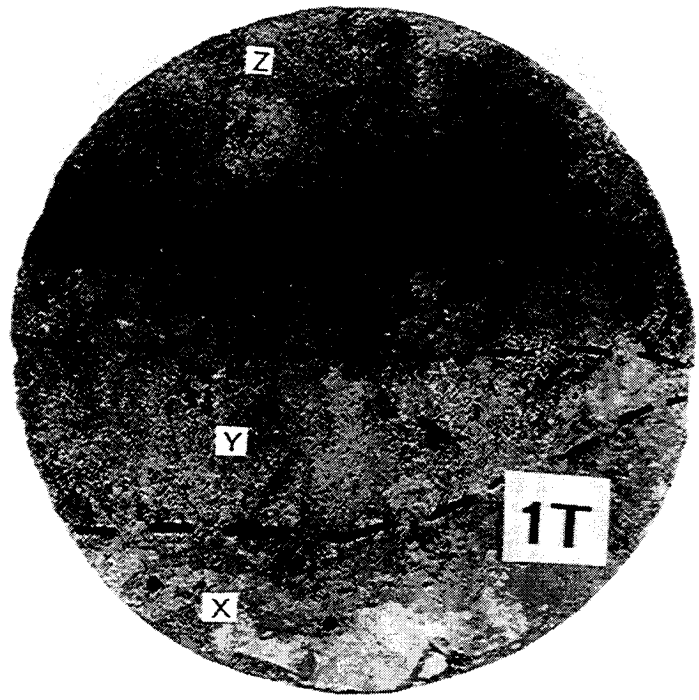

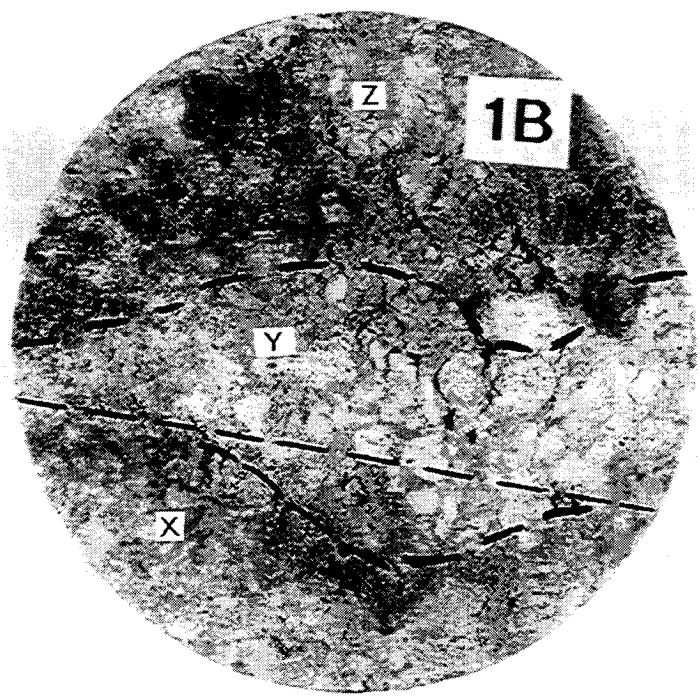

The pH of the slab concrete interface with the anode was measured on fresh fracture surfaces. In the top 1/2 in. (1.27 cm) thickness of the slab concrete wearing surface under the anode, the pH varies from 7 to 10. The lowest pH value is in the top 1 mm to 2 mm thickness of the wearing surface.

Figure 5-70 (1B) shows the overlay/base slab interface surface on the base slab concrete. Zone (X) is the original concrete wearing surface not covered by the anode. In Zone (Y), the covering layer of cement paste has been removed, revealing coarse limestone aggregate particles. In Zone (Z), the cement paste is still intact but is characterized as a very thin, hard skin which can be easily probed to reveal underlying very soft cement paste (similar to the condition observed with the Ferex™ Wire anode).

SEM/EDS examinations were made of the various features just described on the interface surface of Sample 1B (Figure 5-69).

Zone (X) Sample 1B This is the portion of the base slab concrete not in contact with the conductive polymer anode. Figure 5-71 shows the EDS spectrum and the microstructure of the base slab concrete in Zone (X) at a point about 0.05 in. (1.3 mm) below the actual wearing surface. The type and amount of elemental chemical species at this site are relatively "normal" except for slightly higher levels of potassium (K) and sulfur (S). When the actual wearing surface in Zone (X) is examined, the EDS spectrum looks similar to Figure 5-71 except that sulfur (S) and potassium (K) are present in only trace amounts. Chlorine (Cl) was not observed in the EDS spectrum at either site in Zone (X).

The microstructure of the Zone (X) concrete (Figure 5-71) is grainy, showing slight relief and very little porosity.

Figure 5-71. EDS Spectrum (60X) and Microstructure (1000X) of Zone X (Figure 5-70) on the Wearing Surface of the Base Slab in Core 1.

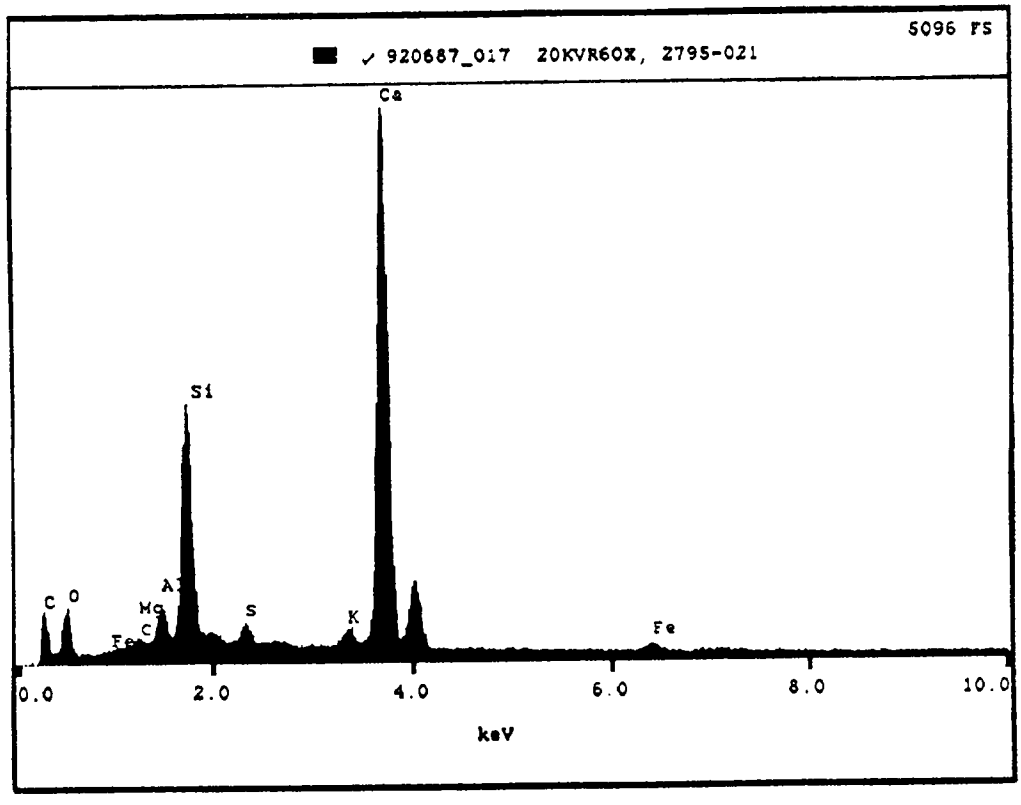

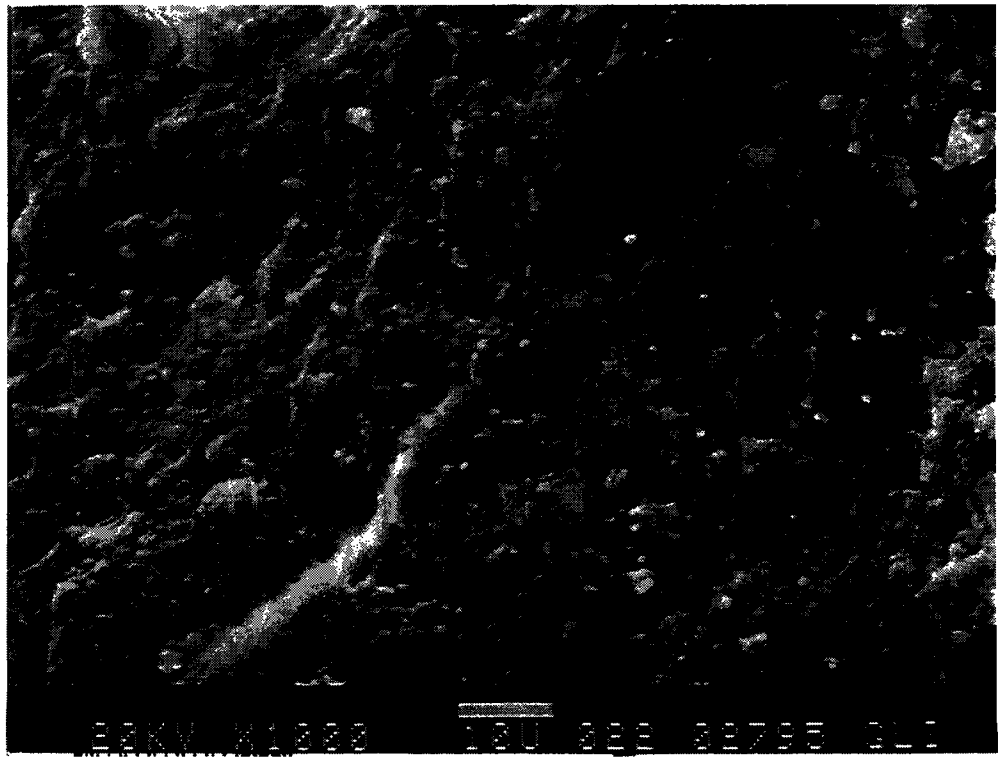

Zone (Y) and Zone (Z) Sample 1B These zones of the interface surface on Sample 1B (Figure 5-70) represent the area on the base slab wearing surface directly under the anode. In Zone (Y), the cement paste is missing, revealing limestone coarse aggregate particles. In Zone (Z), the cement paste remains intact but has been discolored by contact with the anode.

SEM/EDS analyses of Zones (Y) and (Z) show that the chemistry of the concrete under the anode is variable. At some locations, the type and amount of elemental species is similar to "normal" hydrated portland cement paste. At other locations, especially in Zone (Z), there is a significant reduction in calcium (Ca) bearing phases and significant increases in the levels of iron (Fe), aluminum (Al), and potassium (K) bearing phases. Additionally, chlorine (Cl) is relatively high at many of the sampling sites in Zones (Y) and (Z). Figure 5-72 shows these features at one of the sampling sites in Zone (Z).

Characterization of the Conductive Polymer Anode and the Anode Interface With the Overlay Concrete This interface surface is shown in Figure 5-70 (Sample 1T). Zone (X) is the superplasticized, dense concrete overlay. Zones (Y) and (Z) represent the actual bottom surface of the conductive polymer anode. The imprint made by the carbon strand (secondary anode) can also be seen.

The conductive anode mound was roughly semi-elliptical in cross-section and was about 1 in. (2.54 cm) thick at its thickest point. At this coring site, the polymer was not fully consolidated, showing a significant amount of fine porosity (less than 0.1 mm) and a slight amount of relatively coarse porosity up to 3 mm (typical of honeycomb structure). Where the anode material has been fully consolidated, it appears monolithic to the unaided eye, black in color, and is relatively hard (not easily scratched with a knife blade). No cracking was observed within the anode material itself.

In this core, a good bond persists between the polymer anode material and the overlay concrete. In general, the overlay concrete surrounding the anode appears to be relatively unaffected by the cathodic protection treatment. However, along the thin edges of the anode strip, the cement paste phase of the concrete contacting the anode is moderately softer than in concrete that has been unaffected.

Figure 5-72. EDS Spectrum (40X) of Cement Paste Comprising a Portion of Zone (Z) in Core Sample 1B (Figure 5-70).

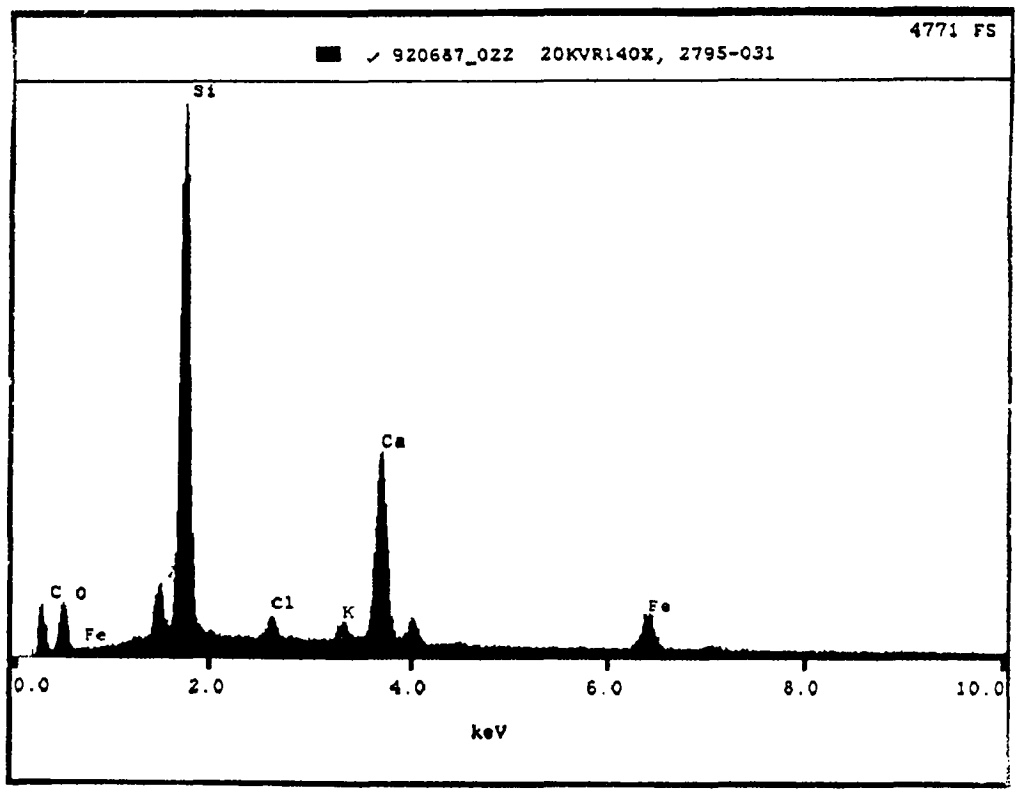

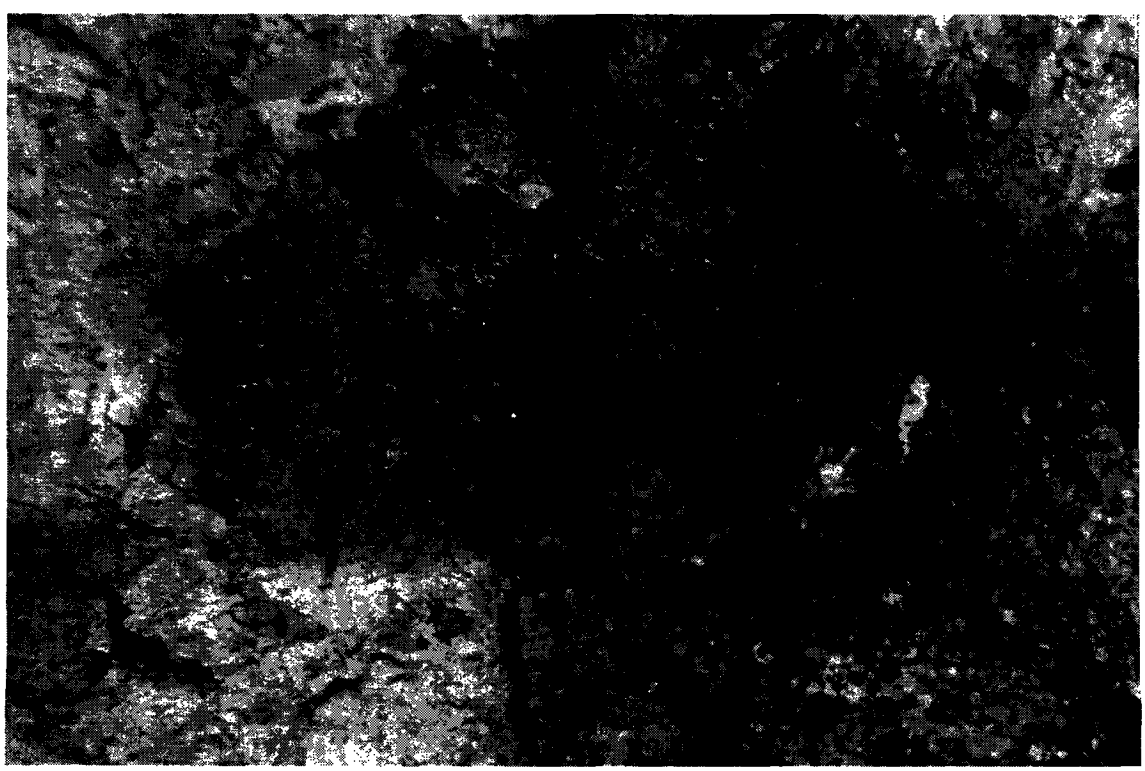

As can be seen in Figure 5-69, there is a thin band of white color near the interface between the anode and the overlay concrete. This white color is caused by cementitious materials that were present in the porosity of the anode. This migration of cementitious materials into the anode pore spaces very likely took place before the overlay concrete had achieved initial set. This migration of cementitious materials into the conductive polymer anode occurred on all of the free anode surfaces to a depth of 0.08 in. to 0.20 in. (2 mm to 5 mm) from the anode/overlay concrete interface.

SEM/EDS analyses were conducted on the anode material - both on existing surfaces and on fresh fracture surfaces. Figure 5-73 shows the EDS spectrum and the microstructure of the bottom surface of the conductive polymer anode in contact with the wearing surface of the base slab. Of particular interest is the very high chlorine (Cl) level and the high sulfur (S) level. The high silicon (Si) level is partially due to the fact that a number of the rounded nodules encapsulated in the matrix are silica particles. The matrix material at Sites 1-2 and 3-4 show chlorine (Cl) as the most abundant elemental species.

Figure 5-74 is the EDS spectrum and microstructure of a fresh fracture surface of the conductive polymer anode at a point 0.2 in. (5 mm) from the anode interface with the base slab wearing surface. The polymer anode has been completely infiltrated at this point with extremely high levels of chlorine (Cl) and moderately high levels of sulfur (S). The intrusion of these species appears to have had no significant detrimental effect on the integrity of the anode. This condition of high levels of chlorine (Cl) and sulfur (S) prevailed throughout the conductive polymer anode at this coring site.

Figure 5-73. EDS Spectrum (20X) and Microstructure (120X) of the Existing Contact Surface on the Conductive Polymer Anode (Figure 5-70 - Sample 1T) Where it Separated from the Base Slab Concrete Wearing Surface. This sampling site is near the carbon strand slot in Zone (Z - Sample 1T - Figure 5-70).

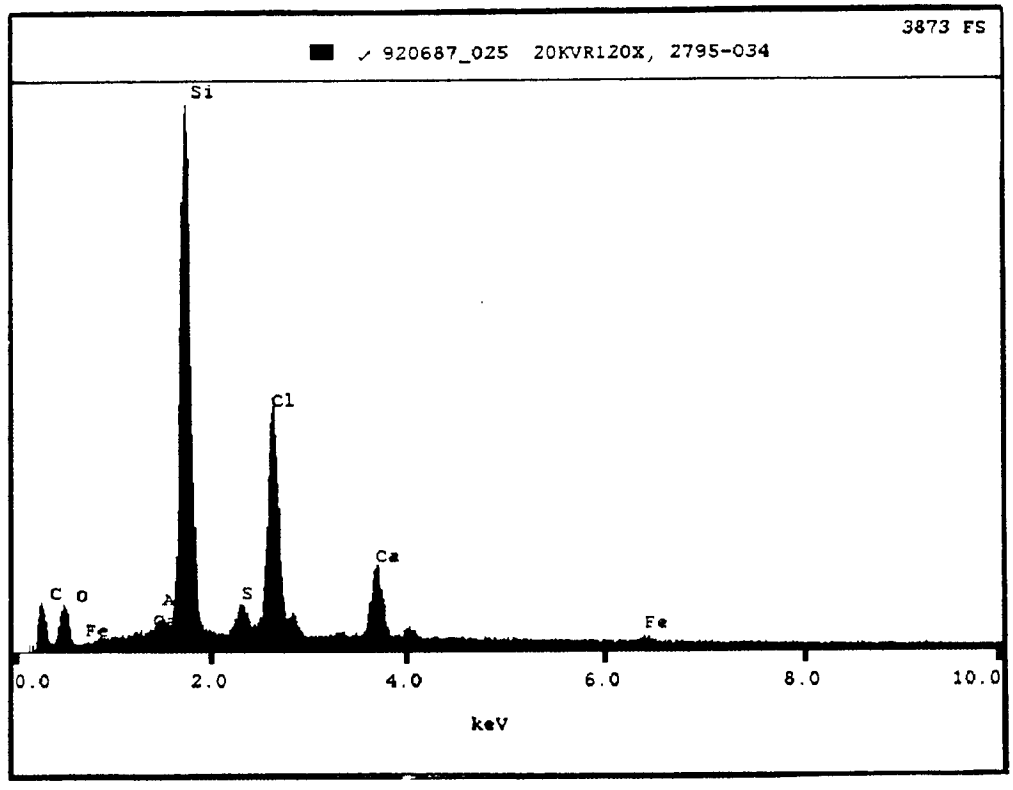

Figure 5-74. EDS Spectrum (60X) and Microstructure (70X) on a Fresh Fracture Surface of the Conductive Polymer Anode at a Point 0.2 in. (5 mm) from the Anode/Base Slab Concrete Interface Surface.

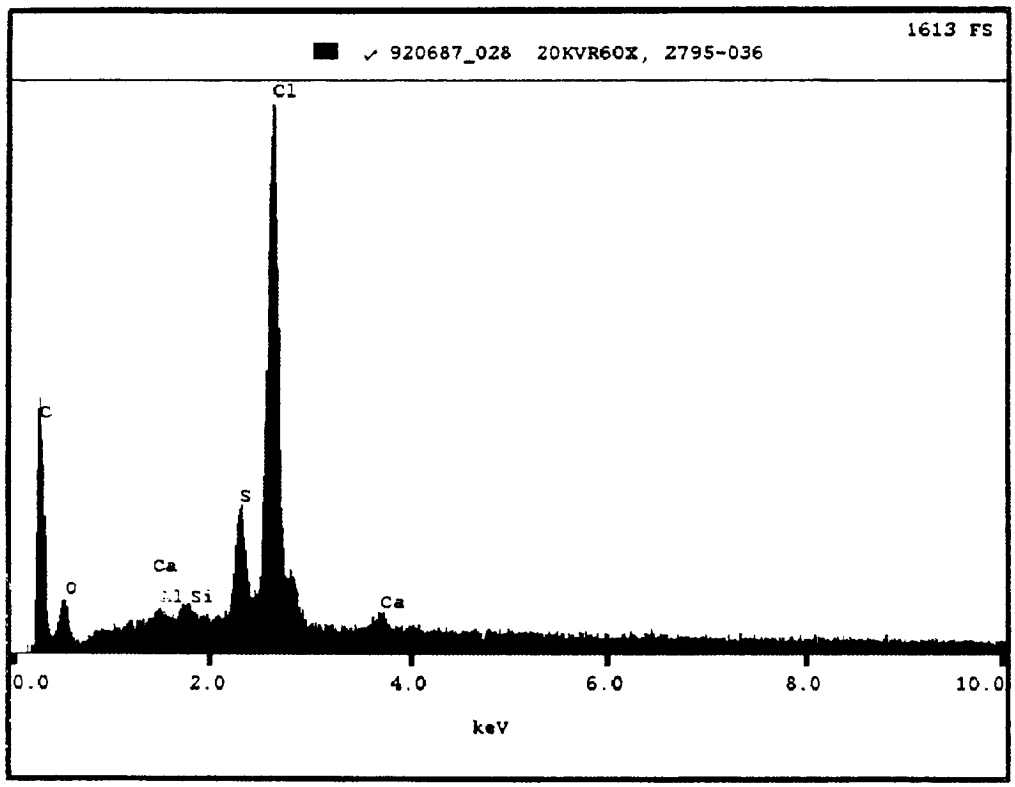

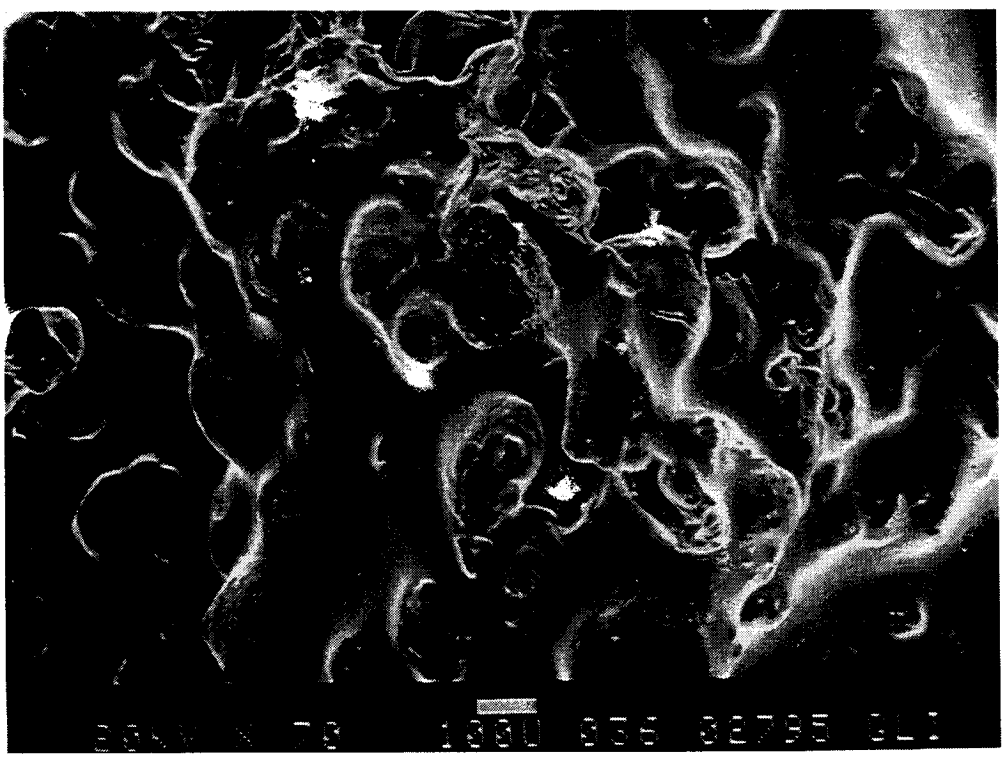

Condition of the Base Slab Concrete Between the Anode and Cathode The concrete surrounding the top rebar (cathode) in Core 1 was judged to be unaffected by the 30-month cathodic protection treatment at 20 mA/ft^2 (215 mA/ft^2). Cement paste defining the concrete/rebar interface shows the same hardness as the cement paste in other parts of the core at depths below the top rebar.

When the base slab concrete portion of this core was destructively examined, the bottom reinforcing bar pulled cleanly from the concrete with only trace amounts of iron oxides and scale remaining on the concrete. When the top reinforcing bar was destructively removed, the bar adhered firmly to the cement paste and pulled more of the paste from the concrete surface. Additionally, more scale and oxides remained on the concrete interface surface relative to the bottom bar. The oxide scale associated with the top bar was black relative to the rust-red color of the oxides on the bottom bar. At three sites along the top bar interface with the concrete, large air voids (>1 mm) were present in the concrete. These air voids were virtually filled with deposits of black iron (Fe) oxides. All of these features confirm that the top bar did experience a period of active corrosion at this coring site.

The majority of the concrete interface with the cathode showed a pH in the range of 12 to 13. EDS spectra of the slab concrete/steel rebar interface surfaces were very similar for the top and bottom rebar in Core 1. Both spectra were typical of "normal" hydrated portland cement paste with the exception that trace amounts of chlorine (Cl) were present in the spectrum of the concrete contacting the top bar. The potassium (K) level in the concrete contacting the top bar did not exceed that of the concrete contacting the bottom bar.

SEM/EDS examinations were also carried out on the base slab concrete positioned directly between the cathode (top rebar) and the conductive polymer anode (about a 1-3/8 in. [3.49 cm] thickness). The chemistry of the concrete lying between the cathode and anode is somewhat complicated as shown in figures 5-75A to 5-75E. The figures show EDS spectra on fracture surfaces at various levels in this concrete interval (and including one elevation below the top bar [3 in. (7.62 cm) below the wearing surface]). Potassium (K) levels are highest around 0.3 in. (0.76 cm) below the wearing surface and virtually disappear above this level. Chlorine (Cl) is relatively high at 0.2 in. (0.51 cm) below the wearing surface and does not show up again until depths of 1.5 in. (3.81 cm) below the wearing surface. Sulfur (S) is not present in the interval from 0.3 to 0.5 in. (0.76- 1.27 cm) below the wearing surface.

Figure 5-75A. **EDS Spectra (60X) on Fresh Fracture Surfaces of the Base Slab Concrete at Various Depths Below the Base Swearing Surface Directly under the Conductive Polymer Anode.**

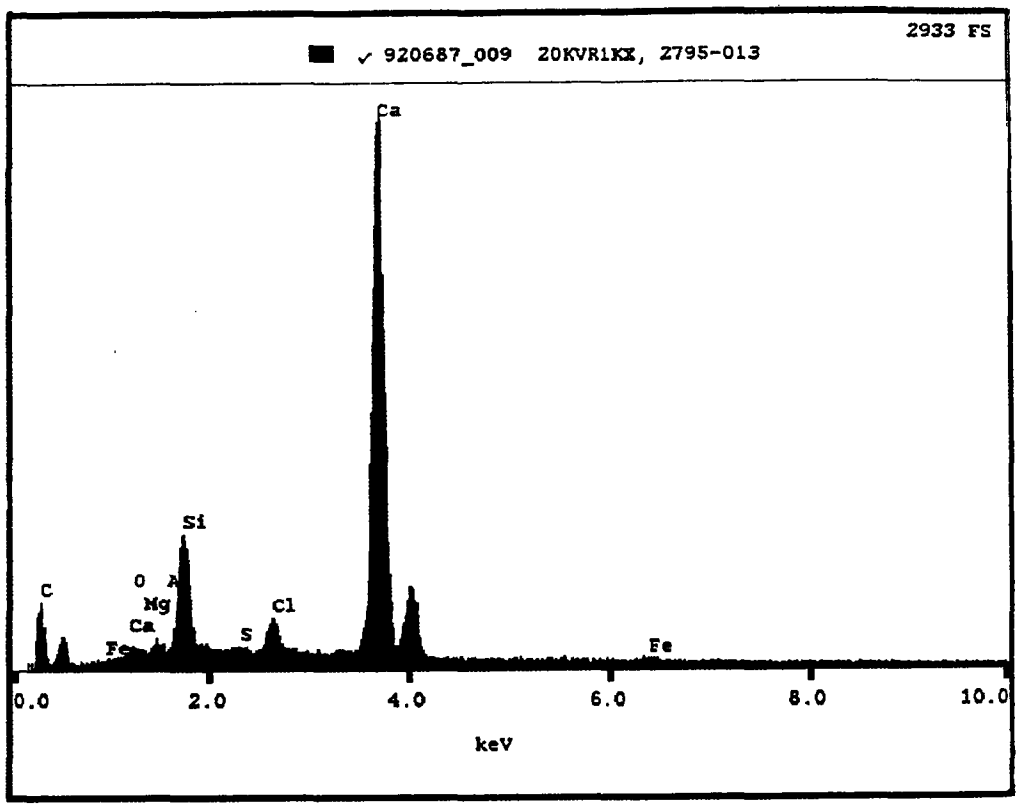

Figure 5-75B. **EDS Spectra (60X) on Fresh Fracture Surfaces of the Base Slab Concrete at Various Depths Below the Base Swearing Surface Directly under the Conductive Polymer Anode.**

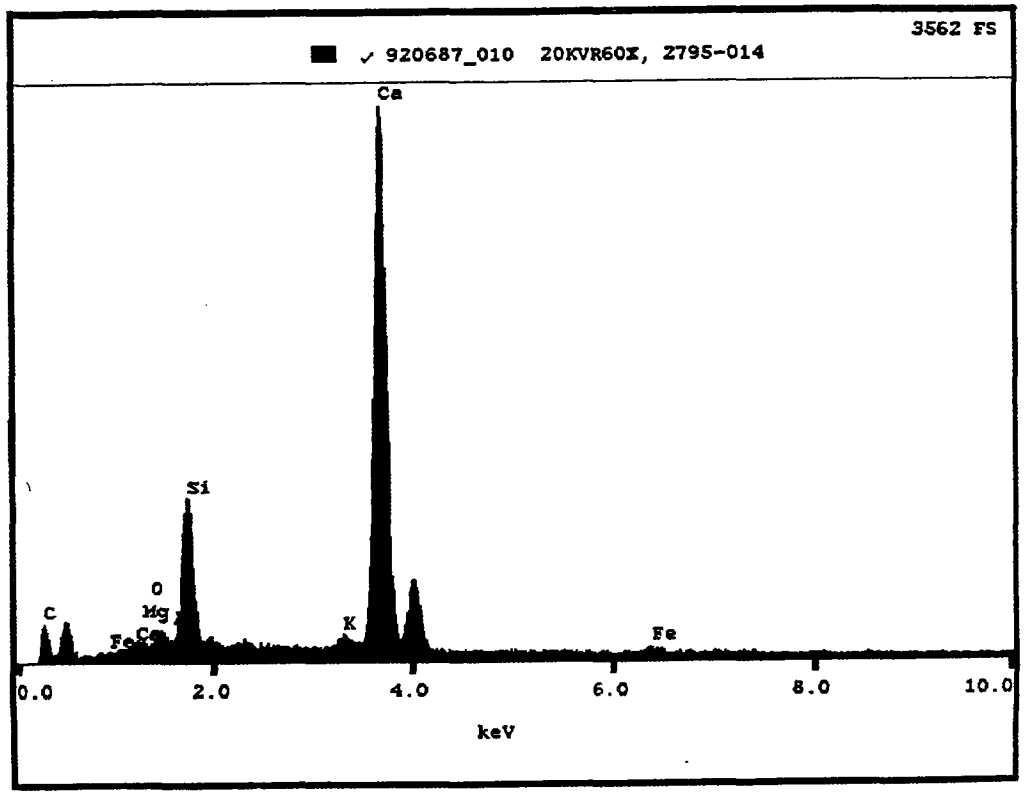

Figure 5-75C. **EDS Spectra (60X) on Fresh Fracture Surfaces of the Base Slab Concrete at Various Depths Below the Base Swearing Surface Directly under the Conductive Polymer Anode.**

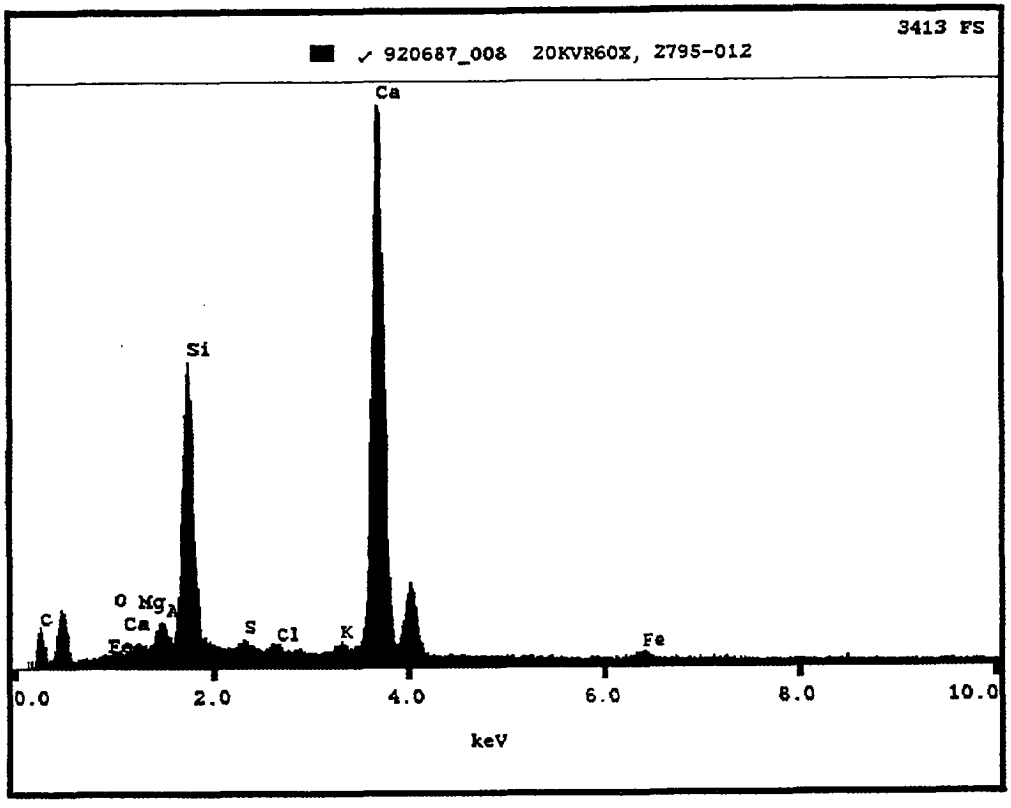

Figure 5-75D. **EDS Spectra (60X) on Fresh Fracture Surfaces of the Base Slab Concrete at Various Depths Below the Base Swearing Surface Directly under the Conductive Polymer Anode.**

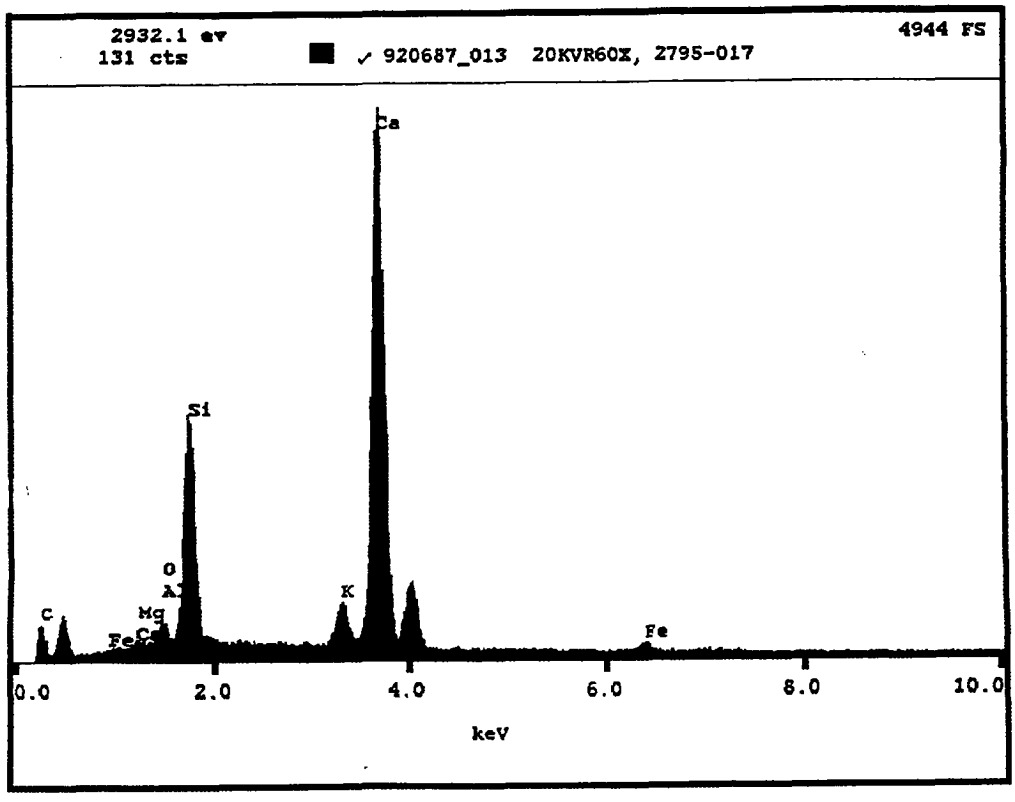

Figure 5-75E. **EDS Spectra (60X) on Fresh Fracture Surfaces of the Base Slab Concrete at Various Depths Below the Base Swearing Surface Directly under the Conductive Polymer Anode.**

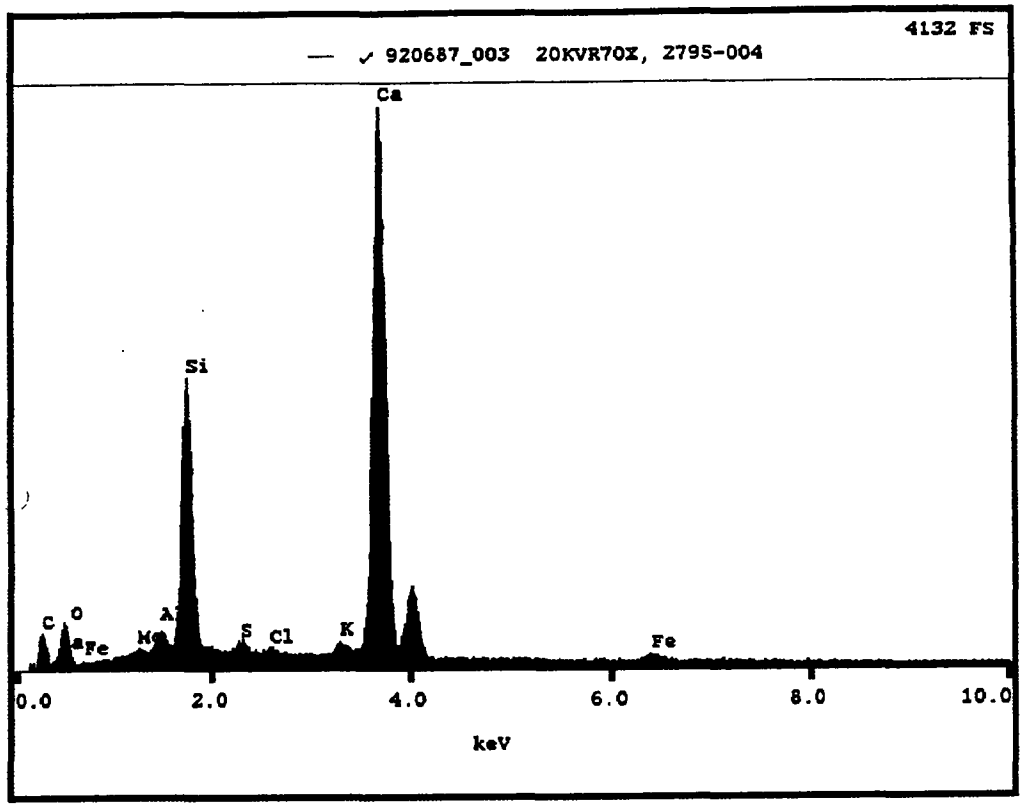

Examination of the microstructures at these elevations indicate that some chemical attack (dissolution) of the hydrated cement paste phases had occurred to depths somewhere between 0.3 in. and 0.5 in. (0.76 and 1.27 cm) below the wearing surface. Measurements of pH made on fresh fracture surfaces of the base slab concrete lying between the top rebar (cathode) and the anode showed values as low as 7 at depths up to 0.5 in. (1.27 cm) from the anode and 9 to 11 at depths up to 3/4 in. (1.91 cm) below the wearing surface. From 3/4 in. (1.91 cm) to the top of the cathode (1-3/8 in. [3.49 cm] below the wearing surface), the concrete pH is at a normal level of 12 to 13.

Chloride Analyses Results

Total chloride ion content measurements were made on samples taken from various levels of the six cores (AASHTO T260-82). Table 5-21 lists the results for Core 1, Table 5-22 lists the results for Core 2, and Table 5-23 lists the results for Cores 3, 4, and 5.

Table 5-21. Core 1 Chloride Analysis: Conductive Polymer Anode at 20 mA/ft^2 (215 mA/ft^2)

Sample Number	Sample Location	%Cl-(a)	#Cl$^-$/yd^3(b)
1-1	Composite sample of the conductive polymer anode	0.058	1.57*
1-2	Slab concrete - Composite of first 1-1/4 in. of concrete over the top rebar (cathode)	0.103	4.03
1-3	Slab concrete: 1/8 in. thickness of concrete directly over the top rebar (cathode)	0.178	6.97
1-4	Slab concrete: 1-1/4 in. of concrete under the top rebar (cathode)	0.150	5.87

Table 5-22. Core 2 Chloride Analysis: ELGARD™ Ribbon Anode at 20 mA/ft² (215 mA/ft²)

Sample Number	Sample Location	%Cl⁻(a)	#Cl⁻/yd³(b)
2-1	Overlay concrete - 1/4 in. thickness of overlay concrete encapsulating the ribbon anode	0.218	8.53
2-2	Slab concrete - Composite sample representing 0 to 1 in. depths below the wearing surface directly over the top rebar	0.265	10.37
2-3	Slab concrete - Composite sample representing 1 in. to 2 in. level below wearing surface directly over top rebar	0.298	11.67
2-4	Slab concrete - Composite sample representing 1 in. below the top rebar	0.216	8.46

(a) Based on dry concrete weight
(b) Based on a concrete unit weight of 145.0 lb/ft3

The same three sampling levels were used on all three of these cores. They included:

- Sampling site in the overlay concrete
- In the base slab concrete representing the 7/8 in. (22 mm) thickness of concrete directly under the slab wearing surface.
- In the base slab concrete in concrete directly over the top rebar (cathode) in all cases

The results are listed in Table 5-23.

Table 5-23. Cores 3, 4, and 5 Chloride Analysis: ELGARD™ Mesh 210 Anode

Core No.	Current Density mA/ft²	mA/m²	Sampling Site[a]	%Cl⁻[b]	#Cl⁻/yd³[c]
3	40	430	1	0.144	5.64
3	40	430	2	0.136	5.32
3	40	430	3	0.116	4.54
4	20	215	1	0.211	8.26
4	20	215	2	0.167	6.54
4	20	215	3	0.155	6.07
5	10	107	1	0.222	8.69
5	10	107	2	0.207	8.10
5	10	107	3	0.211	8.26

(a) Sampling Site 1 is the 1/2 inch thickness of overlay concrete directly above the interface between the overlay concrete and the slab wearing surface. Sampling Site 2 is a composite sample from the base concrete slab representing the 7/8 inch thickness of concrete directly under the slab wearing surface. Sampling Site 3 is a composite sample of the 7/8 inch thickness of concrete directly over the top rebar. All three samples were taken in the same vertical plane.

(b) Based on dry concrete weight

(c) Based on a concrete unit weight of 145.0 lb/ft³

For Core 6 the total chloride ion content was measured at the same sampling sites used for Cores 3, 4, and 5. The results are listed in Table 5-24.

Table 5-24. Core 6 Chloride Analyses: Ferex 100 Anode at 20 mA/ft² (215 mA/m²)

Sample Number	Sample Location	%Cl-(a)	#Cl⁻/yd³(b)
6-1	Overlay concrete - 1/2 in. thickness above the base slab concrete	0.085	3.33
6-2	Slab concrete - Composite sample representing 7/8 in. thickness under slab wearing surface	0.113	4.42
6-3	Slab concrete - Composite sample representing 7/8 in. thickness over rebar	0.141	5.52

(a) Based on dry concrete weight
(b) Based on a concrete unit weight of 145.0 lb/ft3

Summary As discussed earlier in the report, it was the intent to provide 15 lb Cl^-/yd^3 (9 kg/m^3) in the top 2-1/2 in. (6.4 cm) thickness of the 6 in. (15 cm) thick slabs. The chloride ion content results obtained here on the six cores show that this level of chloride ion content was not achieved. In fact, the chloride ion content varies from slab to slab and appears to be closer to a value to 6 to 8 lb Cl^-/yd^3 (3.6 to 4.8 kg/m). However, the average chloride ion content is considerably higher in the top 2 in. (5 cm) of Core 2 (10 to 12 lb Cl^-/yd^3) (6.0 to 7.0 kg/m^3) and lower in Core 6 (4.5 to 5.5 lb Cl^-/yd^3) (2.7 to 43.3 kg/m^3).

In all of the cores, a significant quantity of chloride ion has moved into the portion of the overlay concrete in contact with the base slab wearing surface. As seen in the results for Core 1, a significant amount of chloride ion moved into the conductive polymer anode material.

Discussions and Conclusions

During the operation of an impressed current cathodic protection systems a number of events occur that can have consequences regarding the physical and chemical integrity of the various components of the cathodic protection system. These events include:

- The migration of anions and cations in the concrete pore-water toward the anode and cathode.
- Electrochemical reactions at the anode/concrete interface.
- Electrochemical reactions at the cathode/concrete interface.

The movement of ions through concrete under the influence of an electrical field is well established.[33,34]. Ionic movement can occur in concrete even under the relatively low potential differences characteristic of cathodic protection. Specifically, in a cathodic protection environment, Ca++, Na+, and K+ can migrate toward the cathode (top reinforcing steel) while OH- and Cl- can migrate toward the anode. One concern associated with these events is the possibility that an increased concentration of alkali cations near the cathode may initiate alkali-aggregate reactions under conditions which prior to the cathodic protection treatment were innocuous.

The potentially deleterious effects of anodic reactions on concrete has long been recognized within the cathodic protection industry. When current passes from an anode into an electrolyte (i.e., concrete) electrochemical reactions occur at the surface of that anode. In the case of chloride contaminated concrete, two reactions are possible when using inert anodes:

$$2H_2O \rightarrow O_2 + 4H^+ + 4e^- \quad \text{and/or} \quad 2Cl^- \rightarrow Cl_2 + 2e^-$$

In the presence of water and a pH greater than 4, the latter reaction will be followed by rapid hydrolysis of chlorine as follows:

$$Cl_2 + H_2O \rightarrow ClO^- + Cl^- + 2H^+$$

In either case, one mole of acid (H^+) will be generated for each Faraday of current passed. When carbon-based anodes are used a small amount of current will be expended for the oxidation of carbon as follows:

$$C + H_2O \rightarrow CO + 2H^+ + 2e^-$$

and/or

$$C + 2H_2O \rightarrow CO_2 + 4H^+ + 4e^-$$

In the presence of water and a pH greater than 10, carbon dioxide will be converted to carbonate, as follows:

$$CO_2 + H_2O \rightarrow CO_3^{-2} + 2H^+$$

In all cases (except in the case of sacrificial anodes such as zinc) the passage of anodic current through concrete will generate acid. The calcium silicate hydrate phases and the calcium hydroxide phases in concrete are vulnerable to acid attack. Carbonate aggregates (limestones/dolomites) are also vulnerable to acid attack.

Under normal conditions, the electrochemical reaction occurring at the cathode is:

$$2H_2O + 0_2 + 4e^- \rightarrow 4OH^-$$

Additionally, at high electrical potentials, molecular hydrogen can be generated at the cathode via the following reaction:

$$2H^+ + 2e^- \rightarrow H_2$$

This latter reaction is of concern regarding the phenomenon of hydrogen embrittlement of the reinforcing steel.

Concern has also been expressed regarding the effect of the ionic migration on the bond strength of the reinforcing steel.

In summary, the potential adverse effects of cathodic protection treatments on the various components of the cathodic protection system include:

- Acid attack of concrete surrounding and adjacent to the anode (principally manifested as a dissolution/softening of the hydrated cement phases and carbonate aggregate phases).

- Initiation of alkali-silica reactions in concrete surrounding and adjacent to the cathode (manifested as both a softening and cracking adjacent to the reacting particles).

- Chemical changes at the cathode/concrete interface resulting in a reduction in bond strength.

Based upon the results of the present petrographic examination at LML, the principal consequences of the 30-month cathodic protection treatment of the reinforced concrete slabs at FAU were:

- Alteration of the concrete in the vicinity of the anode.
- Alteration of the base slab concrete lying between the cathode and anode.
- Deterioration of the anode.
- Disruption of the bond between the overlay concrete and the base slab concrete.

The extent of deterioration was influenced by the independent variables in the present investigation (type of anode and current density).

Alteration of Concrete in Contact With the Anode

A principal event which occurred in all of the slabs treated here, was the alteration of concrete in direct contact with the cathodic protection anode. In the case of the titanium mesh and ribbon anodes and the wire anode, only the overlay concrete was in contact with the anode. The conductive polymer anode was in contact with both the overlay concrete and the base slab concrete.

Following the 30-month cathodic protection treatment, chloride ions moved into the overlay concrete in the region of the anode so that post-treatment levels were as high or higher than those found in the wearing surface of the base slab concrete. Alteration of concrete adjacent to the anode is characterized as a color change in the hydrated cement paste phase and a softening of both the cement paste phase and limestone aggregate particles in close proximity to the anode. This discoloration/softening phenomenon is further characterized as a classic acid attack of the portland cement concrete. In the hydrated portland cement phase contacting the anode, the calcium-bearing phases are dissolved, rendered into soluble forms, and transported away from the reaction site by alternate wetting/drying cycles. The altered cement paste shows a significant reduction in binding quality and a significant increase in porosity relative to the unaltered concrete.

In these experiments, the most extensive alteration of concrete adjacent to the anode occurred with the titanium ribbon anode and the wire anode. The least alteration occurred with the use of the titanium mesh anode. This alteration is viewed as a deterioration of the concrete encapsulating the anode, and is expected to have an adverse effect on the ionic conductivity communication between the anode and the cathode.

An increase in the extent of acid attack of concrete in contact with the anode also accompanied an increase in the cathodic protection current density.

Alteration of Concrete Between the Cathode and Anode

Where titanium mesh and ribbon were used as the anode, there was no significant alteration of the base slab concrete lying between the cathode and anode.

With the wire anode and the conductive polymer anode, there was some acid attack of the base slab concrete in close proximity (and contacting) these anodes. Further, the extent of this type of distress was greatest with the conductive polymer anode which was in direct contact with the base slab concrete.

Alteration of Concrete in Contact With the Cathode

There was no significant alteration of base slab concrete in direct contact with the cathode in any of the reinforced concrete slabs in this experiment. In all cases, concrete surrounding the cathode (top rebar) showed no dissolution, softening, or color change and retained a normal pH level (12.5).

Anode Deterioration

The titanium mesh and ribbon anodes showed virtually no deterioration as a result of the 30 month cathodic protection treatment. A slight amount of deterioration was observed in the Ferex™ wire anode and in the conductive polymer anode.

Overlay Bond

In the slabs having the wire anode and the conductive polymer anode, the bond between the overlay concrete and the base slab concrete was disrupted at some point during the course of the 30-month cathodic protection treatment. Additionally, in the case of the Ferex wire anode, there was a significant amount of distress (cracking) in the overlay concrete emanating from the anode position.

The core taken from the slab containing the titanium ribbon anode also showed a disruption of the bond between the overlay concrete and the base slab concrete. However, this disbonding is judged to be related to factors other than effects of the cathodic protection treatment. Disbonding occurred during the coring operation.

Performance of the Four Anode Types Operated at 20 mA/ft^2 (215 mA/m^2)

An effort was made to rate the performance of the four anode types in the trial slabs which were operated for 30 months at 20 mA/ft^2 (215 mA/m^2). The criteria used in the assessment of relative performance include:

- Deterioration of the anode.
- Alteration of the overlay concrete encapsulating the anode.
- Alteration of the base slab concrete between the anode and cathode.
- Loss of bond between the overlay and the base slab.

Table 5-25 compares the performance of the anodes on the basis of these criteria. At a current density of 20 mA/ft^2 (215 mA/m^2), the titanium mesh had the highest performance rating on the basis of this subjective, unweighted ranking. The conductive polymer had the poorest performance rating.

Effect of Cathodic Protection Current Density

Current density was studied as a variable only with the titanium mesh anode where three levels of current density were used, 10, 20, and 40 mA/ft^2 (107, 215, and 430 mA/m^2).

For several of the performance rating criteria used here, current density had no significant effect. Specifically, current density for the levels used, had no effect on:

- Deterioration of the anode (there was no anode deterioration in any of the slabs containing the titanium mesh anode).
- Alteration of the base slab concrete lying between the anode and cathode and surrounding the cathode (there was no significant alteration of this concrete in any of the slabs containing the titanium mesh anode).
- Bond between the overlay concrete and the base slab concrete (the bond remained intact in all three slabs containing the titanium mesh anode).

The most significant effect of the variation in current density was an increase in the extent of alteration of the overlay concrete in contact with the anode. The greatest alteration of anode encapsulating concrete occurred at 40 mA/ft^2 (430 mA/m^2). At the lower normal operating current densities, alteration of the concrete was significantly less and there was very little difference in the extent of alteration at 10 and 20 mA/ft^2 (107, and 215 mA/m^2).

Table 5-25. Relative Performance of the Four Anode Types Following 30 Months of Cathodic Protection at 20 mA/ft² (215 mA/m²)

Type of Anode	Physical Deterioration				Bond Loss[a]				Overlay Change[b]				Slab Concrete Change[c]				Total Rating[d]
	H	I	L	N	H	I	L	N	H	I	L	N	H	I	L	N	
Titanium Mesh				x			x				x					x	11
Titanium Ribbon				x			x				x					x	9
Ferex Wire			x				x				x				x		5
Conductive Polymer			x				x				x		x				4

(a) Loss of bond between the overlay and the base concrete slab.
(b) Alteration of the overlay concrete encapsulating the anode.
(c) Alteration of the base slab concrete between the anode and the cathode.
(d) Total rating equals the sum of the point values assigned below.
H= High (0) I= Intermediate (1) L= Low (2) N= None (3)

6

Intermittent Cathodic Protection

Impressed current cathodic protection systems usually require a source of electric power. In some instances, electric power may not be readily available, or be cost prohibitive to install. An example of this would be offshore piers and pilings. Also, certain circumstances present themselves where power might only be available at a particular time of day, as in the case of nighttime roadway lighting. In each case, the use of intermittent cathodic protection would be an attractive alternative for providing protection to the steel. To this end, experiments were conducted to determine the feasibility of intermittent cathodic protection.

Alternative DC power sources include photovoltaic arrays and possibly even wind power. Experiments were conducted to simulate a system powered either by a photovoltaic array without battery back-up or by part-time DC power. If intermittent cathodic protection is feasible, it could be very cost effective. A photovoltaic array and support structure capable of supplying 20 watts, or enough power to operate a 1000 ft^2 at 2 mA/ft^2 (21.5 mA/m^2), would cost between \$0.15-0.20/ft^2.

Results

The experiments were conducted on two of the corrosometer probe test slabs. Slabs 13656-4 and 13656-9, which contained 5 and 10# Cl^-/yd^3 respectively. The slabs had previously operated, on full time cathodic protection, at 1.37 and 2.74 mA/ft^2 concrete area respectively (14.7 and 29.4 mA/m^2). To evaluate intermittent cathodic protection, the current on each block was doubled and cycled on and off every twelve hours. In this way, the amount of charge passed would be equal to the other tests, and provide a basis for comparison.

Both blocks had operated for 13 weeks on a full-time cathodic protection basis. At that point the corrosion rate of blocks 13656-4 and 13656-9 was 0.049 and 0.099 mil/yr respectively and still decreasing (see Table 3-10). After instituting the intermittent cathodic protection regime, corrosion rates continued to decrease for two months. However, the corrosion rate of

block 13656-9 has begun to increase as of the writing of this report. Figure 3-11 illustrates these results. Further investigation is necessary to fully understand this phenomenon. Results to date indicate that intermittent cathodic protection is feasible under certain conditions, but further field work is necessary to verify the laboratory results.

7

Mathematical Modeling

The changes which occur near the steel/concrete interface as a result of the application of current have been scantily documented in the literature. Experience has shown, both from electrochemical theory and from indirect measurements, that with the passage of current, chloride ions will migrate toward the anode and away from the reinforcing steel. As concentration gradients develop, this will be counteracted by the back migration of chloride due to diffusional processes. The result will be an equilibrium profile of chloride ions in which electrochemical migration is balanced by diffusion.

Likewise, the passage of current will generate hydroxide ions at the steel surface. These will be produced at a rate according to Faraday's Law since the two possible cathodic reactions are as follows:

$$O_2 + 2H_2O + 4e^- \rightarrow 4OH^-$$

and

$$2H_2O + 2e^- \rightarrow H_2 + 2OH^-$$

Hydroxide ion produced at the steel surface will also tend to equilibrate as the OH^- ions migrate toward the anode.

Both of these events tend to passivate the steel through the formation of γ-ferric oxide.[1]

More importantly for the repassivation process than either of these factors alone is the Cl^-/OH^- ratio. The equilibrium concentration profiles and Cl^-/OH^- profile shown in Figure 7-1 are established during cathodic protection. The shape of these curves depends on many factors including current density, initial chloride concentration, initial pH, temperature, transference numbers and diffusion coefficients.

Figure 7-1 . Concentration Profiles after Cathodic Protection is Applied and Equilibrium is Established

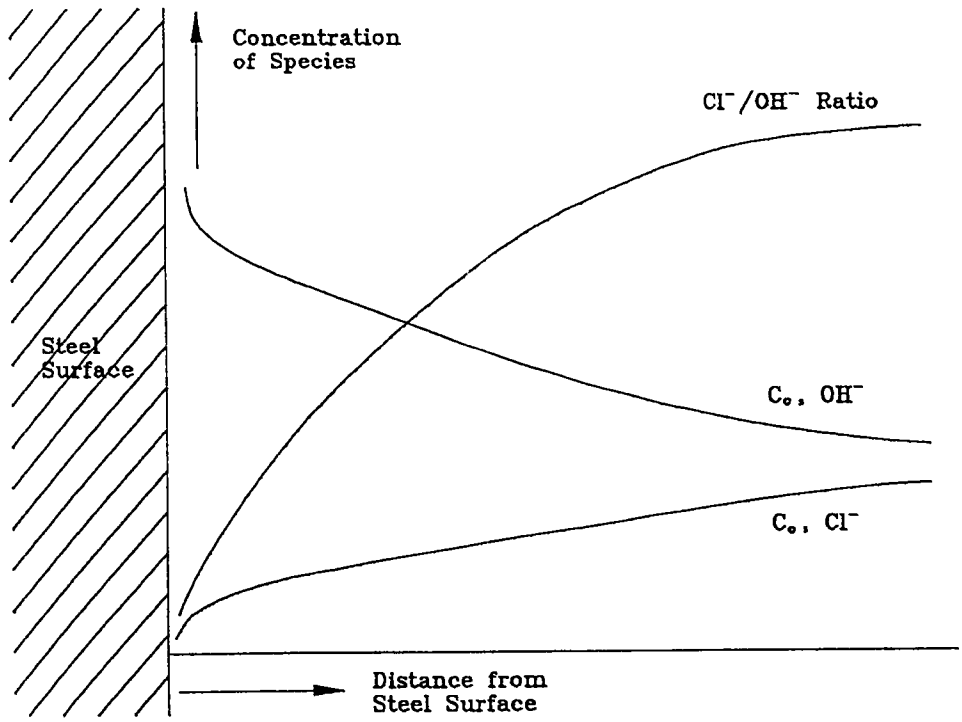

A mathematical model was made to predict the transient ion concentration gradients near a planar steel element embedded in concrete.

Four ions, chloride, hydroxide, sodium and potassium, were considered. Mass balance equations for each ionic species were written and with the electrical neutrality relationship, 4 equations with 4 unknowns were generated. The equations, with appropriate boundary conditions, were solved by a numerical technique introduced by Newman.[35] The solutions to the equations provided estimates of chloride and hydroxide concentrations as a function of time, and were used to predict the relaxation of the concentration profiles after current was stopped.

Refining of the model was made by the introduction of coupling equations and corrosion data developed in this contract. The model was used to predict polarization criterion to meet an acceptable rate of corrosion.

Real world structures are far more complex and non-uniform than the ideal geometry described in the model above. Separate modeling was done to quantify the effect of inhomogeneities to help insure that the criteria would be usable for real world structures.

Concentration Profile Modeling

Model Formulation

The mathematical model describes the transient concentration distributions of chloride, hydroxide and sodium ions in the vicinity of steel imbedded in concrete. The model is based on a differential mass balance and flux expressions described by dilute solution theory.[35] The systems of equations are shown in Table 7-1. The subscripts represent 1-chloride, 2-hydroxide, 3-sodium. Calcium ion was not included since it is a very minor carrier of current in concrete due to its low solubility. The three mass balances equations A, B, and C involve four unknowns (C_1, C_2, C_3, and ϕ). Equation D represents the electroneutrality condition and provides the fourth relationship.

In equations A, B, and C the left hand side represents the accumulation of ions in a volume element of concrete. The first term on the right hand side of these equations represents net diffusion by concentration gradient into the volume element. The second term on the right hand side represents the net transport of ions into the volume element by way of the electric field effect in the charged species.

The three differential equations and consequently the concentration distribution of each species are coupled through the electric potential gradient, i.e., $\nabla\phi$. The boundary conditions at the cathode are given as equations E, F, G, which state that the flux is zero for the chloride and sodium ions and the flux of hydroxide ion is governed by the applied current.

Table 7-1. Model Equations of Cathodic Protection of Steel in Concrete

$$\frac{\partial \varepsilon C_1}{\partial t} = D_1 \frac{\partial^2 C_1}{\partial y^2} + z_1 u_1 F \varepsilon \left[C_1 \frac{\partial^2 \phi}{\partial y^2} + \frac{\partial C_1}{\partial y} \frac{\partial \phi}{\partial y} \right] \quad \text{(A)}$$

$$\frac{\partial \varepsilon C_2}{\partial t} = D_2 \frac{\partial^2 C_2}{\partial y^2} + z_2 u_2 F \varepsilon \left[C_2 \frac{\partial^2 \phi}{\partial y^2} + \frac{\partial C_2}{\partial y} \frac{\partial \phi}{\partial y} \right] \quad \text{(B)}$$

$$\frac{\partial \varepsilon C_3}{\partial t} = D_3 \frac{\partial^2 C^3}{\partial y^2} + z_3 u_3 F \varepsilon \left[C_3 \frac{\partial^2 \phi}{\partial y^2} + \frac{\partial C_3}{\partial y} \frac{\partial \phi}{\partial y} \right] \quad \text{(C)}$$

$$C_3 - C_1 - C_2 = 0 \quad \text{(D)}$$

At Cathode (y=0)

$$-\frac{i}{F} = -D_2 \frac{\partial C_2}{\partial y} - z_2 u_2 F \varepsilon C_2 \frac{\partial \phi}{\partial y} \quad \text{(E)}$$

$$0 = -D_1 \frac{\partial C_1}{\partial y} - z_1 u_1 F \varepsilon C_1 \frac{\partial \phi}{\partial y} \quad \text{(F)}$$

$$0 = -D_3 \frac{\partial C_3}{\partial y} - z_3 u_3 F \varepsilon C_3 \frac{\partial \phi}{\partial y} \quad \text{(G)}$$

At $y \rightarrow \infty$

$$C_1 = C_1^\circ;\ C_2 = C_2^\circ;\ C_3 = C_3^\circ \quad \text{(H)}$$

NOTE: $D_j = \frac{\varepsilon \acute{D}_j}{\tau}$ where $\acute{D}_j$ is free solution diffusivity in $\frac{cm^2}{s}$, τ is tortuosity.

$u_j = \frac{D_j}{\varepsilon RT}$ = effective mobility corrected by porsity.

C_j are concentrations of species subscript i in the pure liquid, $\frac{mole}{cm^3}$

subscript i ≡ ionic species: 1-chloride, 2-hydroxide, 3-cation such as sodium
ε ≡ porosity, or pore volume fraction
ϕ ≡ solution phase potential, volts
i ≡ applied cathodic protection current density, A/cm^2
z_1 ≡ charge on ion, equiv/mole; $z_1 = z_2 = -1$, $z_3 = +1$
F ≡ Faradays constant, 96500 Amp-sec/equiv
R ≡ ideal gas law constant, 8.314 J/mole-°K ; T ≡ temperature, °K

In these expressions, D_i is the effective diffusion coefficient for concrete and takes into account porosity and tortuosity. The porosity corrects for the fact that the concentration gradient driving force only exists in the solution pore. The tortuosity corrects for the fact that the diffusion path length is increased due to the tortuous path of the pores.

The mobility is estimated by using the effective diffusivity and the Nernst-Einstein relation. The resulting effective mobility is corrected for porosity since the balance equations specifically include porosity in the migration terms, i.e., the second term on the right hand side of equations A, B, and C of Table 7-1.

The boundary conditions at the anode shown as Equation H represent constant compositions, i.e., at a distance far enough away from the cathode the concentration of the ions are constants and not perturbed by the events taking place near the cathode.

The non-linearity and coupling of Equations A-C contributes to the difficulty in obtaining a numerical solution to these equations. For the first approximation, the problem was simplified by assuming that the electric field is constant, or:

$$\nabla\phi \approx -\varrho i = E$$

Where ρ is the concrete resistivity, i is the applied current density and E is the electric field. The simplified equations are shown in Table 7-2 as equations I, J, K. These equations are decoupled and can be solved independently of each other. However, a validity of the approximation can be checked by the extent in which the electroneutrality condition is satisfied, i.e.,

$$\Sigma z_j C_j = 0$$

Where z_j is the charge of ion j.

The boundary conditions at the cathode for the approximate model are similar to the rigorous model and are given by equations L, M, N in Table 7-3.

The boundary conditions at the anode are represented by equations O, P, Q. These equations, are based on two possible anode reactions:

$$Cl^- \rightarrow \frac{1}{2}Cl_2 + e^-$$

$$OH^- \rightarrow \frac{1}{2}H_2O + \frac{1}{4}O_2 + e^-$$

The quantity α, in equation O, represents the fraction of current contributing to the chloride oxidation reaction (α=0 when the second reaction is 100% efficient). The flux of species out of the anode region into the overlayer is given by $N_{1,OL}$ and $N_{2,OL}$., in equations O and P. Any contribution of the cation from the overlayer was neglected. Note that if $N_{2,OL}$ is negative, then species *j* near the anode is being replenished by the overlayer. An example might be chloride from de-icing salt penetrating through the overlayer into the region near the anode. This flux of chloride through the overlayer is represented as being related to the rate of reaction at the cathode by introducing the factor β_j. Some extreme examples of the magnitude of β_j are:

- $\beta_j = 1$ No overlayer effect
- $\beta_j = 0$ Amount of species *j* disappearing by reaction is balanced by flux from the overlayer.
- $\beta_j > 1$ Species *j* is being removed from the anode region into the overlayer region.
- $\beta_j < 1$ Species *j* near the anode is being replenished by the overlayer.

Table 7-2. Constant Electric Field Model Equations

$$\frac{\partial \varepsilon C_1}{\partial t} = D_1 \frac{\partial^2 C_1}{\partial y^2} + z_1 u_1 F E \varepsilon \frac{\partial C_1}{\partial y} \qquad \text{(I)}$$

$$\frac{\partial \varepsilon C_2}{\partial t} = D_2 \frac{\partial^2 C_2}{\partial y^2} + z_2 u_2 F E \varepsilon \frac{\partial C_2}{\partial y} \qquad \text{(J)}$$

$$\frac{\partial \varepsilon C_3}{\partial t} = D_3 \frac{\partial^2 C_3}{\partial y^2} + z_3 u_3 F E \varepsilon \frac{\partial C_3}{\partial y} \qquad \text{(K)}$$

NOTE: $D_j = \frac{\varepsilon \acute{D}_j}{\tau}$ = effective diffusion mobility, where $\acute{D}_j$ is free solution diffusivity, cm_2/s

$u_j = \frac{D_j}{\varepsilon RT}$ = effective mobility corrected by porosity

$E = \left[F^2 \frac{\Sigma z_j^2 D_j C_j}{RT} \right] i$ = pi = electric field strength, V/cm

C_j are concentrations in the pore liquid

Table 7-3. Constant Electric Field Model Equations Boundary Conditions

At Cathode (y = 0)

$$-\frac{i}{F} = -D_2\frac{\partial C_2}{\partial y} - z_2u_2\varepsilon FEC_2 \qquad (L)$$

$$0 = -D_1\frac{\partial C_1}{\partial y} - z_1u_1\varepsilon FEC_1 \qquad (M)$$

$$0 = -D_3\frac{\partial C_3}{\partial y} - z_3u_3\varepsilon FEC_3 \qquad (N)$$

At Anode (y = L)

$$-D_1\frac{\partial C_1}{\partial y} - z_1u_1\varepsilon FEC_1 = \frac{\alpha i_A}{F} + N_{1,OL} \qquad (O)$$

$$= \frac{\alpha\beta_1 i_A}{F} \qquad (O')$$

$$-D_2\frac{\partial C_2}{\partial y} - z_2u_2\varepsilon FEC_2 = \frac{(1-\alpha)i_A}{F} + N_{2,OL} \qquad (P)$$

$$= \frac{(1-\alpha)\beta_2 i_A}{F} \qquad (P')$$

$$-D_3\frac{\partial C_3}{\partial y} - z_3u_3\varepsilon FEC_3 = 0 \qquad (Q)$$

Model Solution

The model equations were cast into finite difference equations of an implicit form. The time derivative also was kept in an implicit form to guarantee convergence. These difference equations form a tridiaganol matrix.

The subroutines "BAND" and "MATINV"[35] were employed to solve the system of equations to calculate C_j as a function of time and position. Since the equations are decoupled, only one iteration was required for each time step. The concentration profiles using a two-hour time step over a six-month period could be calculated in ten minutes on a PC/486SX machine (33Mhz).

The electroneutrality condition was found to be satisfied except for the region close to the cathode where cations were in excess. This region where electroneutrality was violated became larger at longer times. This comparison indicates that although the trends of anion concentration distribution are correct, the actual magnitude may be influenced by a non-linear electric field. A more rigorous model, or experimental data, is needed to further examine this issue.

The numerical calculation method could handle various initial concentration distributions. Normally, initial uniform concentration distributions were considered. However, in some cases, an initial linear distribution for the chloride ion was utilized (e.g., 1/2 of average at cathode and 2X average at anode).

The program was modified so it could change the applied current depending on the magnitude of the cathode surface hydroxide/chloride concentration distributions.

After a predetermined length of time, the current could be turned off and the resulting concentration relaxation profiles could be determined

Program Verification

In order to confirm that the model program developed in this work was predicting correct results, the following test was performed. An initial linear concentration distribution and zero applied current was programmed. This situation corresponds to the following differential equation:

$$\frac{\partial \varepsilon C}{\partial t} = D\frac{\partial^2 C}{\partial x^2}$$

$$\frac{\partial C}{\partial x} = 0 \text{ at } x = 0 \text{ and } L \text{ for all time } t$$

$$C = f(x) \text{ at } t \leq 0$$

Where L is the distance between the boundaries, x is the position coordinate between the boundaries and $f(x)$ is an initial concentration distribution. The quantities C, D, and ε are the concentration, diffusivity and porosity, respectively.

The concentration distribution will then relax to the average value. The solution to this equation is given as:[36]

$$C = \frac{1}{L}\int_0^L f(x')dx' + \frac{2}{L}\sum_{n=1}^{\infty} e^{\frac{-Dn^2\pi t}{L^2}} \int_0^L f(x')\cos\frac{n\pi x'}{L}dx' \qquad (1)$$

In our case:

$$f(x)=\frac{3}{2L}\bar{C}x + \frac{1}{2}\bar{C} \qquad (2)$$

or with L = 5cm, $\bar{C}$ = 0.5 molar:

$$f(x) = 0.15x - 0.25$$

Integrating equation (1) and evaluating the first 5 terms at x = 0 gives:

$$C = 0.075L + 0.25 - \frac{2}{L}\left[0.0304L^2e^{\frac{-9.86Dt}{L^2}} + 0.00338L^2e^{\frac{-88.74Dt}{L^2}} + 0.00122e^{\frac{-246.5Dt}{L^2}}\right] \qquad (3)$$

This time-dependent concentration was compared with the concentration at x = 0 calculated by the model program. In order to do this, the diffusion coefficient of the program input must be divided by ε (pore volume of concrete) to yield the correct value for this analytical solution. The results are tabulated below in Table 7-4 and shown graphically in Figure 7-2.

Table 7-4. Comparison of Calculated Program Output with Analytical Solution

Time, Hrs.	Calculated by Program Cement7 (moles/μL)	Analytical Solution Eqn 3 (moles/μL)
0	0.25	0.287
120	0.308	0.313
240	0.333	0.334
360	0.351	0.3513
480	0.367	0.3667
600	0.380	0.380
720	0.393	0.393

Concentration at x = 0, molar

Figure 7-2. Comparison of Program Calculation versus Analytical Solution

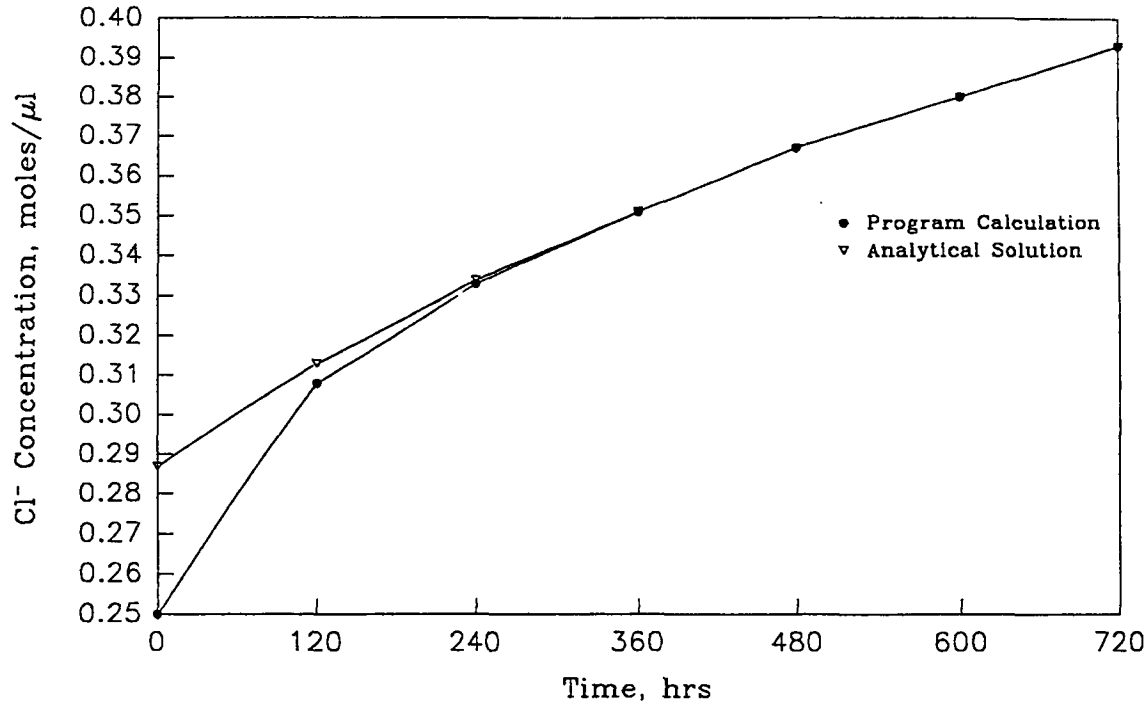

Only the first two exponential terms were used in equation 3 which explains the deviation between the model program and equation 3 at short times. The agreement was quite good and we concluded that the model program was providing reasonable results.

A number of test cases were run to determine the effects on:

- Cl^- concentration at the steel surface
- Cl^-/OH^- ratio at the steel surface
- pH

The results are presented graphically in Appendix C, Figures C-1 through C-44.

Program Results

The effects of variables were examined by first running a base case, and then changing each variable from the base case. The base case consisted of the following parameters:

Chloride diffusion coefficient	= 2.03 x 10^{-8} cm^2/sec
Hydroxide diffusion coefficient	= 5.27 x 10^{-8} cm^2/sec
Diffusion coefficient of other ions	= Ratios of above
Temperature	= 25°C
Concrete resistivity (calc.)	= 11,390 ohm-cm
Concrete pore-water fraction	= 0.17
Initial chloride concentration	= 5#/yd^3
Initial chloride distribution	= uniform
Initial pore-water pH	= 13.0
Anode reaction	= O_2 evolution
Steel geometry	= planar
Anode geometry	= planar
Steel-anode distance	= 5.0 cm
Current density	= 2.0 mA/ft^2

Certain variables were changed independently to examine their effect as shown in Appendix C. For each case run, four figures are presented: chloride concentration versus distance from steel, pH versus distance from steel, chloride concentration at the steel versus time, and Cl^-/OH^- ratio at the steel versus time.

In all cases, the application of cathodic protection current results in a significant reduction of chloride, increase of pH, and a dramatic reduction of Cl^-/OH^- ratio at the steel. Cl^-/OH^- ratio is probably the most significant parameter, and is related to corrosion rate of the steel by the corrosion rate studies presented in this report. The Cl^-/OH^- ratio is most affected by initial chloride concentration, current density and temperature.

The effect of initial chloride concentration on Cl^-/OH^- ratio for the first 6 months of operation is shown on Figure 7-3 for chloride concentrations of 2, 5, and 10 #/yd^3 (1.2, 3.0, and 5.9 gm/l) at 2 mA/ft^2 (21.5 mA/m^2). Even though the Cl^-/OH^- ratio drops rapidly with time, it is difficult to reduce the ratio below 0.6, the threshold for corrosion as determined by Hausmann[3], when chloride concentrations at the steel are very high. With an initial chloride concentration of 10 #/yd^3, the base case current of 2.0 mA/ft^2 (21.5 mA/m^2) is insufficient to protect the steel in the first 6 months of operation.

The effect of current density is shown in Figure 7-4. Current density has an important effect on the concentration profiles which develop. In this case a current density of 1.0 mA/ft^2 (10.7 mA/m^2) is not adequate protection for the first 6 months of operation. Cl^-/OH^- is dependent upon current density, not necessarily charge. For example, a current density of 2.0 mA/ft^2 (21.5 mA/m^2) for 2000 hours drops the Cl^-/OH^- ratio to 0.43, while a current density of 1.0 mA/ft^2 (10.7 mA/m^2) for 4000 hours drops the ratio to only 0.69. This occurs since the back migration of ions is significant.

Figure 7-3. Effect of Initial Chloride Concentration on Cl^-/OH^- Ratio

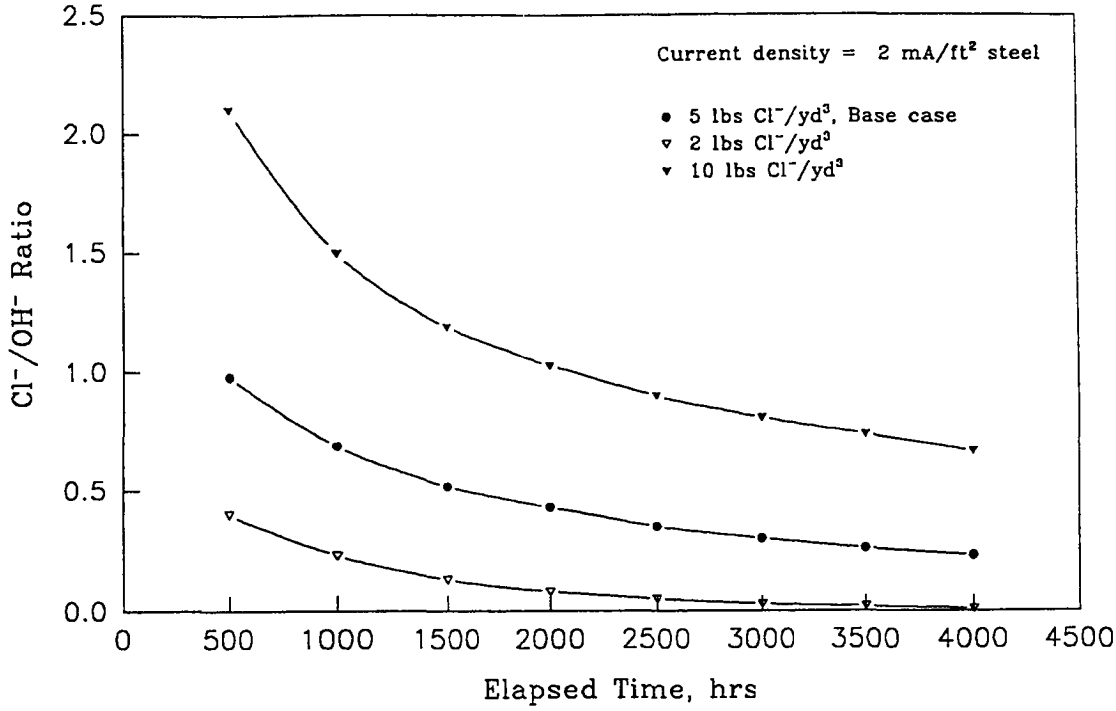

Figure 7-4. Effect of Current Density on Cl^-/OH^- Ratio

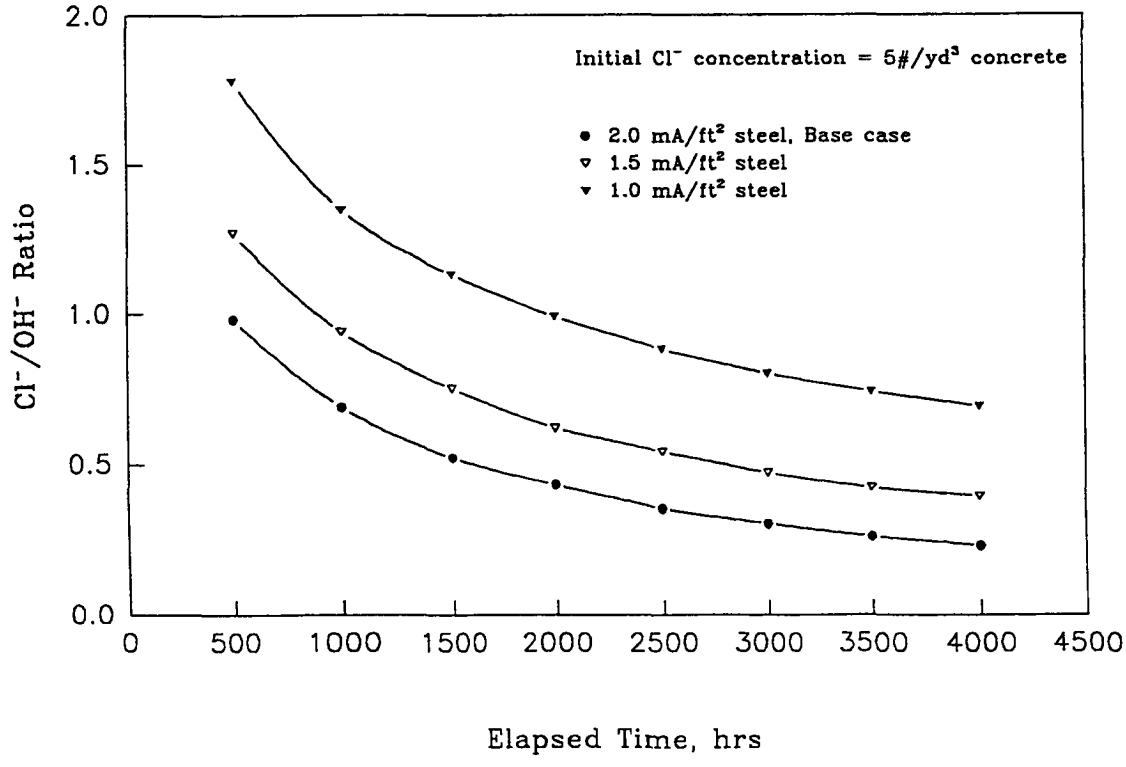

Figure 7-5 shows a surprisingly large effect of temperature on the decay of the Cl^-/OH^- ratio. This is due entirely to the effect of temperature on the back migration of ions. Ionic diffusion is much slower at cold temperatures, which allows a more rapid build-up of concentration gradients. This suggests that lower current would be required to protect steel at low temperatures.

Figure 7-5. Effect of Temperature on Cl^-/OH^- Ratio

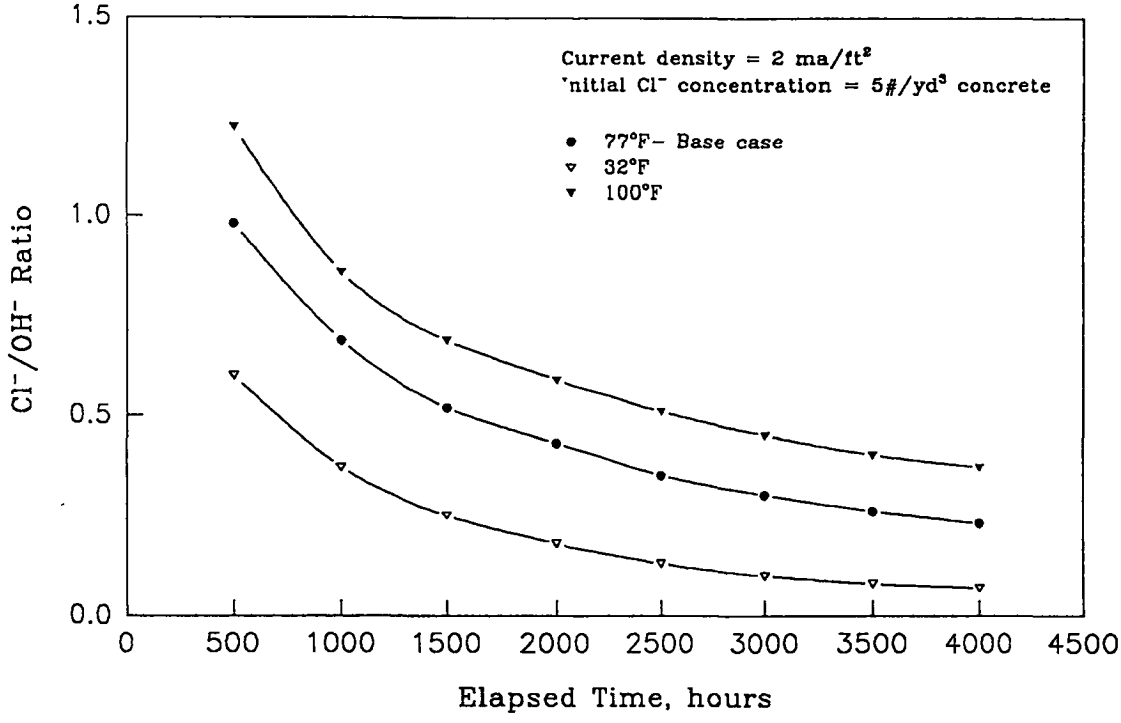

The initial concrete pH has surprisingly little effect on the decay of the Cl^-/OH^- ratio. This occurs because hydroxide concentration tends to reach a limiting value after long periods of operation, regardless of starting conditions.

Cement 8

A final modification of the model was made to incorporate the corrosion rate data developed under this contract, and to allow for changing current density with time. The model established the current density needed to maintain a corrosion rate of 0.1 mil/year based on the Cl^-/OH^- ratio at the surface of the steel. As cathodic protection continued and as concentration profiles developed, current density automatically adjusted downward. Equilibrium was reached when the diffusion of ions toward the steel was balanced by the migration of ions away from the steel due to the cathodic protection current. At this point, the Cl^-/OH^- ratio at the surface of the steel remained constant . The value of this final ratio was directly proportional to the magnitude of the initial ratio. Results of three such runs, for severe, moderate and light chloride contamination, are shown on Table 7-5. Initial conditions are the same as the base case above, except for the changing current density, and that the

chloride contamination is initially present as a linear profile, with concentration at the surface being 4 times that at the surface of the steel.

For the severe chloride contamination case, the initial current density required is quite high, about 5.0 mA/ft^2 (53 mA/m^2). The current requirement quickly dropped, and after one month of operation was reduced to 2.0 mA/ft^2 (21.5 mA/m^2). By three months of operation the required current density equilibrated at 1.6 mA/ft^2 (17.2 mA/m^2). The light and moderately chloride contaminated cases both equilibrate in less that one month at 0.5 and 1.1 mA/ft^2 (5.3 and 11.8 mA/m2) respectively. Both the changing current density and the linear profile of chloride contamination help the systems to equilibrate quickly.

Table 7-5. Cathodic Protection Current Density Requirement as a Function of Time

A. Severe Chloride Contamination
(10# Cl^-/yd^3 @ Steel Surface, 25# Cl^-/yd^3 Average)

Time (months)	Current Density Requirement (mA/ft^2)
Start-up	5.0
1	2.0
3	1.6
12	1.6

B. Moderate Chloride Contamination
(5# Cl^-/yd^3 @ Steel Surface, 12.5# Cl^-/yd^3 Average)

Time (months)	Current Density Requirement (mA/ft^2)
Start-up	1.3
1	1.1
3	1.1
12	1.1

C. Light Chloride Contamination
(2# Cl^-/yd^3 @ Steel Surface, 5# Cl^-/yd^3 Average)

Time (months)	Current Density Requirement (mA/ft^2)
Start-up	0.8
1	0.5
3	0.5
12	0.5

Since the adjusted current density equilibrates so quickly, the usefulness of changing current density at all becomes questionable. If, for the three cases presented, a constant current of 1.6, 1.1 and 0.5 mA were set, the total amount of corrosion that occurs in the first month would be insignificant. This conclusion leads to a very simple current-based criterion. A potential survey could first be used to identify areas of greatest corrosion, and presumably highest chloride concentration. A few concrete samples would then be taken and analyzed to determine chloride concentration at the level of the reinforcement. Cathodic protection current could be set based on chloride concentration, plus a small safety factor. No future reduction of current would be necessary. This procedure is supported by the good correlation found to exist between chloride concentration and required cathodic protection current. Adequate protection would be assured without overprotection. The computer model could be run for special cases.

These correlations were found to exist very late in this contract. It is strongly recommended that this approach be further explored, both mathematically and experimentally. Such a criterion would be simple to apply and interpret, and does not rely on the long-term stability of embedded reference electrodes.

Structure Related Modeling

Objective

This investigation is intended to provide quantitative information on the distribution of protective current and steel polarization in typical bridge deck arrangements, as a function of system parameters that include concrete resistivity, concrete cover, anode polarizability, anode resistance, and steel conditions. Special attention is given to the polarization distributions that may result when cathodic protection criteria involve 100 mV steel polarization or 1.5 mA/ft^2 (16 mA/m^2) cathodic current density delivery, at various positions with respect to the location of the anode power feed strip. The computations are not intended to reproduce likely field performance conditions, but rather to examine often extreme cases to reveal the relative importance of selected parameters. The results are presented to aid in the development of cathodic protection criteria that take into consideration the effect of uneven protective current delivery in an actual bridge deck environment.

Approach

All calculations addressed a section of bridge deck of uniform width and length. Figure 7-6 shows the system geometry and Table 7-6 lists the nomenclature used in the calculations. A single mat of reinforcing steel was placed under the bridge surface at a designated cover depth. A cathodic protection anode was placed coincident with the upper deck surface. The anode was energized by a feed strip located at one of the ends of the deck length.

Figure 7-6. Slab Model Showing Notation and Partitioning into Elements

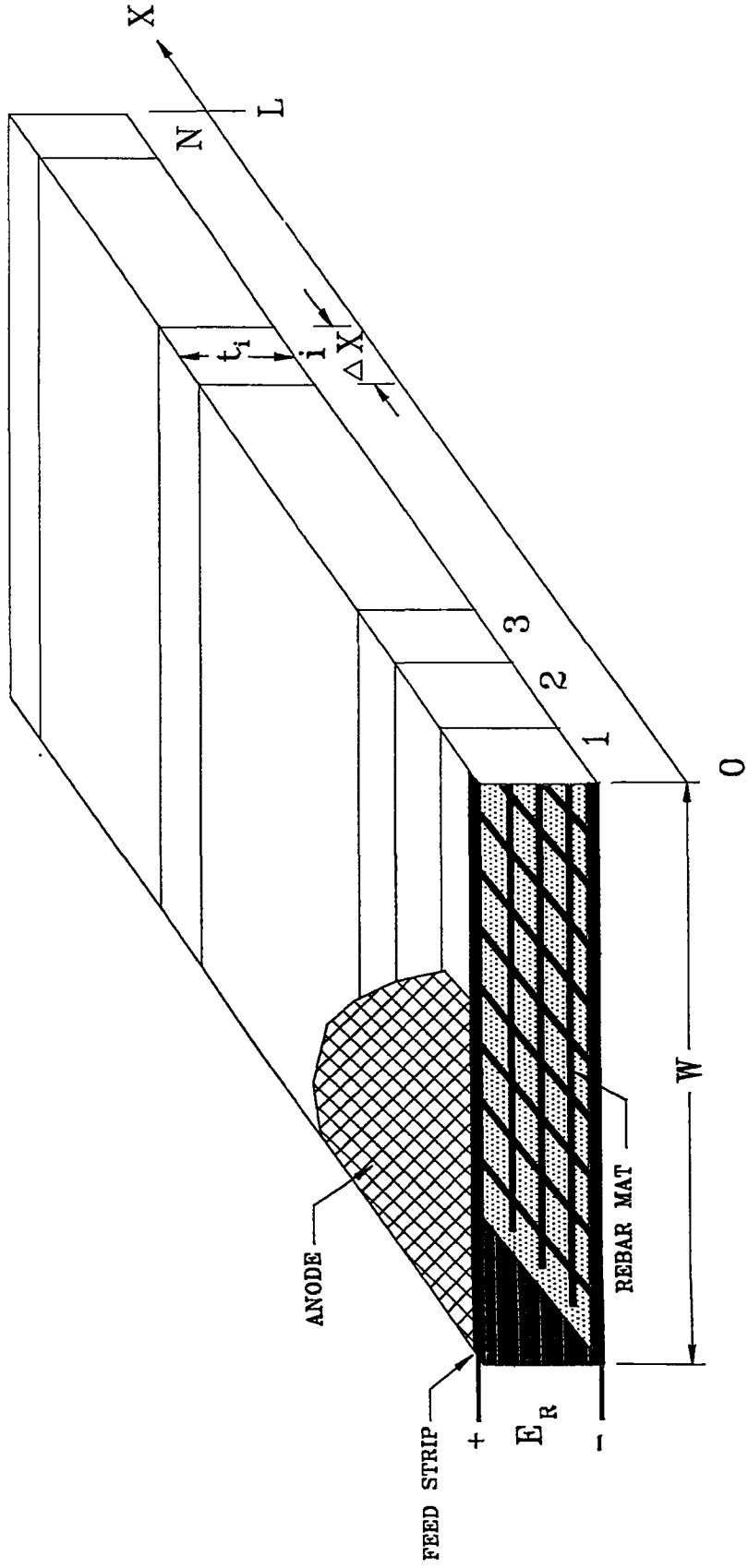

Table 7-6. Nomenclature used in the Calculations

Case Name	Base	Base Lo_ρ	Base Hi	Base Pass	Paint	Paint Pas	Zn
Case No.	**2**	**4**	**5**	**6**	**7**	**8**	**9**
L(ft)	60	60	60	60	**5**	**5**	60
W(ft)	30	30	30	30	30	30	30
t(in)	2	2	2	2	2	2	2
Steel	ACT	ACT	ACT	**PAS**	ACT	**PAS**	ACT
Anode	Ti-mesh	Ti-mesh	Ti-mesh	Ti-mesh	**Paint**	**Paint**	**Zinc**
Sdens	1	1	1	1	1	1	1
Adens	0.21	0.21	0.21	0.21	**1**	**1**	**1**
ρCon (Ω-cm)	10K	**3K**	**30K**	10K	10K	10K	10K
ρAno(Ω)	0.056	0.056	0.056	0.056	**40**	**40**	**.00012**

Case Name	Zn Pas	Zn Old	Base-VY Hi Res	Var.Res 1	Var.Res 2	Act/Pas Mix
Case No.	**10**	**11**	**12**	**13**	**15**	**16**
L(ft)	60	60	60	60	60	60
W(ft)	30	30	30	30	30	30
t(in)	2	2	2	2	2	2
Steel	**PAS**	ACT	ACT	ACT	ACT	**ACT/PAS**
Anode	**Zinc**	**Zinc old**	Ti-mesh	Ti-mesh	Ti-mesh	Ti-mesh
Sdens	1	1	1	1	1	1
Adens	**1**	**1**	0.21	0.21	0.21	0.21
ρCon (Ω-cm)	10K	10K	**100K**	**10K Feed 3K Far**	**10K Feed 30K Far**	10K
ρAno(Ω)	**.00012**	**.0036**				

Act,Pas:	Active, Passive Steel
Sdens:	Steel Density (ft^2 steel/ft^2 concrete)
Adens:	Anode Density (ft^2 anode/ft^2 concrete)
ρCon:	Concrete resistivity
ρAno:	Anode linear resistivity (ohm-cm/cm)
Ti mesh:	Titanium mesh-Type 210
Paint:	0.25 mm Thick, 1 ohm-cm resistivity
Zn:	Newly deposited Zn anode, ideal conductivity
Zn old:	Partially consumed anode, 30 times more resistive than ideal

The polarization properties of the anode and the rebar mat were specified to fit the experimental potential-current density diagrams of the material chosen for modeling. The concrete resistivity and cover thickness were likewise chosen to represent the desired conditions. All properties and dimensions were uniform across the bridge deck width. Because the concrete cover thickness was much smaller than the deck length, a one-dimensional approximation was made.

The deck length was divided into a number of equally long elements. Within each element the anode and rebar polarization characteristics, as well as the product of concrete resistivity by concrete cover, were considered to be uniform.

The electrical behavior of the deck section was modeled by the equivalent electric circuit shown in Figure 7-7. The system was energized by a rectifier with DC output E_r, delivering a current I_{cp} to the deck. The current was distributed to each element by the anode, which is assumed to have a finite resistance distributed as shown in the figure. Each element consumed a current I_i, which is a fraction of the current I_{Li} entering the element from element i-1. The anode and mat of each element were treated as current-dependent voltage sources with voltages E_{Ai} and E_{Mi} respectively, with polarity as shown in the figure. The rebar mat was treated as a zero resistance bus. The concrete resistance of each element was treated as a resistor R_{Ci}. E_i is the potential difference between the center of the anode of each element and the mat.

Figure 7-7. Circuit Diagram of Model

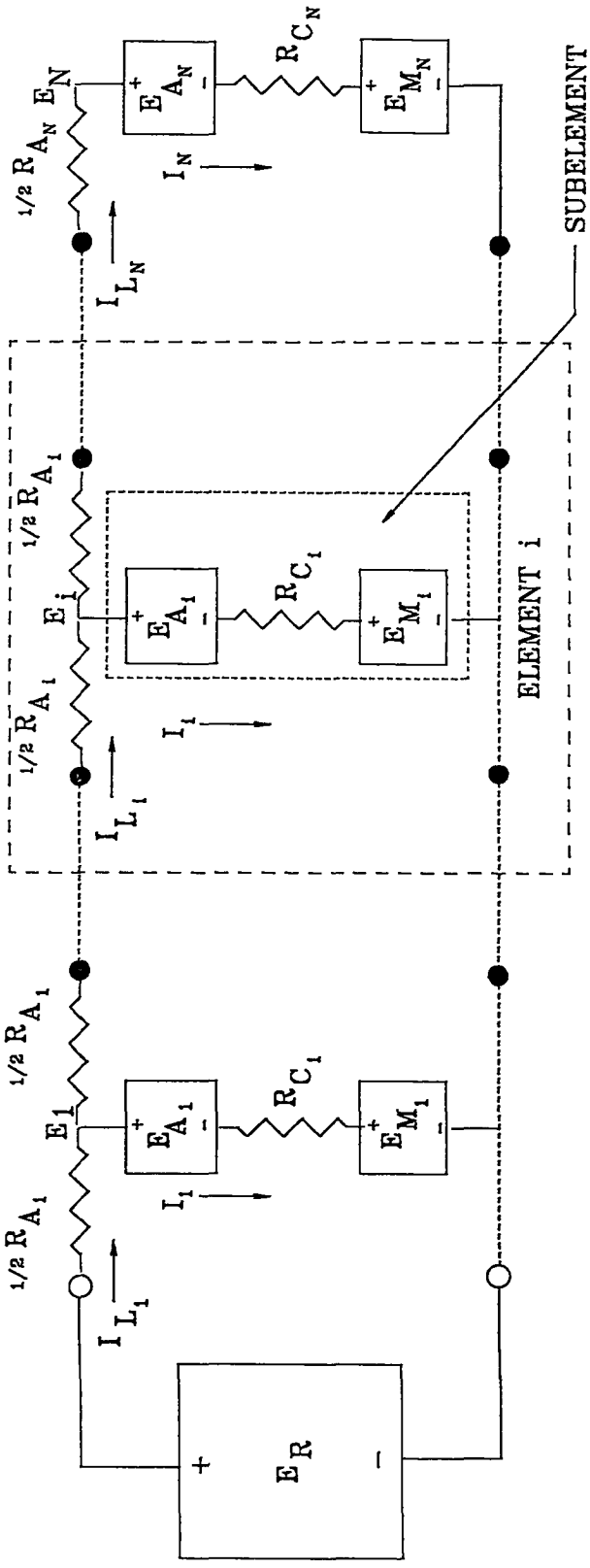

By application of Kirchhoff's laws:

$$I_i = I_{Li} - I_{Li+1} \qquad \text{(for i=1 to N-1)} \tag{1}$$

$$I_N = I_{LN} \tag{2}$$

$$I_{L1} = I_{CP} \tag{3}$$

Within each element:

$$E_i = E_{Mi} + R_{Ci} I_i + E_{Ai} \tag{4}$$

and:

$$E_i = E_{i-1} - (R_{Ai}/2)\, I_{Li} \text{ (for i=2 to N)} \tag{6}$$

$$E_1 = E_R - (R_{A1}/2)\, I_{CP} \tag{7}$$

In order to model individual elements, experimental data for the anode behavior and the active and passive steel mat were smoothed by hand and fitted to cubic splines, a sequence of third order polynomials which provide a smooth approximation in a piecewise fashion. To provide information for behavior outside the experimental range (cathodic regime for the anode, anodic regime for steel), representative values for the Tafel slopes were added. All information was available in terms of current density so that in the process of constructing an element, steel and anode density factors (square feet of anode or steel per square foot of concrete) could be introduced.

To construct a numerical representation of the element behavior, mat and anode voltage drops were combined with the concrete voltage drop at a number of current values to give a total voltage drop for the subelement as shown in Figure 7-7. This data set was then fitted to a spline and stored.

At a particular rectifier voltage, the impressed current was determined by first proposing a trial current. The voltage drop along the anode to the first subelement was computed, then the current was divided into a component through the first subelement and a component traveling on through the anode. The current flow through the subelement was obtained from the numerical representation described above. Following the remaining current along the anode, this process was continued to element N. As a termination criterion, the residual current after the Nth subelement should be 0. The computational scheme operated by seeking to minimize this residual current.

System performance was obtained by repeating this process for a number of rectifier voltages. This information was stored and used to derive performance at any particular rectifier voltage by interpolation. At any operating point all underlying information regarding local voltage drop or current flow inside any subelement was readily available by back computation. To examine a condition of interest, such as a specific impressed current at one element, a trial

and error procedure was required. A rectifier voltage (or current) was imposed, then the various parameters were computed at the specified location. This process was repeated until the criterion was met.

Cases Examined

Table 7-6 summarizes the cases examined. The deck length was always divided into 20 equal elements. The baseline case consisted of a deck section with uniform concrete resistivity (10,000 ohm-cm), 60 ft long and 30 ft wide. The concrete cover of the base case was 2 inches (5.08 cm). Actually, the base case corresponded to any thickness-resistivity combination with a product equal to 50,800 ohm-cm^2 since only the product of those two parameters enters in the circuit equations. The steel in the base case is all in the active state, and the anode is the ELGARD titanium mesh anode Type 210. This anode has an anode density (anode surface area/deck surface area) of 0.21, and a linear resistivity (resistance of a square of anode material measured across opposite sides of the square) of 0.056 ohm cm/cm. The reported anode linear resistivity takes into consideration the anode density. The polarization characteristics of the anode and the active steel were derived from experimental data generated by ELTECH Research Corporation and are shown in figures 7-8 and 7-9, (all polarization values shown are in terms of current per unit area of the anode or of the steel). Current densities per unit of concrete area were obtained by multiplying by the density factor.

Other cases examined included variations of the concrete resistivity-thickness product, steel condition (active versus passive), anode material (titanium mesh anode, conductive paint, sprayed zinc [ideal], sprayed zinc [aged], and a combination of active/passive steel behavior.

Polarization curves used to represent the passive steel and the other anode materials were derived from data provided by ELTECH and the University of South Florida (USF). The conductive paint anode was assumed to consist of a material 0.25 mm thick and with a resistivity of 1 ohm-cm, with polarization characteristics similar to those of carbon FHWA polymer anodes. The zinc polarization behavior represents a composite of polarization curves measured with sprayed zinc anodes in an ongoing investigation at USF. The zinc anode linear resistivities chosen for modelling correspond to ideally pure zinc deposited to a thickness of 0.5 mm, and to an aged anode example assuming that zinc loss leads to a linear resistivity 30 times greater. The polarization curves chosen for modeling purposes for these materials are shown also in figures 7-8 and 7-9.

While only anodic and cathodic polarization data were available for the anodes and steel respectively, it was desirable to extend the simulation slightly in the opposite polarization direction to treat cases of mixed active and passive regions. This extension is shown by the dashed lines in figures 7-8 and 7-9, which start at a current density representative of the lowest available current density data point in the experimental curves used. The simulation for the active steel assumes that the system behaves as having an effective anodic Tafel slope of 60 mV/decade. For the passive steel, it is assumed that the system has a limited passive current in the anodic direction, but that a breakdown potential is encountered at 50 mV versus Cu/$CuSO_4$. Except for Case 16 (figures C-69 & C-70), the results of the calculations are completely independent of the behavior assumed for the dashed line portion

of the polarization curves. In Case 16, the reverse behavior of the passive steel and the titanium mesh anode defines the extent of the initial system configuration, because of macrocell coupling between active and passive zones through the anode material.

The length of the deck was always considered to be 60 ft except for the conductive paint anode case, where a 5 ft length was used. Because of the treatment used, all cases examined are equivalent to having a deck twice as long, but with feed strips placed at each end.

Figure 7-8. Polarization Diagrams for Steel

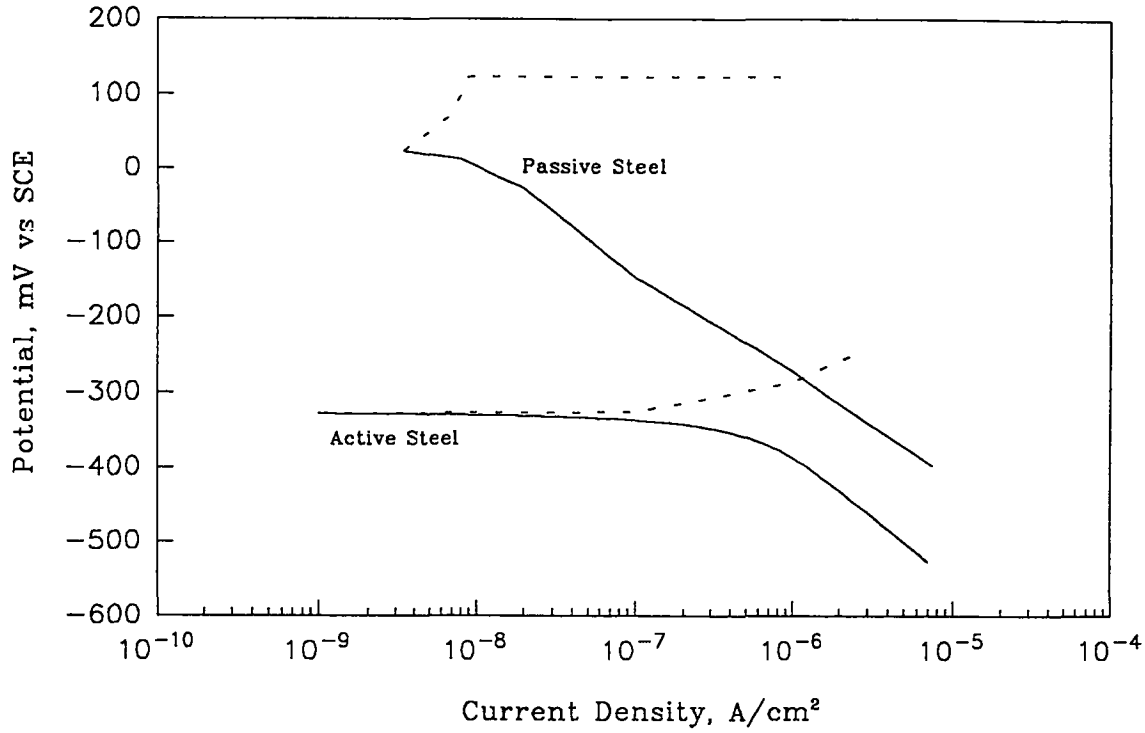

Figure 7-9. Polarization Diagrams for Anode Materials

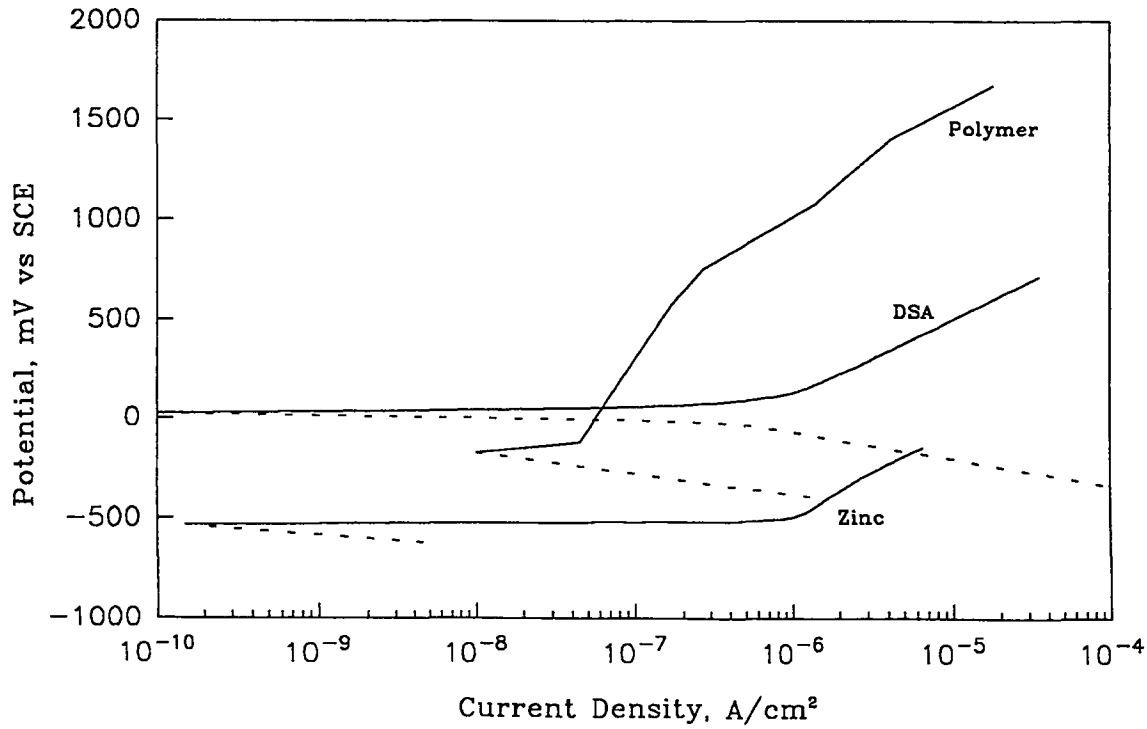

Results and Discussion

For each of the cases examined, subcases were selected corresponding to the conditions shown as A through D in Figure 7-10. Subcases A and B correspond to developing a 100 mV polarization of the steel in the cathodic direction (with respect to the steel potential of zero current in the polarization curve of the material) at either the deck segment closest to the feed point (B), or at the far end of the deck (A). Subcases C and D corresponded to obtaining a protective current density of 1.5 mA/ft^2 at each deck extreme.

Appendix C contains the polarization and protective current curves versus deck position for all subcases examined, keyed to the listing in Table 7-6. Table 7-7 summarizes the results for the deck extremes for all subcases examined, using the nomenclature shown in Figure 7-7. In some instances, the case conditions prevented satisfying the desired polarization extent at the deck far end without exceeding at the power feed point the maximum amount of current density (typically about 10 mA/ft^2 of concrete) available in the experimental anode polarization curve. Space for those cases was left blank in Table 7-6.

In all instances there was a decay in the amount of polarization impressed and current density delivered to the rebar mat, as the distance from the feed point increased. The decay, in cases of uniform concrete resistivity, was due to the resistance of the anode. The magnitude of the decay varied significantly from case to case.

Figure 7-10. Notation for Cases Examined

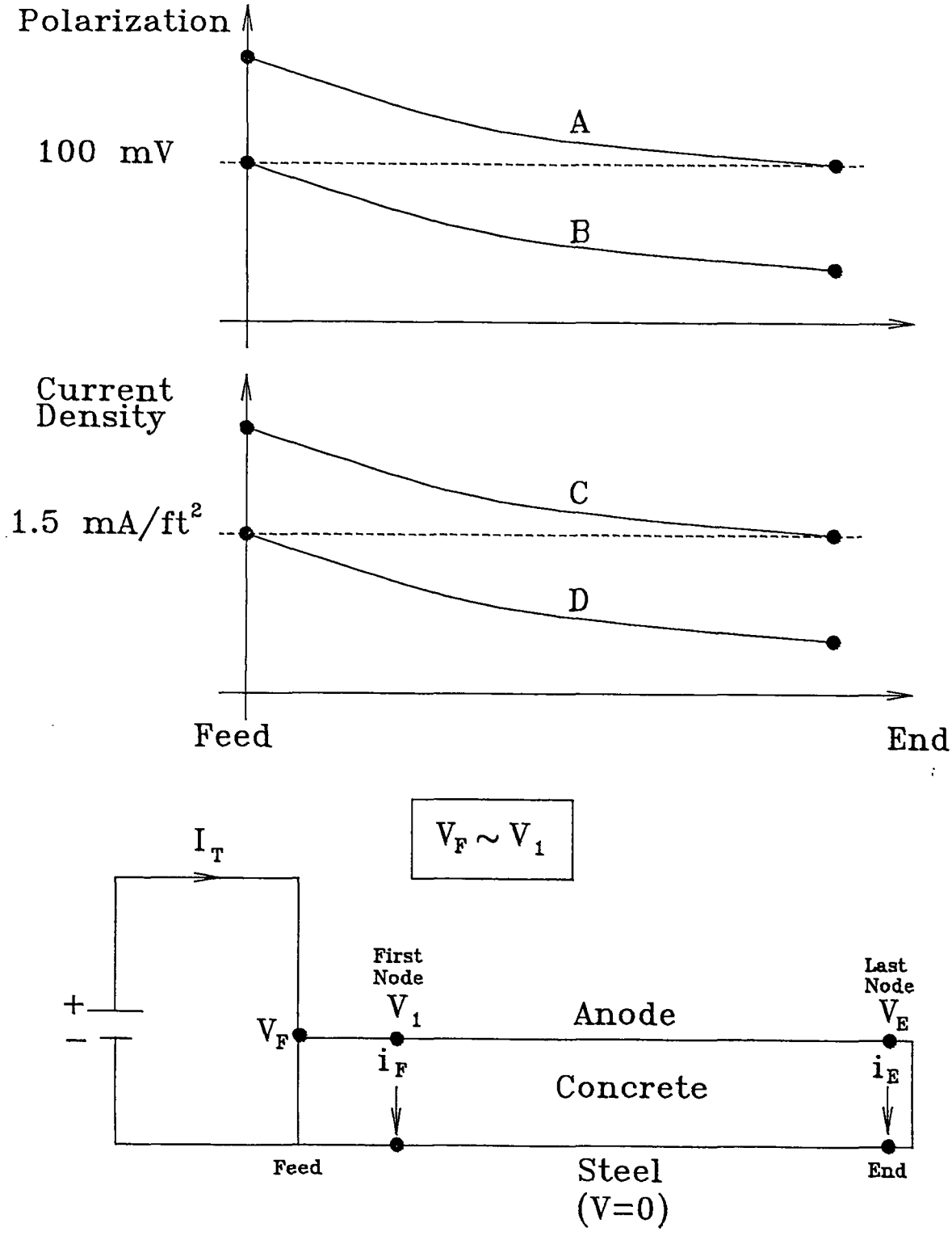

P_F : Steel Polarization, First Node

P_E : Steel Polarization, Last Node

Table 7-7. Results for Cases Considered.

Case Subcase	Vf (mV)	ve (mV)	Pf (mV)	Pe (mV)	if (mA/ft^2)	ie (mA/ft^2)	Vf-Ve (V)	V1 (mV)	It (A)
2A	1395	1112	140	100	4.4	2.5	283	1379	5.6
2B	1125	944	100	76	2.5	1.7	181	1115	3.5
2C	1065	903	92	70	2.2	1.5	162	1060	3.1
2D	910	793	70	56	1.5	1.1	117	903	2.2
4A	1313	1019	160	100	5.4	2.5	294	1296	6.1
4B	10	858	100	72	2.5	1.5	171	1019	3.3
4C	1028	857	100	72	2.5	1.5	171	1018	3.3
4D	854	742	71	54	1.5	1.0	112	848	2.1
5A	1598	1345	117	96	3.3	2.4	253	1585	3.8
5B	1405	1205	100	83	2.5	1.9	200	1394	3.8
5C	1228	1069	85	71	1.9	1.5	159	1219	3.0
5D	1077	952	71	59	1.5	1.2	125	1070	2.3
6A	143	138	103	99	0.04	0.04	5.1	143	0.1
6B	141	136	102	98	0.04	0.04	5	141	0.1
6C	966	802	337	321	2.3	1.5	164	9576	3.2
6D	807	689	320	307	1.5	1.1	118	801	2.2
7B	1886	1387	100	44	2.5	0.8	499	1853	0.2
7D	1630	1295	71	34	1.5	0.6	335	1609	0.13
8A	-5	-23.6	107	100	0.04	0.04	18.6	-5.9	0.01
8B	-23	-40	100	92	0.04	0.03	16.7	-24	0.01
8C	1525	1184	320	273	1.5	0.58	341	1504	0.13
9A	233	232	100	100	2.5	2.5	0.52	232	4.6
9C	49	49	70	71	1.5	1.5	0.33	49	2.7
10A	-441	-441	100	100	0.04	0.04	0	-441	0.07
10C	-56	-56	321	321	1.5	1.5	0.32	-56	2.7
11A	248	231	102	100	2.6	2.5	16.6	237	4.6
11B	233	217	100	98	2.2	2.4	16.1	232	4.5
11C	59	49	72	71	1.6	1.5	10	59	2.7
11D	49	39	70	69	1.5	1.4	9.5	48	2.6
12A	2630	2368	109	100	2.9	2.5	262	2616	4.8
12B	2375	2147	100	92	2.5	2.2	228	2363	4.2
12C	1795	1641	77	71	1.7	1.5	154	1787	2.8
12D	1648	1515	71	64	1.5	1.3	136	1641	2.5
13A	1280	1018	123	100	3.5	2.5	262	1266	5.0
13B	1125	927	100	84	2.5	1.9	198	1115	3.7
13C	1001	848	83	70	1.9	1.5	153	993	2.9
13D	912	786	71	61	1.5	1.2	126	905	2.3
15B	1125	977	100	62	2.5	1.2	148	1116	3.0
15C	1251	1069	119	71	3.3	1.5	182	1240	3.8
15D	911	812	71	47	1.5	0.9	99	905	2.0

Pf and Pe are steel polarization values at the feed strip and deck end respectively.

The subcase parameters can be found in Table 7-6

Effect of Concrete Resistivity.

Cases 2, 4, 5 and 12 (figures C-45 through C-50 and C-63 & C-64 respectively) explore the effect of having various uniform concrete resistivity values while keeping the other parameters equal to those of the base case. The relative variation of the extent of protection provided at the deck extremes can be described by means of the ratio of current density at the power feed point to the current density at the far end of the deck. Figure 7-11 shows graphically the effect of resistivity changes. The polarization at both deck extremes tends to be the same (current ratio approaching 1) as the concrete resistivity increases. This is to be expected, since at high concrete resistivity the IR drop across the concrete cover is the dominant contribution to the potential difference across each individual element. At the smaller concrete resistivities, representative of commonly encountered corroding deck conditions, the protective current disparity can be quite significant (from about 1.5:1 to 2:1), suggesting that the effect of anode resistance should be considered carefully in cathodic protection system design. Subcase A tends to give the greatest disparity because it imposes the most demanding polarization conditions (100 mV at the far end of the deck). With the active steel polarization curves used, delivery of 1.5 mA/ft^2 (Subcases C and D) requires only about 75 mV polarization.

As the concrete resistivity increased, the polarization tended to become more even along the deck. The dashed line in Figure 7-11 suggests that the current density ratio will tend to converge as the concrete resistivity becomes very large.

Figure 7-11. Effect of Resistivity Changes on Feed/End Current Density

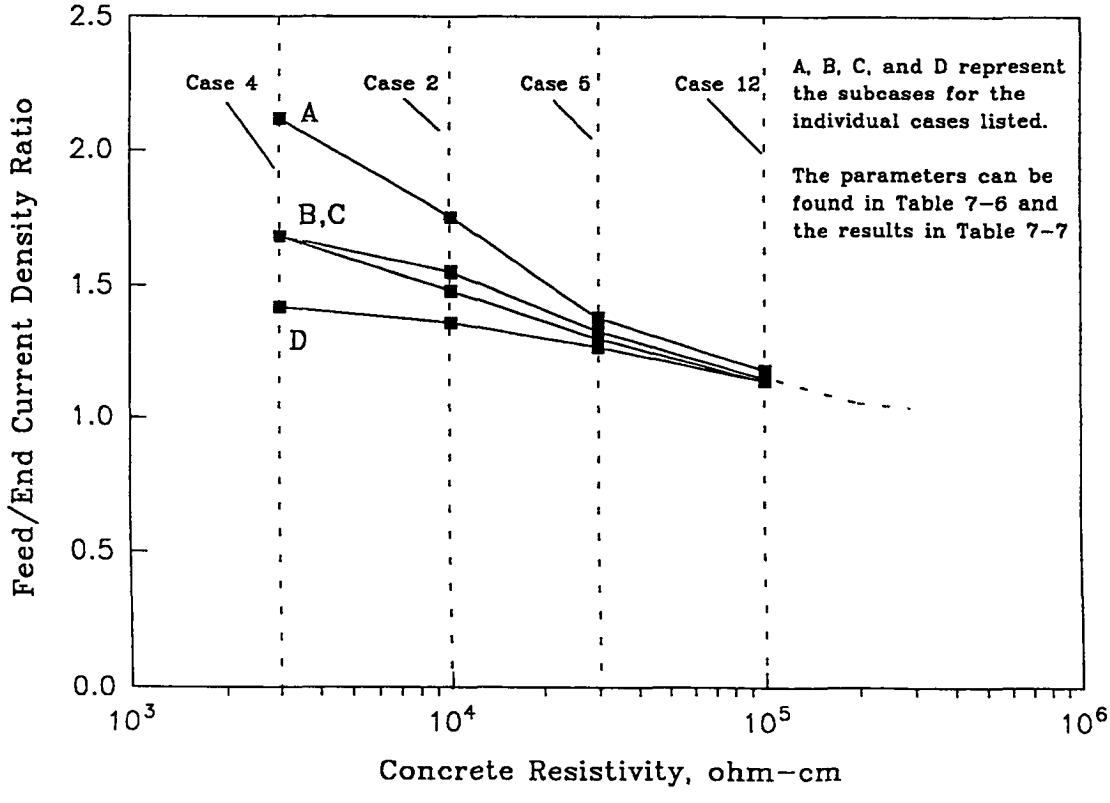

The integrated potential drop across the anode length (Vf-Ve) is also a function of the concrete resistivity. As shown in Figure 7-12, the potential drop tends to reach a limiting value at high concrete resistivities depending on the protection extent desired. Since at the high resistivity limit the current distribution under the assumed deck conditions is uniform, simple integration shows that

$$(Vf\text{-}Ve)_{high\ \rho\ limit} = i\ \rho\ L^2/2 \qquad (8)$$

For the conditions examined, Equation (8) predicts that the (Vf-Ve) limit is 151 mV for i=1.5 mA/ft^2 and 255 mV for the 100 mV polarization case (equivalent to 2.53 mA/ft^2 for the active steel case). These values are shown in Figure 7-15, indicating good agreement between the model computations and the analytical limit calculations.

Cases 13 and 15 (figures C-65 & C-66 and C-67 & C-68 respectively) correspond to equal concrete resistivity values (10 k ohm-cm) at the feed point, but different resistivity values at the far end of the deck (3 and 30 k ohm-cm respectively), with linear variation of resistivity with distance in between. All other parameters were kept the same. As shown in Figure 7-13 (which also includes Case 2), a resistivity decreasing with deck distance causes the current distribution to be more uniform for either protection criterion. The effect of the potential drop along the anode is counteracted by the reduction in the ohmic component of the potential across each element when moving away from the feed strip. As shown by the distribution curves for Case 13 (figures C-65 and C-66), the polarization can actually begin to increase after a minimum if the concrete resistance reduction is pronounced enough.

Figure 7-12. Effect of Resistivity Changes on Anode Voltage Drop

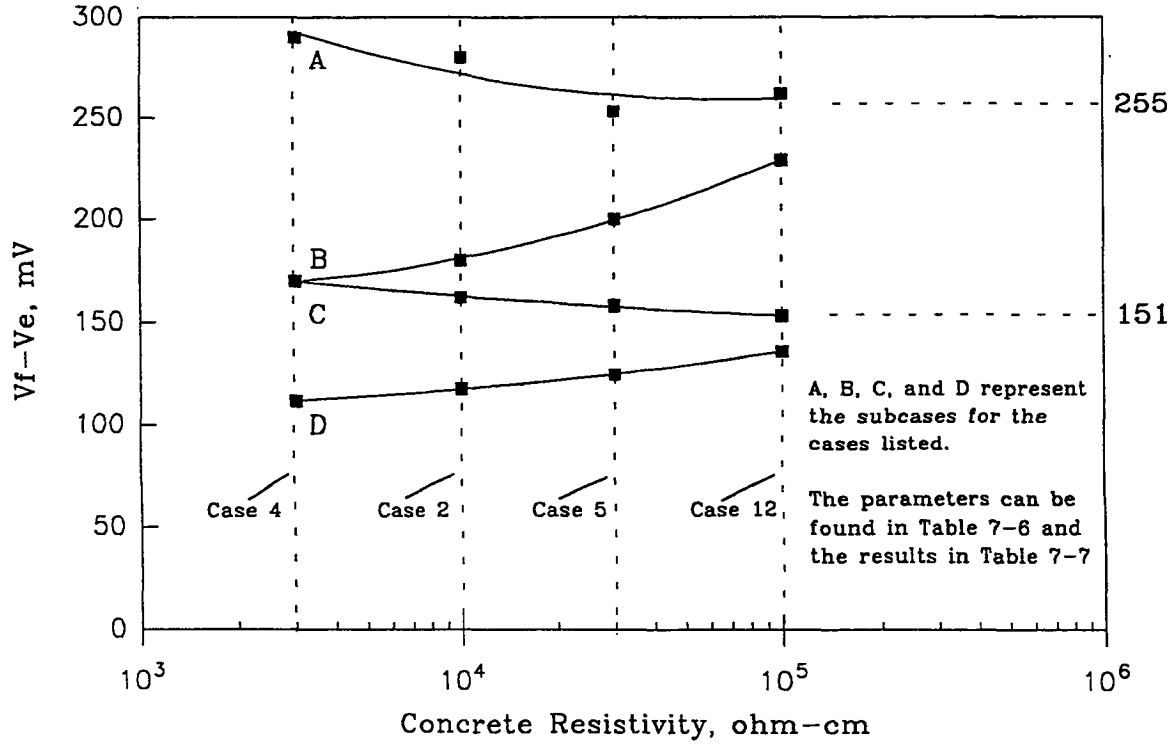

Figure 7-13. Feed/End Current Density Ratio as a Function of Feed/End Resistivity Ratio

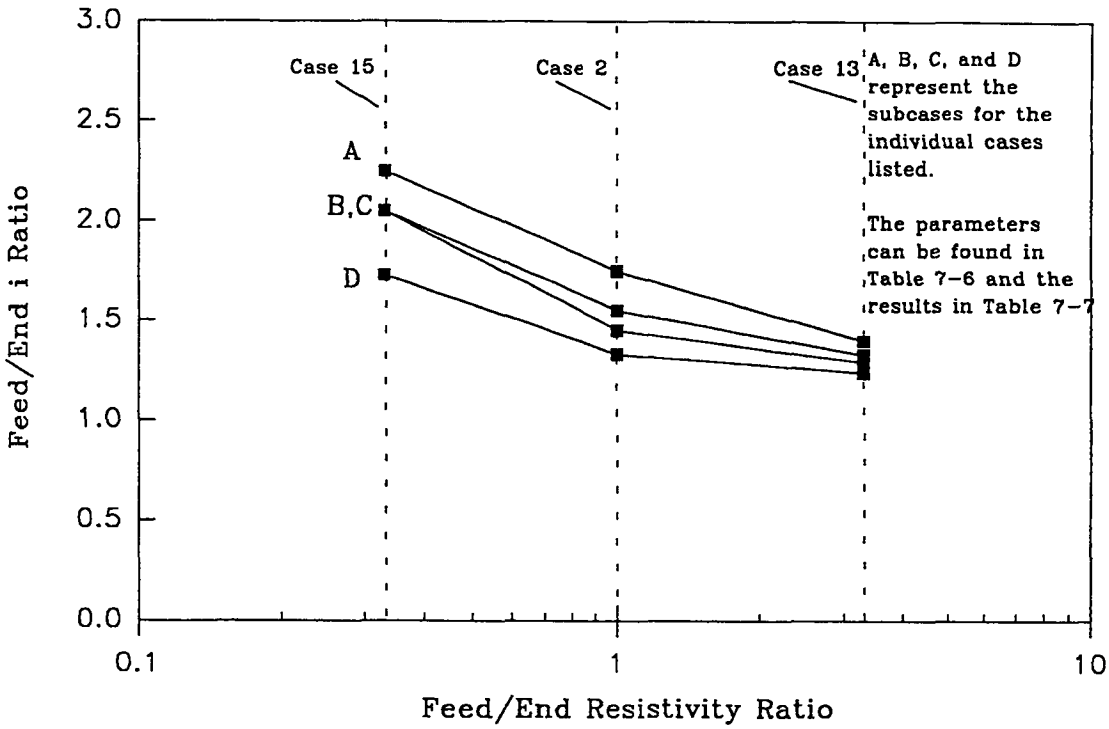

Effect of Concrete Cover

The cases discussed above are (within the model simplifications) fully equivalent to examining variations in the concrete cover along the deck length, as long as the product of concrete resistivity by concrete cover is equivalent to those of the cases treated. Thus for example, cases 13 and 15 (figures C-65 & C-66 and C-67 & C-68 respectively) are equivalent to a deck with uniform concrete resistivity of 10 KΩ-cm, but where the cover varies from 2 inches at the feed strip to 0.6 inches at the far end as in Case 13 (figures C-65 & C-66) or from 2 inches at the feed strip to 6 inches at the far end as in Case 15 (figures C-67 & C-68).

Effect of Anode Linear Resistivity (Active Steel Mat)

Figure 7-14 shows the feed/end current density ratio as a function of anode linear resistivity for cases with active steel and similar deck dimensions, cases 2, 9, and 11 (figures C-45 & C-46, C-57 & C-58, and C-61 & C-62 respectively). The zinc anode polarization characteristics for Cases 9 and 11 (figures C-61 & C-62 and C-65 & C-66) are the same, but different from the polarization characteristics for the titanium mesh anode, Case 2 (figures C-49 & C-50). The dominant cause of the displayed behavior is likely to be the anode resistance; for the zinc cases the potential drops along the anode have negligible effect on the distribution of the protective current. As shown in Table 7-7 and figures C-53 and C-54, the high anode linear resistivity for the conductive paint anode causes strong disparity

between the current delivery at the feed and end points, even though the region length is only 5 ft. The high resistivity of that material also prevented achieving 100 mV polarization decay at the far end of the deck region without exceeding the maximum documented anode current delivery performance at the feed strip.

Figure 7-14. Feed/End Current Density Ratio as a Function of Anode Linear Resistivity

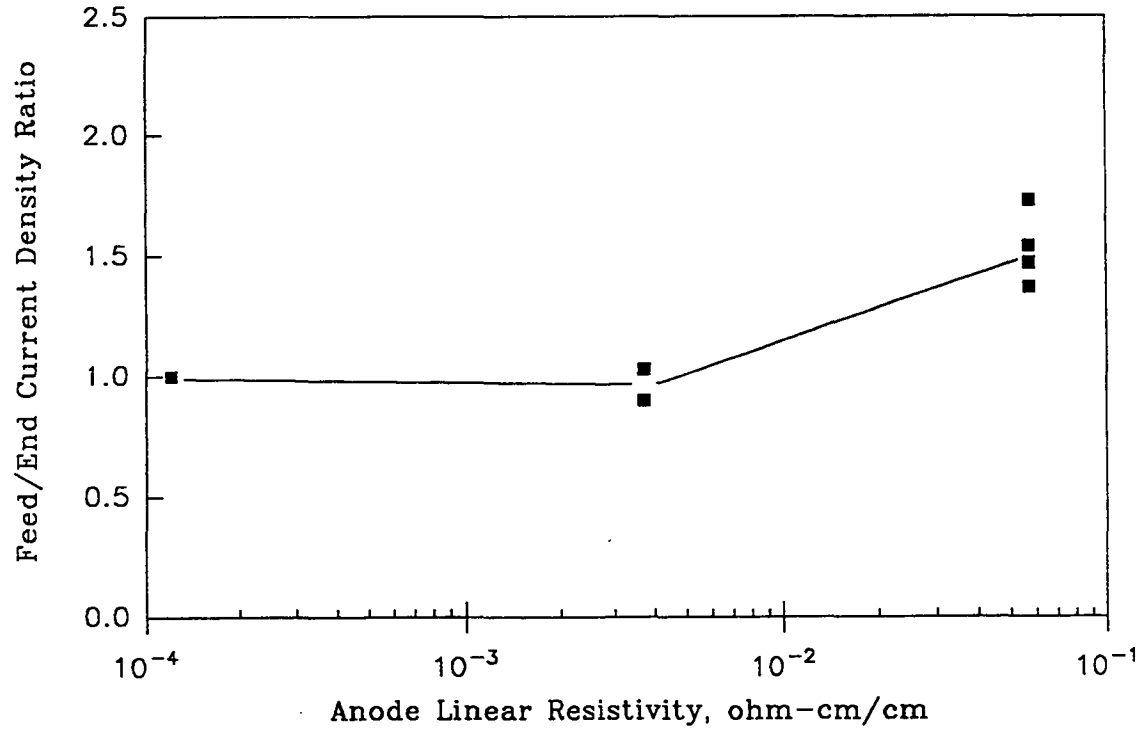

Effect of Active/Passive Steel Condition

As shown in Table 7-7 and in figures C-51 & C-52, C-55 & C-56, and C-61 & C-62, the 100 mV polarization of the passive steel could be achieved easily and with good uniformity even when using the conductive paint anode. This finding is explained by the very small current densities required to significantly polarize the passive steel. When attempting to deliver 1.5 mA/ft^2 to the passive steel the task wa .nuch more difficult except for the case of the zinc anodes. This is to be expected since the system, once adjusted to deliver the specified current density, will have to deliver it through the anode and cause ohmic potential drops that will tend to be the same regardless of the nature of the steel being protected.

Case 16 examines a combination of mixed active-passive steel regions (figures C-69 & C-70). Elements 6, 7 and 8 are active, while the rest of the deck is passive. Figure 7-15 shows the steel potential with the anode in place but without applied protective current. The system is a corrosion macrocell, with the active zone behaving as an anode and the passive zone as a cathode. To simulate this condition it was necessary to add plausible reverse polarization regimes to the steel and anode performance curves, as shown in figures 7-8 and 7-9. Subcase A′ corresponds to the application of protection to polarize the steel at the far end of the active

zone 100 mV in the protective direction, away from the local macrocell potential. Subcase C' corresponds to 1.5 mA/ft^2 of protective current at the far end of the active zone.

Figure 7-15. Mixed Active/Passive Case

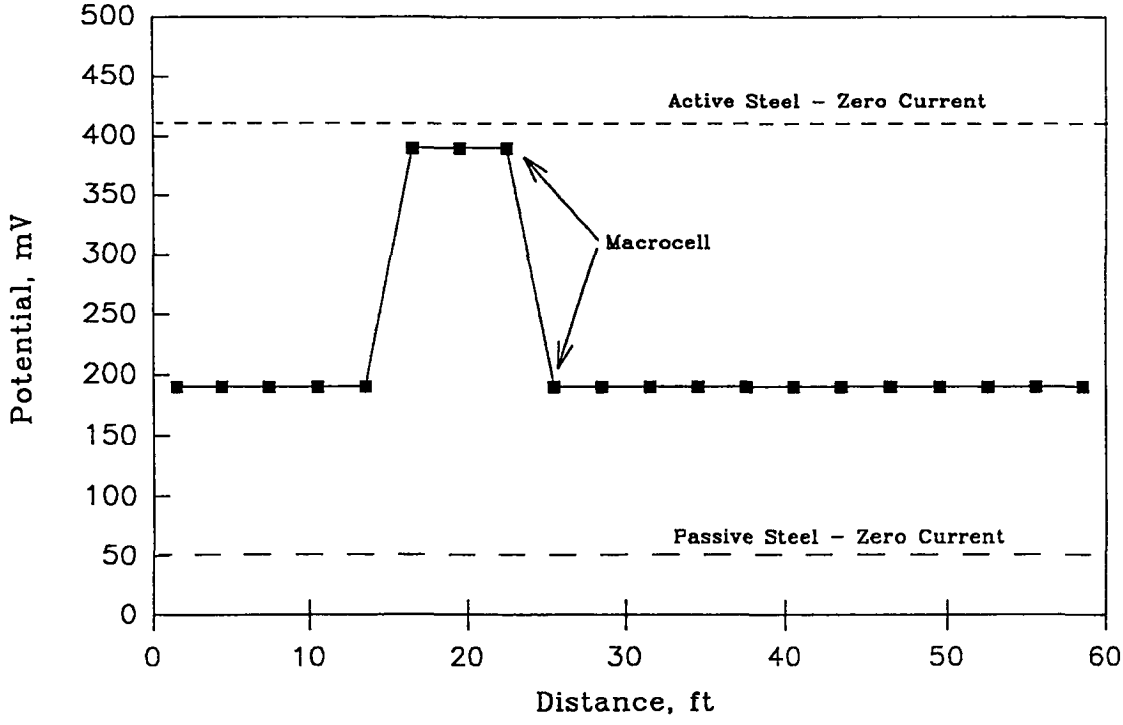

Because of the behavior assumed for the steel in Figure 7-8, substantial polarization (and consequent cathodic current delivery) needs to be applied to the surrounding passive steel to adequately polarize the active region. Thus, shifts of about 200 mV and currents as high as 3.5 mA/ft^2 were required in the passive region to allow for 100 mV or 1.5 mA/ft^2 delivery in the active region. These results underscore the importance of properly identifying regions of high corrosion activity and properly placing reference electrodes in addition to considering likely current consumption for adequate cathodic protection system setup.

Effect of Anode Material

The principal effect of changing the anode material appears to be related to the linear anode resistivity. Thus, the conductive paint anode shows the greatest unevenness of current delivery even with a much reduced deck region length.

The potential of zero current of each anode affects the overall operating point of the system, by creating different amounts of backvoltage. It should be noted that the zinc anode could operate as an efficient galvanic anode in the case of passive steel for both the 100 mV and the 1.5 mA/ft^2 conditions. Actually, to keep the protective action within the limits specified for Case 10, in Table 7-6, it would be necessary to connect the external power backwards to the levels shown in Table 7-7. A similar hypothetical situation would be reached with the

conductive paint anode and passive steel for the 100 mV condition. For active steel and the zinc anode, Cases 9 and 11 (figures C-57 & C-58 and C-61 & C-62) respectively, the desired protection could be achieved with modest external power applied voltages. The results of these cal8culations are in agreement with the observation of significant current delivery in galvanic sprayed anode systems presently undergoing field testing.

The linear resistivity of the zinc anodes is so small that even in the case of the aged anode example (30 times more resistive than in the ideal Case 9) the distribution of protective current was very uniform.

Anode polarizability is expected to affect the current distribution to some extent. However, for the current densities demanded in the active steel cases (about 1 mA/ft^2 or more) all three anode systems operate with comparable polarization slopes (see Figure 7-8) so that anode polarizability effects are likely to be secondary to those resulting from differences in linear resistivity. For passive steel systems operating at 100 mV polarization, where the current demand is much lower, the greater polarizability of the conductive paint anode may be a more important factor in differentiating performance compared with the titanium mesh or zinc anode cases.

Conclusions

1. Anode resistance can be an important factor in determining the uniformity of protective current distribution. The delivered current density tends to decay away from the power feed point. Under representative bridge deck conditions, the resistance of a type 210 titanium mesh anode could cause differences in current delivery on the order of 2:1 between the power feed point and the other end of the deck region protected.

2. Anode resistance could cause severe lack of protection uniformity when using conductive paint anodes having resistance within the expected range. This would require placing supplemental power feed strips only five or ten feet apart.

3. Sprayed zinc anodes are not expected to originate severe resistance effects in the freshly applied condition.

4. The effect of anode resistance on current distribution uniformity is significantly reduced as the resistivity-thickness of the concrete cover increases.

5. Uneven current distribution due to anode resistance is less important when the steel is passive and a polarization potential cathodic protection criterion is used. However, if a sizable value of current delivery is specified (typically 1.5 mA/ft^2) as the protection criterion then anode resistance becomes important even for passive steel.

6. Increasing concrete resistivity (or concrete cover) along the deck length away from the feed strip creates a more uneven current distribution than that obtained with uniform resistivity (cover) equal to that present at the feed point.

7. Decreasing concrete resistivity (cover) away from the feed strip promotes a more uniform current distribution. Depending on the resistivity (cover) profile, current density can begin to increase again after an intermediate distance along the deck.

8. When attempting to protect steel in a small active region surrounded by passive steel, significant disparity of polarization and current delivery could result along the deck. The calculations show that the surrounding passive steel might need to be polarized by 200 mV to achieve 100 mV polarization of the active portion. Current density demand could also be greater in the surrounding passive region. The results suggest that identification of highly corroding regions and appropriate reference electrode placement is critical to obtain adequate protection, as discussed previously.

9. In general, the 100 mV polarization criterion required large impressed current densities to be achieved with fully active steel mats. Examination of the model predictions based on other sources of experimental polarization data would be desirable to determine whether this is a general trend.

8

Discussions and Conclusions

Introduction

The objective of this task was to investigate the feasibility of identifying improved and simplified control criteria for cathodic protection of reinforced concrete structures.

Although several criteria have been proposed for use in concrete, none have been rigorously studied and verified for concrete. No criterion had been quantitatively correlated to actual rate-of-corrosion of steel in concrete by experimental data. Such data are very difficult to establish. This has been a major contributor to the lack of a universally accepted criterion for cathodic protection in concrete.

Concrete is very inhomogeneous and difficult to test. Weight loss experiments are especially hard to conduct. The objectives of establishing a criterion which is both technically accurate and simple, appeared, at first, to be mutually exclusive. It was first decided to eliminate certain approaches.

The criterion based on current-potential relationship (E-log I) was rejected since it is too complicated to test and interpret. The theoretical basis for the E-log I test, as used in concrete, is questionable, but it has provided reasonable guidance. This criterion is normally only conducted by experienced consultants and experts in the field. Furthermore, it very often cannot be interpreted, since a significant straight line portion cannot be found.

An absolute potential-based criterion was not pursued because of the unreliability of long-term measurements, and has been found to be generally unworkable in the past. This criterion has often been found to result in overprotection.

A criterion based on a statistical treatment of static steel potentials is an attractive concept, but the one listed in NACE Recommended Practice RPO-0290-90 is questionable. It is also dependent on the accuracy of steel potentials as recorded from the surface of the concrete. Although this approach has the advantage of simplicity, it was not pursued extensively under this contract.

A criterion based on operating voltage was also rejected. It was felt that such an approach would not be sophisticated enough to be technically accurate. System voltage is affected by changes at the anode or in the concrete which may not necessarily reflect the corrosive state of the steel.

Potential Shift Criterion

The 100 mV polarization decay criterion was already the most popular criterion for use in concrete since the test is relatively simple to conduct and interpret. Although a few details of the test procedure are still debated, its use has generally proven to be acceptable. The initial work of this study was focused on determination of the correct amount of polarization to use. Literature values of acceptable polarization range from 220 mV down to 50 mV for corrosive conditions, and even lower for steel with static potentials more positive than -350 mV versus CSE.

The "correct amount of polarization" depends on the actual rate of corrosion of the steel. Consequently, the first task was to determine an acceptable rate of corrosion for steel in concrete. This was defined as the corrosion rate which would not cause cracking of the concrete over a period of 20 years. The amount of corrosion needed to cause concrete cracking was 2-10 mil.[17,37] Using the conservative number of 2 mil over a period of 20 years, the acceptable rate of corrosion of 0.1 mil/yr was established. Thus, the cathodic protection system needs to operate at conditions which will keep the corrosion rate <0.1 mil/yr.

Corrosion rate experiments were conducted in sand wetted with pore-water solution to simulate a concrete environment while also allowing access of oxygen for the corrosion process. This technique allowed easy determination of corrosion rate by weight loss measurement. The results of these experiments, expressed as corrosion rate versus polarization, are shown on Figure 3-8 for chloride concentrations ranging from 1-30 #/yd^3. Each data point on this graph is an average of data from five cells. Although much more data would be needed to establish the rates quantitatively, general relationships can be seen. Increasing chloride concentration increases corrosion rate, and increasing cathodic polarization sharply decreases corrosion rate. These relationships are further complicated by pH and temperature effects. Figure 3-8 is valid only at pH = 13.37, and will vary considerably at other pHs.

The exact amount of polarization needed to limit corrosion rate to <0.1 mil/year is quite complex, and depends on several variables. This makes the use of polarization, as a criterion, very difficult, if it is to be technically accurate.

A criterion which uses polarization decay as a technique is limited in its accuracy because of the 4-hour test period typically used. It is often necessary to wait much longer than four hours for complete decay, especially for systems which are water saturated or which have been under cathodic protection for a long period of time. Waiting a longer period of time is often misleading, since changes in environmental conditions can significantly affect the potential readings.

In summary, although the data in this study seem to generally support a polarization criterion of 150 mV, it was concluded that the use of this criterion is not simple, and therefore did not fully meet the objectives.

Corrosion Null Probe

Based on the above results, it was decided to shift attention toward current-based criteria. This decision was supported by the results shown on Figure 4-1, which is a plot of corrosion rate versus corrosion current, for various chloride concentrations, flowing to the anode. This figure implies that if corrosion current could be measured and controlled, it could be used as an accurate and relatively simple control criterion. In other words, making the steel net cathodic effectively stops corrosion. This is a well accepted principle of cathodic protection, but this is the first confirmation of its effectiveness in concrete.

Most of the corrosion occurring in these tests can be attributed to pitting corrosion, which measured weight losses include. Cathodic protection current controls both macrocell and pitting corrosion.

A series of experiments were conducted to determine the cathodic current needed to control corrosion at various salt concentrations. The results of these experiments are shown in Figure 4-11. For these tests, cathodic protection current was gradually increased using auxiliary anodes placed near the corroding steel coupon. The null point, the point when the corrosion current was exactly balanced by the cathodic protection current, was recorded. The technique of arresting corrosion by making the corroding steel net cathodic is valid regardless of salt concentration, pH or temperature.

To use the Corrosion Null Probe technique in the field, a short length of reinforcing steel in the most anodic area is cut without further disturbing the native concrete matrix. Current flowing to or from the probe is monitored by measuring voltage drop across a resistor connected between the probe and system negative.

This approach appears to offer a technically accurate and simple to apply criterion for cathodic protection of reinforcing steel in concrete. It is site specific, and will reflect diminishing current requirement with time. Installation is simple, and the criterion test is quick and easy to perform. Significantly, it does not rely on the long-term stability of embedded reference electrodes.

The Corrosion Null Probe technique does require that reinforcing steel be cut and isolated, and in some cases this may be objectionable. One such case would be where prestressed steel is involved.

Another concern is the need to select the most anodic area for construction of the probe. This must be done very carefully using ASTM C-876-91, "Standard Test Method for Half-Cell Potentials of Uncoated Reinforcing Steel in Concrete" after patching has been completed. If the probe is installed in the wrong location, the cathodic protection current will be misjudged. Locating the probes in sites which are not the most anodic will cause inadequate cathodic protection current to be applied to the reinforcing steel. It is also important to keep the probes electrically connected to the system negative during construction or the macrocell action will be destroyed. This can cause even very actively corroding steel to go passive.

Despite these concerns, the Corrosion Null Probe is considered a promising criterion for the control of cathodic protection systems, and further field testing is recommended. The major question remaining is whether it is reasonable to expect contractors to exercise the care necessary for proper installation. Close involvement or inspection by the corrosion engineer is recommended.

Other Approaches Based on Current

A very attractive concept is to select a cathodic protection current based on the corrosive state of the reinforcing steel. For example, a statistical treatment of potentials from a corrosion potential survey might be used to establish start-up current. In theory, a relationship might be established which would indicate a high protective current for a structure with very negative static potentials, and little or no current for structures with passive steel. Current could then be adjusted downward with time-on-line based on the computer modeling of concentration profiles (see next section). The problem with this approach lies with the fact that corrosion potentials do not necessarily relate to corrosion rate, but only indicate probabilities of corrosion activity. If structures are very saturated or submerged, for example, corrosion potentials may be very negative even though very little corrosion is occurring. In this study, the relationship between corrosion potentials and required cathodic protection current was generally poor. Therefore, the approach of relating cathodic protection current to a potential survey appears unlikely.

Another possibility would be to relate start-up current to linear polarization measurements, which relate directly to corrosion rate. For this case, a potential survey might be utilized to identify the areas of most probable corrosion activity. Linear polarization measurements could then be made in those areas of greatest activity. Here again, current could be adjusted downward with time-on-line based on the expected change of concentration profiles. The major concern lies with the sophistication of the linear polarization measurements. This test requires a special piece of equipment which is not trivial to operate or interpret. Also, significant differences exist in measurements taken using different devices.

A better approach takes advantage of the relatively good correlation between chloride concentration and cathodic protection current requirement. This relationship is shown in

Table 4-1. Here again, a potential survey could be used to identify the areas of most probable corrosion activity. Samples of concrete could then be taken at the level of the reinforcement for chloride analysis. Start-up cathodic protection current is then based on the level of chloride contamination. Once again, the protective current would be adjusted downward with time-on-line. This approach, based on chloride concentration, appears to offer a simple criterion with reasonably good accuracy. The required tests are straightforward and familiar to the construction industry. This approach, in addition to the Corrosion Null Probe, warrants further consideration and testing.

A final possibility based on current is the "worst-case" approach. Here a relatively high current would be applied at start-up, and this would be adjusted downward with time-on-line. This approach requires no knowledge of steel potentials, chloride concentration or rate of corrosion. It requires no special testing or care during installation. Unfortunately, it is also relatively inaccurate, and will often result in overprotection. This approach sacrifices too much for the sake of simplicity, but others may have a different view.

All of these current-based criteria have major advantages over those presently in use. They are simple to apply and interpret. They do not rely on the long-term stability of embedded reference electrodes, and this is certainly a major benefit.

Mathematical Modeling

Several factors have an effect on the distribution of current to the reinforcing steel. These can be separated into factors which can be controlled, and those which cannot. Variations of current density due to resistance in the anode is one factor which can be controlled by proper design. The modeling done at the University of South Florida confirms the importance of design for certain types of anodes. Conductive paint systems, which have a relatively high linear resistance, can result in very poor current distribution, even with a current distributor spacing of only a few feet. Conversely, the distribution of current from a sprayed zinc anode is almost completely uniform due to its very high conductivity. Titanium mesh anodes are intermediate in conductivity and must be properly designed for current distribution. Results indicated that total voltage drop in the anode structure must not exceed 250 to 300 mV for adequate current distribution.

This modeling also serves to underscore the importance of locating the reference electrodes in the most anodic (negative) portions of the structure. It has been observed that, in practice, reference electrodes are often located carelessly, despite the clear statements in recommended practices and specifications. Incorrect location of reference electrodes clearly compromises the effectiveness of the cathodic protection criteria.

Variations in concrete resistivity and/or cover (anode/steel spacing) can have a significant effect on the distribution of current. Changing the concrete resistivity or cover by a factor of three will change the difference in current delivery by 50 percent. Since we cannot always locate reference electrodes ideally in this regard, this has an effect on how criteria should be applied. Once the proper current has been determined for a cathodic protection zone, it should be increased by a safety factor to compensate for disparity in current. For a bridge

deck, an appropriate safety factor might be about 20 percent. For bridge substructures or parking garage structures which are less uniform, a safety factor of 50 percent would be more appropriate.

Mathematical modeling was conducted at Case Western Reserve University to establish the profiles of concentrations which develop at the surfaces of electrodes in concrete. This work, which was based on solution theory and a technique developed by Newman, was especially revealing. As expected, the passage of cathodic current results in the migration of chloride away from the steel, and the build-up of hydroxide and cations at the steel surface. Since diffusion coefficients are small in concrete, these concentration profiles are dramatic, and have a profound effect on the corrosion rate of the steel. The effects of chloride concentration, chloride distribution, temperature and current density are especially significant on the development of such profiles. The model can also be used to predict the relaxation of concentration profiles after current is turned off.

The most significant assumption in this model is a chloride diffusion coefficient in concrete of 2.0×10^{-8} cm^2/sec, and a hydroxide diffusion coefficient of 5.3×10^{-8} cm^2/sec. These coefficients were based on a combination of literature values and work conducted under SHRP-C-103. Other diffusion coefficients were determined from these figures based on solution theory. The use of other diffusion coefficients will significantly alter results. The degree of saturation, or water/cement ratio may cause deviations.

This model greatly improves the understanding of the consequences of the passage of current through concrete. Further development and verification of this model is highly recommended.

Major Conclusions of This Work

1. Corrosion cells filled with sand wetted with pore-water solution offer a relatively simple means of measuring corrosion rate of steel in a simulated concrete environment. In this case, corrosion rate can easily be determined from weight loss measurements.

2. The rate of corrosion of steel in concrete is strongly dependent on chloride concentration, pH, and temperature.

3. The application of cathodic protection current is a highly effective means of controlling corrosion of steel in concrete.

4. The criterion of 150 mV polarization (or polarization decay) is a reasonably accurate criterion for new cathodic protection systems, over time, it is likely to result in overprotection. Also, this criterion has inherent complexities, such as the use of reference electrodes and the need to measure complete polarization decay in a period of four hours.

5. Where polarization-based criteria are being used, it is very important to locate the reference electrodes in the most anodic (most negative) area of the cathodic protection zone.

6. Cathodic protection systems which have been operating for long periods of time, may take much longer than 4 hours to depolarize. In fact, complete polarization decay may take up to four days. Unfortunately, potentials taken over this period of time are likely to be significantly influenced by environmental conditions.

7. The Corrosion Null Probe (CNP) appears to be a relatively simple and effective criterion for cathodic protection of steel in concrete. Additional field experience is recommended.

8. Other current-based criteria appear promising. In particular, the simple application of a current based on the concentration of chloride initially present at the steel appears to be a promising approach.

9. The passage of cathodic protection current results in a dramatic reduction of Cl^-/OH^- ratio with time. This reduction results in a reduction of corrosion rate and, therefore, a reduction in the current needed to maintain an acceptable rate of corrosion. Concentration profiles which develop are especially sensitive to chloride concentration, chloride distribution, temperature and current density.

10. The anode resistance should cause less than 300 mV IR-drop across the anode. This will require closer spacing of primary feed wires than is commonly specified for carbon based paint systems. Conversely, sprayed zinc systems show negligible resistance and no significant IR-drop was observed.

11. Concrete resistance, depth-of-cover and the existence of active/passive regions all have significant effects on current distribution. A general safety factor in current of 20 percent for bridge decks, and 50 percent for bridge substructures is recommended to accommodate such variations. A thorough knowledge of the structure may suggest otherwise.

12. Cathodic protection current may initiate or slightly accelerate alkali-silica reactivity in structures containing alkali sensitive aggregate.

13. Anode reaction products generated at the anode can result in discoloration and softening of the concrete near the anode surface. This effect is most severe for carbon-based anodes. Although this reaction did not result in system failure for any of the systems tested during the test period, it suggests that overprotection should be avoided.

14. The combination of mathematical modeling and corrosion studies as conducted in this contract offers important new insights into the subject of criteria for cathodic protection of concrete structures. Continued studies along these lines are strongly recommended.

Appendix A

Null Probe Installation Specifications

Installation Specifications

General

This specification covers the materials and installation of the Corrosion Null Probe (CNP) shown in Figure 4-4. It is recommended to install at least two CNPs for each cathodic protection zone.

Materials

Lead Wire

The lead wire shall be AWG No. 16 stranded copper with XLPE insulation (Alpha Wire Corp. # 7045) or approved equal.

Terminal Connectors

The terminal connector used to connect the lead wire to the reinforcing steel shall be a solderless, non-insulated ring connector sized to fit a No. 8 screw and No. 16 wire. The terminal connector used to connect the lead wire to the system negative at the rectifier shall be a solderless spade connector sized to fit a No. 16 wire.

Resistors

Resistors used to measure current shall be wire wound resistors with a 10 ohm resistance, Dale No. 13F136 or approved equal.

Conduit

The conduit used shall be that specified for the project.

Junction Box

The junction boxes used shall be those specified for the project.

Epoxy Filler

The epoxy filler used to seal the bottom of the probe excavation sites shall conform to ASTM C 881, Standard Specification for Epoxy-Resin-Base Bonding systems for Concrete, Type I, Grade 3, Class B. The manufacturer's proportioning, mixing, placement specifications and recommendations shall be followed. Pre-proportioned dispensing cartridges with an integral motionless mixing tube may be used in lieu of manual proportioning and mixing.

Grout

The grout used to fill the upper portion of the probe excavation sites shall be Masterpatch 230 VP, manufactured by Master Builders, Inc. Filler aggregate shall not be added to the mix for extending the quantity of grout yield. The manufacturer's proportioning, mixing, and placement specifications and recommendations shall be followed.

Construction

This section details the installation procedures for the CNP's at locations identified on the plan sheets. The lead wire shall be attached to the reinforcing steel and the excavation backfilled prior to the installation of the anode. The junction box and conduit shall be installed after the anode installation.

Concrete Removal

As indicated in Figure 4-15, individual reinforcing bars must be severed and concrete must be removed to allow for installation of the instrumentation. The bars shall be cut and the concrete removed by dry abrasive cutting or grinding. Water shall not be used as a coolant or removal medium. A six inch diameter cutting or abrasive wheel should be used to avoid removing an excessive amount of concrete.

The exposed surface of each reinforcing bar shall be cleaned to grey metal in the area where the lead wire will be connected to insure a positive electrical connection.

The entire excavated areas shall be blown clean with clean, dry, oil-free compressed air prior to the installation of any hardware.

Lead Wire Installation

The lead wire shall be attached to the reinforcing bar by means of a pan head Phillips stainless steel No. 8-32 x 3/8 inch screw. Using a #21 drill, a pilot hole 1/2" deep shall be drilled into the reinforcing bar and threaded with an 8-32 tap prior to securing the lead wire. The lead wire shall extend above the excavation area. The excavation shall be filled as specified prior to installation of the junction box and conduit.

Patching

After the lead wire is installed on the reinforcing bar the excavation shall be patched. The epoxy filler shall be applied to the bottom of the excavation and shall extend to the upper limit as shown on the plans. Care shall be taken to cover all exposed steel, the screw, and wire connector, and to avoid spreading the epoxy filler on the area of the excavation that will be filled with grout. The epoxy filler shall be proportioned, mixed, and applied according to the manufacturer's specifications and recommendations.

Once the epoxy filler has hardened, the grout can be applied. If more than 24 hours has elapsed prior to grout installation, the exposed surface of the epoxy filler shall be lightly abraded to provide surface roughness. The grout shall be proportioned, mixed, and applied according to the manufacturer's specifications and recommendations.

Temporary Ground Connection

Following installation, the CNP should be electrically connected to the reinforcing steel (system negative). This connection is intended to be temporary and serves to maintain the probe in its originally corroding state until construction is complete. The probes should never be discontinuous to the steel for more than two days. If the probes are left disconnected for more than two days, they shall be rejected. New probes shall be installed at no additional cost.

Conduit and Junction Boxes

The junction box shall be placed over the excavation area and shall be secured to the concrete as shown on the plans. The lead wire may be spliced in the junction box before it is run in the conduit. Splices shall be approved by the Engineer. Location of the conduit runs shall be as shown on the plans.

Rectifier Connection

A 10 ohm resistor shall be connected to the rectifier end of the lead wire with a butt splice connector. The other end of the resistor shall be connected to the negative pole in the rectifier for that zone by means of a lug connector.

Test Procedure

1. Using a digital multimeter, connect the red lead to the "probe side" of the 10 ohm resistor. Connect the black lead to the system negative side of the resistor. If the probe is corroding, a negative voltage should be read on the multimeter. Corrosion current is calculated by dividing the voltage reading by 10 according to Ohm's Law, I = E/R.

2. The following step is dependent upon the magnitude of the corrosion currents measured in step 1. Slowly increase the cathodic protection current in steps, pausing between the steps to record both cathodic protection current and macrocell currents. If multiple probes are located in one zone remember to measure each probe's current.

3. Continue to adjust the cathodic protection current until the corrosion currents on all the probes are positive indicating net cathodic current flow.

4. Data can be plotted as cathodic protection current versus macrocell current to aid in the final determination of the requisite cathodic protection current.

5. The final cathodic protection current is calculated by using the highest cathodic protection nulling current and adding current equal to 0.25 mA/ft^2 of steel. However, at no time should the final cathodic protection current exceed the maximum allowable current density recommended for the anode being used.

Appendix B

ASR Aggregate Descriptions

The aggregates used in the study include an opal from Nevada, a chert from Missouri, and a quartz from Colorado. The opal and chert aggregates were obtained as particles ranging in size from 1/2 in. to 2 in. from Geosciences Resources.[1]

The quartz is the same aggregate used as the fine and coarse aggregate in a number of concrete specimens prepared for earlier work on the SHRP-87-C102A project. The quartz aggregate was obtained from Fister/Warren Company.[2]

Quartz Aggregate

The quartz aggregate is characterized as a very coarsely crystalline, translucent, white quartz showing parting planes and a grain size on the order of several centimeters. In thin section, large areas of uniform extinction cover the field of view. Abundant fluid inclusions up to several microns are present, mostly concentrated along subparallel surfaces and linear trends. Rare, 0.1 mm elongated vugs are lined with comb-like quartz crystals. Infrequent, very thin fractures are healed with fine polycrystalline quartz. The low porosity and high degree of crystallinity are characteristic of a quartz that is not expected to be prone to alkali-silica reactions in concrete.

1. Geosciences Resources, Burlington, North Carolina. The chert source is identified as Stock No. 30-1725. The opal is identified as Stock No. 30-1770.

2. Fister/Warren Company, Des Plaines, Illinois. The coarse quartz aggregate is identified as FW302 "Milky Quartz" Size C (3/4 in. to 1/2 in.). The fine quartz aggregate is identified as FW302 "Milky Quartz" sand.

Chert Aggregate

The chert is medium grey in color with waxy luster and exhibiting conchoidal fracture. Hand specimens are translucent on edges, have a fine, smooth, mottled appearance, and are cut by numerous thin fracture lines that are mostly healed with tiny, drusy quartz crystals. Weathered edges appear lighter in color and are more porous.

In plane light, the thin section shows a few regions up to 3 mm across composed of banded, pale-brown, radial, fibrous, chalcedonic quartz. Under crossed polars, the chalcedonic quartz is composed of radiating sheaf-like bundles of fibrous chalcedony up to 200 microns across. The main matrix is composed dominantly of microquartz (up to 10 microns) with abundant coarser chalcedonic quartz of an average grain size of 15 microns.

This is a typical waxy, mottled chert common to a number of lower paleozoic carbonate units in Missouri. The porosity is relatively low and confined to submicroscopic pores in chalcedony and minute openings at grain boundaries. Because the chalcedony is abundant, the overall silica content is very high, the degree of crystallization is low, and the potential surface area is large, this chert is characterized as suspect with regard to the possibility of

undergoing alkali-silica reactions in concrete. This chert is, in fact, characterized by Cornell researchers as showing moderate ASR activity.

Opal Aggregate

Opal is a hydrous, amorphous silica containing up to 10 percent water. It has a lower density and refractive index than chalcedony or quartz. Opal is essentially a consolidated gel that x-rays as crystobalite and contains submicroscopic pores in cavities filled with hydrated solutions.

The opal for this study is a vitreous to waxy, translucent, pale, greenish to yellowish color, with bands of earthy, white porcellanite. The porcellanite is slightly more porous than the opal. The massive opal shows abundant, irregular fractures and subconchoidal fracture. Under the microscope, the opal is a massive, isotropic material showing small cracks and occasional diatom remnants. In plane light, occasional, tiny, anhedral quartz grains are seen in relief against the opal matrix.

This type of opaline aggregate is well known as being prone to ASR activity in concrete.

Appendix C

Mathematical Modeling Figures

Figure C-1. Cl^- Concentration versus Distance from the Cathode

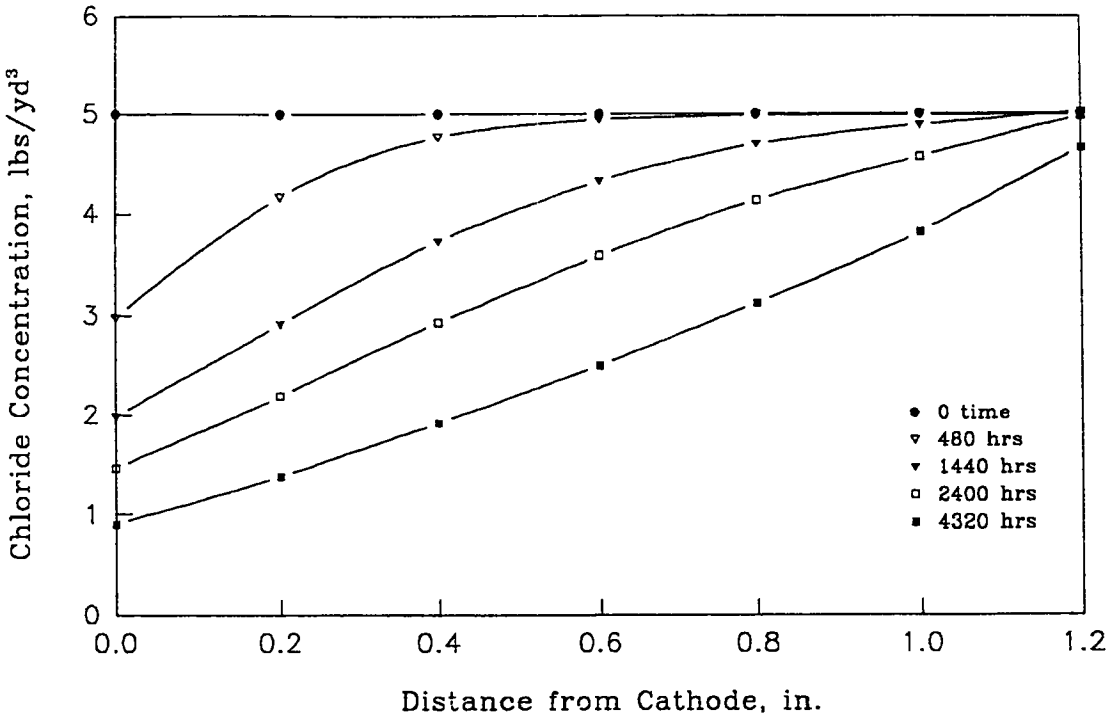

Figure C-2. pH versus Distance from the Cathode

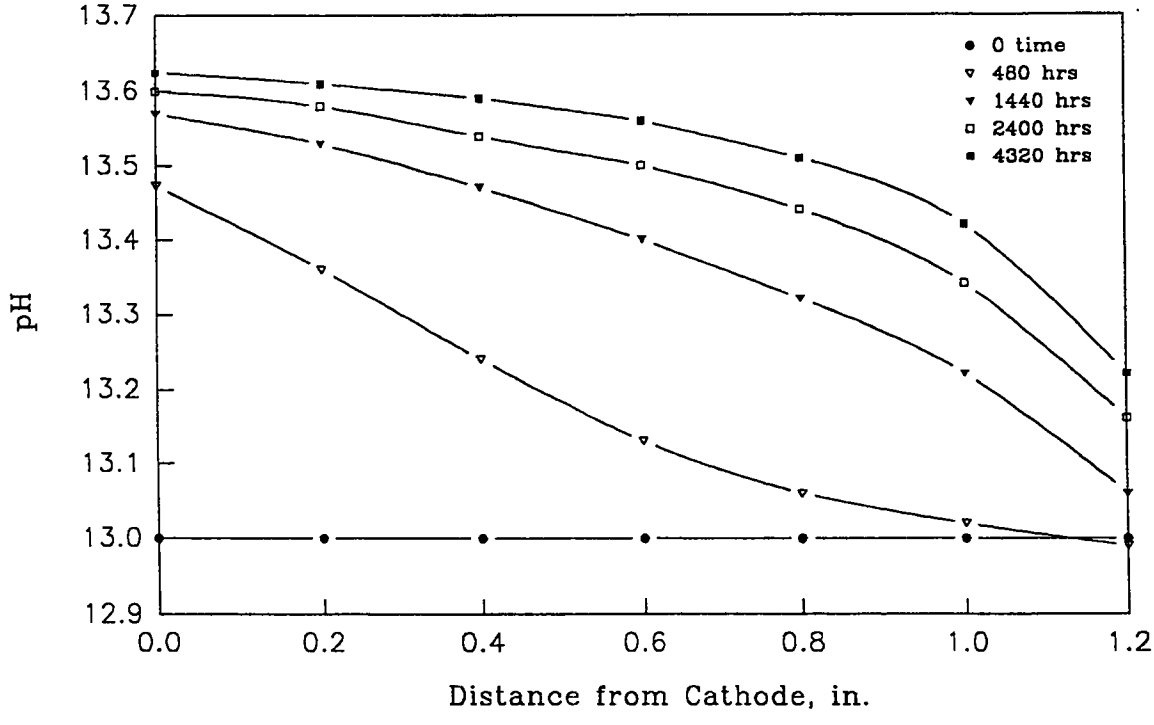

Figure C-3. Cl^- Concentration at the Cathode versus Time

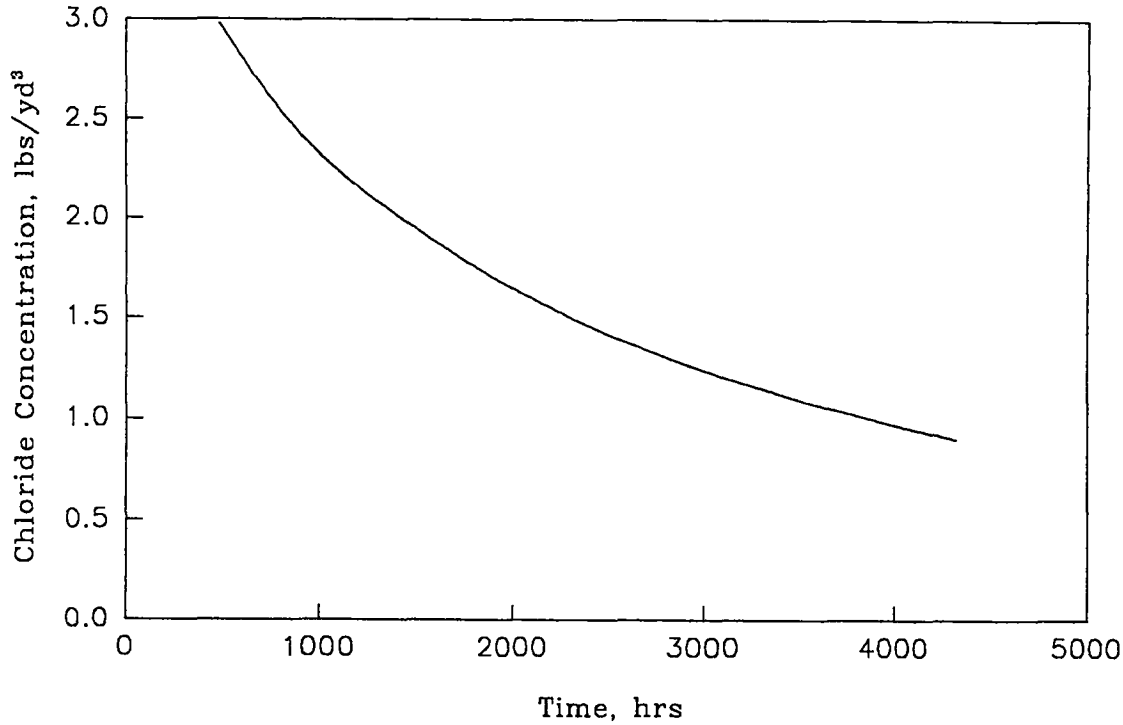

Figure C-4. Cl^-/OH^- Ratio at the Cathode versus Time

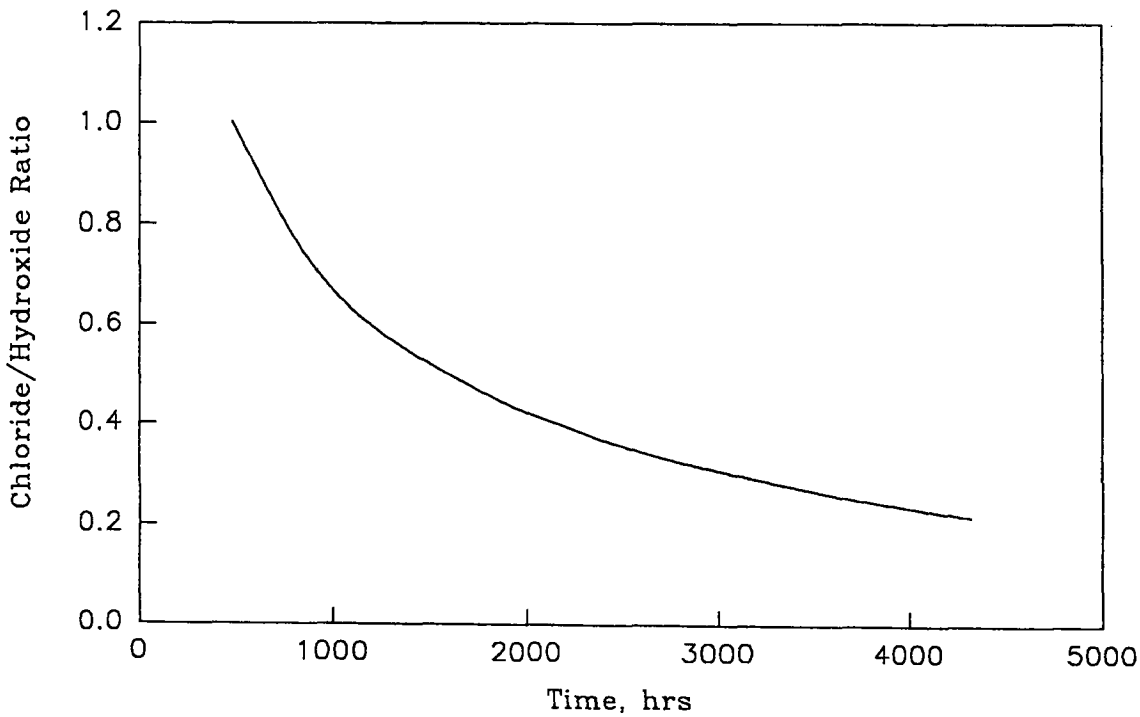

Figure C-5. Cl^- Concentration at the Cathode versus Time : Current Off @ 4320 Hrs.

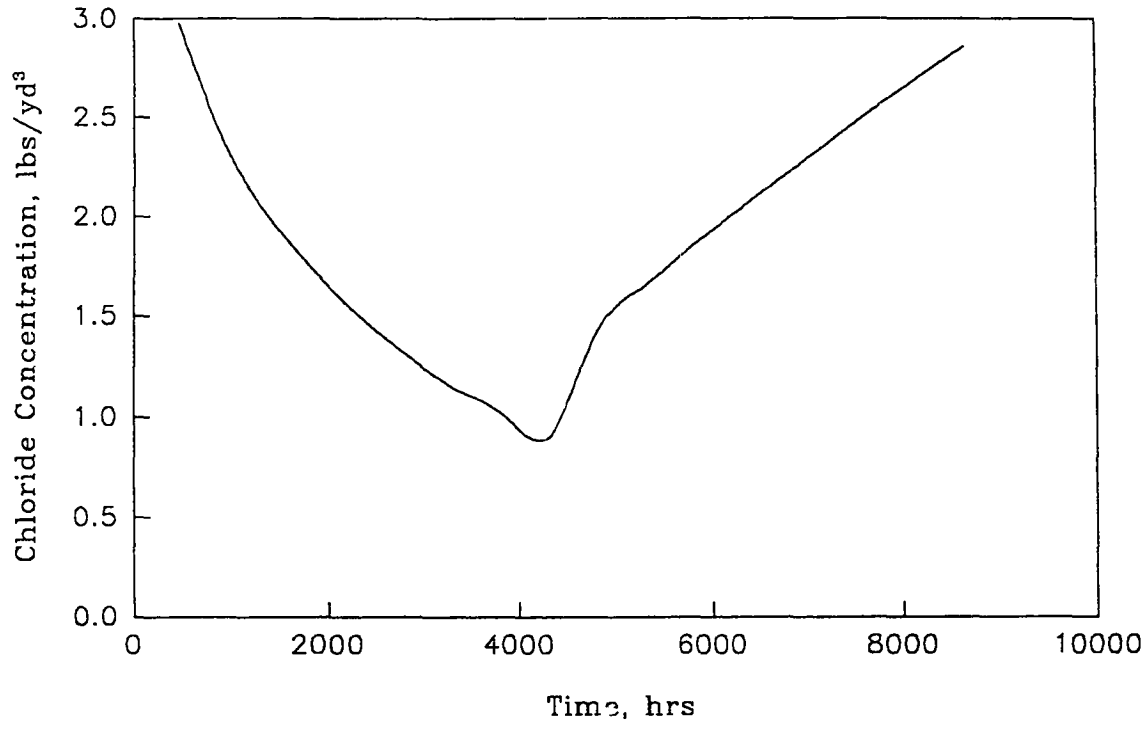

Figure C-6. Cl^-/OH^- Ratio at the Cathode versus Time : Current Off @ 4320 Hrs.

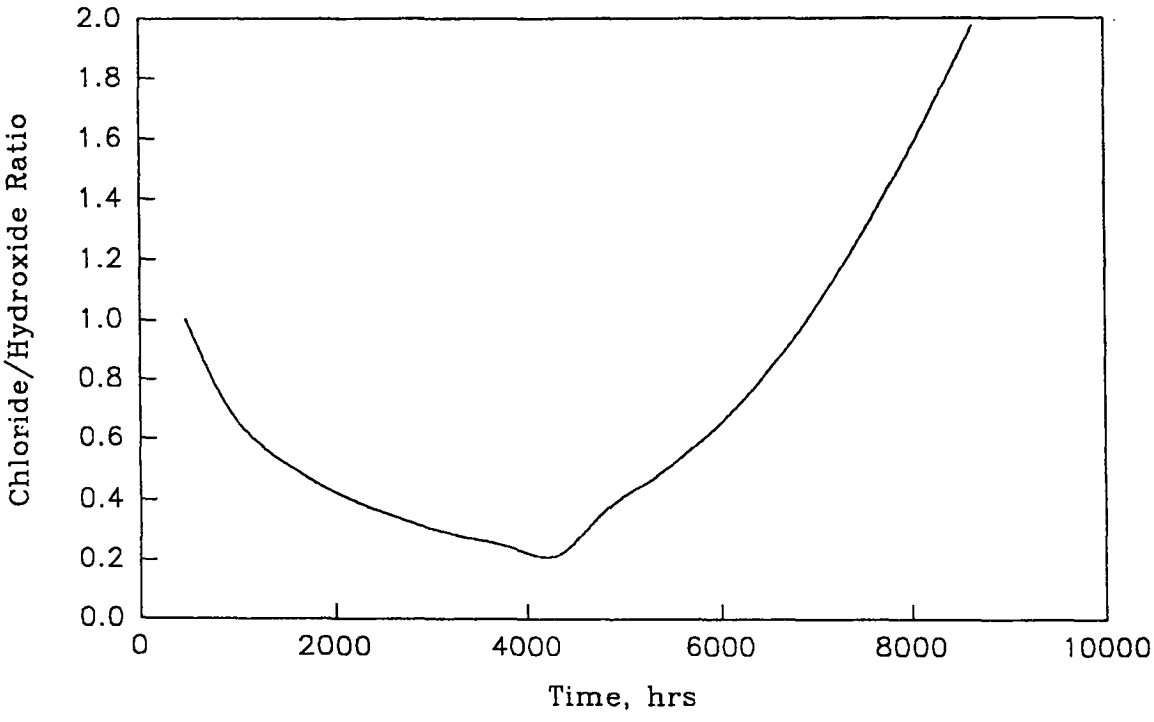

Figure C-7. Cl^- Concentration versus Distance from the Cathode @ 2# Cl^-/yd^3

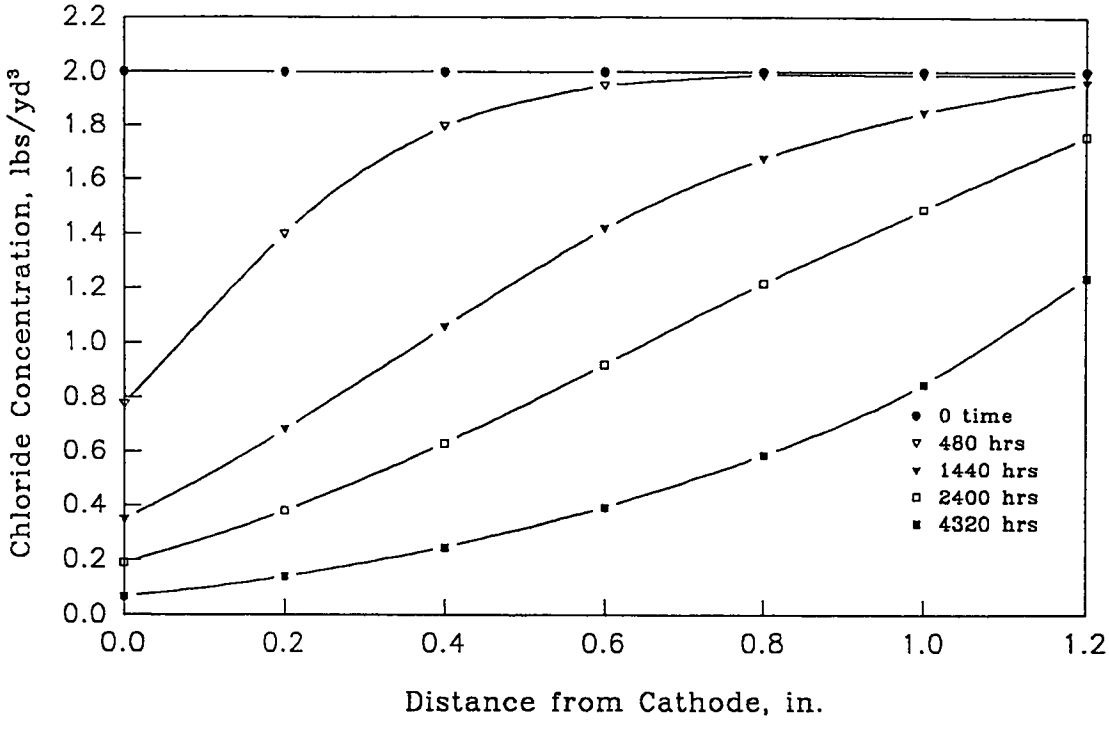

Figure C-8. pH versus Distance from the Cathode @ 2# Cl^-/yd^3

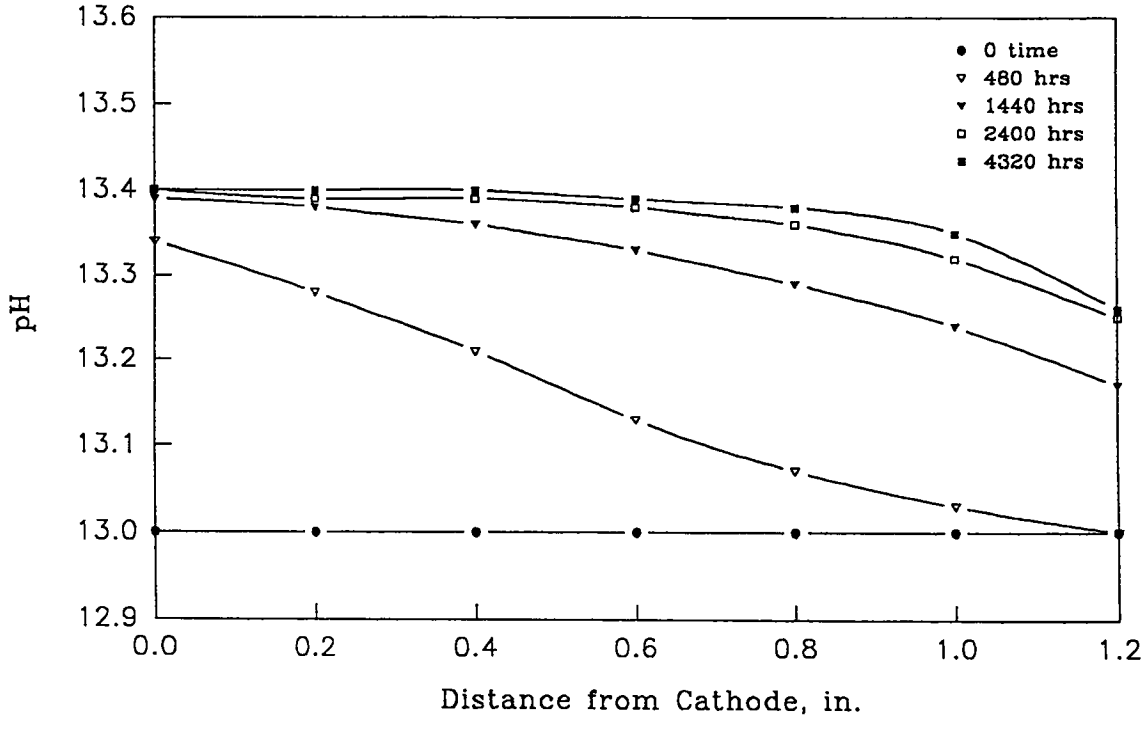

Figure C-9. Cl^- Concentration at the Cathode versus Time @ 2# Cl^-/yd^3

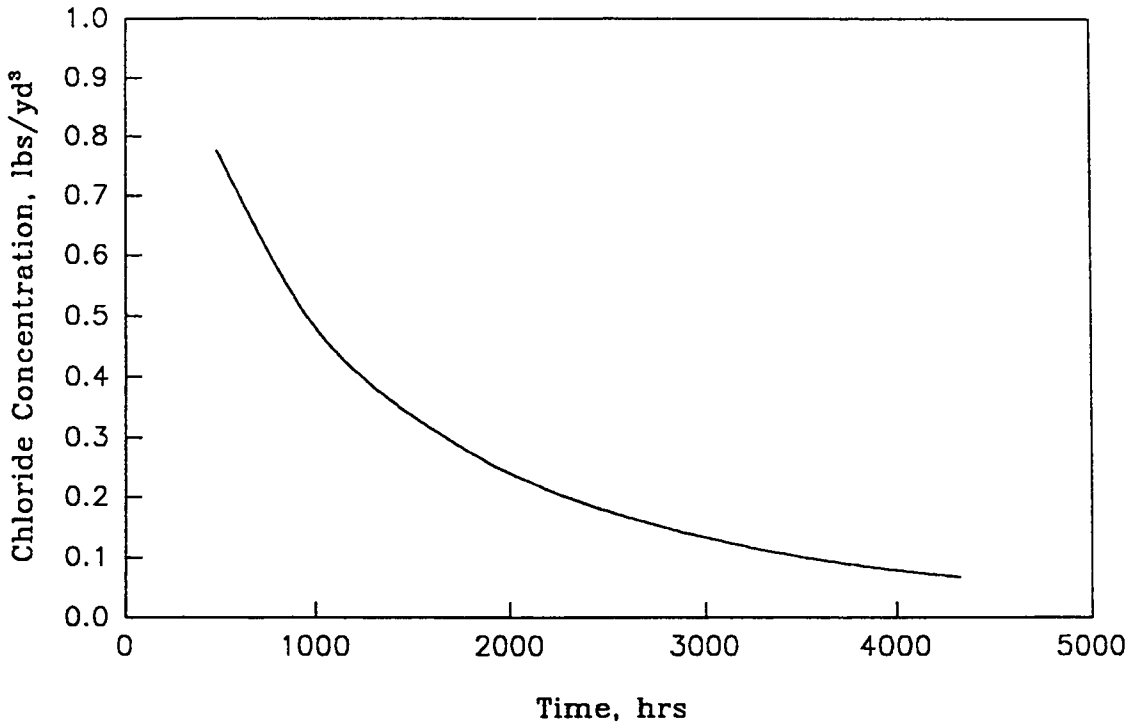

Figure C-10. Cl^-/OH^- Ratio at the Cathode versus Time @ 2# Cl^-/yd^3

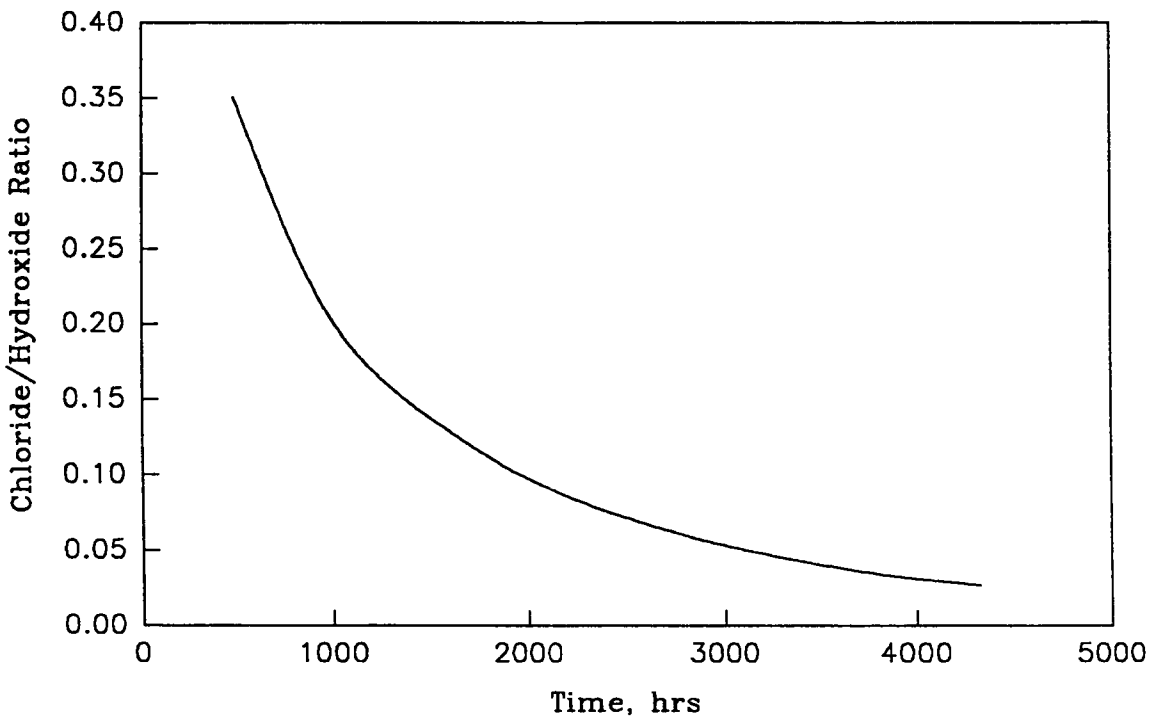

Figure C-11. Cl^- Concentration versus Distance from the Cathode @ 10# Cl^-/yd^3

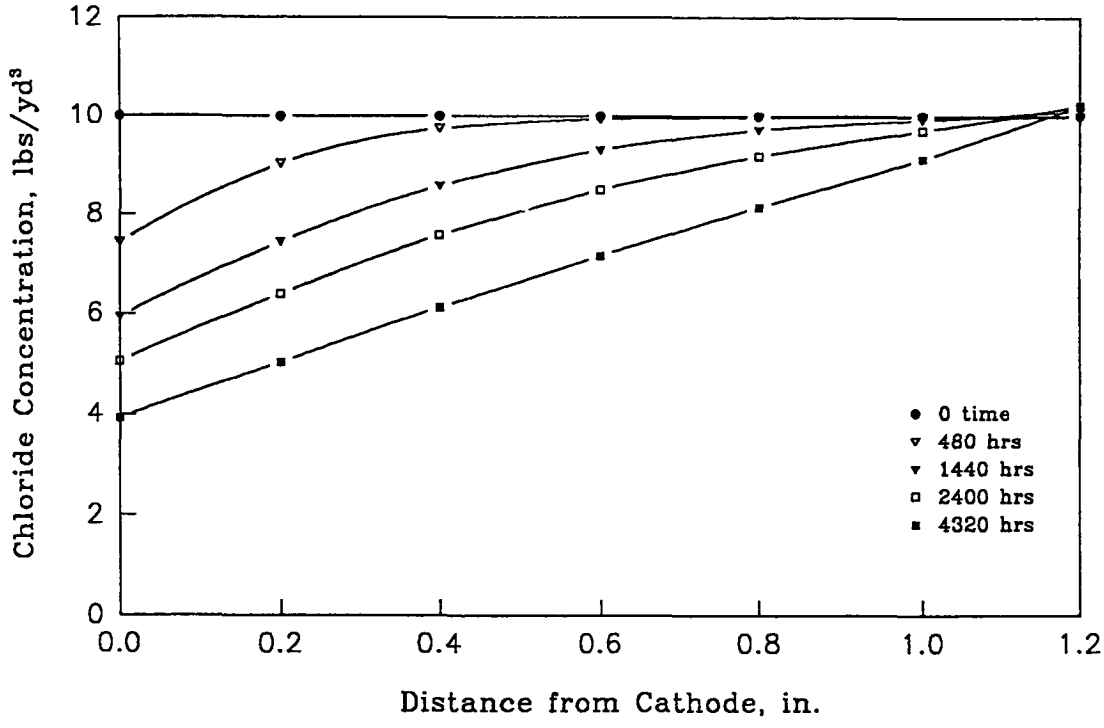

Figure C-12. pH versus Distance from the Cathode @ 10# Cl^-/yd^3

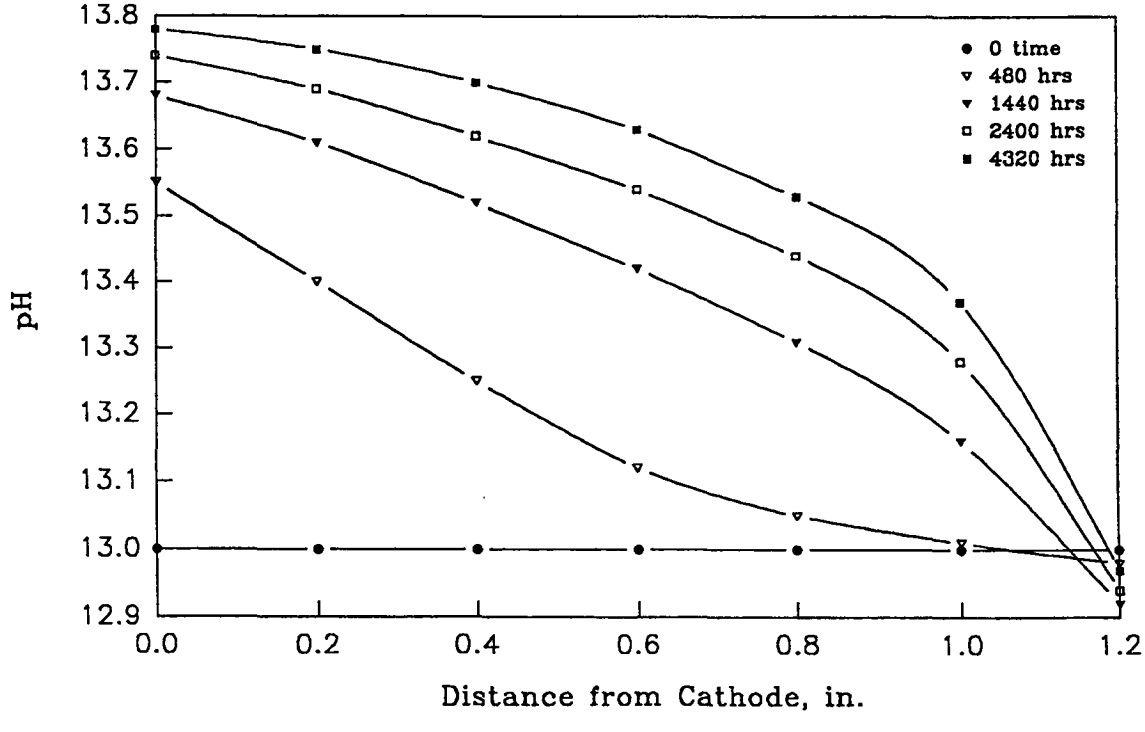

Figure C-13. Cl^- Concentration at the Cathode versus Time @ 10# Cl^-/yd^3

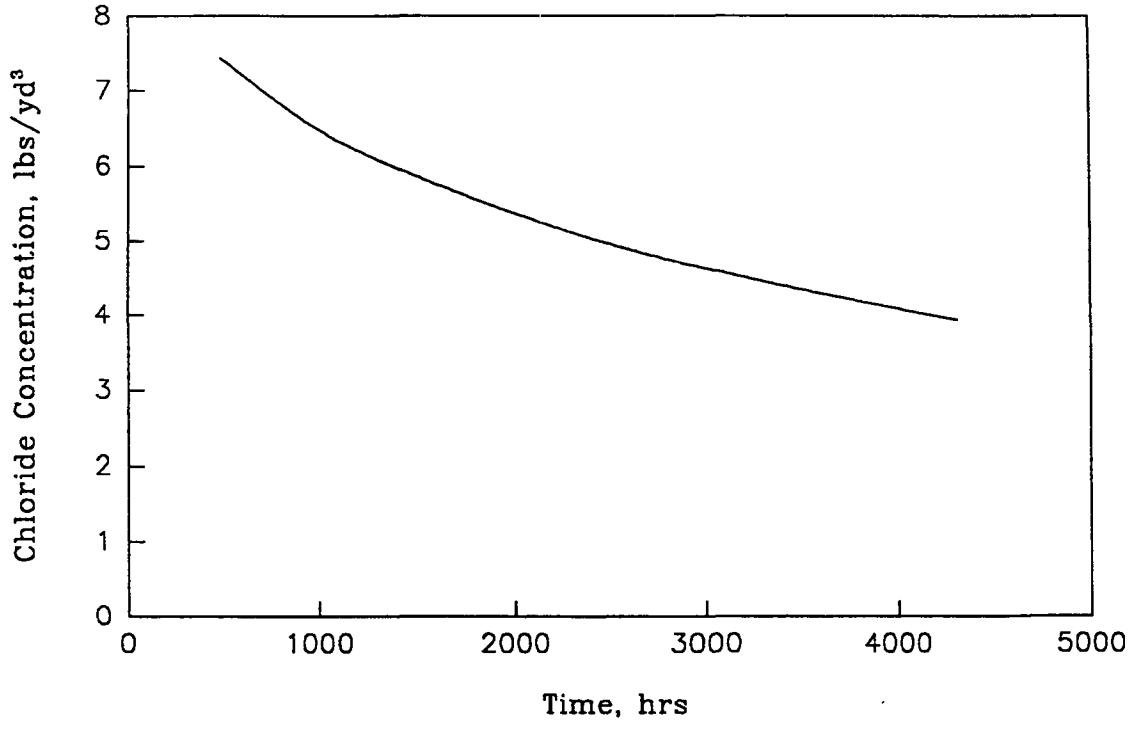

Figure C-14. Cl^-/OH^- Ratio at the Cathode versus Time @ 10# Cl^-/yd^3

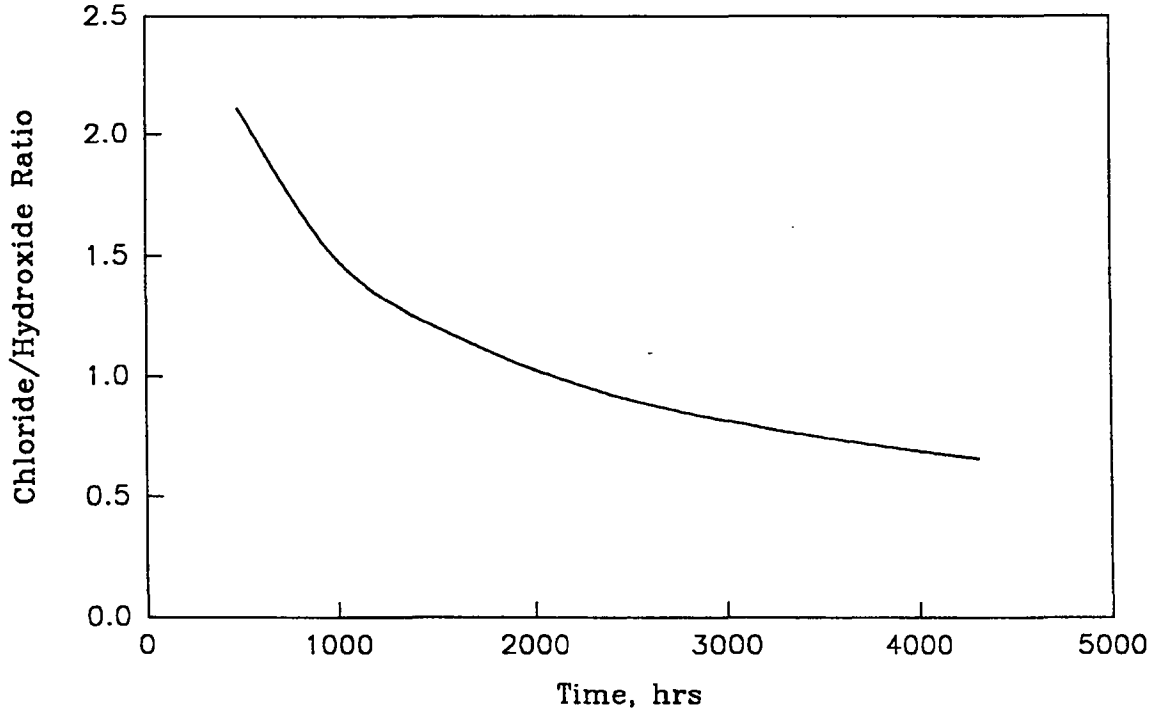

Figure C-15. Cl^- Concentration versus Distance from the Cathode (Linear Distribution)

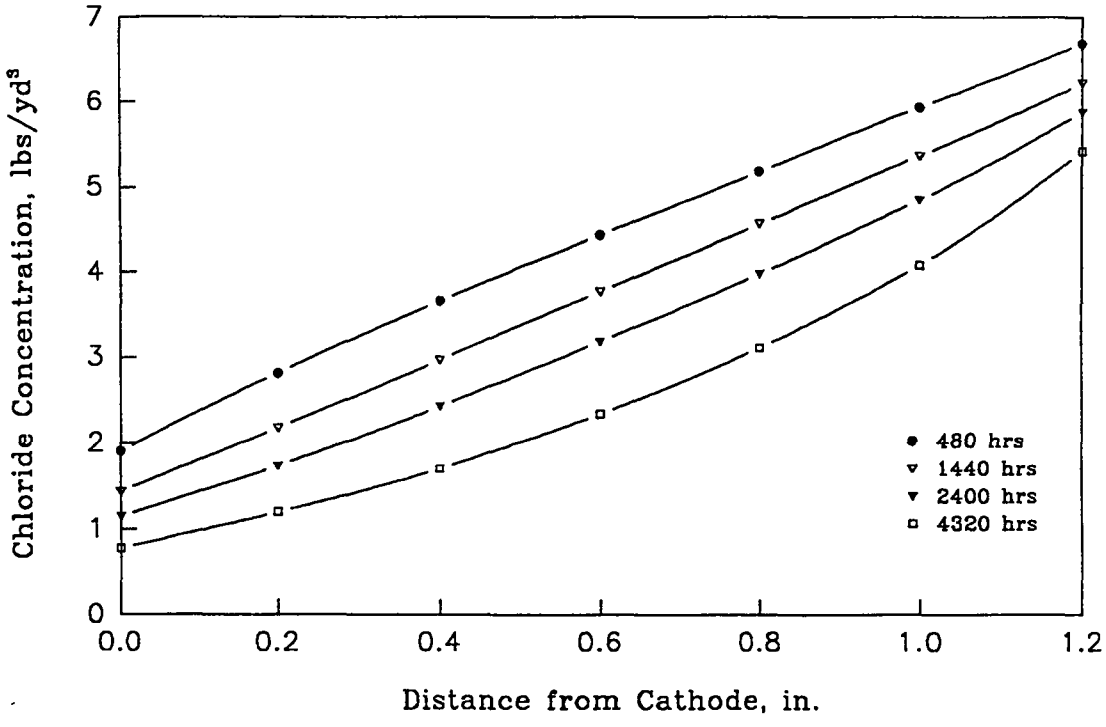

Figure C-16. pH versus Distance from the Cathode (Linear Distribution)

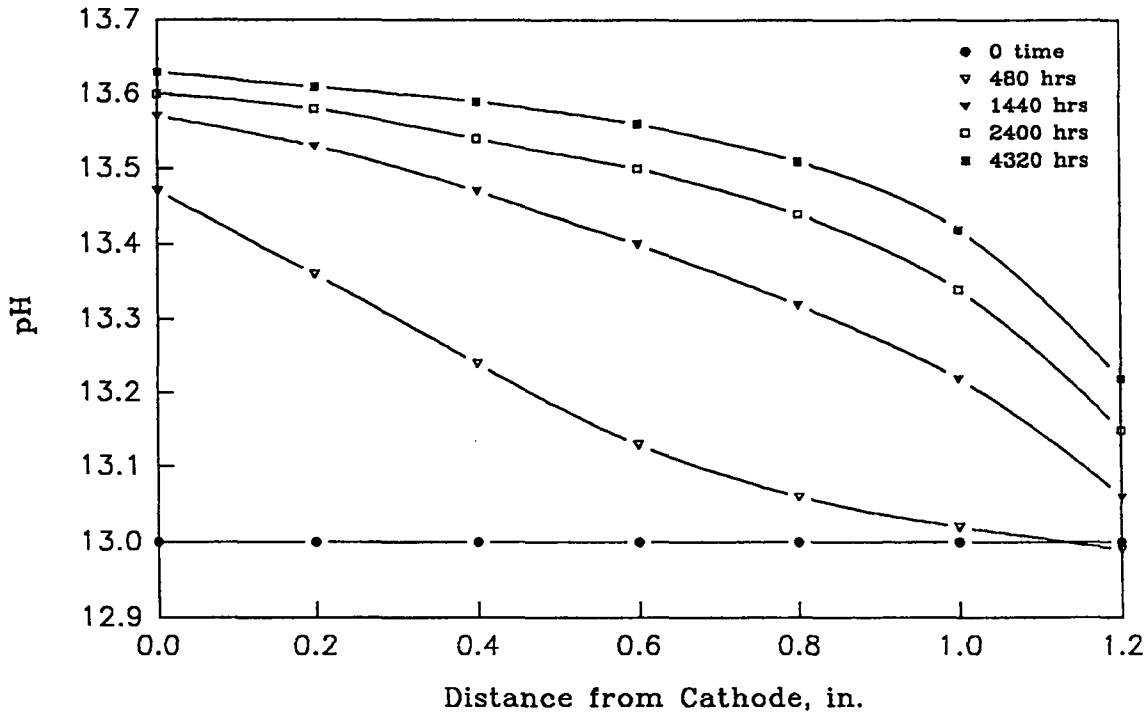

Figure C-17. Cl^- Concentration at the Cathode versus Time (Linear Distribution)

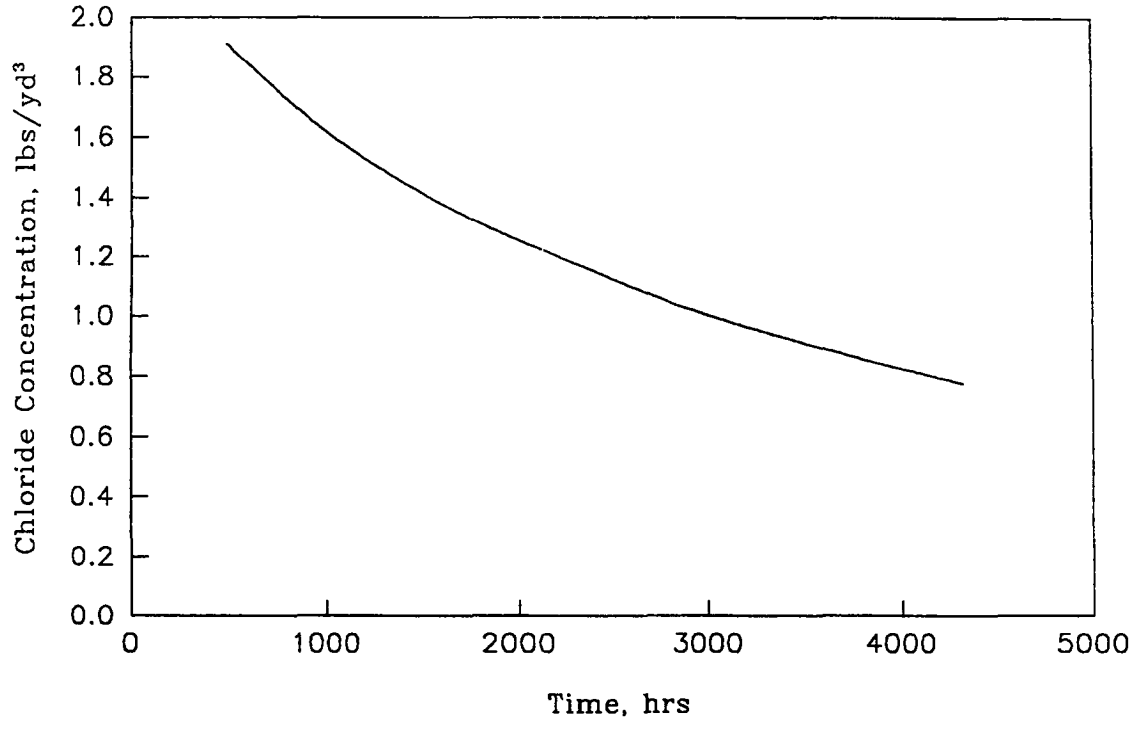

Figure C-18. Cl^-/OH^- Ratio at the Cathode versus Time (Linear Distribution)

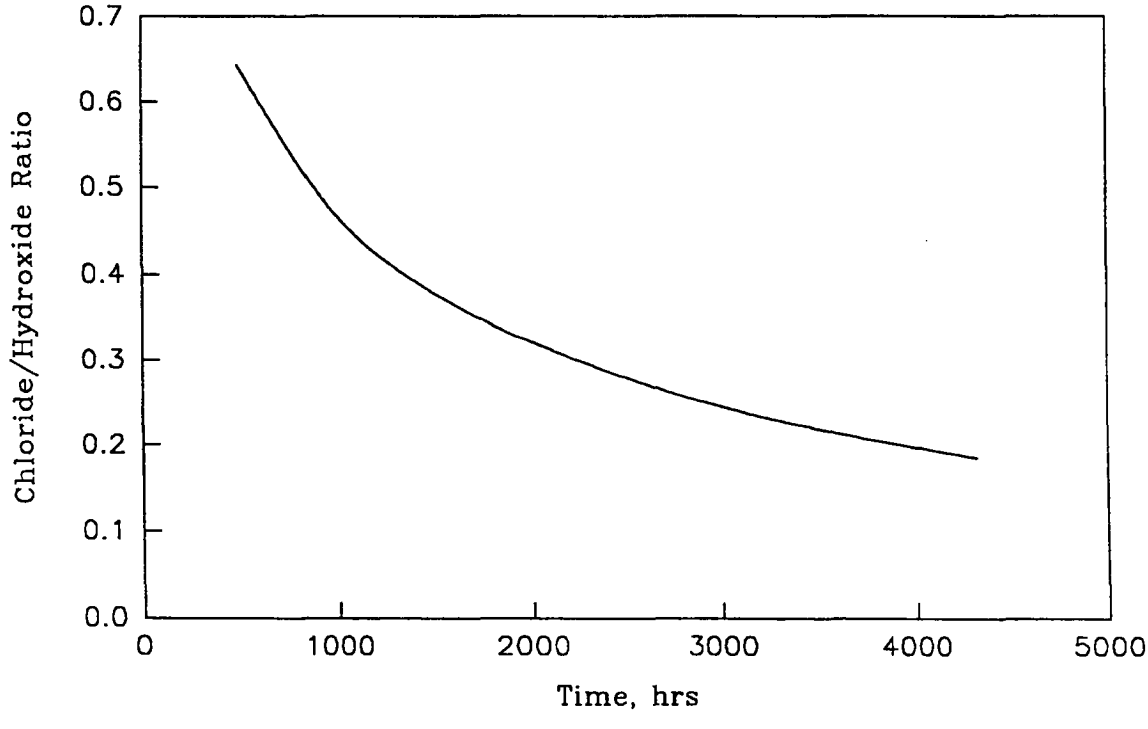

Figure C-19. Cl^- Concentration versus Distance from the Cathode @ pH = 12.5

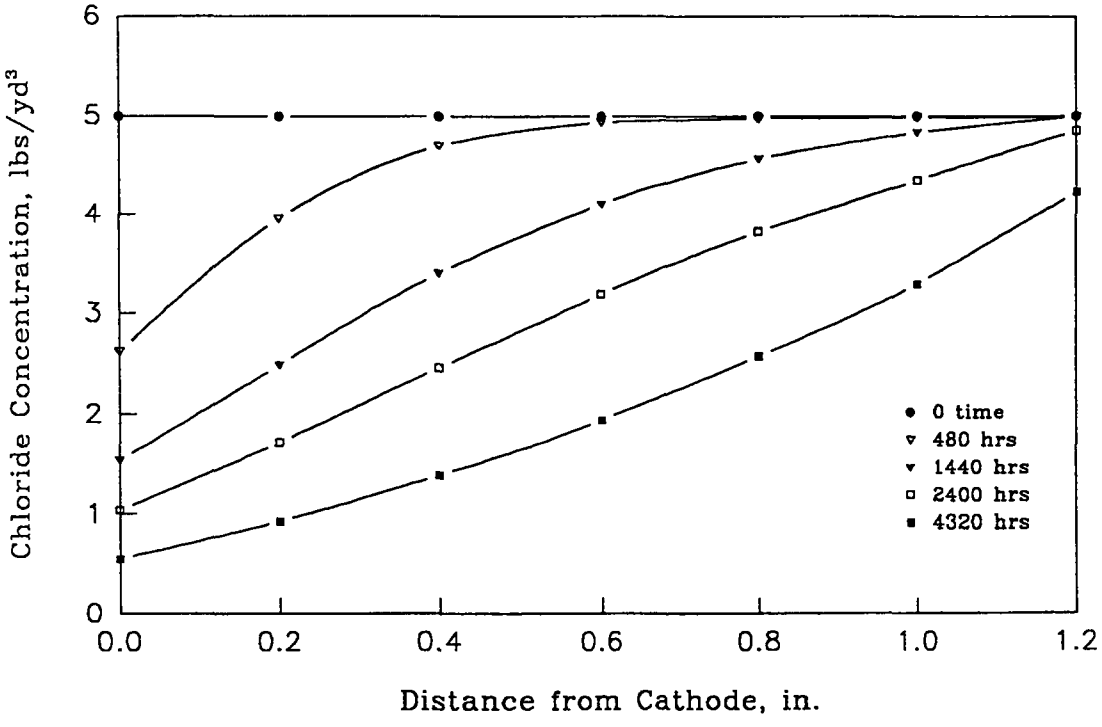

Figure C-20. pH versus Distance from the Cathode @ pH = 12.5

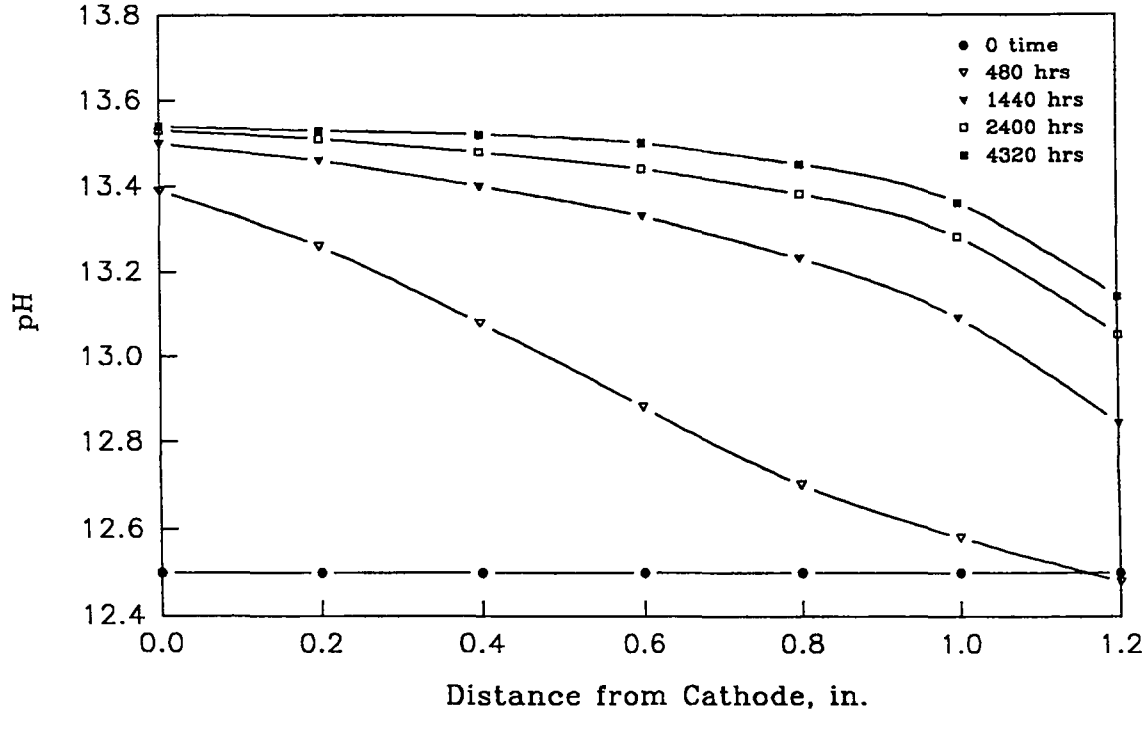

Figure C-21. Cl^- Concentration at the Cathode versus Time @ pH = 12.5

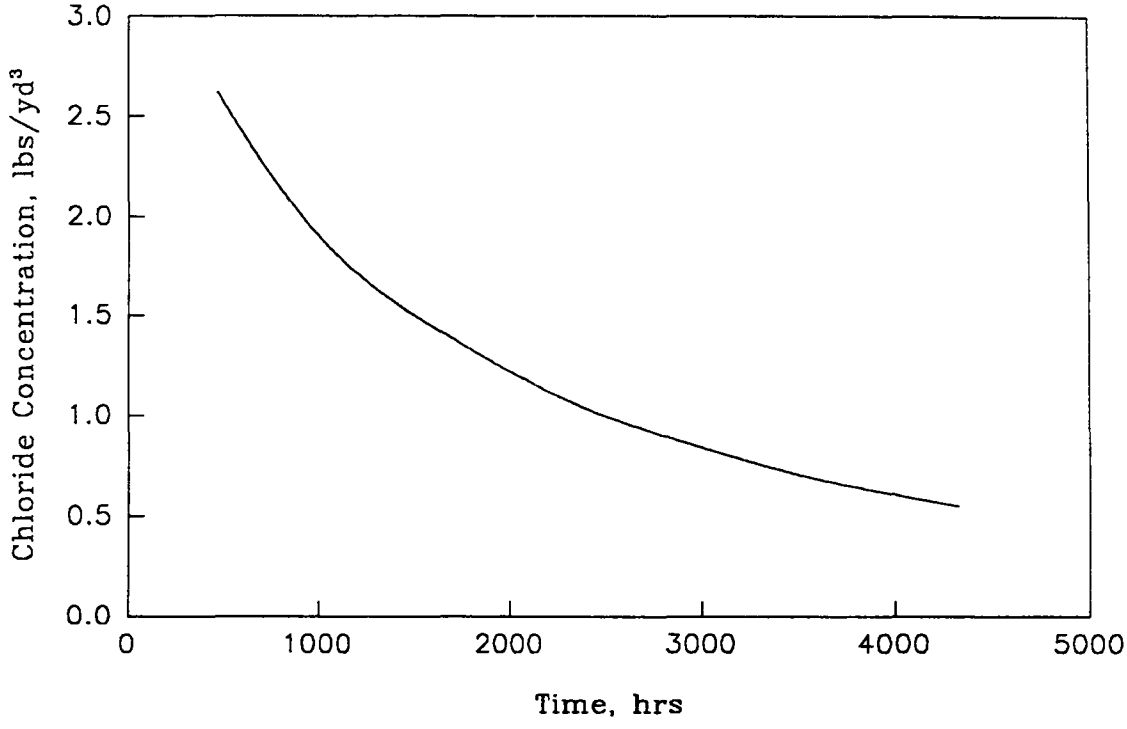

Figure C-22. Cl^-/OH^- Ratio at the Cathode versus Time @ pH = 12.5

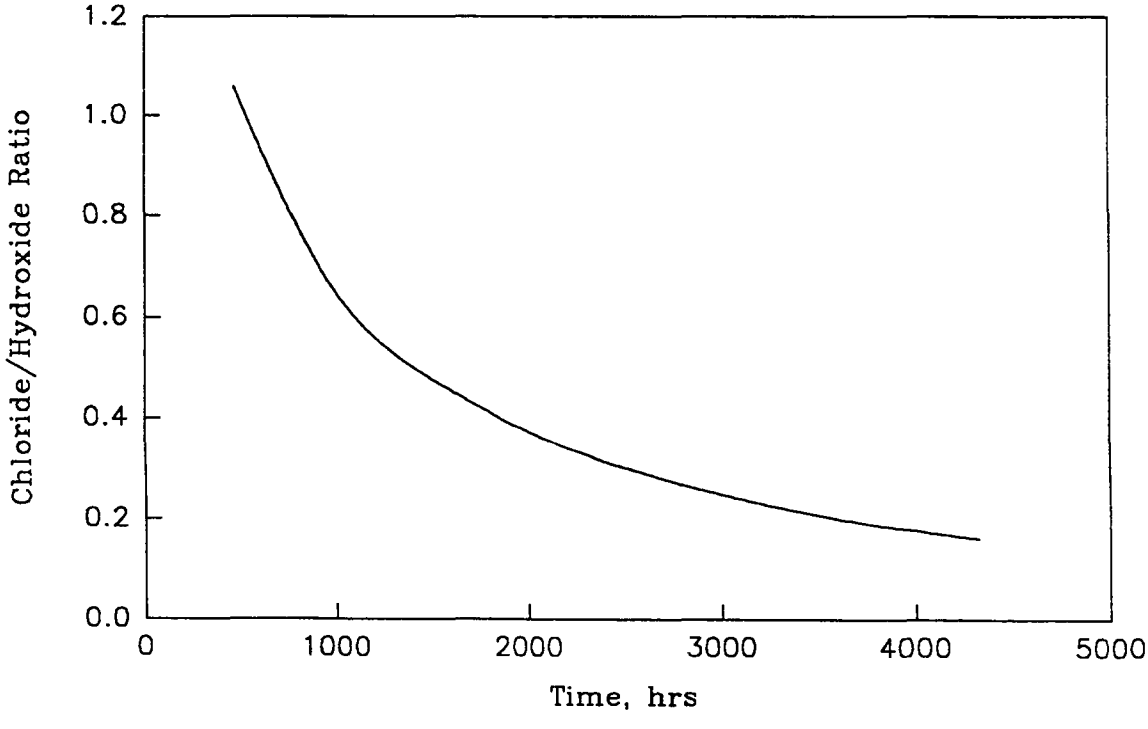

Figure C-23. Cl^- Concentration versus Distance from the Cathode @ pH = 13.5

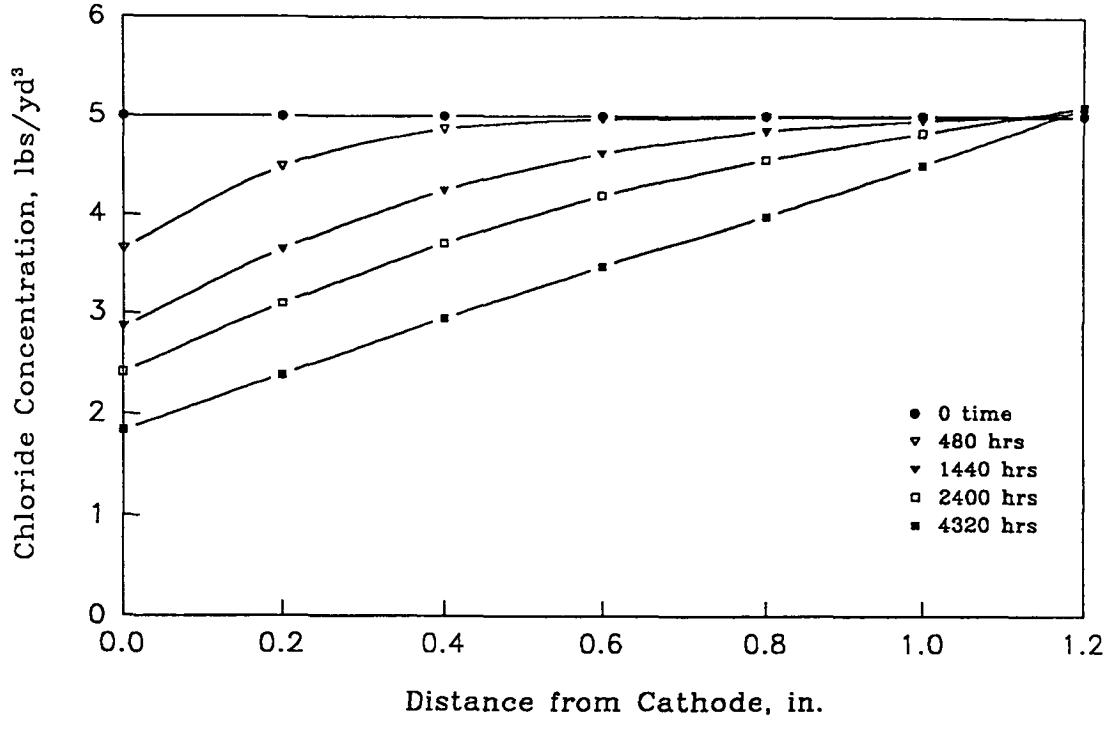

Figure C-24. pH versus Distance from the Cathode @ pH = 13.5

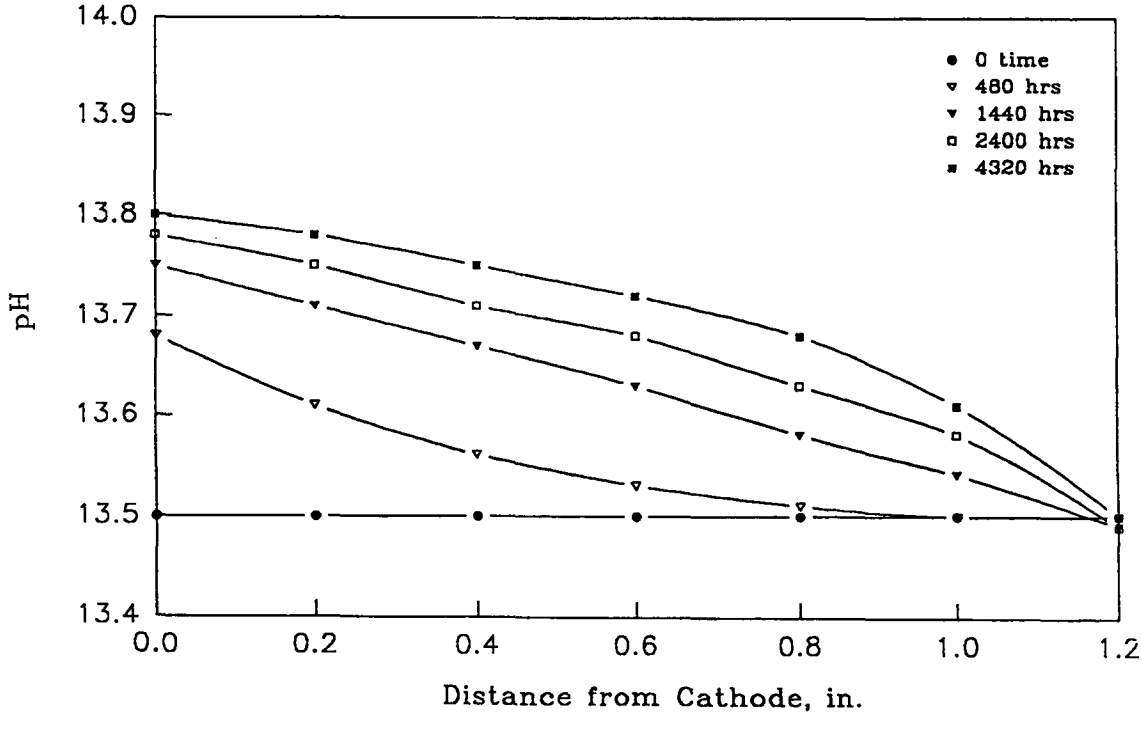

Figure C-25. Cl^- Concentration at the Cathode versus Time @ pH = 13.5

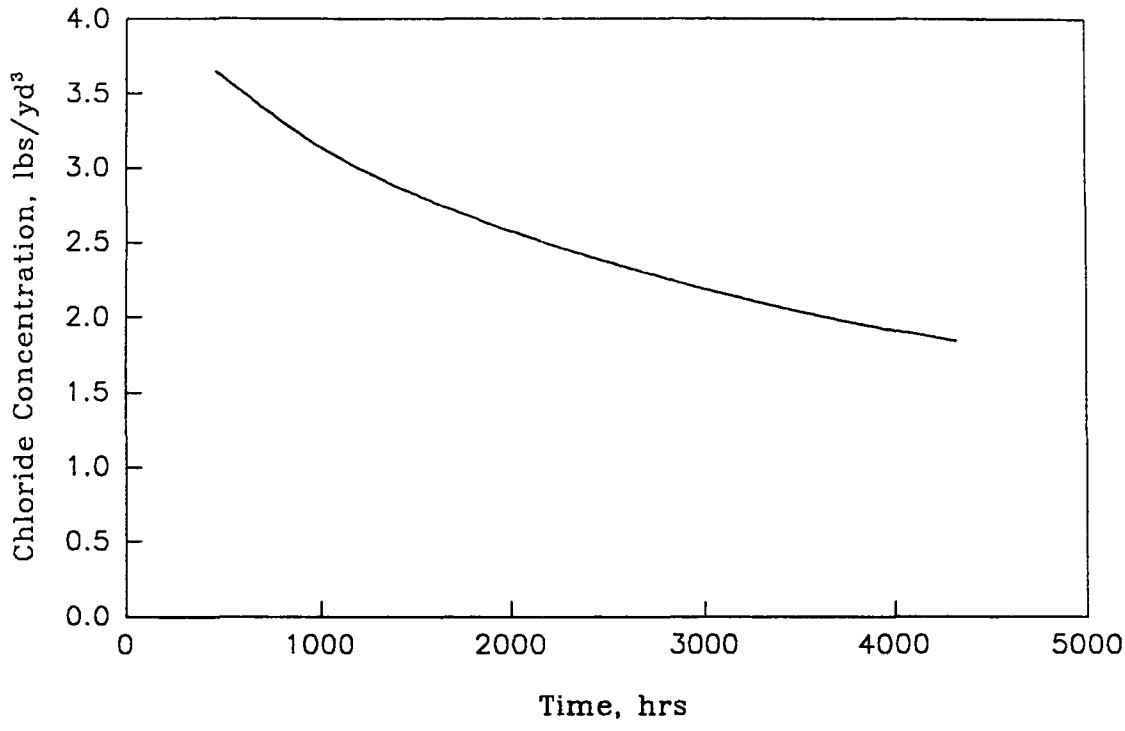

Figure C-26. Cl^-/OH^- Ratio at the Cathode versus Time @ pH = 13.5

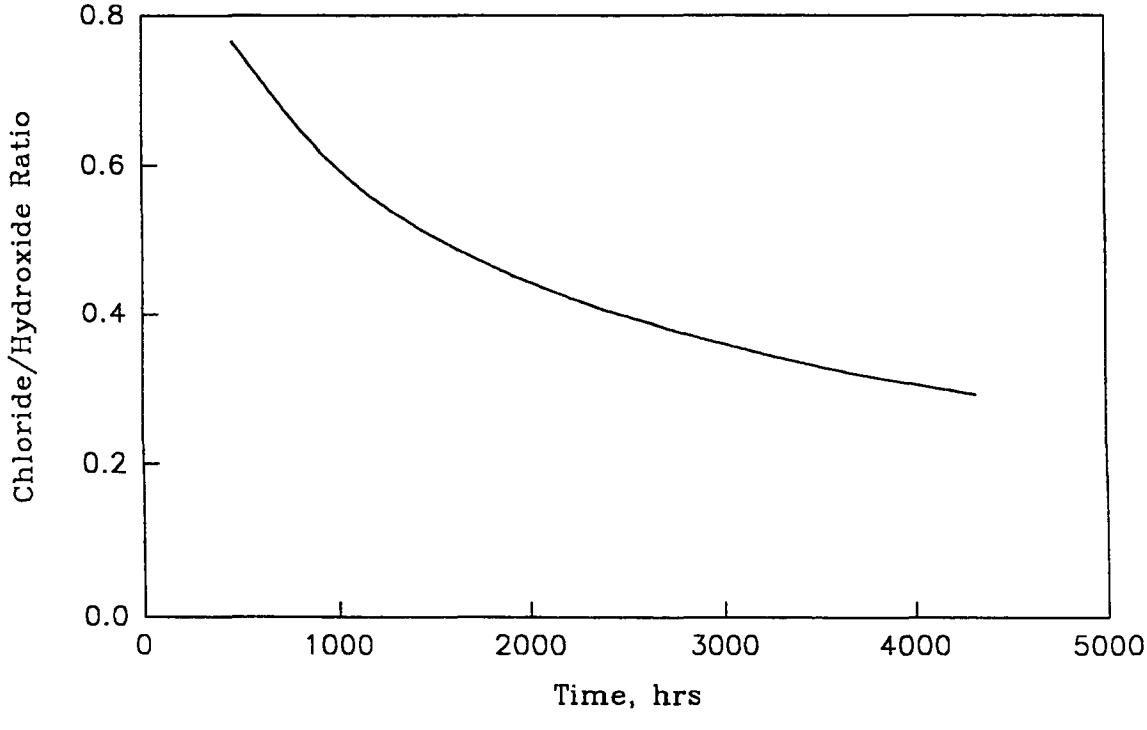

Figure C-27. Cl^- Concentration versus Distance from the Cathode @ 1.5 mA/ft²

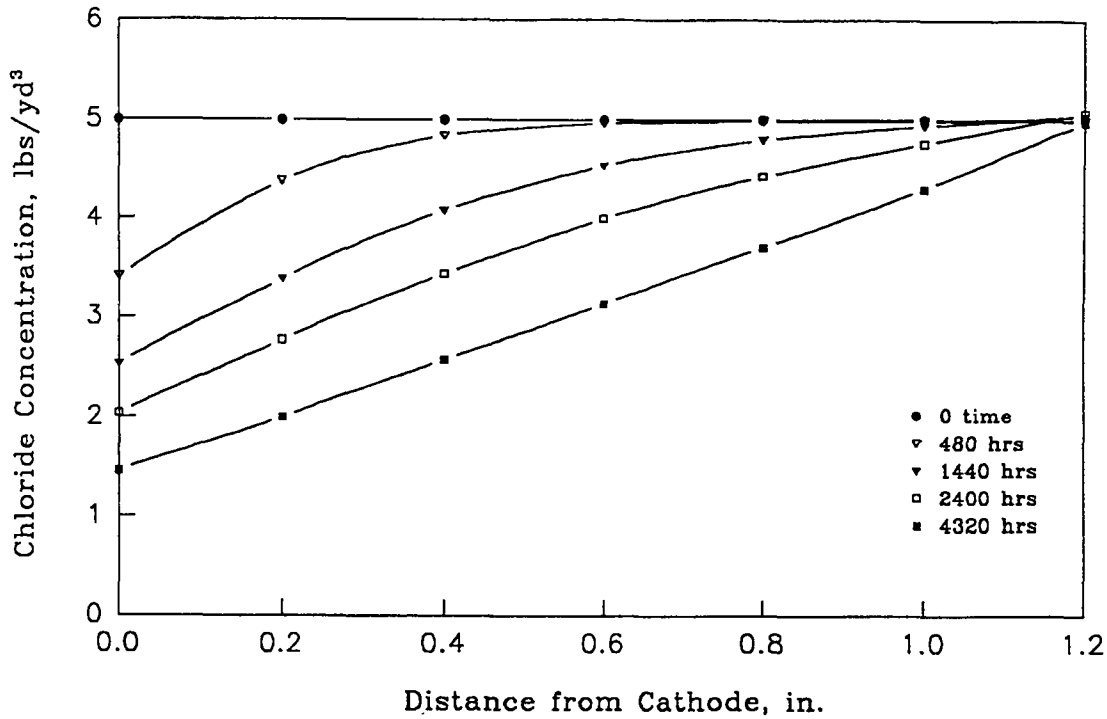

Figure C-28. pH versus Distance from the Cathode @ 1.5 mA/ft²

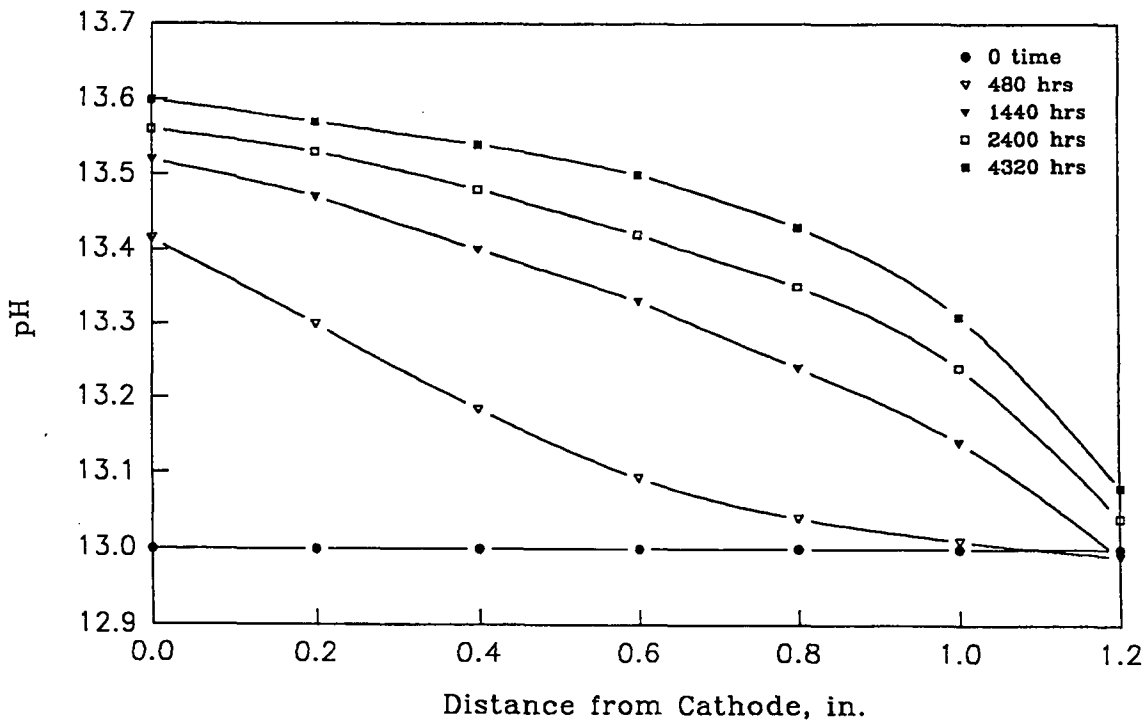

Figure C-29. Cl^- Concentration at the Cathode versus Time @ 1.5 mA/ft²

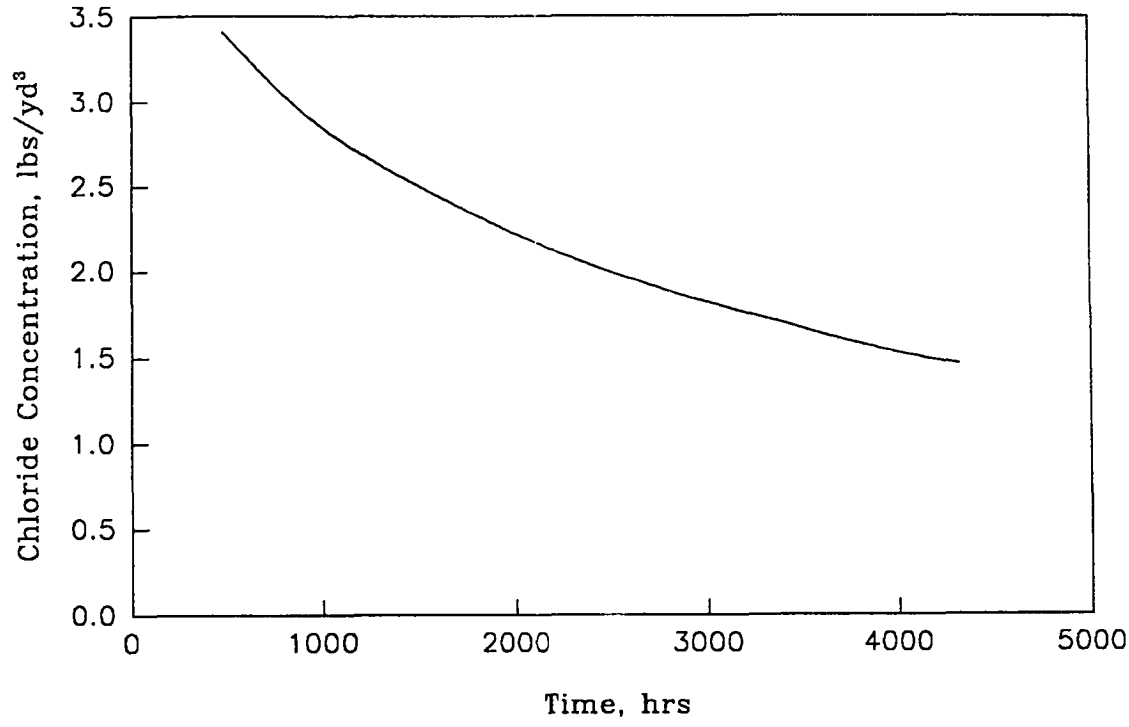

Figure C-30. Cl^-/OH^- Ratio at the Cathode versus Time @ 1.5 mA/ft²

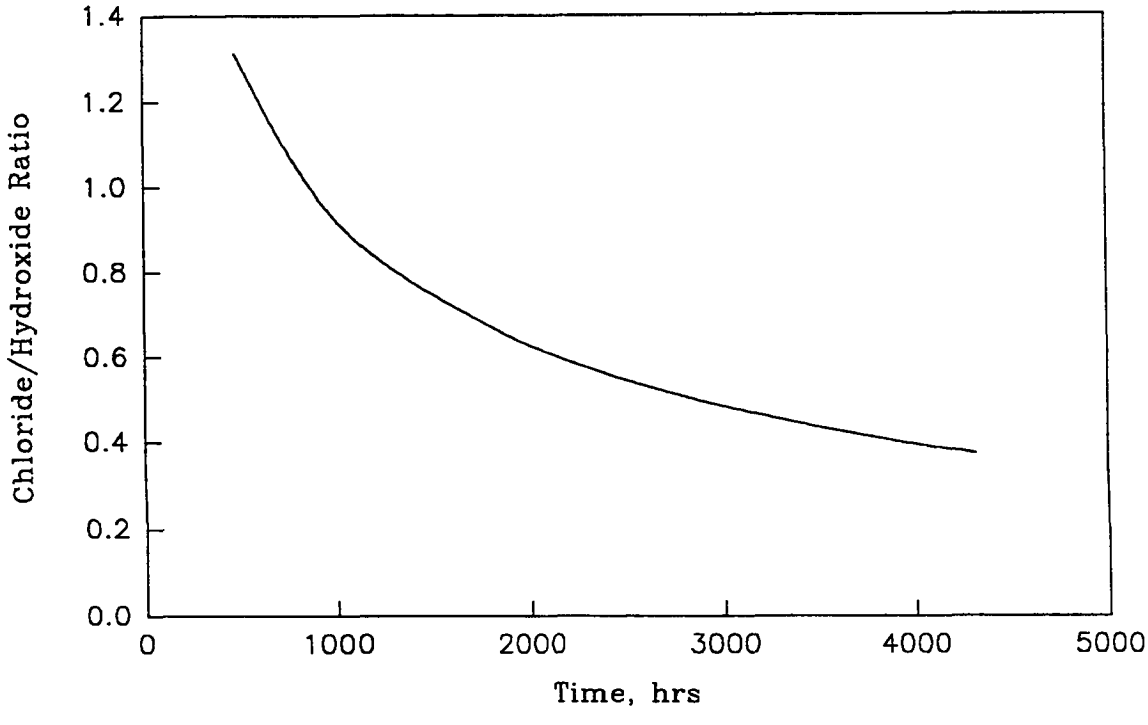

Figure C-31. Cl^- Concentration versus Distance from the Cathode @ 1.0 mA/ft²

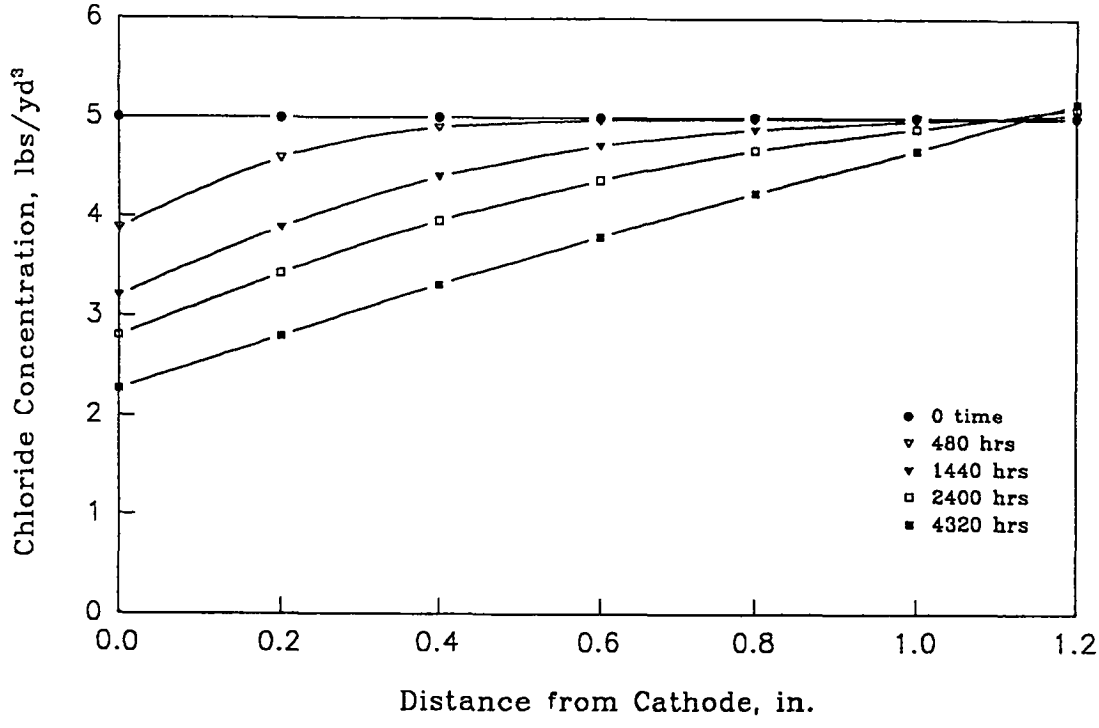

Figure C-32. pH versus Distance from the Cathode @ 1.0 mA/ft²

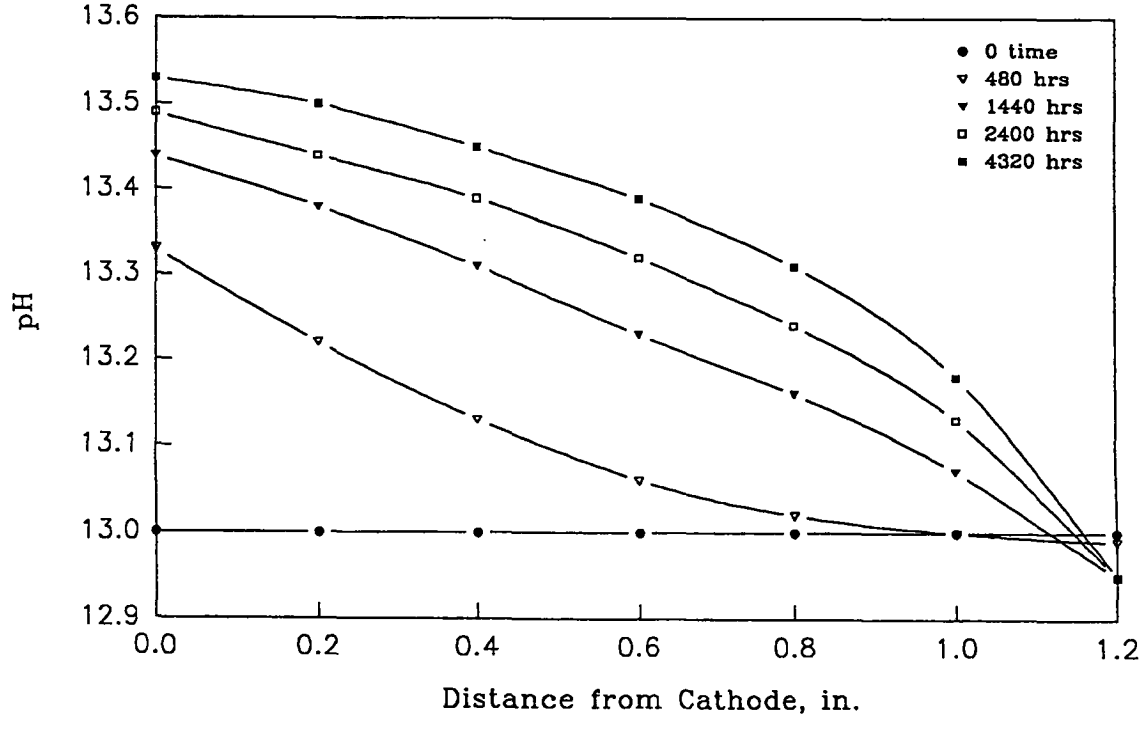

Figure C-33. Cl^- Concentration at the Cathode versus Time @ 1.0 mA/ft²

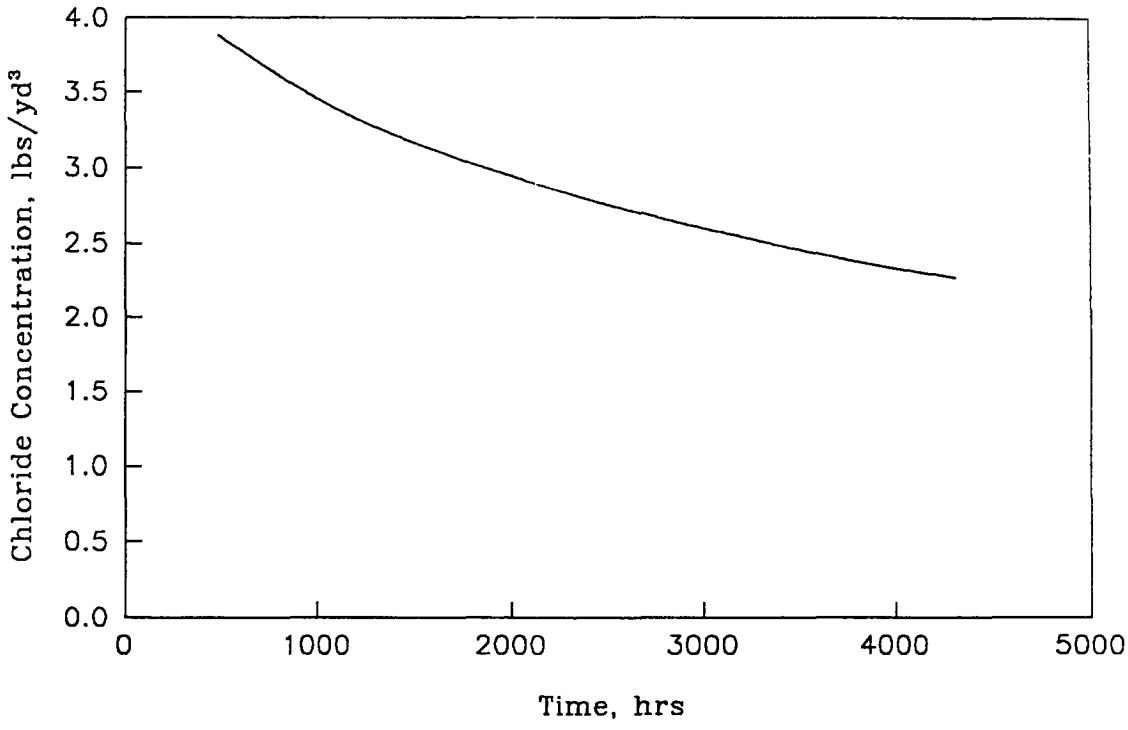

Figure C-34. Cl^-/OH^- Ratio at the Cathode versus Time @ 1.0 mA/ft²

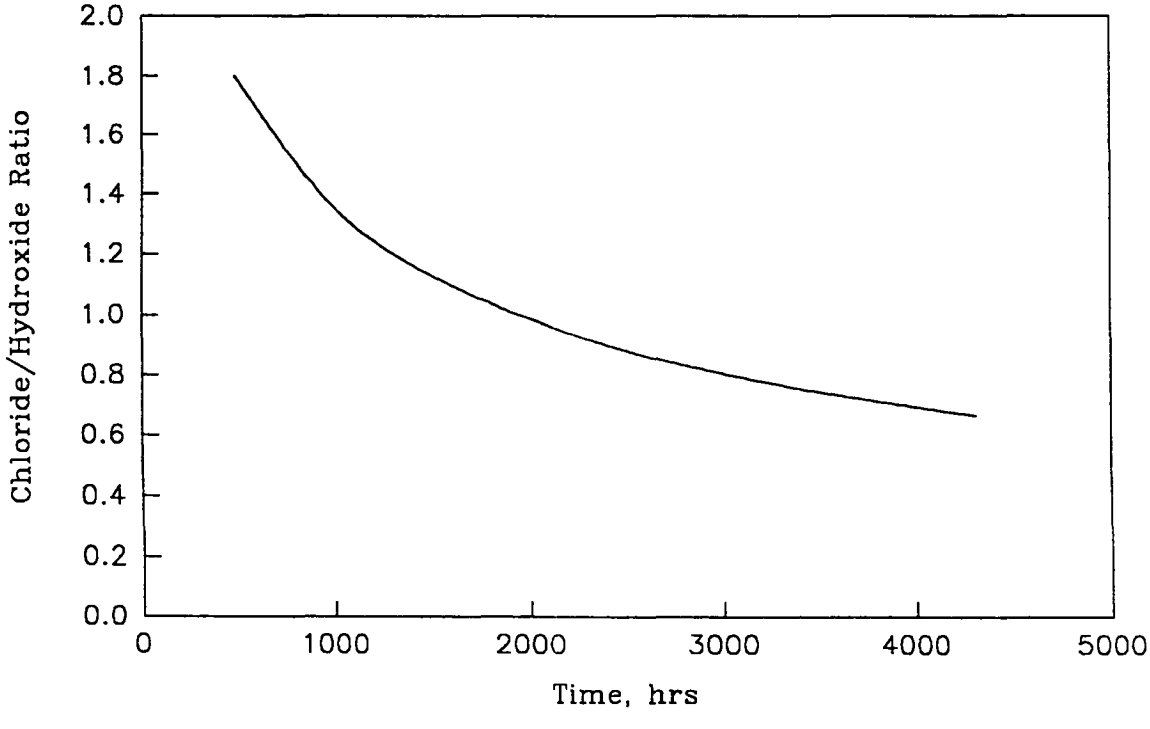

Figure C-35. Cl^- Concentration versus Distance from the Cathode, 200 mA/ft^2,720hrs.

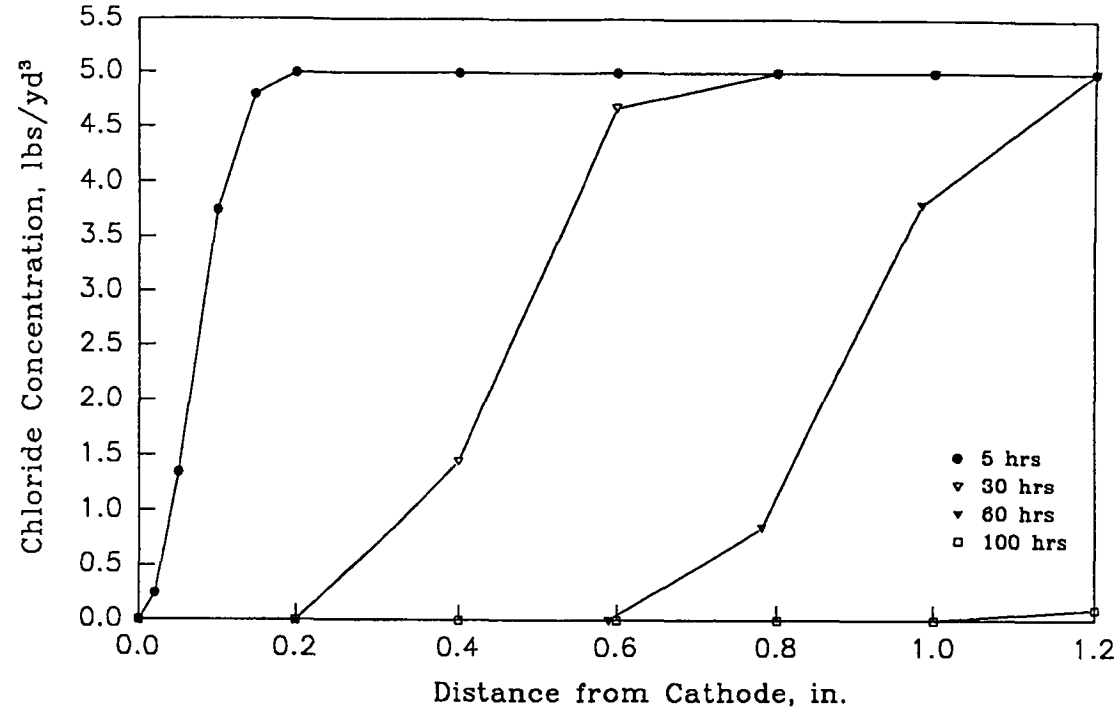

Figure C-36. pH versus Distance from the Cathode @ 200 mA/ft^2, 720 hrs.

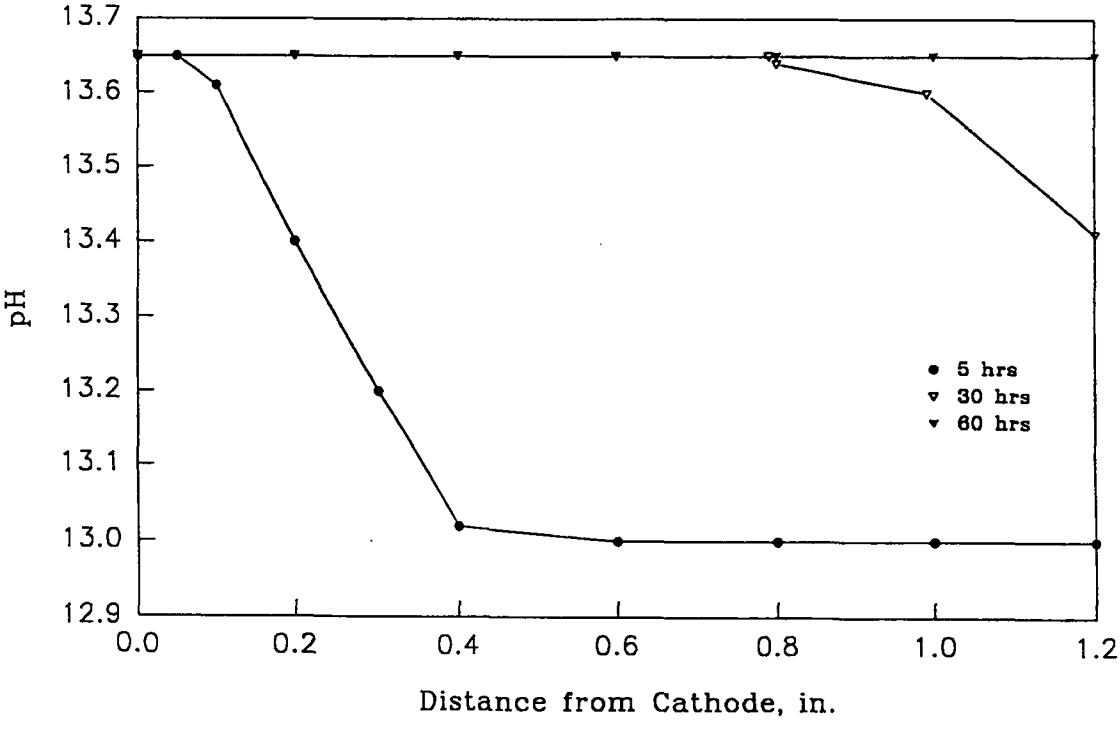

Figure C-37. Cl^- Concentration versus Distance from the Cathode @ 273°K

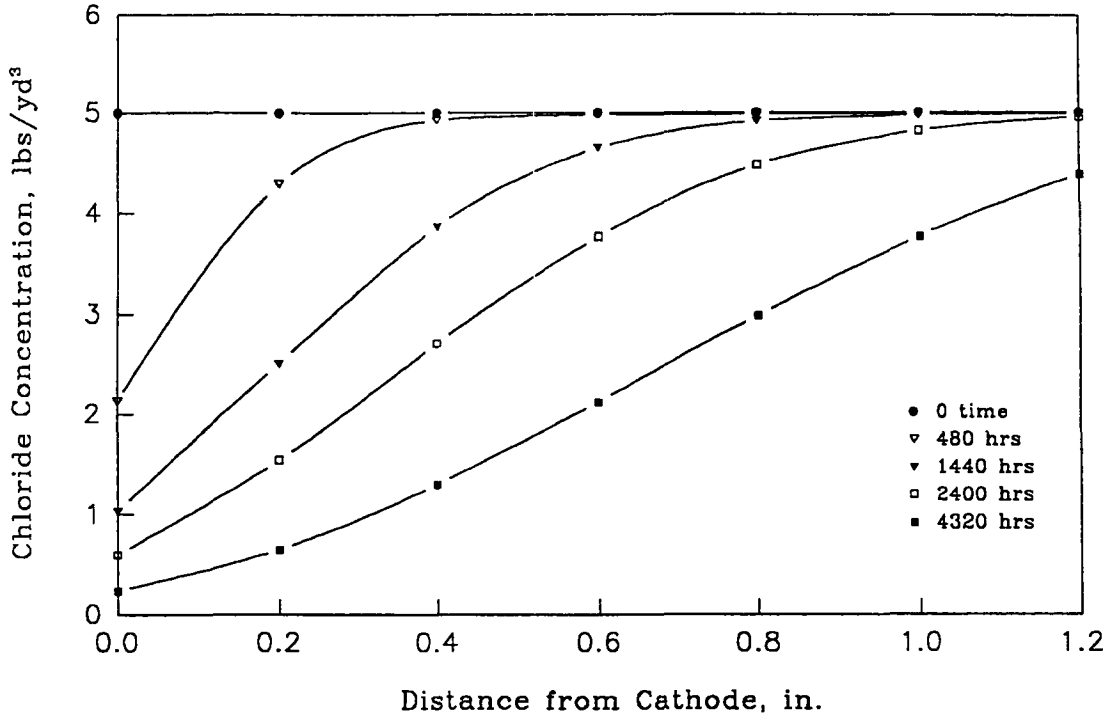

Figure C-38. pH versus Distance from the Cathode @ 273°K

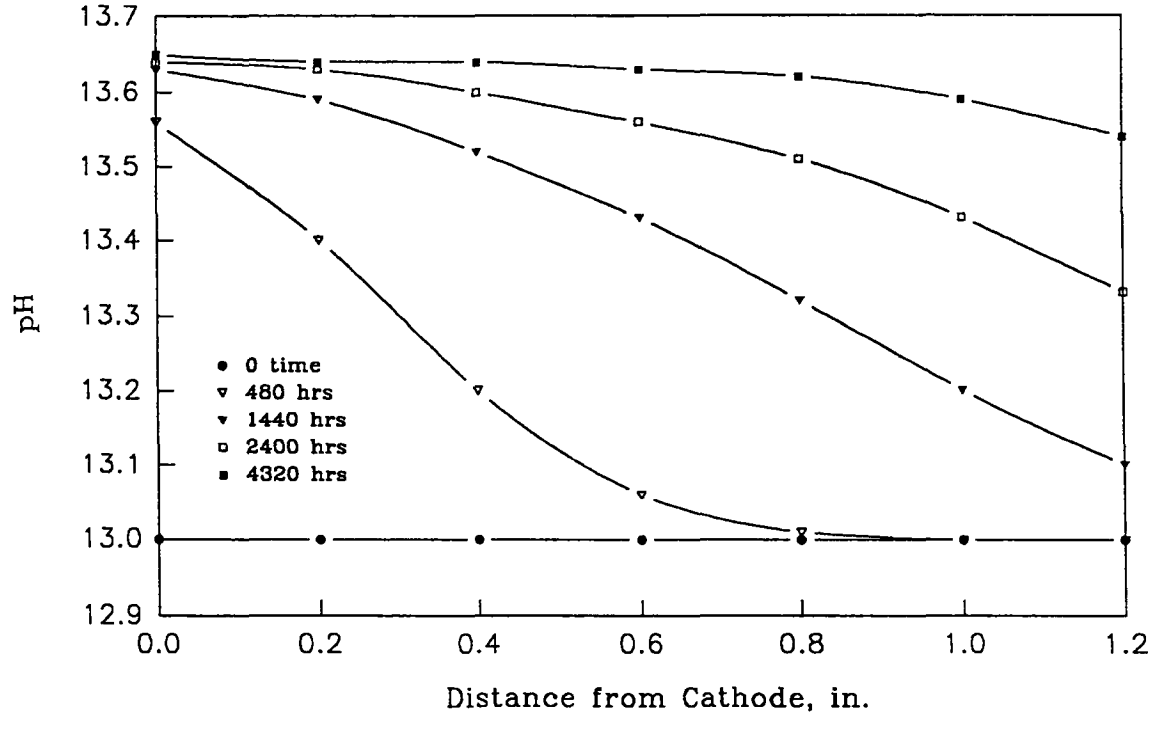

Figure C-39. Cl^- Concentration at the Cathode versus Time @ 273°K4

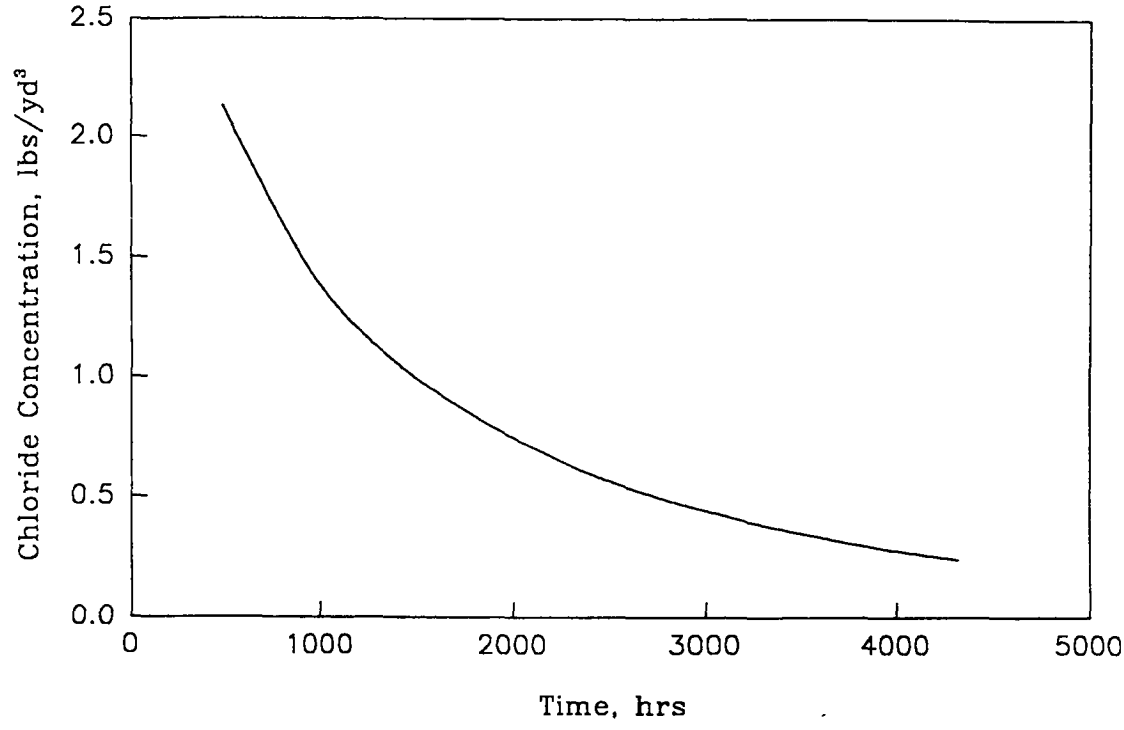

Figure C-40. Cl^-/OH^- Ratio at the Cathode versus Time @ 273°K

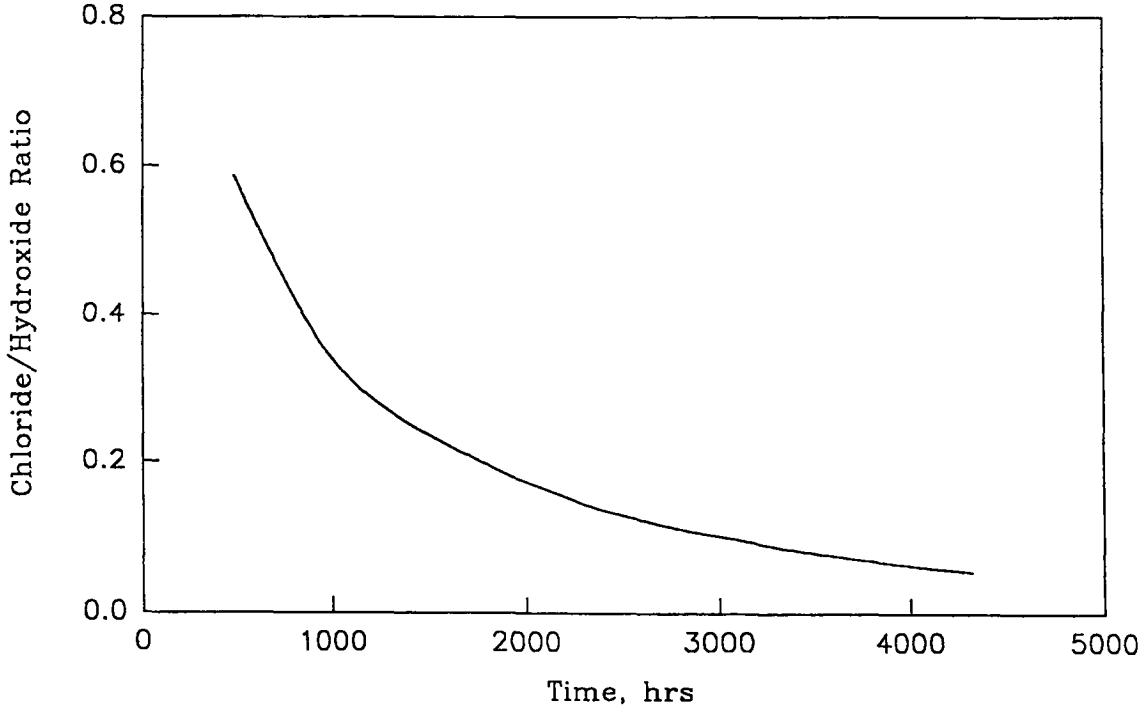

Figure C-41. Cl^- Concentration versus Distance from the Cathode @ 311°K

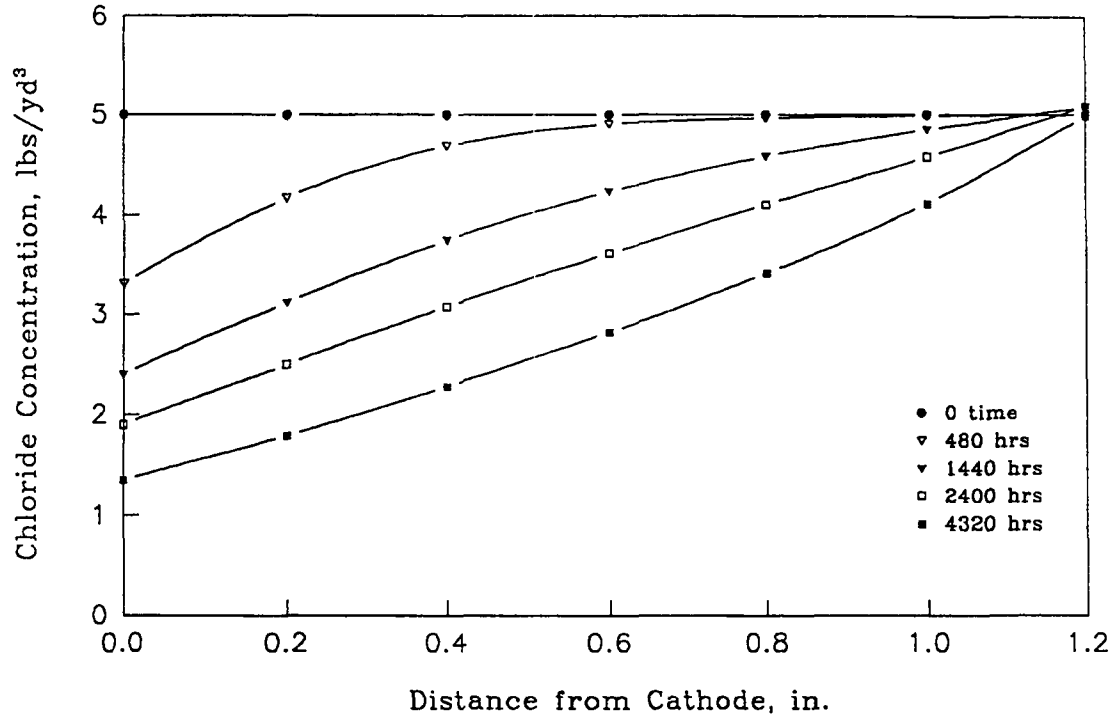

Figure C-42. pH versus Distance from the Cathode @ 311°K

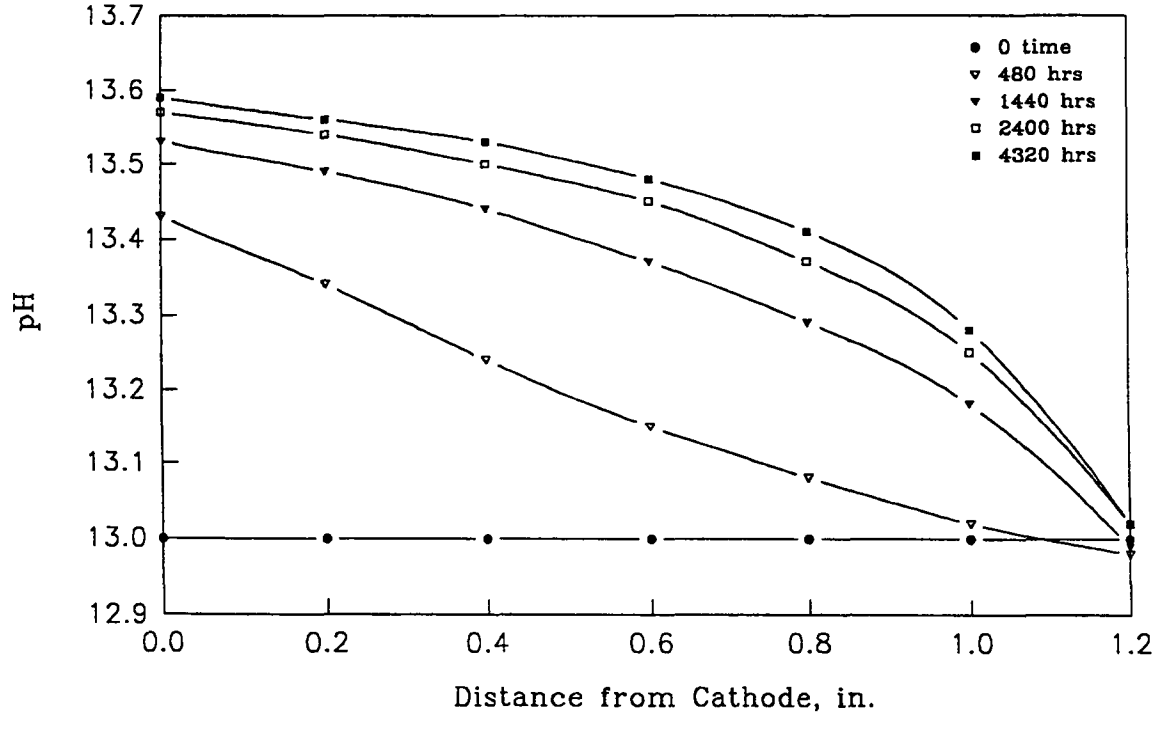

Figure C-43. Cl^- Concentration at the Cathode versus Time @ 311°K

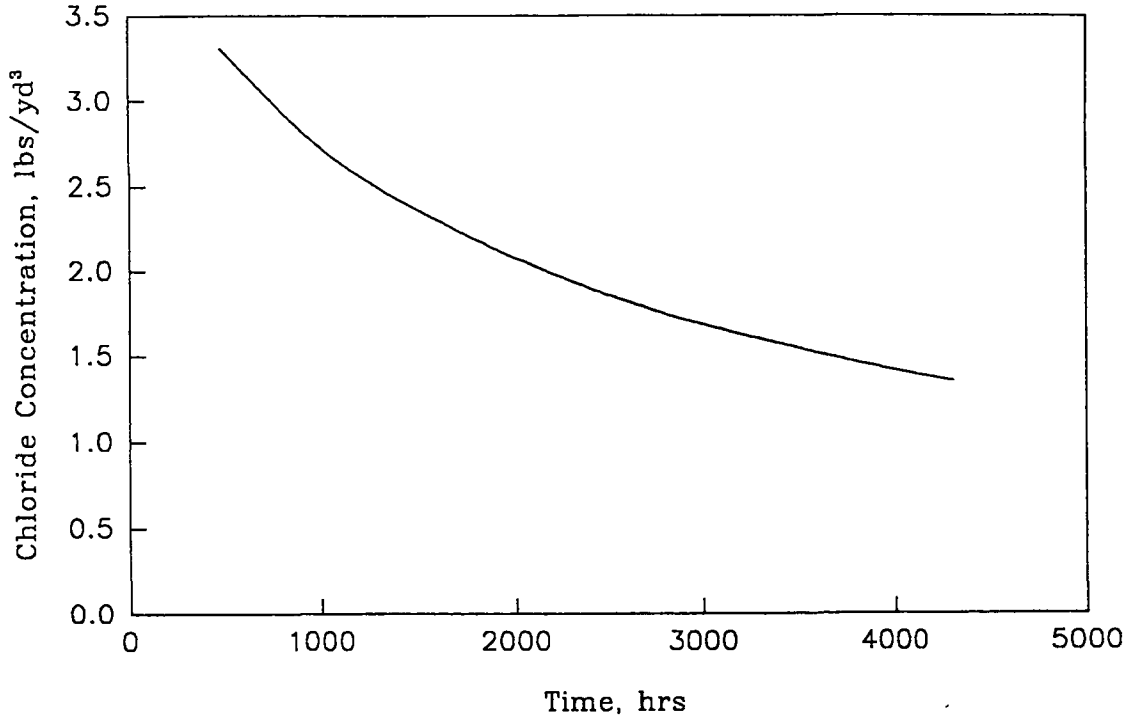

Figure C-44. Cl^-/OH^- Ratio at the Cathode versus Time @ 311°K

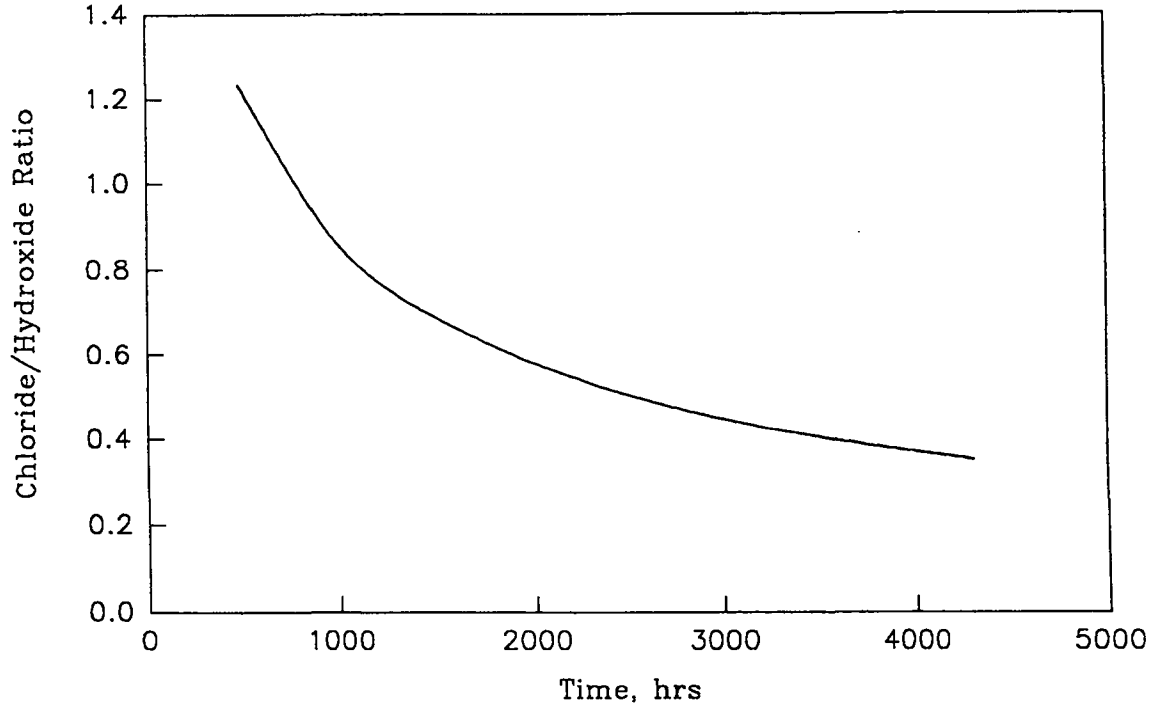

Figure C-45. Steel Polarization versus Distance from the Power Feed Strip.

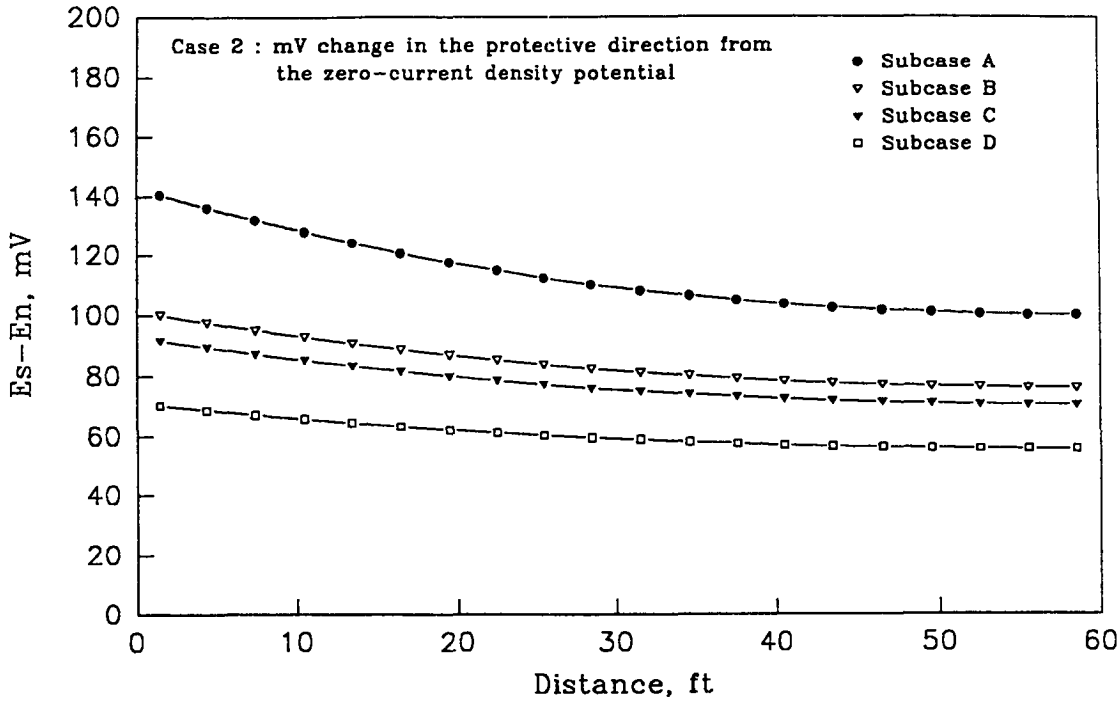

Figure C-46. Current Density to Steel versus Distance from the Power Feed Strip.

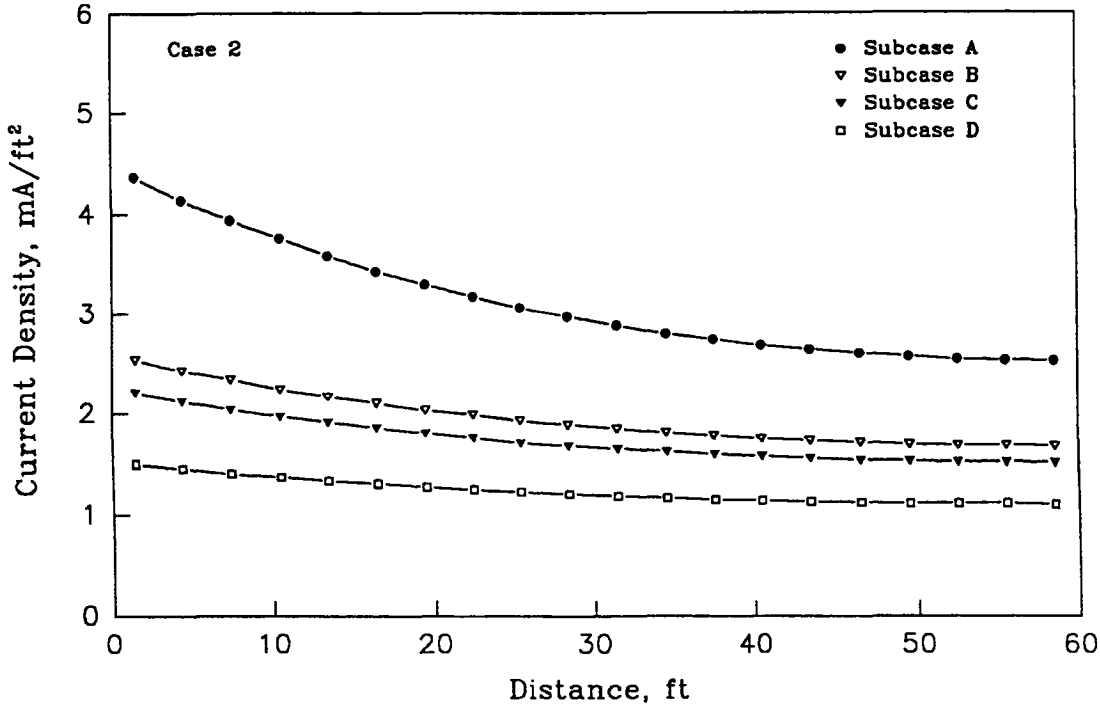

Figure C-47. Steel Polarization versus Distance from the Power Feed Strip.

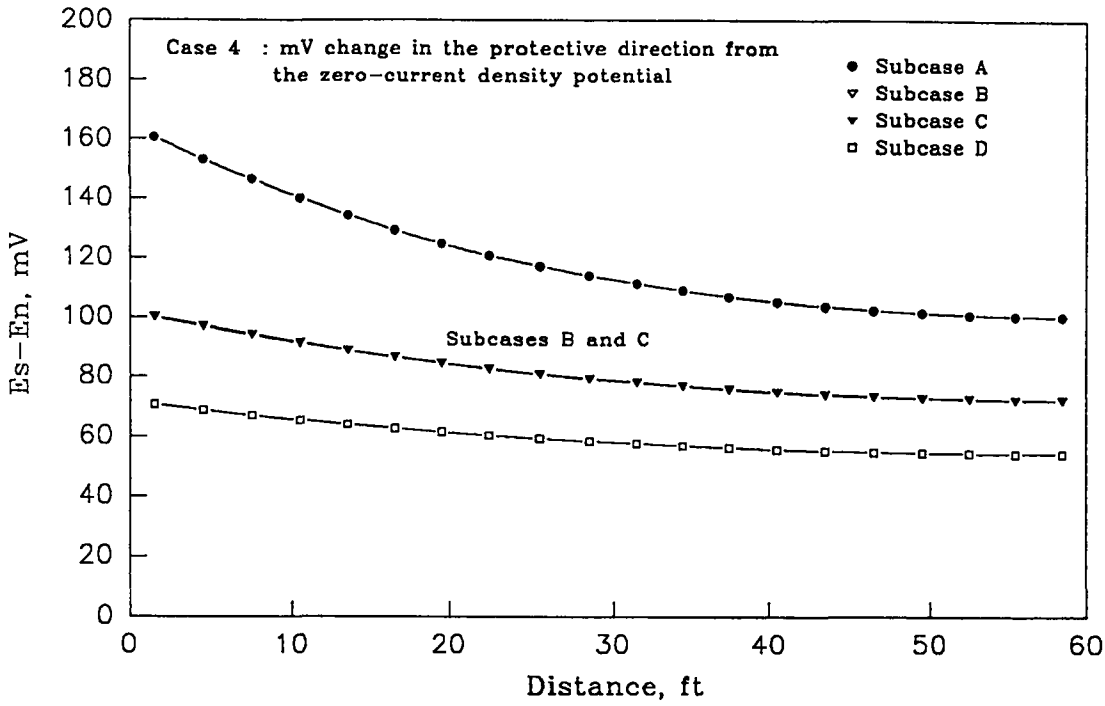

Figure C-48. Current Density to Steel versus Distance from the Power Feed Strip.

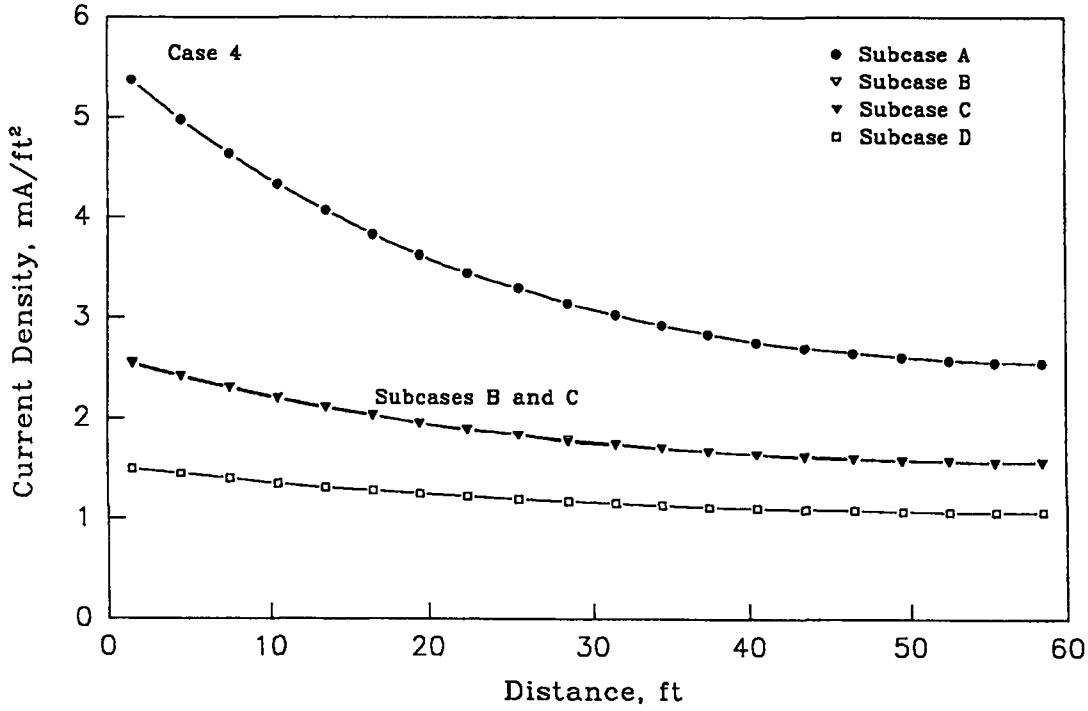

Figure C-49. Steel Polarization versus Distance from the Power Feed Strip.

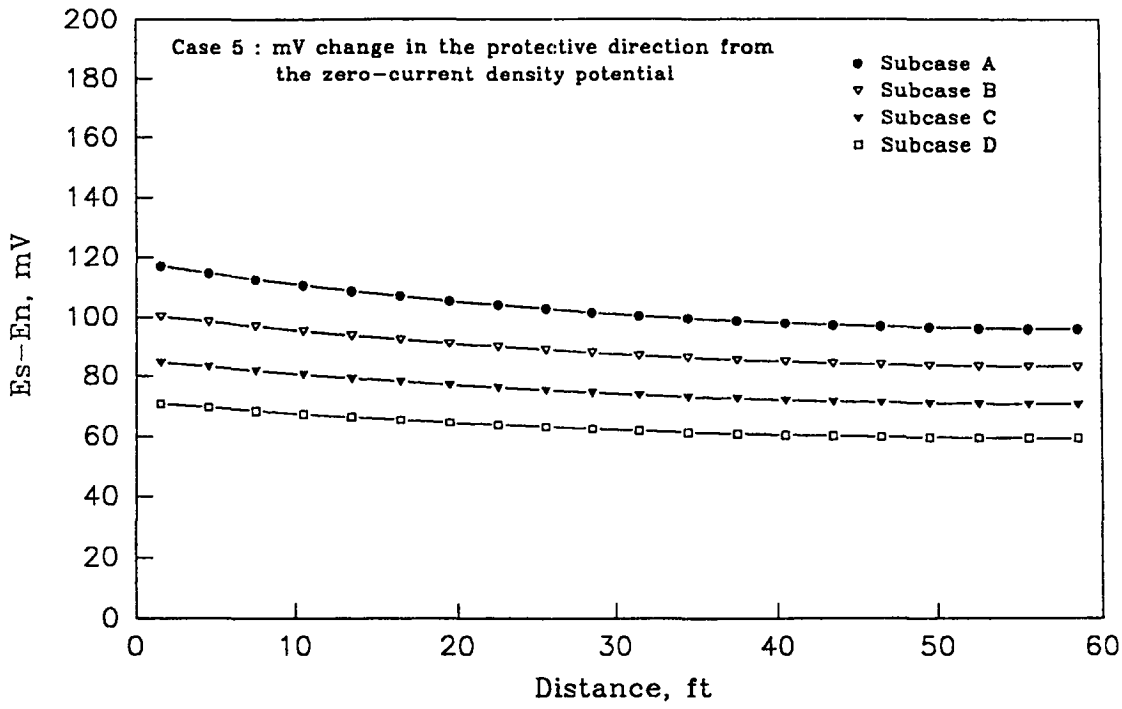

Figure C-50. Current Density to Steel versus Distance from the Power Feed Strip.

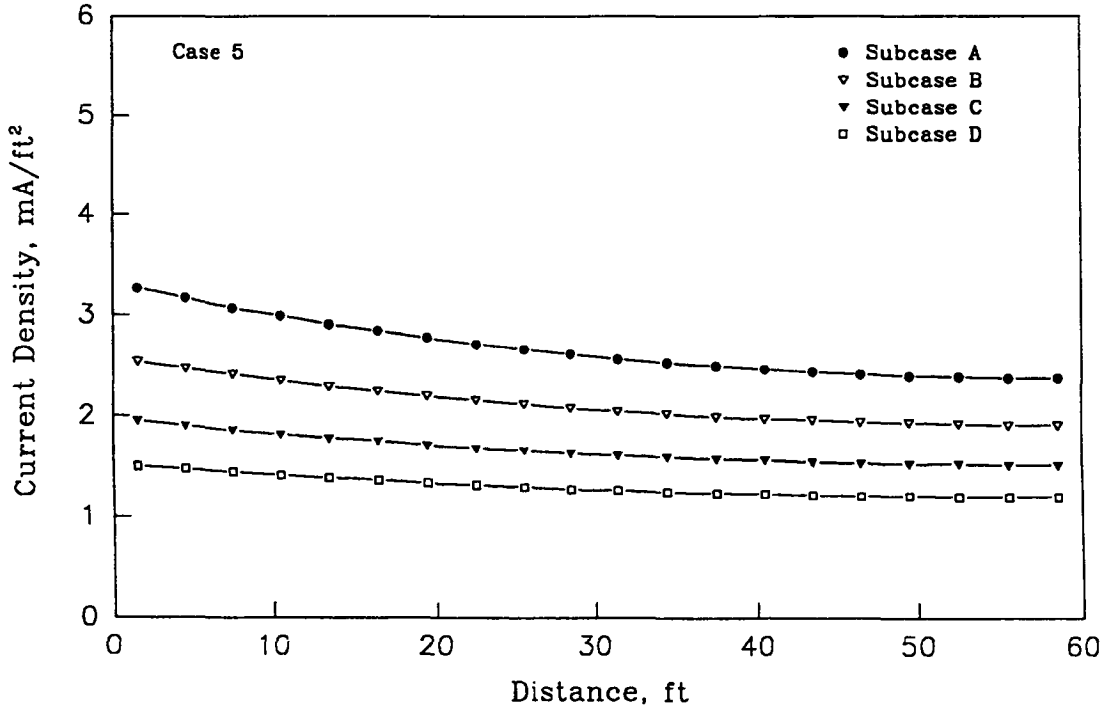

Figure C-51. Steel Polarization versus Distance from the Power Feed Strip.

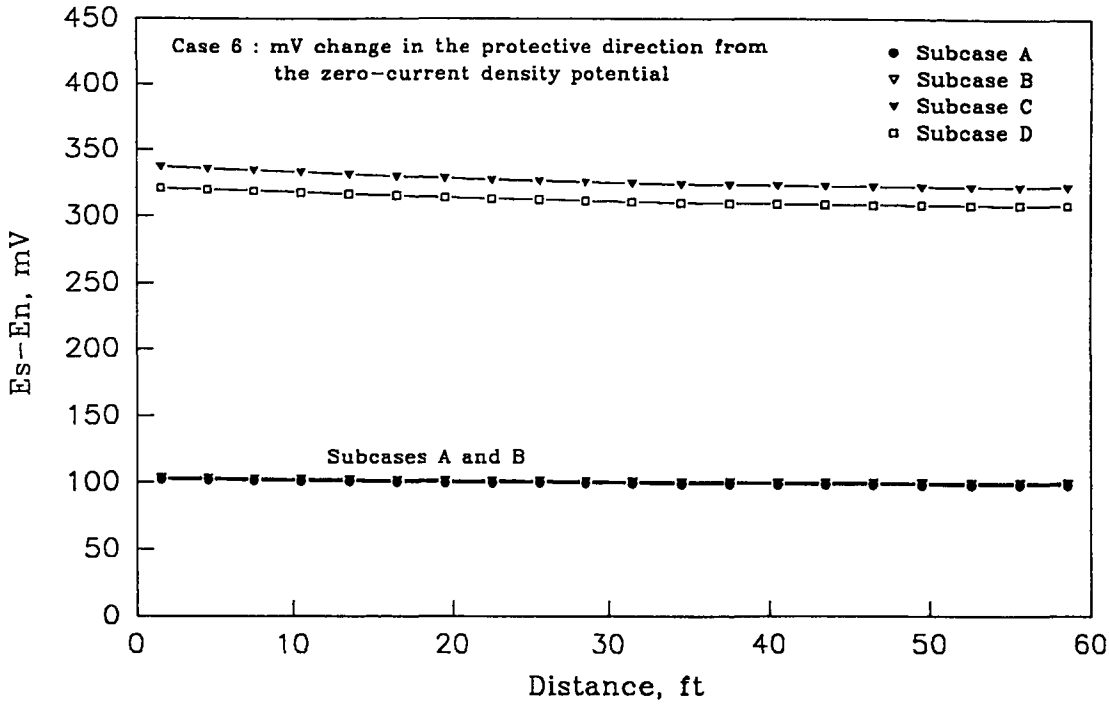

Figure C-52. Current Density to Steel versus Distance from the Power Feed Strip.

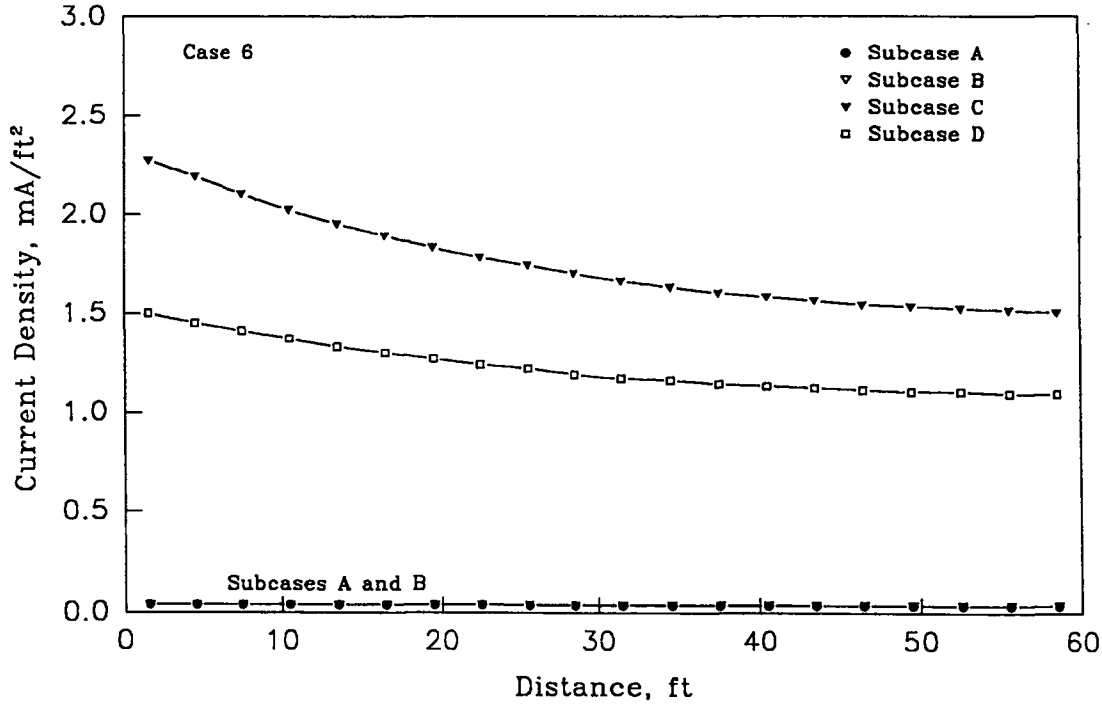

Figure C-53. Steel Polarization versus Distance from the Power Feed Strip.

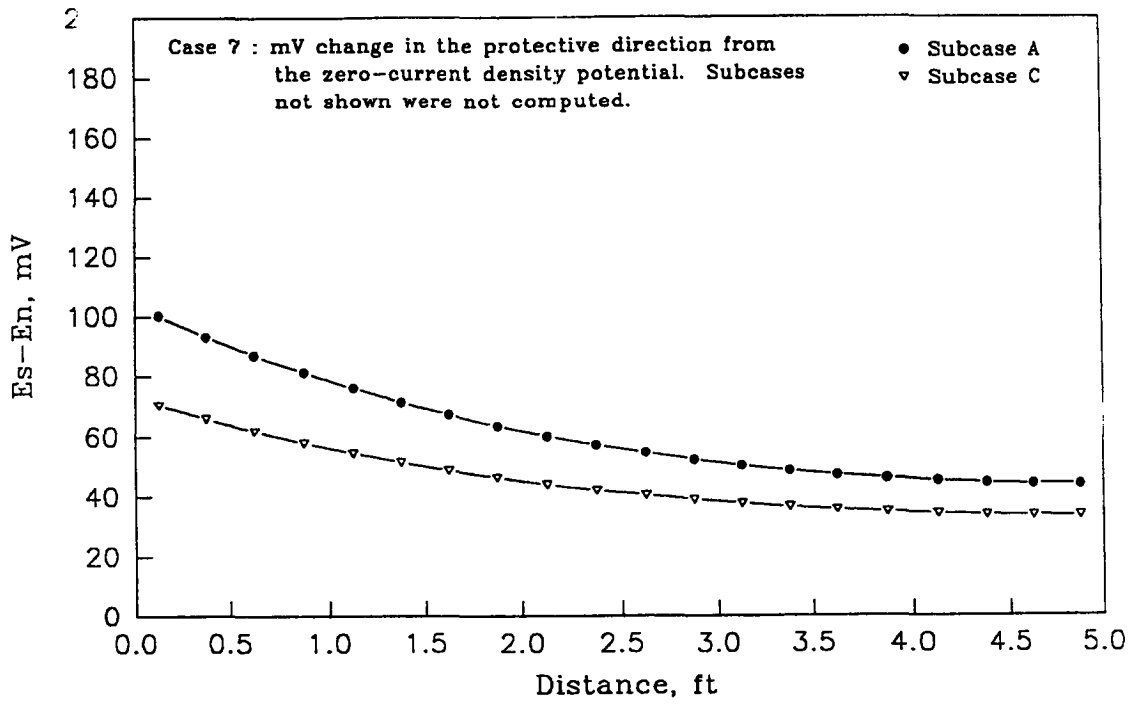

Figure C-54. Current Density to Steel versus Distance from the Power Feed Strip.

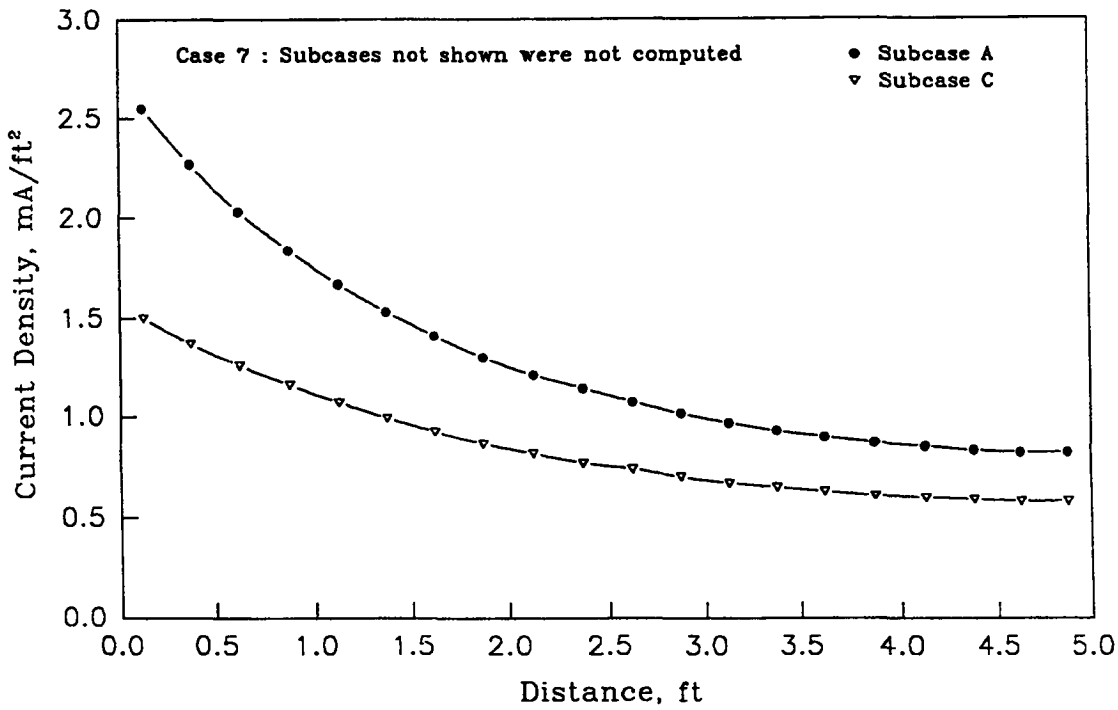

Figure C-55. Steel Polarization versus Distance from the Power Feed Strip.

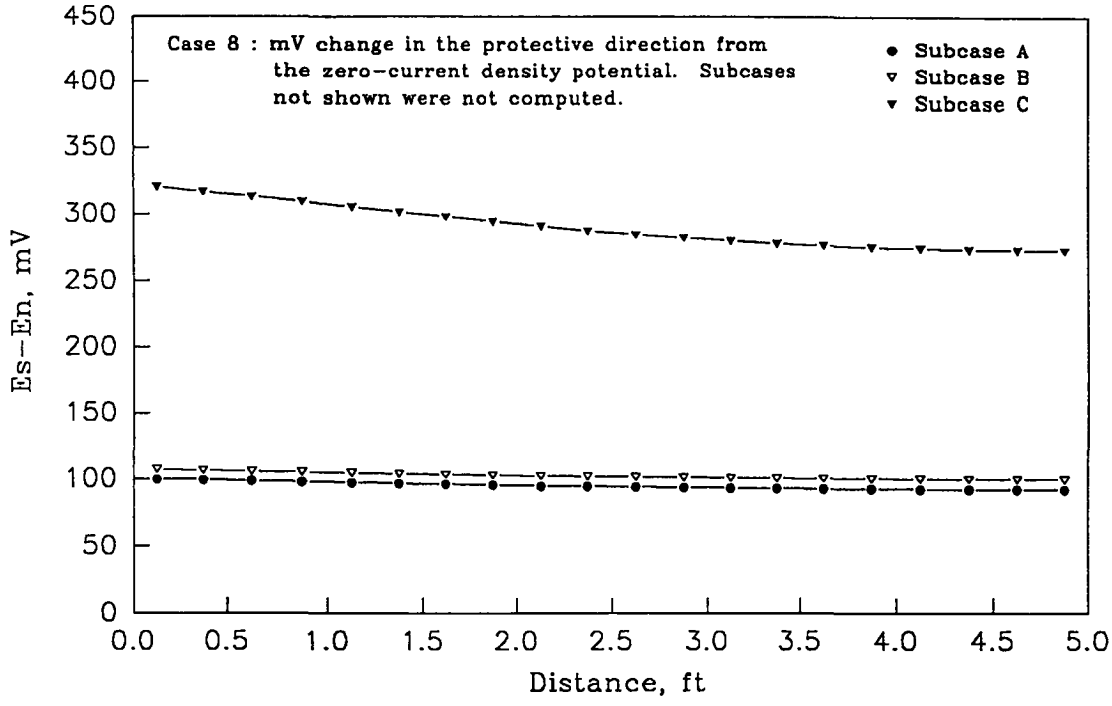

Figure C-56. Current Density to Steel versus Distance from the Power Feed Strip.

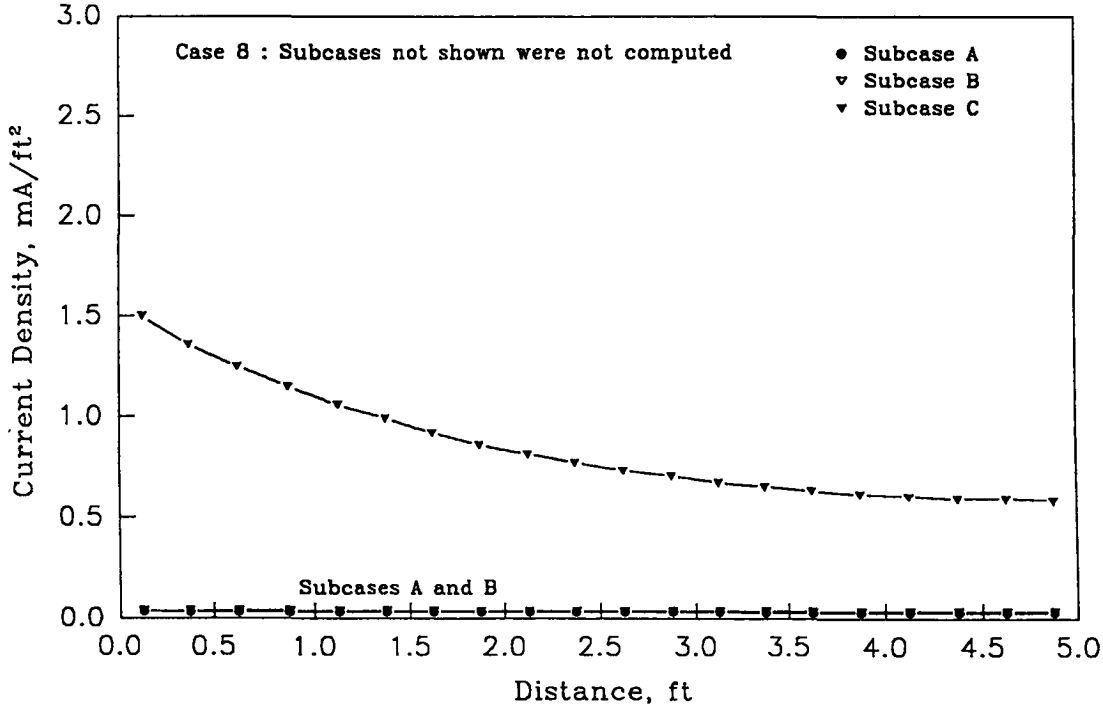

Figure C-57. Steel Polarization versus Distance from the Power Feed Strip.

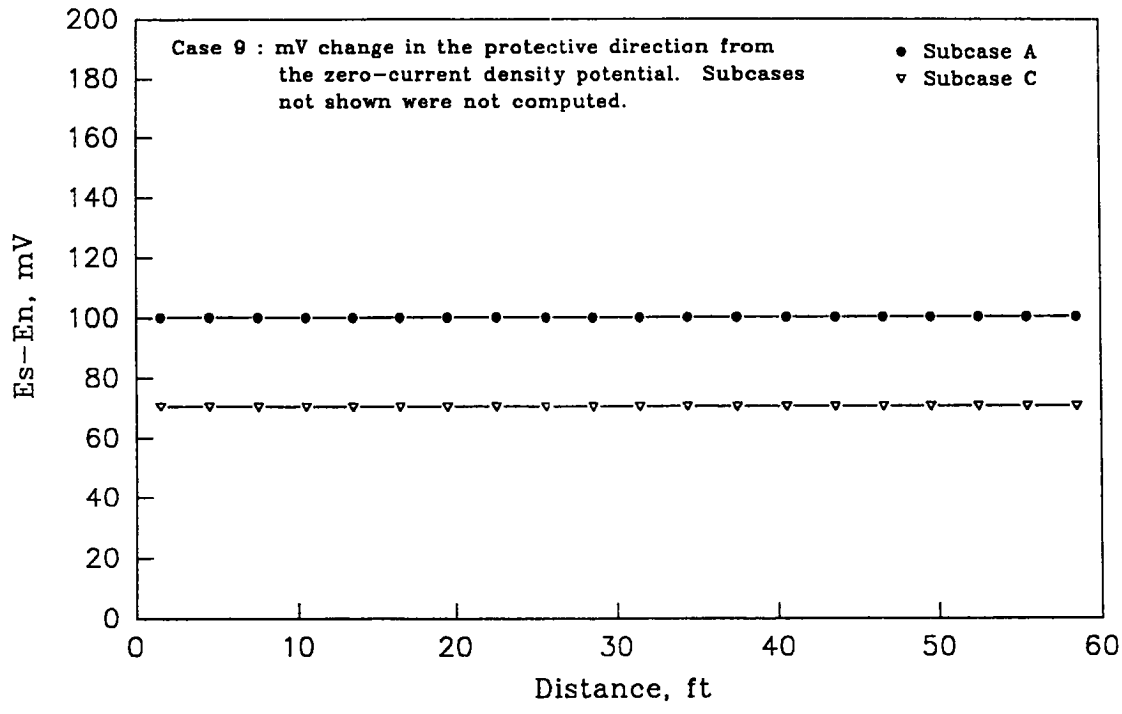

Figure C-58. Current Density to Steel versus Distance from the Power Feed Strip.

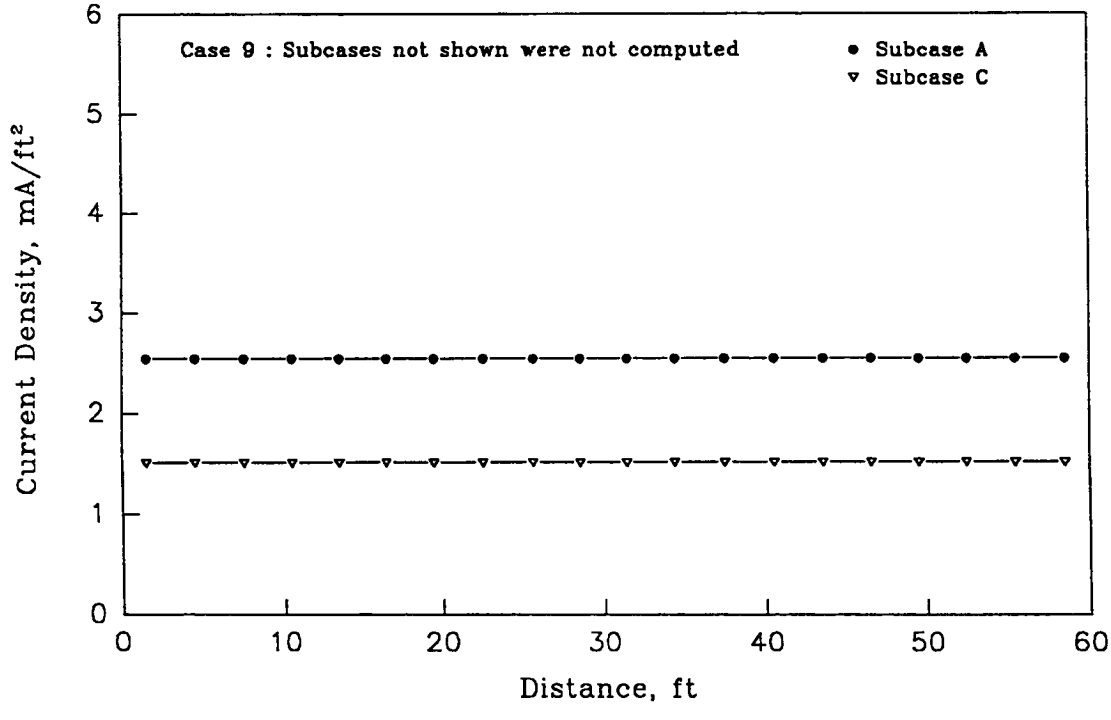

Figure C-59. Steel Polarization versus Distance from the Power Feed Strip.

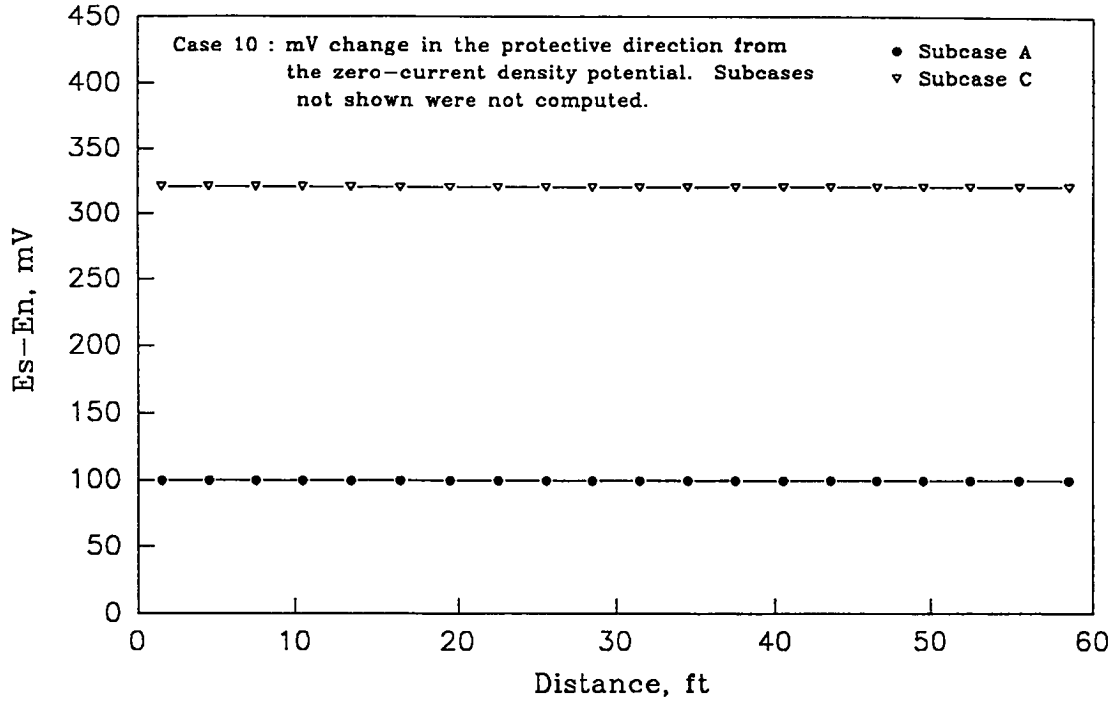

Figure C-60. Current Density to Steel versus Distance from the Power Feed Strip.

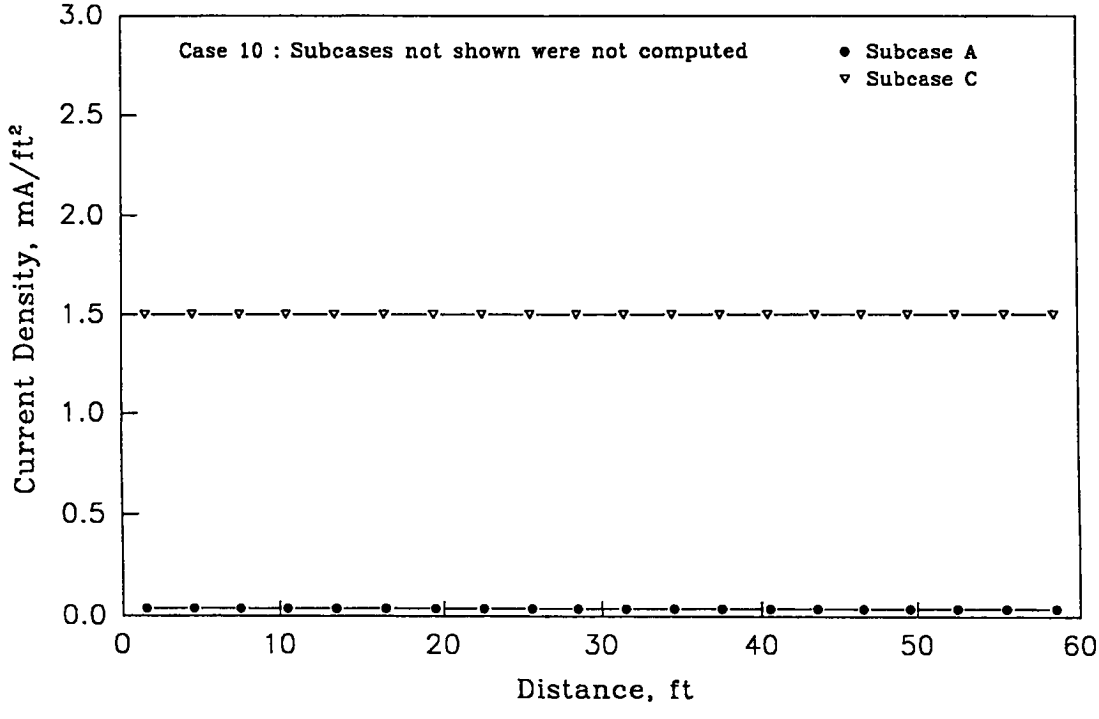

Figure C-61. Steel Polarization versus Distance from the Power Feed Strip.

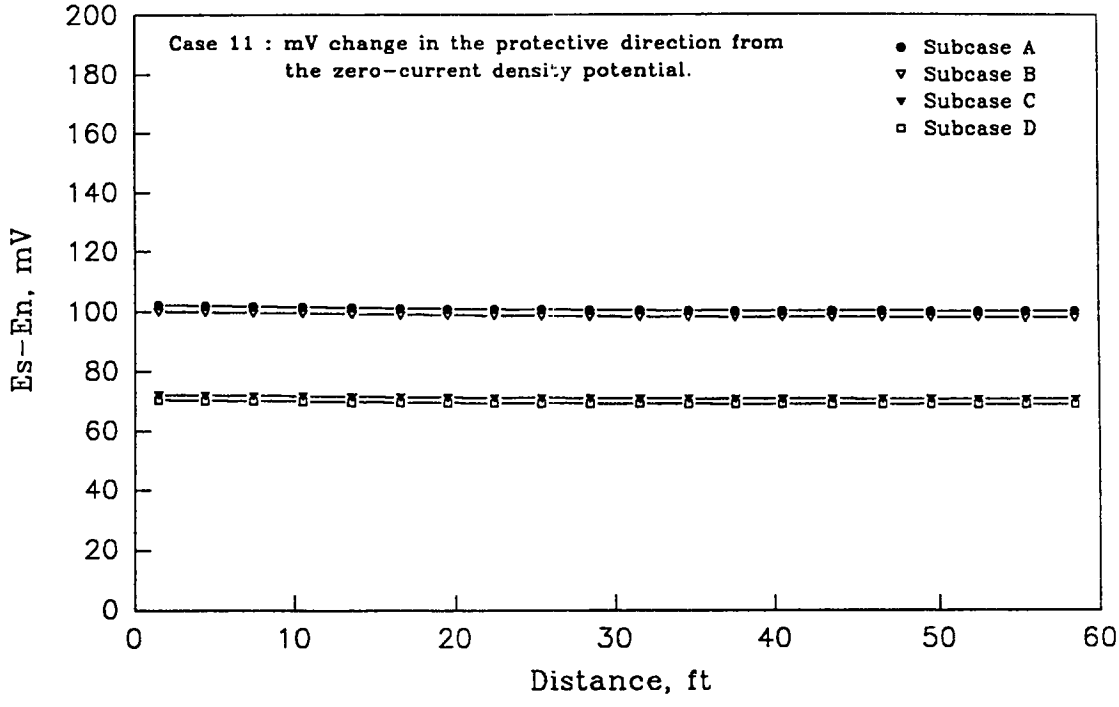

Figure C-62. Current Density to Steel versus Distance from the Power Feed Strip.

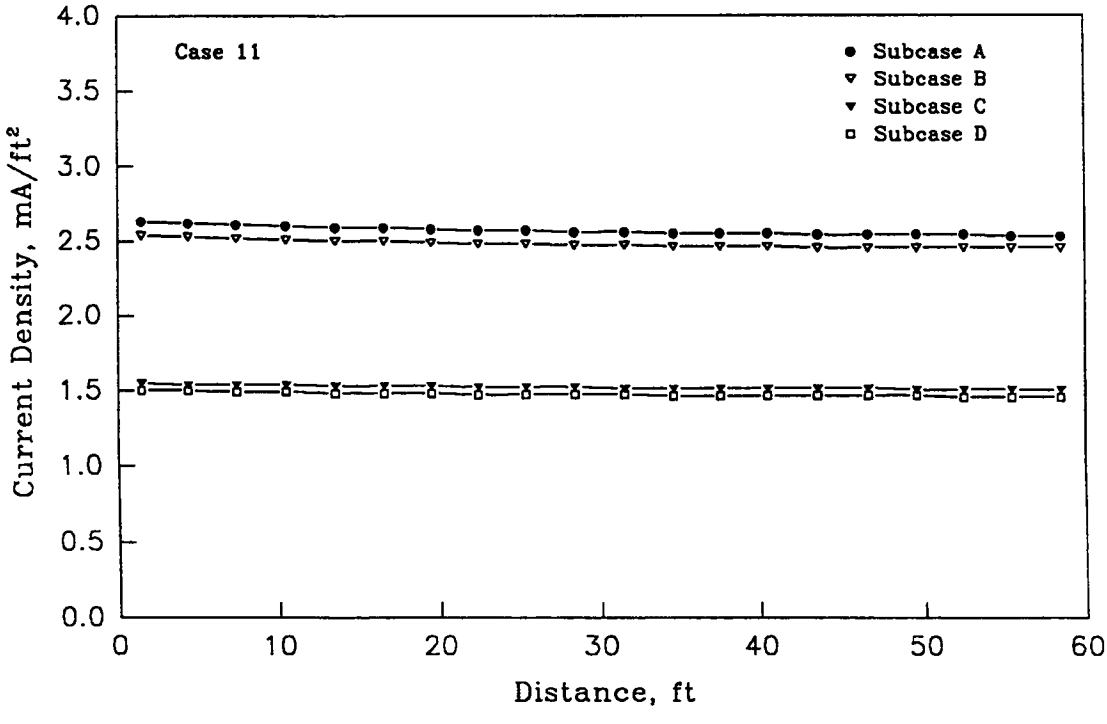

Figure C-63. Steel Polarization versus Distance from the Power Feed Strip.

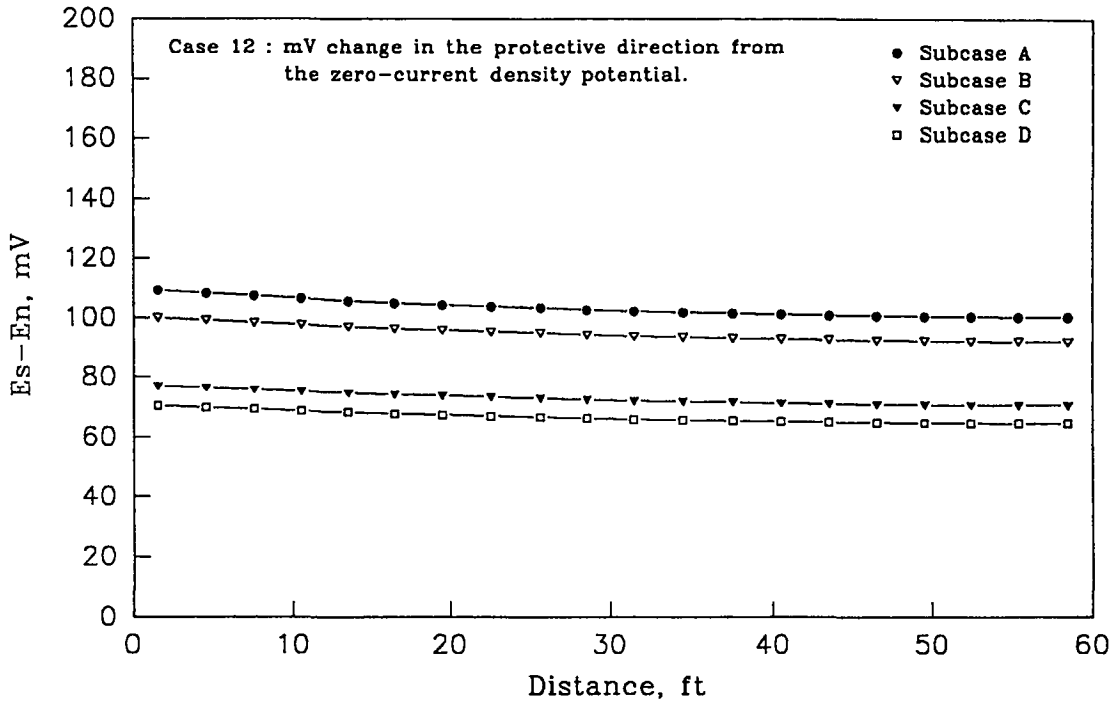

Figure C-64. Current Density to Steel versus Distance from the Power Feed Strip.

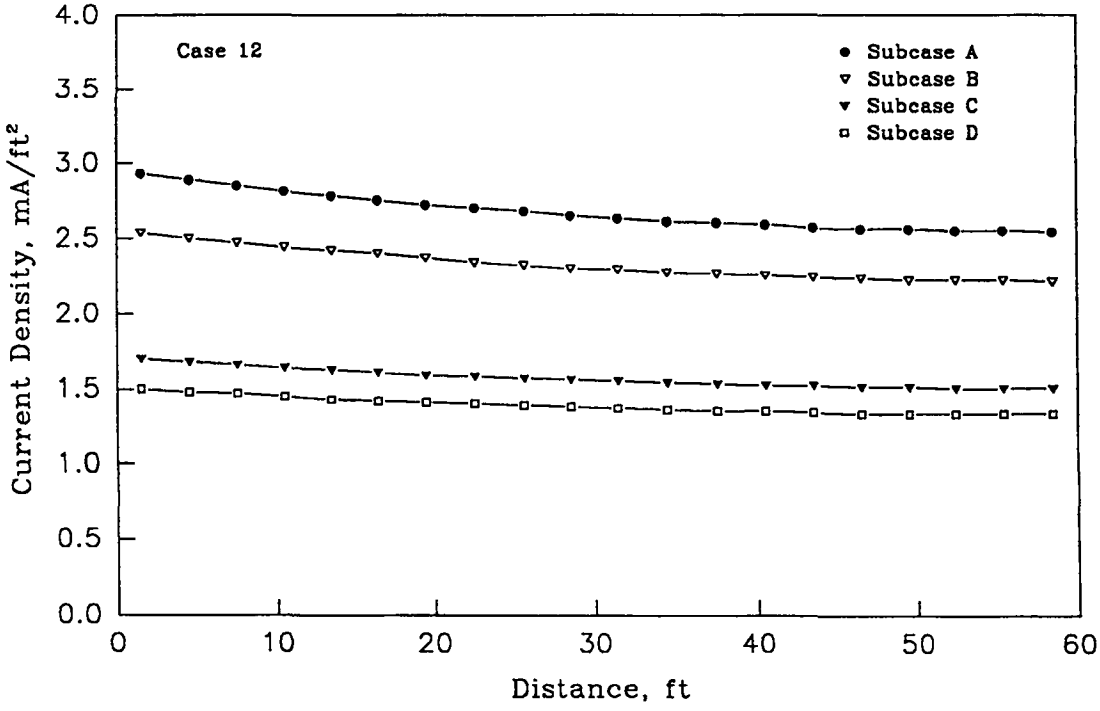

Figure C-65. Steel Polarization versus Distance from the Power Feed Strip.

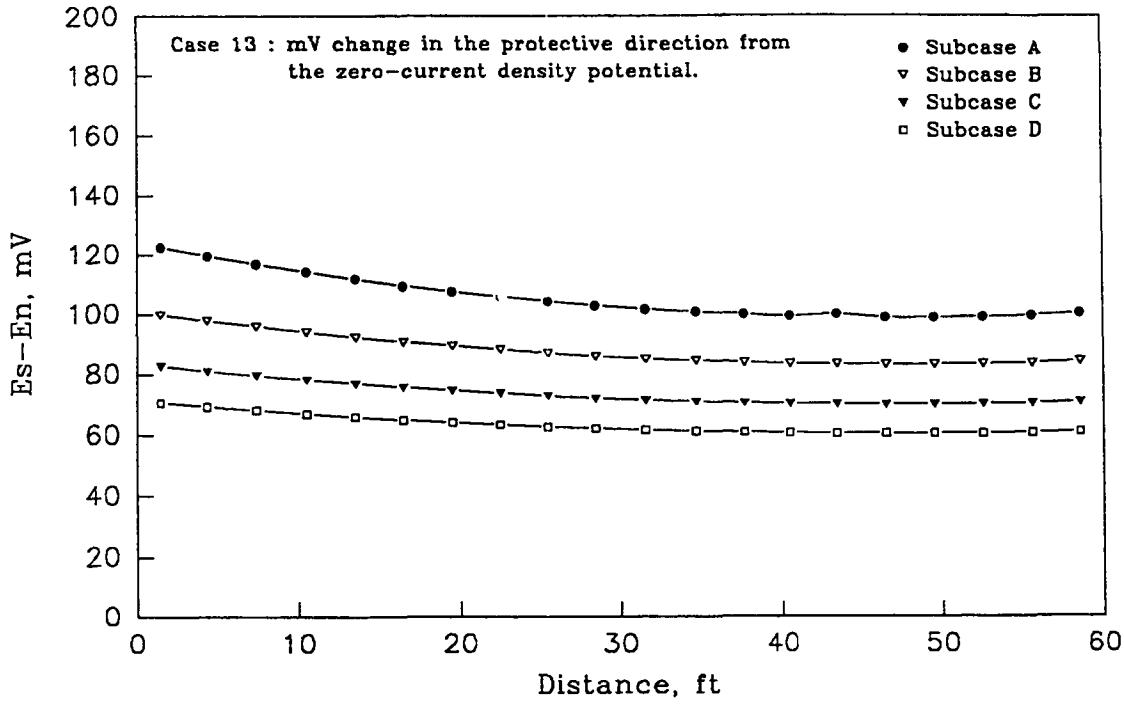

Figure C-66. Current Density to Steel versus Distance from the Power Feed Strip.

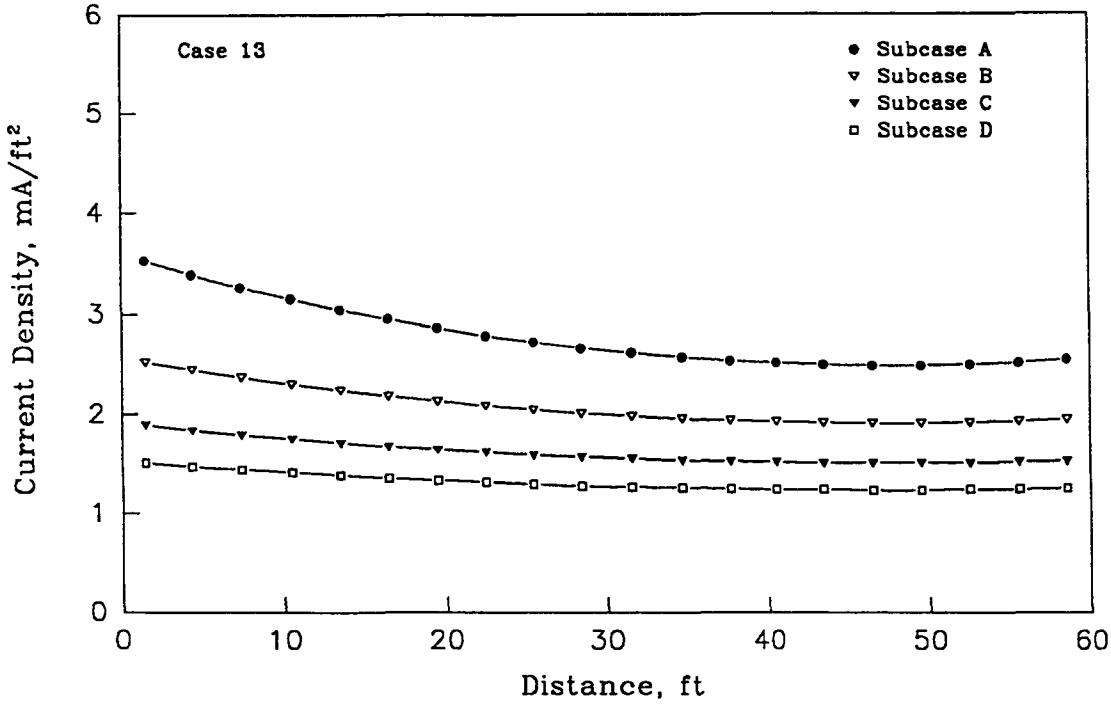

Figure C-67. Steel Polarization versus Distance from the Power Feed Strip.

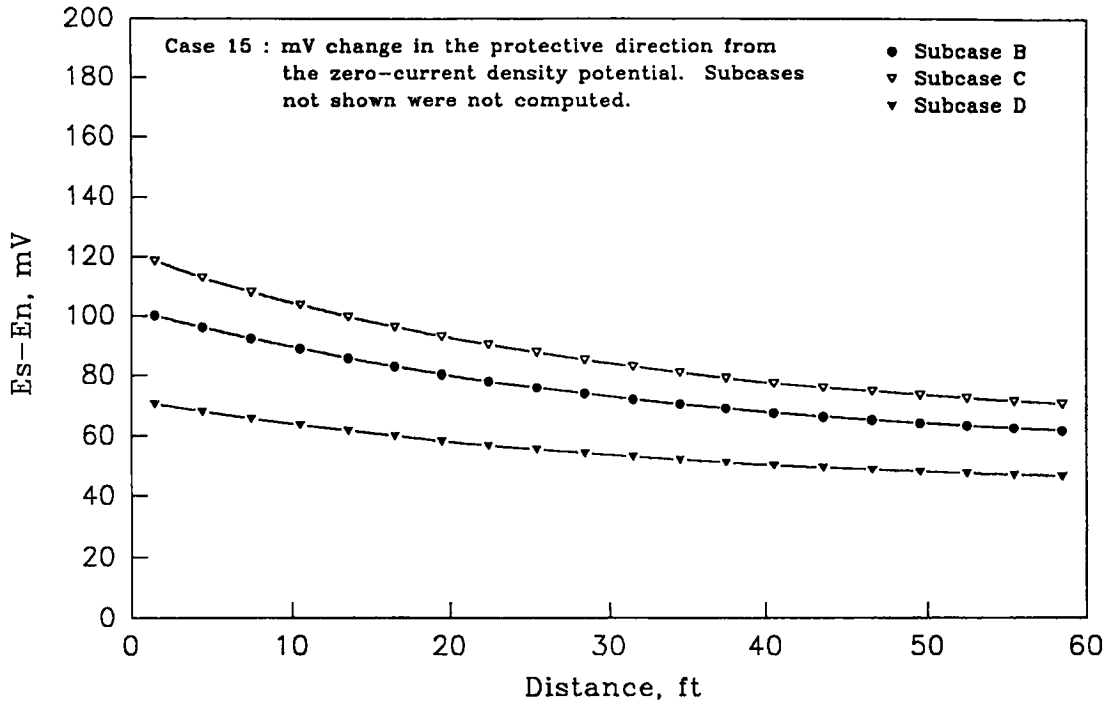

Figure C-68. Current Density to Steel versus Distance from the Power Feed Strip.

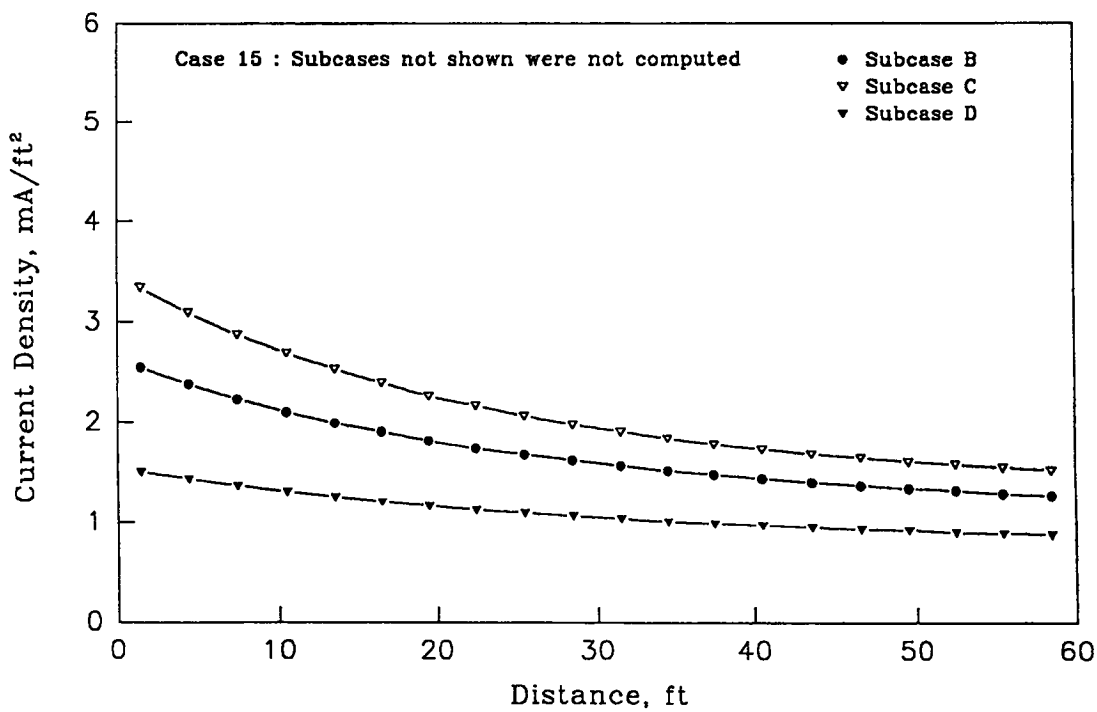

Figure C-69. Steel Polarization versus Distance from the Power Feed Strip.

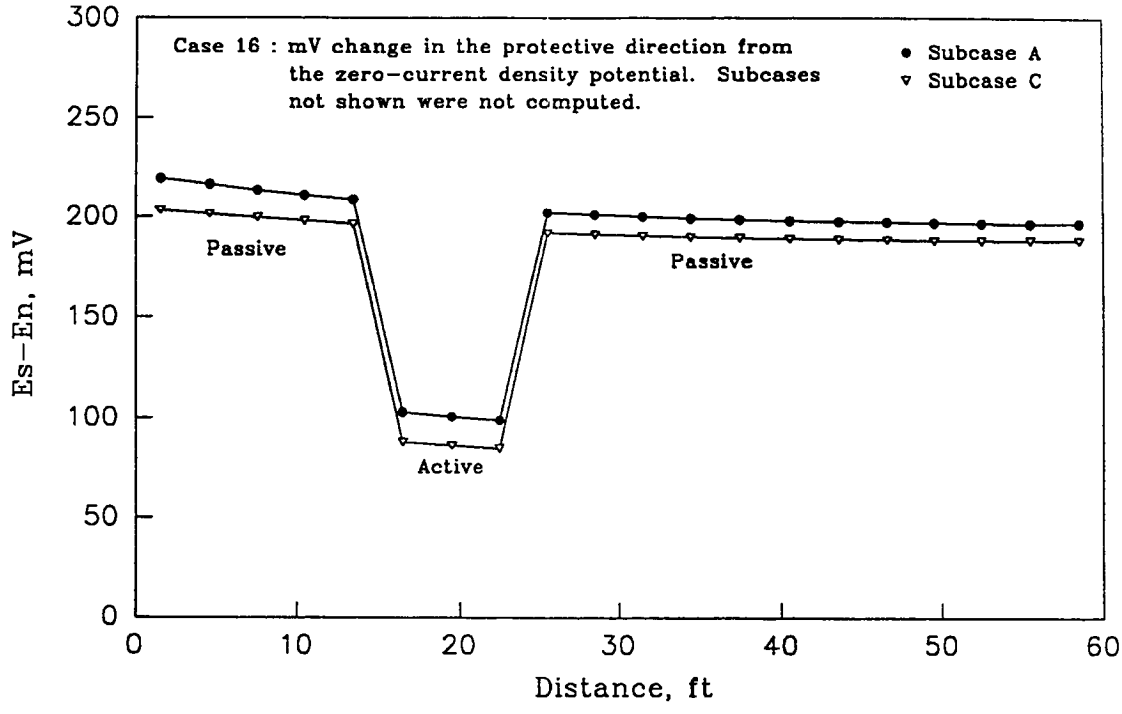

Figure C-70. Current Density to Steel versus Distance from the Power Feed Strip.

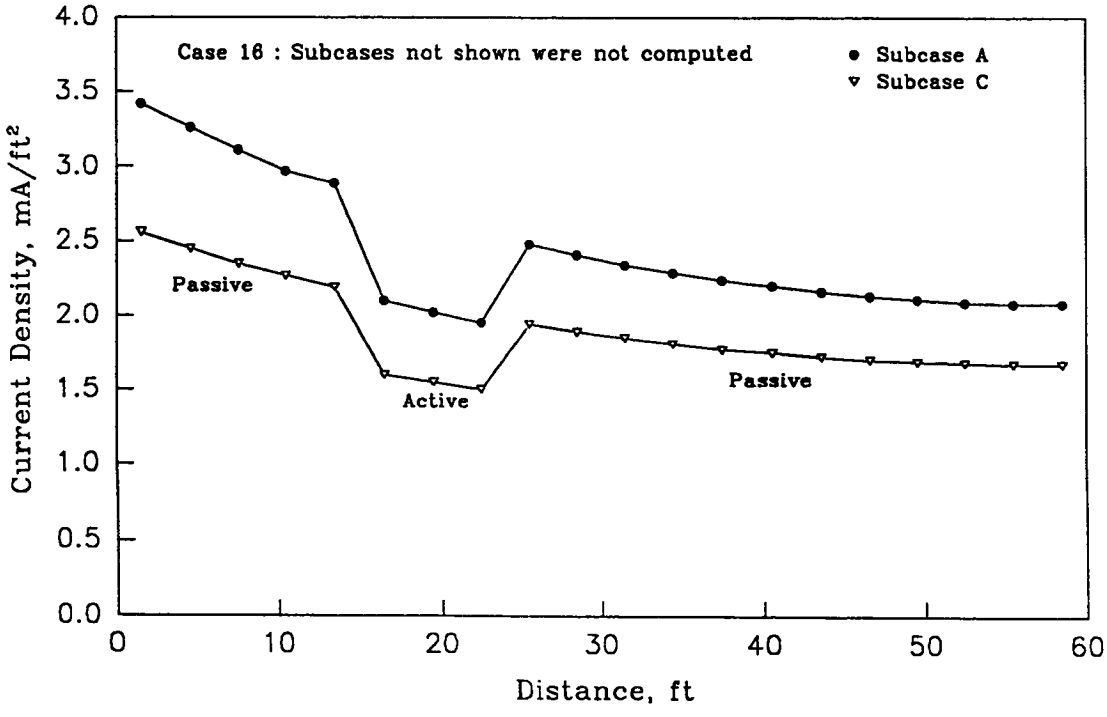

References

1. Clear, K.C. *"Growth and Evolution of Bridge Deck Cathodic Protection,"* NACE 1985 Bridge Deck Seminar, San Antonio, Texas, February 1985.

2. Mayne, J.E.O. and M.J. Pryor. *"The Mechanism of Corrosion of Iron by Sodium Hydroxide Solution,"* J. Chem. Soc., (1950), p. 3229.

3. Hausmann, D.A. *"Steel Corrosion in Concrete,"* Materials Protection, November 1967.

4. Clear, K.C. *"Chloride at the Threshold - Comments and Data,"* American Concrete Institute Convention Debate, Anaheim, California, March 1983.

5. Clear, K.C. and R.E. Hay. *"Time to Corrosion of Reinforcing Steel in Concrete Slabs, Volume 1: Effect of Mix Design and Construction Parameters,"* Federal Highway Administration Report FHWA-RD-73-32, April 1973.

6. Chamberlain, W.P., R.J. Irwin and D.E. Amsler. *"Waterproofing Membranes for Bridge Deck Rehabilitation,"* Research Report No. 52, New York State Department of Transportation, May 1977.

7. Stratful, R.F. *"Experimental Cathodic Protection of a Bridge Deck,"* Transportation Research Record, No. 550, 1974

8. Broomfield, J.P. and J.S. Tinnea. *"Cathodic Protection and Reinforced Concrete Bridge Components: Volume 1, Report of Survey and Field Data,"* Strategic Highway Research Program Report SHRP-C/WP-92-618 May 14, 1991.

9. NACE Standard Recommended Practice RP0290-90, RP0290-90 *"Cathodic Protection of Reinforcing Steel in Atmospherically Exposed Concrete." 1990*

10. Bennett, J.E. and T.A. Mitchell. *"Depolarization of Cathodically Protected Reinforcing Steel in Concrete,"* Paper No. 373, NACE CORROSION/89, New Orleans, April, 1989.

11. Funishashi, M. and J.B. Bushman. *"Technical Review of 100 mV Polarization Shift Criterion for Reinforcing Steel in Concrete,"* Corrosion, Vol. 47, No. 5, National Association of Corrosion Engineers, Houston, Texas, 1989.

12. Funihashi, M. and W.T. Young. *"Investigation of 100 mV Polarization Shift Criterion for Reinforcing Steel in Concrete,"* Paper No. 193, NACE CORROSION/92, Nashville, 1992.

13. Laird, R.C.G. *"Performance Evaluation Testing of Conductive Coating Cathodic Protection Systems on Thin Parking Garage Slabs,"* Paper No. 553, NACE CORROSION/91, Cincinnati, 1991.

14. Stratfull, R.F. *"Criterion for the Cathodic Protection of Bridge Decks,"* Corrosion of Reinforcement in Concrete Construction, Society of Chemical Industry, London, Chapter 18, 1983.

15. Vrable, J.B. *"Cathodic Protection for Reinforced Concrete Bridge Decks,"* NCHRP Report 180, 1977.

16. Jurach, P.J. *"An Evaluation of the Effectiveness of Cathodic Protection on Seven Bridge Decks,"* California Department of Transportation, Report No. FHWA-CA-SD-80/1, 1981.

17. Burke, N.D. and J.B. Bushman. *"Corrosion and Cathodic Protection of Steel Reinforced Concrete Bridge Decks,"* Federal Highway Administration Report No. FHWA-IP-88-007, 1988.

18. Clear, K.C. *"Measuring Rate of Corrosion of Steel in Field Concrete,"* June, 1988, (Available from Kenneth C. Clear, Inc., Rt. 1, Box 347, Boston, VA 22713).

19. Van Delinder, L.S. Ed. *"Corrosion Basics, An Introduction,"* National Association of Corrosion Engineers, p. 184, Houston, Texas, 1984.

20. Burke, N.D. and J.B. Bushman. *"Corrosion and Cathodic Protection of Steel Reinforced Concrete Bridge Decks,"* FHWA Report No. FHWA-IP-88-007, p. 45, 56, 58, CORRPRO Companies, Inc., 1988.

21. Swiat, W.J. *"Evaluation Report, Bridge No. B-645 on I-64 Over 13th View Street, Norfolk, Virginia,"* Prepared for Strategic Highway Research Program Contract SHRP C-102F, CORRPRO Companies, Inc., December, 1991.

22. Moore, A.E. *"Effect of Electric Current on Alkali-Silica Reaction,"* in Ion Effects of Alkalies in Cement and Concrete, pp. 69-72, Purdue University, West Lafayette, Indiana, 1978.

23. Nixon, P.J. and I.P. Gillson. *"An Investigation Into Alkali-Silica Reaction in Concrete Bases at An Electricity Substation at Drakelow Power Station, England,"* in Concrete Alkali-Aggregate Reactions, Patrick Grattan-Bellew, Editor, pp. 173-177, Noyes Publications, New Jersey, 1987.

24. Ozol, M.A. *"Alkali-Silica Reaction of Concrete in Electrical Substation Piers Accelerated by Electric Currents,"* in Symposium on Petrography Applied to Concrete and Concrete Aggregates, B. Erlin and D. Stark, Editors, ASTM STP-1061, ASTM 1990.

25. Tashiro, C. and Y. Katsuo. *"Study of Relationship Between Alkali-Aggregate Reaction and Electrical Resistivity,"* 8th International Conference on Alkali-Aggregate Reaction, pp. 381-384, Kyoto, Japan, 1989.

26. Natesaiyer, K. and K.C. Hover. *"Investigation of Electrical Effects on Alkali-Aggregate Reaction,"* in Concrete Alkali-Aggregate Reactions, Patrick Grattan-Bellew, Editor, pp. 466-472, Noyes Publications, New Jersey, 1986.

27. Natesaiyer, K. *"The Effect of Electric Currents on Alkali-Silica Reaction in Concrete,"* a Ph.D. Dissertation, Graduate School of Cornell University, Ithaca, New York, January 1990.

28. Kawamura, M. and M. Ichise. *"Characteristics of Alkali-Silica Reaction in the Presence of Sodium and Calcium Chloride,"* Cement and Concrete Research, Volume 20, pp. 757-766, 1990.

29. Kawamura, M. and K. Takemoto. *"Correlation Between Pore Solution Composition and Alkali-Silica Expansion in Mortars Containing Various Flyashes and Blast Furnace Slags,"* International Journal of Cement Composites and Lightweight Concrete, Volume 10, No. 4, pp. 215-223, 1988.

30. Kawamura, M., et al. *"Effect of Sodium Chloride Supplied From the Surrounding Solution on the Alkali-Silica Reaction,"* Review of the General Meeting of the Cement Association of Japan, pp. 258-261, 1988.

31. Strategic Highway Research Program. *"Electrochemical Chloride Removal and Protection of Concrete Bridge Components Volume I: Laboratory Studies,"* SHRP-S-657, 1993.

32. Balamuralikrishna, R. *"Glass Electrodes as a Sensor for pH of Pore-Water in Concrete,"* MS Thesis, Florida Atlantic University, Dec., 1990

33. Natesaiyer, K and K.C. Hover. *"Investigation of Electrical Effects on Alkali-Aggregate Reaction in Concrete-Alkali-Aggregate Reactions,"* Noyes Publications, pp. 466-471, 1986.

34. Ali, M.G., et al. *"Migration of Ions in Concrete Due To Cathodic Protection Current,"* Cement & Concrete Research, Vol. 22, pp. 79-94, 1992.

35. Newman, J. *"Electrochemical Systems,"* 1991

36. Carlaws, H. and J. Jaeger. *"Conduction of Heat in Solids,"* pg. 101

37. Clemena, G.C. et al. *"Inclusion of Rebar Corrosion Rate Measurements in Condition Surveys of Concrete Bridge Decks,"* Transportation Research Board Record 1347, Maintenance, pp. 46-55. 1992.

Concrete and Structures Advisory Committee

Chairman
James J. Murphy
New York Department of Transportation (retired)

Vice Chairman
Howard H. Newlon, Jr.
Virginia Transportation Research Council (retired)

Members

Charles J. Arnold
Michigan Department of Transportation

Donald E. Beuerlein
Koss Construction Co.

Bernard C. Brown
Iowa Department of Transportation

Richard D. Gaynor
National Aggregates Association/National Ready Mixed Concrete Association

Robert J. Girard
Missouri Highway and Transportation Department

David L. Gress
University of New Hampshire

Gary Lee Hoffman
Pennsylvania Department of Transportation

Brian B. Hope
Queens University

Carl E. Locke, Jr.
University of Kansas

Clellon L. Loveall
Tennessee Department of Transportation

David G. Manning
Ontario Ministry of Transportation

Robert G. Packard
Portland Cement Association

James E. Roberts
California Department of Transportation

John M. Scanlon, Jr.
Wiss Janney Elstner Associates

Charles F. Scholer
Purdue University

Lawrence L. Smith
Florida Department of Transportation

John R. Strada
Washington Department of Transportation (retired)

Liaisons

Theodore R. Ferragut
Federal Highway Administration

Crawford F. Jencks
Transportation Research Board

Bryant Mather
USAE Waterways Experiment Station

Thomas J. Pasko, Jr.
Federal Highway Administration

John L. Rice
Federal Aviation Administration

Suneel Vanikar
Federal Highway Administration

11/19/92

Expert Task Group

John Apostolos
California Department of Transportation

Robert J. Girard
Missouri Highway and Transportation Department

Richard Kessler
Florida Department of Transportation

Carl E. Locke, Jr.
University of Kansas

David G. Manning
Ontario Ministry of Transportation

Paul Virmani
Federal Highway Administration

8/9/93